THÈSE DE DOCTORAT
DE L'UNIVERSITÉ DE LILLE

Laboratoire de Mécanique Multiphysique Multiéchelle - FRE 2016, CNRS

Présentée par

CAO Yajun

pour obtenir le grade de

DOCTEUR DE L'UNIVERSITÉ DE LILLE

Domaine

GÉNIE CIVIL

Sujet de la thèse

Contribution à la modélisation numérique du comportement non-linéaire des géomatériaux hétérogènes

Soutenue le 15 Novembre 2018 devant le jury composé de :

R. GIOT	Professeur, Université de Poitiers	*Rapporteur*
J.C MICHEL	Directeur de Recherche CNRS, LMA	*Rapporteur*
H. DUMONTET	Professeur, Sorbonne Université	*Examinateur*
J.F. SHAO	Professeur, Université de Lille	*Examinateur*
W.Q. SHEN	Maître de conférences, HDR, Université de Lille	*Co-encadrant*
N. BURLION	Professeur, Université de Lille	*Directeur de thèse*

LaMcube-UNIVERSITÉ DE LILLE

© 2018 Tous droits réservés.

© 2018 Tous droits réservés.

Abstract

The objective of this thesis aims to explore the effective mechanical behaviors of porous materials involved with pore or inclusion problem. The key point to this problem is to homogenize such a highly heterogenous material incorporating more physical geometry information at a given scale and coupling with the interactions among different scales. In this work, several typical microstructures of rock-like materials are respectively considered here covering multiscale constituents. We sought to determine how the presence of pores and inclusion with different morphologies influences the macroscopic elastic, plastic flow and time-dependent behaviors. For this propose, a multiscale homogenization procedure for nonlinear behavior is proposed based on a Fast Fourier Transform(FFT) homogenization method to upscale the local behavior from the micro-scale transition to meso-scale and then to macroscale. Firstly, a class of porous material with two population of pores at two separated scales are investigated. The effect of the ratio between meso-porosity and micro-porosities on its macroscopic elastic properties and plastic yield are specially analysed and compared with the closed-form solutions. Secondly, due to a limitation to obtain an analytical criterion for the materials with both pores and inclusions configured at same scale, particular attentions are focused on the anisotropic behavior induced by the pore and inclusion geometry characters. We provide a reference numerical solution of plastic yield stresses evolution for this class of materials covering the effect of pore and inclusion geometrical characters like the volume fractions, distributions, aspect ratios, orientations and so on. Thirdly, We shall consider a class of three-scale materials with the inclusion embedded at meso-scale and pores configured at micro-scale. An unified multi-scale homogenization method is developed to account for the instantaneous and time-dependent behavior. Hence, we will focus on the effect of geometrical characters of meso-inclusion on the macroscopic plastic yield and viscoplastic deformations. Finally, a macroscopic criterion is obtained to consider a porous material with double porosities and inclusions by using the modified secant method. To estimate the failure of rock-like materials, a time-dependent damage plastic model is developed. Comparisons between numerical results and experimental data show that this model can well characterize its effective behavior with complex micro-structures.

© 2018 Tous droits réservés.

© 2018 Tous droits réservés.

Résumé

L'objectif de cette thèse est d'explorer les comportements mécaniques efficaces des matériaux poreux impliqués dans les problèmes des pores ou d'inclusion. Le point essentiel de ce problème consiste à homogénéiser un matériau très hétérogène en intégrant davantage d'informations de géométrie physique à une échelle donnée et en les couplant aux interactions entre différentes échelles. Dans ce travail, quatre microstructures typiques de matériaux semblables à la roche sont respectivement considérées ici et couvrent différents constituants. Nous avons cherché à déterminer comment la présence de pores et l'inclusion avec différentes morphologies influencent les comportements élastiques, plastiques et dépendants du temps macroscopiques. Pour cette proposition, une procédure d'homogénéisation multi-échelles pour le comportement non linéaire est proposée sur la base d'une méthode d'homogénéisation par Transformation de Fourier Rapide (FFT) pour augmenter le comportement local de la micro-échelle à la méso-échelle puis à la macro-échelle. Tout d'abord, une classe de matériau poreux avec deux populations de pores à deux échelles séparées est étudiée. L'effet du rapport entre la méso-porosité et la micro-porosités sur son rendement élastique et plastique macroscopique est spécialement analysé et comparé aux solutions sous forme fermée. Deuxi èmement, en raison d'une limitation pour obtenir un critère analytique pour les matériaux avec à la fois des pores et des inclusions configurés à la même échelle, des attentions particulières sont focalisées sur le comportement anisotrope induit par les caractères géométriques des pores et des inclusions. Nous fournissons une solution numérique de référence pour l'évolution des contraintes de rendement plastique pour cette classe de matériaux couvrant l'effet des caractères géométriques des pores et des inclusions tels que les fractions volumiques, les distributions, les proportions, les orientations, etc. Troisièmement, nous allons considérer une classe de matériaux à trois échelles avec l'inclusion intégrée à l'échelle méso et les pores configurés à l'échelle micro. Une méthode d'homogénéisation unifiée à plusieurs échelles est développée pour prendre en compte le comportement instantané et dépendant du temps. Nous allons donc nous intéresser à l'effet des caractères géométriques de la méso-inclusion sur le rendement plastique macroscopique et les déformations viscoplastiques. Enfin, un critère macroscopique général est obtenu pour considérer la matrice poreuse de forme elliptique et l'inclusion rigide distribuée de manière aléatoire en utilisant la méthode de la sécante modifiée. Pour estimer la défaillance des matériaux semblables à la roche, un modèle en plastique endommagé en fonction du temps est développé. Les comparaisons entre les résultats numériques et les données expérimentales montrent que ce modèle peut bien caractériser son comportement efficace avec des micro-structures complexes.

© 2018 Tous droits réservés.

© 2018 Tous droits réservés.

Acknowledgement

I would like firstly to express my most sincere gratitude to my main supervisor Professor Jianfu Shao and Professor Nicolas Burlion providing such a chance for me to study here, I am very appreciate for their precious guidances, patiences, confidences and courages during three years of my research and it is a great honour for me to be one of their students.

I would like also to acknowledge my co-supervisor, Professor Wanqing Shen, for his support, motivation and enthusiasm throughout the duration of my research. We often discuss together about my research work and he is like a big brother giving me a lots of help.

I would like to thank to Professor MICHEL and Professor GIOT for being the rapporteurs of my thesis, and also to Professor DUMONTET, who have kindly examined my work.

I am deeply grateful to Professor Wang Wei in China, for his helps, support me and give me a lot of advises.

Great thanks also give to my colleagues and friends for agreeable ambiance, their assistance, in China and in France.

Special thanks also give to Dr.CUI Xiaoyan, she is always with me, with her love and continuous encourage and support and patience. For her, a thousand times over.

Finally, a great appreciation must give to my dear mother, sister and my whole families, for their unconditional love, support and encouragement during my whole life. My dear mother and sister, thanks again, they are so great and important to me. I would never be so happiness and continue my following career without them. I love them. I love my families.

Yajun

© 2018 Tous droits réservés.

© 2018 Tous droits réservés. lilliad.univ-lille.fr

Table Of Contents

© 2018 Tous droits réservés.

Thèse de Yajun Cao, Université de Lille, 2018

© 2018 Tous droits réservés. lilliad.univ-lille.fr

Thèse de Yajun Cao, Université de Lille, 2018

© 2018 Tous droits réservés.

lilliad.univ-lille.fr

Thèse de Yajun Cao, Université de Lille, 2018

© 2018 Tous droits réservés. lilliad.univ-lille.fr

Notations

Tensor notations

a	scalar	$.$	simple contraction
$\underline{a}$	vector	$:$	double contraction
$\mathbf{a}$	second-order tensor	$\otimes$	tensor product
$\mathbb{A}$	fourth-order tensor	$\mathbb{I}$	fourth-order identity tensor
$\boldsymbol{\delta}$	second-order identity tensor	$\mathbb{K}$	$= \mathbb{I} - \mathbb{J}$
$\mathbb{J}$	$= \frac{1}{3}\boldsymbol{\delta} \otimes \boldsymbol{\delta}$		
$\mathbb{E}_i$	fourth order transverse isotropic tensors		
$(\boldsymbol{a} \otimes \boldsymbol{b})_{ijkl}$	$= a_{ij}b_{kl}$		
$(\boldsymbol{a}\underline{\overline{\otimes}}\boldsymbol{b})_{ijkl}$	$= \frac{1}{2}(a_{ik}b_{jl} + a_{il}b_{jk})$		

© 2018 Tous droits réservés.

Thèse de Yajun Cao, Université de Lille, 2018

Common parameters

$\mathbb{C}_m$	elastic stiffness tensor of the solid matrix
$\mathbb{S}_m$	elastic compliance tensor of the solid matrix
$\mathbb{C}_r$	fictitious elastic stiffness tensor of $r-th$ phase
$\mathbb{C}_r^{max}$	elastic stiffness tensor of the hardest phase
$\mathbb{C}_r^{min}$	elastic stiffness tensor of the softest phase
$\mathbb{C}^{hom}$	homogenized drained elastic stiffness tensor
$\mathbb{S}^{hom}$	homogenized drained elastic compliance tensor
$\mathbb{A}_r$	strain concentration tensor of $r-th$ phase
$\mathbb{P}_r$	Hill tensor of $r-th$ phase
$\mathbb{P}_d$	the corresponding distribution tensor
$\mathbb{P}_{hom}$	Hill tensor of homogenized phase
$\mathbb{S}_r$	Eshelby's tensor
f_r	volume fraction of $r-th$ phase
$\mathbf{\Gamma_0}$	Green tensor
Σ_{eq}	the macroscopic equivalent stress
Σ_m	the macroscopic mean stress

© 2018 Tous droits réservés. lilliad.univ-lille.fr

General Introduction

The Callovo-Oxfordian (COx) argillite, is well known as a potential host rock for the geological repository of radioactive wastes. Because of its good geological properties characterized by the absence of major fractures, low permeability, and high mechanical strength. The mineral composition and pores of Cox argillite are observed by the SEM image as shown in Fig.1. The main minerals of Cox argillite are consisted of three components: clay minerals, quartz, and calcite grains. A series of experimental investigations has been carried out by the French Agency for Nuclear Waste Management (Andra) regarding the mineralogical composition, microstructural analysis, and mechanical, thermal, and hydraulic properties of Cox argillite ([Robinet et al., 2012, Zhang et al., 2012, Zhang et al., 2014, Menaceur et al., 2015, Armand et al., 2017, Liu et al., 2018]). From these experimental results, it is found that the macroscopic behaviors of Cox argillite are inherently related to mineralogical composition and microstructural morphology as well as the porosity. The presence of clay minerals can increase the overall deformability of argillite due to the plastic deformation of the clay matrix. However, the fine-grained carbonates seems to cause the opposite trend of clayey matrix with respect to the amount of carbonate present [Klinkenberg et al., 2009]. Meanwhile, the mechanical behavior becomes more brittle due to the increase in the calcite and quartz content ([Hu et al., 2014]).

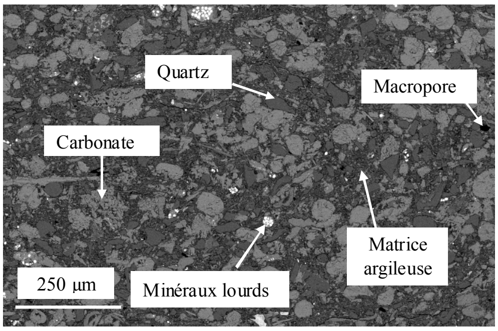

Figure 1: Mineral composition of the Cox argillite by SEM image from [Robinet, 2008].

On the other hand, most composite materials are multi-scale in nature, such as rock,

© 2018 Tous droits réservés.

Thèse de Yajun Cao, Université de Lille, 2018

concrete, metals and polymers, which are characterized as multi-phase porous materials. With the development of digital imaging techniques, their complex microstructure can be directly visualized and quantified across multiple scales. For instance, the mineralogy and microscopic features of shales reported by [Saif et al., 2017a, Saif et al., 2017b] consists of organic matter (kerogen), fine clay structures, inorganic mineral grains and pores at multi-scales. Its complexity is demonstrated in the compositional heterogeneity of the each mineral compositions as well as the microstructure of the pore, which mainly govern its macroscopic behavior. Full-field properties and effective mechanical behaviors involved with multi-scale characterization of these materials can be determined by experimental techniques to study the characteristics of microstructure and local mechanisms at small scales ([Uchic et al., 2006]), also can be estimated by using different homogenization methods on a representative unit-cell([Eshelby, 1957, Mori and Tanaka, 1973, Ponte Castañeda and Willis, 1995, Michel and Suquet, 2004, Moulinec and Suquet, 1998, Ponte Castañeda, 2002, Özdemir et al., 2008, Matouṣ et al., 2017]). Experimental and numerical studies have demonstrated that porous materials have some remarkable properties including pressure sensitivity, anisotropy and time dependent behaviors are related to the physical features of microstructure with embedded pores and mineralogical compositions.

On the other hand, analytical solutions for porous materials also have well been developed. Following the study of [Gurson, 1977] who presented a well investigation on strength homogenization for porous materials with a von Mises matrix , various nonlinear homogenization techniques have been employed to explore closed-form strength criteria for ductile porous media ([Castañeda, 1991, Michel and Suquet, 1992, Gologanu et al., 1994, Gologanu et al., 1993, Garajeu and Suquet, 1997, Monchiet et al., 2011, Monchiet et al., 2014]. For rock-like materials such as rock, concrete and soil, which exhibiting significant frictional properties, assessments of the macroscopic strength properties were inspired by the previous work for nonlinear homogenization theories. The solid matrix obeyed typical Drucker-Prager criterion with one population of voids has been developed which mainly concerned the consideration of porosity, matrix compressibility, plastic anisotropy and so on ([Guo et al., 2008, Maghous et al., 2009, Ortega et al., 2011, Shen et al., 2017b]). Based on these work, some extended to the modeling of porous material reinforced with rigid particles([Shen et al., 2013, He et al., 2013]) or multi-scales materials([Vincent et al., 2009a, Ortega and Ulm, 2013, Shen et al., 2014, Shen and Shao, 2016b, Shen and Shao, 2016a]). With a multi-step homogenization procedure, the microstructure features like porosity and inclusion volume fraction characterized by each well separated scales can be explicitly taken into account, while these closed-form analytical models are usually

© 2018 Tous droits réservés. lilliad.univ-lille.fr

Thèse de Yajun Cao, Université de Lille, 2018

not feasible for complex microstructure. Moreover, the influences of interactions between voids and other microstructure physical information (void shapes, sizes, orientation and distribution, etc.), cavitation, local stress and strain concentrations are not so easily to be considered simultaneously in a criterion and limit to determine a periodic microstructure that is statistically similar to the actual microstructure under consideration.

In order to accurately estimate overall response of heterogeneous material, a FFT-based homogenization method proposed by [Moulinec and Suquet, 1994] devoted to the evaluation of physical properties for periodic boundary conditions to overcome the unit cell problem of complex microstructures ([Jiang and Shao, 2012], [Lebensohn et al., 2012], [Li et al., 2016], [Moulinec and Suquet, 1998], [Vincent et al., 2014b]). Particular attention have been focused on the convergence of FFT iterative schemes([Eyre and Milton, 1999], [Michel et al., 2001], [Monchiet and Bonnet, 2012], [Moulinec and Silva, 2014]) and significant progresses have been well considered for various applications such as linear and nonlinear elastic homogenization([Gélébart and Mondon-Cancel, 2013], [Kabel et al., 2014]), nonlinear elasto-plastic([Jiang and Shao, 2012]) and viscoplastic behavior([Lebensohn et al., 2012]), Darcy problem([Monchiet et al., 2009]) and crack prediction([Li et al., 2012]). Despite this computational homogenization technique do not lead to a closed-form constitutive equations, but make it possible to introduce detailed microstructural information including mechanical properties and physical properties such as different sizes, regular and irregular of pores shape, random distribution and other more complex microstructure.

The main objective of this thesis is to estimate the effective properties for heterogenous materials involved with different multiscale microstructure features. To this end, the FFT-based homogenization method is employed and will be extended to take into account effects of pore and inclusion geometry characters on the macroscopic elastoplastic and time dependent behaviors. The present thesis is composed of the following Chapters.

Chapter I will recall the classical analytical homogenization methods for effective elastic stiffness estimations and recent developments of homogenized strength criteria for porous materials with von-Mises and Drucker-Prager type matrix. Then the estimations predicted by different homogenization methods will be presented. To solve the multi-scale problem proposed in this work, the Fast Fourier Transform homogenization method is employed and basic knowledge of this method will be introduced. Then its efficiency and accuracy will be validated by comparison with the finite element method.

Chapter II will present a two-step homogenization procedure to describe the elastic-plastic behavior of a class of materials with two populations of pores at two separated

© 2018 Tous droits réservés. lilliad.univ-lille.fr

Thèse de Yajun Cao, Université de Lille, 2018

scales using FFT-based homogenization techniques. This method is firstly verified by the finite element method to confirm its accurate estimations of macroscopic behaviors of porous materials with two populations of pores. With the help of the proposed method, the microstructure with different porosity ratios f/ϕ between two populations of pores but having a given total porosity is specially investigated. The emphasis is put on relative roles of both families of pores on the macroscopic elastic and plastic responses. In particular, the simulated results are compared with the existed closed form solutions.

Chapter III is devoted to a numerical study of the microstructure with both inclusions and pores embedded at same scale. We will focused on the anisotropy properties induced by the pore and inclusion geometry. Two specially arrangements of inclusions and pores are considered. The evolution of macroscopic elastic modulus and plastic yield stress with respect to pore and inclusion geometrical characters are presented and discussed in detail. Finally, we will apply this framework to predict the macroscopic yield stresses of Berea sandstone and compare with the experimental data.

Chapter IV is focused on a class of rock-like materials with meso inclusions and micro pores configured at different scales. The aim of this chapter is to study effects of inclusions and pores on plastic and viscoplastic deformation of rock-like materials. A two-step homogenization procedure is also established to consider unified instantaneous plastic and time dependent behavior. A series of numerical results are presented to investigate the effects of inclusion geometrical characters like elastic stiffness, shape, aspect ratio, orientation as well as inclusion volume fraction and porosity on macroscopic plastic yield stress and creep deformation. Finally, we applied the proposed model to simulate the time-dependent behavior of COx claystone in creep and relaxation tests.

Chapter V is aiming to establish a multi-scale elastoplastic damage model to determine the macroscopic mechanical behavior for the geomaterials containing complex multi-scale features. To this end, we will employ the work of [Maghous et al., 2009] and [Shen and Shao, 2016a] to develop a general strength criterion considering the elliptic form porous matrix and randomly distributed rigid inclusions. Typically, due to the fact that the failure of geomaterial always include strain softening behavior, it is assumed that the rock failure is a time-dependent progressive damage process, we will introduce a rate-dependent damage model to describe the degradation effect on the elastic and plastic behavior. Based on these studies, we will apply this damage constitutive relation on the claystone and Vaca

© 2018 Tous droits réservés. lilliad.univ-lille.fr

Thèse de Yajun Cao, Université de Lille, 2018

Muerta shale rock to account for the effect of multi population of inclusions and pores configured in a porous matrix. The modeling results will be compared with the triaxial compressible experimental data.

© 2018 Tous droits réservés. lilliad.univ-lille.fr

Thèse de Yajun Cao, Université de Lille, 2018

© 2018 Tous droits réservés. lilliad.univ-lille.fr

Chapter I

Homogenization methods of hetergenous materials

Contents

© 2018 Tous droits réservés.

Thèse de Yajun Cao, Université de Lille, 2018

1 Classical homogenization theory for elastic composites

Heterogeneity is in nature of engineering materials. Generally, such a heterogenous material often appears to be homogeneous at a enough larger length scale than that of their constituents. Following a theoretical interest focused on that how assemble the heterogenous characters to represent an "effective" or "average" properties and which characters dominate this, the elastic behavior is of the prime interest for the researchers to seek for the more accurate estimations of macroscopic stiffness tensor. In this section, several classical homogenization methods for elastic constant estimation will be recalled.

Generally, the effective elastic properties in most cases cannot be determined exactly due to the complexity of microstructure and its random arrangement. One approach is to estimate them using rigorous upper and lower bounds. [Voigt, 1889] adopted isotropic strain assumption to obtain the estimation of the effective composite stiffness matrix as the weighted volume average of the stiffness matrices of constituent phases. In addition, according to the isotropic stress assumption, [Reuss, 1929] estimated the effective composite compliance matrix as the weighted volume average of the compliance matrices of constituent phases. [Hill, 1952] has proven that for isotropic constituent phases and composites, Voigt estimation and Reuss estimation, respectively, provide the upper and lower bounds for the effective bulk and shear moduli of composites. A narrower upper and lower bounds was obtained based on the Hashin shtrikman variational principle ([Hashin and Shtrikman, 1962,Hashin and Shtrikman, 1963]), by respectively choosing the homogeneous reference material with modulus tensor $\mathbb{C}_0$ to be equal to the "maximum" and "minimum" modulus tensors of the phases $\mathbb{C}_r$. Then it was generalized for random composites and nonlinear composite ([Willis, 1977,Willis, 1983] and [Talbot and Willis, 1985]).

a) Bound of Voigt and Reuss:

$$\begin{aligned} Voigt : \mathbb{A}_r = \mathbb{I}, \quad \mathbb{C}^{hom}_{vogit} &= \sum_{r=1}^{N} f_r \mathbb{C}_r \\ Reuss : \mathbb{B}_r = \mathbb{I}, \quad \mathbb{S}^{hom}_{Reuss} &= \sum_{r=1}^{N} f_r \mathbb{C}_r^{-1} \end{aligned} \tag{I .1}$$

b) Bound of Hashin-Shtrikman:

$$\begin{aligned} upper\ bound : \mathbb{T}_r^{HS+} &= [\mathbb{C}_r + \mathbb{C}_r^{max}(\mathbb{S}_r^{-1} - \mathbb{I})]^{-1}\mathbb{C}_r^{max}\mathbb{S}_r^{-1} \\ \mathbb{A}_r^{HS+} &= \mathbb{T}_r^{HS+}(\sum_{r=1}^{N} f_r \mathbb{T}_r^{HS+})^{-1} \\ \mathbb{C}^{hom}_{HS+} &= \sum_{r=1}^{N} f_r \mathbb{C}_r \mathbb{A}_r^{HS+} \end{aligned} \tag{I .2}$$

© 2018 Tous droits réservés. lilliad.univ-lille.fr

Thèse de Yajun Cao, Université de Lille, 2018

$$\begin{aligned} lower\ bound: \mathbb{T}_r^{HS-} &= [\mathbb{C}_r + \mathbb{C}_r^{min}(\mathbb{S}_r^{-1} - \mathbb{I})]^{-1}\mathbb{C}_r^{min}\mathbb{S}_r^{-1} \\ \mathbb{A}_r^{HS-} &= \mathbb{T}_r^{HS-}(\sum_{r=1}^{N} f_r \mathbb{T}_r^{HS-})^{-1} \\ \mathbb{C}_{HS-}^{hom} &= \sum_{r=1}^{N} f_r \mathbb{C}_r \mathbb{A}_r^{HS-} \end{aligned} \tag{I .3}$$

Since the excellent work of Eshelby [Eshelby, 1957] who developed an elegant formalism to determine the elastic solution of a single inclusion embedded in an infinite matrix of material with uniform exterior loading. The classical dilute scheme is the primary use of this theory based on the eigenstrain concepts for the prediction of effective modulus. It requires the assumption that the inhomogeneities or inclusions in the composite are dilutely distributed in the homogeneous matrix. Due to fact that the effect of stress-field interactions between inclusions is negligible, thus it is generally not suit for high fraction of inclusion configured composites. However, this method provides a good basis for the development of many approximation methods. Since then, to account for the interactions between inclusions, a so-called self-consistent method is proposed by [Hill, 1965b].

Different from the dilute method, in the standard Self-Consistent method, the idea is that the Eshelby equivalent principle is applied with respect to homogenized medium, not for the matrix. Unfortunately, the self-consistent method can produce negative effective bulk and shear responses, for voids, with pore volume fractions of 50% and higher. For rigid inclusions, it produces infinite effective bulk responses for any volume fraction and infinite effective shear responses above 40% ([Zohdi and Wriggers, 2008]). This method also has various extensions, such as differential self consistent (DSC) scheme and iterative self consistent (ISC) scheme.

Another widely used mean-field homogenization method named Mori Tanaka method ([Mori and Tanaka, 1973]). This method has also developed in the framework of Eshelby's inclusion theory [Eshelby, 1957] to correlate averaged stresses and strains of the constituents with those of the matrix in a composite. Meanwhile, it is known that for composites with randomly oriented microcracks or disks, the Mori-Tanaka method violates the corresponding rigorous bounds of the Hashin Shtrikman type ([Ponte Castañeda and Willis, 1995, Zheng and Du, 2001]) and fails to satisfy a necessary symmetry requirement. In this case, the Mori Tanaka estimate is generally lack of accuracy for non-dilute concentrations of non-spherical inclusions.

Motivated by this reason, [Ponte Castañeda and Willis, 1995] precisely considered both the role of the inclusions interaction and spatial distribution with respect to two independent function in the framework of Hashin-Shtrikman principle. The idea is based

© 2018 Tous droits réservés. lilliad.univ-lille.fr

Thèse de Yajun Cao, Université de Lille, 2018

on correlation functions of inclusion pairs, which can characterize the inclusion distribution to the second order in a statistical sense. However, it seems to have practically difficulties to give an explicit expression if the inclusion distribution is not identical.

Although these methods have limitations to some special cases, all the schemes provide efficient and straight forward algorithms for the prediction of elastic constants. For each scheme, the strain concentration tensor and effective stiffness tensor are respectively taken the following forms.

a) Dilute scheme estimations:

$$\begin{aligned}\mathbb{A}_r^{dl} &= [\mathbb{I} + \mathbb{P}_r(\mathbb{C}_r - \mathbb{C}_m)]^{-1} \\ \mathbb{C}_{dl}^{hom} &= \mathbb{C}_m + \sum_{r=2}^{N} f_r(\mathbb{C}_r - \mathbb{C}_m)\mathbb{A}_r^{dl}\end{aligned} \tag{I .4}$$

b) Mori-Tanaka scheme estimations:

$$\begin{aligned}\mathbb{A}_r^{MT} &= \mathbb{A}_r^{dl}[\sum_{s=1}^{N} f_s\mathbb{A}_s^{dl}]^{-1} \\ \mathbb{C}_{MT}^{hom} &= \sum_{r=1}^{N} f_r\mathbb{C}_r\mathbb{A}_r^{MT}\end{aligned} \tag{I .5}$$

c) PCW scheme estimations:

$$\begin{aligned}\mathbb{A}_r^{PCW} &= [\mathbb{I} + \mathbb{P}^r : (\mathbb{C}_r - \mathbb{C}_m)]^{-1} : [f_m\mathbb{I} + \sum_{s=1}^{N} f_s[\mathbb{I} + \mathbb{P}_s : (\mathbb{C}_s - \mathbb{C}_m)]^{-1}]^{-1} \\ \mathbb{C}_{PCW}^{hom} &= \mathbb{C}^m + (\mathbb{I} - \sum_{r=1}^{N} f_r[(\mathbb{C}_r - \mathbb{C}_m)^{-1} + \mathbb{P}_r]^{-1} : \mathbb{P}_d)^{-1} : \sum_{r=1}^{N} f_r[(\mathbb{C}_r - \mathbb{C}_m)^{-1} + \mathbb{P}_r]^{-1}\end{aligned} \tag{I .6}$$

d) Self consistent scheme estimations:

$$\begin{aligned}\mathbb{A}_r^{SC} &= [\mathbb{I} + \mathbb{P}_{hom}(\mathbb{C}_r - \mathbb{C}_{hom})]^{-1} \\ \mathbb{C}_{SC}^{hom} &= \mathbb{C}_m + \sum_{r=2}^{N} f_r(\mathbb{C}_r - \mathbb{C}_m)\mathbb{A}_r^{SC}\end{aligned} \tag{I .7}$$

As an example, the effective elastic properties of a two-phase composite with spherical rigid inclusion is estimated. A direct comparison of effective bulk and shear modulus predicted by these classic homogenization methods has been shown in Fig.I .1. At a first view, significant differences are presented for each other. It should be pointed out that the Mori Tanaka method is consistent with the Hashin Shtrikman lower bound for a two-phase matrix-rigid inclusion composite. However, for the porous material, the MT method

© 2018 Tous droits réservés. lilliad.univ-lille.fr

Thèse de Yajun Cao, Université de Lille, 2018

estimation is corresponding to the Hashin Shtrikman upper bound. On the other hand, the PCW microstructure for the MT model indicates that the MT moduli could be found from the PCW formulation, but this would require a spatial distribution that is identical to the oriented inclusion shape ([Hu and Weng, 2000]).

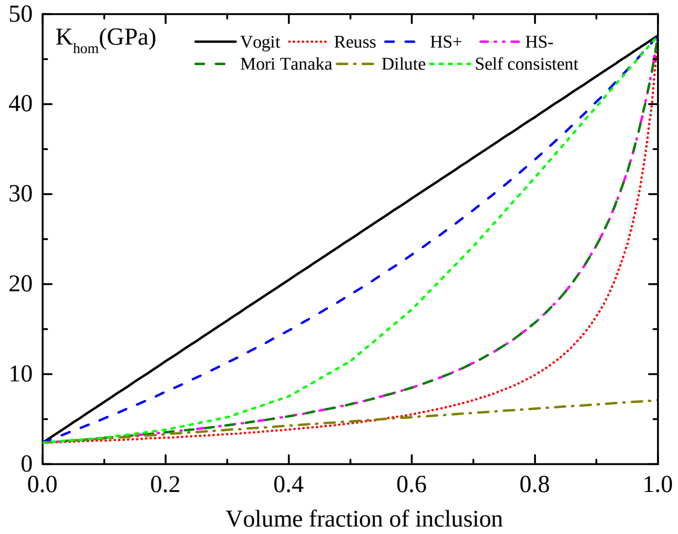

(a) K_{hom}

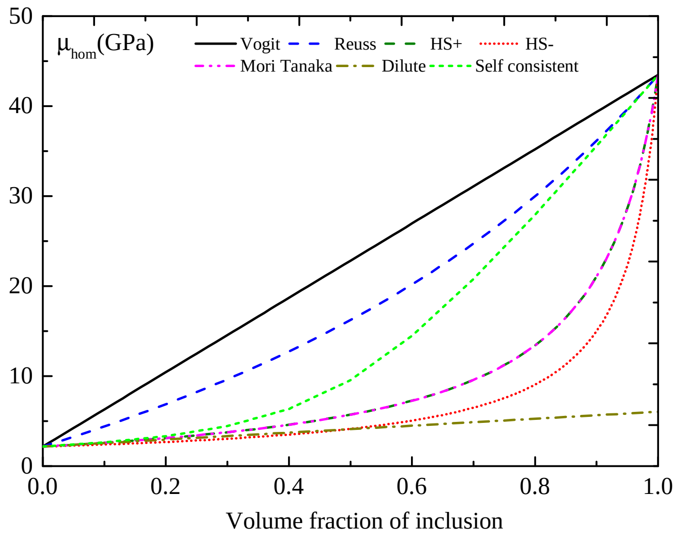

(b) μ_{hom}

Figure I .1: A comparison of effective bulk and shear modulus predicated by different classical homogenization methods: for matrix, E_m=5GPa, $v_m = 0.15$; for inclusion: E_i=100GPa, $v_i = 0.15$

© 2018 Tous droits réservés. lilliad.univ-lille.fr

Thèse de Yajun Cao, Université de Lille, 2018

2 Strength homogenized criteria for heterogenous materials

2.1 Plastic criteria for porous materials with spherical voids

2.1.1 Case of Von Mises matrix

Concerning the upscaling of strength behavior of porous material, the pioneering work of Gurson ([Gurson, 1977]) initially developed a widely accepted strength criterion for a hollow sphere with a von-Mises matrix based on a limit analysis method. Though taking into account two velocities corresponding to a homogenous strain rate and the cavity expansion, this model covers the exact solution of the hollow sphere subjected to a hydrostatic loading.

$$\frac{\Sigma_{eq}^2}{\sigma_0^2} + 2f\cosh(\frac{3}{2}\frac{\Sigma_m}{\sigma_0}) - 1 - f^2 = 0 \tag{I .8}$$

Since then, based on this framework, it has been followed up by lots of researchers who provide various improvements and extensions to the original Gurson model to better reproduce the unit cell modeling ([Tvergaard, 1981,Tvergaard and Needleman, 1984,Gologanu et al., 1993,Gologanu et al., 1994,Gologanu et al., 1997]). Later, [Castañeda, 1991] adopted a variational method, assuming that the effective energy potentials of nonlinear composites was in terms of the corresponding energy potentials for linear comparison composites with the same microstructural distributions. The obtained criterion has the following form:

$$(1 + \frac{2}{3}f)\frac{\Sigma_{eq}^2}{\sigma_0^2} + \frac{9}{4}f\frac{\Sigma_m^2}{\sigma_0^2} - 1 - f^2 = 0 \tag{I .9}$$

This criterion was later improved by [Michel and Suquet, 1992] incorporating exactly a closed-form solution of a hollow sphere under hydrostatic tension.

$$(1 + \frac{2}{3}f)\frac{\Sigma_{eq}^2}{\sigma_0^2} + \frac{9}{4}(\frac{1-f}{\ln(f)})^2\frac{\Sigma_m^2}{\sigma_0^2} - (1-f)^2 = 0 \tag{I .10}$$

[Monchiet et al., 2007] used an Eshelby-like trial velocity fields to determine the macroscopic dissipation. The following criterion is proposed:

$$\frac{\Sigma_{eq}^2}{\sigma_0^2} + 2f\cosh(\sqrt{\frac{9}{4}\frac{\Sigma_m^2}{\sigma_0^2} + \frac{2}{3g(f)}\frac{\Sigma_{eq}^2}{\sigma_0^2}}) - 1 - f^2 = 0 \tag{I .11}$$

[Shen et al., 2015a] adopted the framework of the Stress Variational Homogenization (SVM) involving Hill's variational principal coupled to the homogenization concepts. By using a new statically admissible stress field, the new criterion improved the one proposed

© 2018 Tous droits réservés. lilliad.univ-lille.fr

Thèse de Yajun Cao, Université de Lille, 2018

by [Cheng et al., 2014] and derived a more accurate value for the pure shear loading case. The closed form formula is given as follows:

$$\sqrt{\frac{P_0(f)}{(1-f+P_1)^2}\frac{\Sigma_{eq}^2}{\sigma_0^2}+\frac{9}{4ln(f)^2}\frac{\Sigma_m^2}{\sigma_0^2}}\xi(\zeta)-1=0 \qquad \text{(I .12)}$$

where $P_0(f)$, P_1 and $\xi(\zeta)$ are functions with J_3 and f:

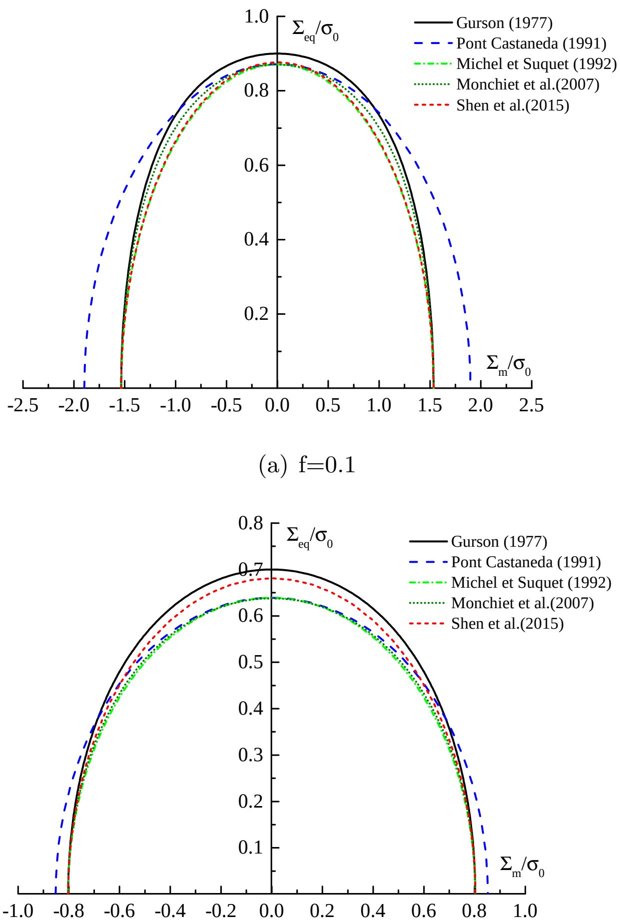

(a) f=0.1

(b) f=0.3

Figure I .2: A comparison of plastic surfaces with different criteria

With these criteria in hand, a series of plastic yield surfaces are predicted by these criteria. The results are presented in Fig.I .2 for different porosities. Remarkably, except for the one proposed by [Castañeda, 1991], all the criteria cover the exact solution for hydrostatic loading. Then for a higher porosity, the model of [Castañeda, 1991] is gradually closed with the model of [Monchiet et al., 2007].

© 2018 Tous droits réservés. lilliad.univ-lille.fr

Thèse de Yajun Cao, Université de Lille, 2018

2.1.2 Case of Drucker-Prager matrix

Above, the mentioned macroscopic criteria are mainly for ductile porous materials. For geomaterial, it always behaves as a pressure-sensitive properties. Many works have been well established for this class of porous materials with Drucker-Prager matrix. [Guo et al., 2008] obtained an expression of the macroscopic criterion for a hollow sphere with a Drucker-Prager type matrix by means of limit analysis technique, having the following form:

$$[\frac{\Sigma_{eq}/\sigma_0}{\Theta(\Sigma,T,f)}]^2 + 2f\cosh[\gamma^{-1}\ln(1-3T\frac{\Sigma_m}{\sigma_0})] - 1 - f^2 = 0 \tag{I .13}$$

where $\Theta(\Sigma,T,f) = 1 - \frac{3T}{\sigma_0(1-f)^{1-s/2}}$.

[Maghous et al., 2009] considered the strain heterogeneity in the solid phase and derived a new criterion for frictional geomaterials. The strategy of this resolution implements a non-linear homogenization technique based on the modified secant method. So the following criterion is derived:

$$F = \frac{1+2f/3}{\alpha^2}\tilde{\Sigma}_d^2 + (\frac{3f}{2\alpha^2} - 1)\tilde{\Sigma}_m^2 + 2(1-f)h\tilde{\Sigma}_m - (1-f)^2h^2 = 0 \tag{I .14}$$

[Shen et al., 2017b] incorporated a trial velocity field for spheroidal void. A macroscopic criterion for a porous material having spheroidal void was established based on a kinematical limit analysis. For a particular case of the matrix with a spherical void, the model is reduced to the following form:

$$[\frac{\Sigma_{eq}/\sigma_0}{1-\frac{3T}{(1-f)}\frac{\Sigma_m}{\sigma_0}}]^2 + 2f\cosh[\frac{2T+sgn(\Sigma_m)}{2T}\ln(1-3T\frac{\Sigma_m}{\sigma_0})] - 1 - f^2 = 0 \tag{I .15}$$

The theorial surfaces predicted by previous mentioned criteria are shown in Fig.I .3 for different porosities. As shown in Fig.I .3, the estimations between [Shen et al., 2017b] and [Guo et al., 2008] are closed. They have found to be a well agreement with the numerical lower and upper bounds ([Pastor et al., 2010, Shen et al., 2017b]).

The above criteria are mainly corresponding to an isotropic case. In order to consider anisotropy induced by the spheroidal pores, criteria considering oblate and prolate pores have also been developed with different type of matrix, so the aspect ratio of pores can be taken into account. The detailed criteria can be referred to the references [Gologanu et al., 1993, Gologanu et al., 1994, Monchiet et al., 2014, Shen et al., 2011, Shen et al., 2017b].

© 2018 Tous droits réservés. lilliad.univ-lille.fr

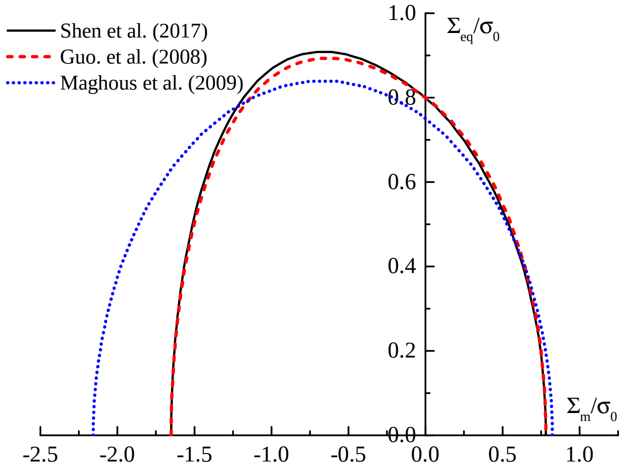

(a) f=0.2

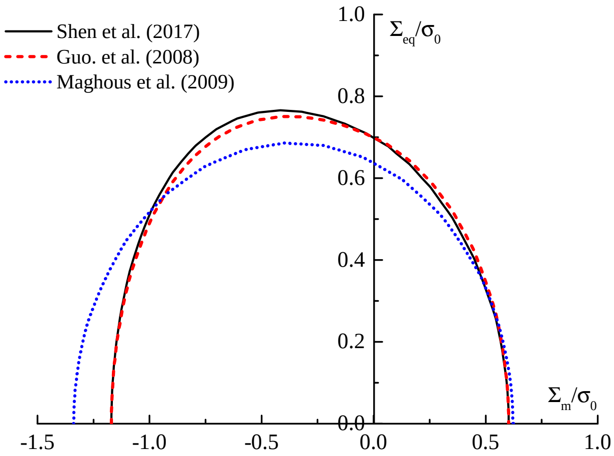

(b) f=0.3

Figure I .3: Plastic yield surfaces predicted by different criteria for different porosities with: $T = 0.1$, and $\alpha = \sqrt{6}T$

2.2 Plastic criteria for matrix-inclusion materials

[Barthélémy and Dormieux, 2004] have proposed an analytical approach for the strength homogenization of cohesive-frictional matrix materials rigid inclusions as expressed in eq.(I .16). The main idea of this approach is to replace the corresponding limit analysis by a equivalent viscous problems, so the modified secant method is used to determine the yield surface.

$$\Sigma_d + \sqrt{\frac{1+\frac{3}{2}\phi}{1-\frac{2}{3}\phi\alpha^2}}\alpha(\Sigma_m - \sigma_0) = 0 \tag{I .16}$$

© 2018 Tous droits réservés. lilliad.univ-lille.fr

Thèse de Yajun Cao, Université de Lille, 2018

Later [Maghous et al., 2009] extended this model concerned with local non-associated plastic behavior. The methodology considered the macroscopic limit stress states as a sequence of viscoplastic problems which solution leads asymptotically to the set of macroscopic limit stress states. The microscopic velocity solution of this nonlinear viscous problem is characterized by an effective strain rate. So the following criterion was obtained.

$$\Sigma_d + \alpha\sqrt{1+\frac{3}{2}\phi}\frac{\sqrt{1-\frac{2}{3}\phi\beta^2}}{1-\frac{2}{3}\phi\alpha\beta}(\Sigma_m - \sigma_0) = 0 \tag{I .17}$$

where β is the dilatancy coefficient and α defines as the frictional coefficient. ϕ is the volume fraction of inclusions.

[Ortega et al., 2011] incorporated the linear comparison composite (LCC) theory [Castañeda, 1991, Castaneda, 1992], though resolving the strength properties of the heterogeneous medium by estimating the effective properties of a suitable linear comparison composite with same microstructure. A new criterion contained Drucker-Prager solid and rigid inclusions was derived:

$$\Sigma_d + \alpha\sqrt{\frac{(1-\phi)M^{II}}{2-\alpha^2 K^{II}(1-\phi)}}(\Sigma_m - \sigma_0) = 0 \tag{I .18}$$

where M^{II} and K^{II} are the inclusion morphology factors related with the selected homogenization methods of effective modulus.

3 Fast Fourier Transform based homogenization method

As presented in previous section, the analytical solutions are mainly forcused on the effect of porosity on the macroscopic mechanical behavior, and a few studies concerns the shape effect. However, it is not easy to obtain an exactly analytical solution which can consider all the geometrical information of microstructure. The evolutions of local field is largely affected by the microstructure geometry. For this reason, it is necessary to introduce a computational method to predict the macroscopic behavior as accurately as possible.

3.1 Basic knowledge of FFT-based method

Materials with periodic microstructure can be represented by a periodic arrangement of similar unit cells. One only needs to pick up the detail mechanical behavior of one unit cell so that the macroscopic properties of whole structure can be represented. So the periodic boundary condition should be considered for the computations. According to the

© 2018 Tous droits réservés. lilliad.univ-lille.fr

Thèse de Yajun Cao, Université de Lille, 2018

presentation of previous section, the closed form solutions are mainly determined by the porosities. In this context, the Fast Fourier Transforms (FFT) homogenization method is introduced here which was proposed by Moulinec and Suquet [Moulinec and Suquet, 1994, Moulinec and Suquet, 1998]. This method operates on regular spatial grids and can directly be applied to analyze RVE with complex microstructure by direct using image technique. Moreover, it is efficient for numerical resolution of the cell problem arising in homogenization of periodic media. Here the basic framework of this method will be presented.

3.1.1 Description of local problem

To begin with, considering the unit cell with complex microstructure subjected to a macroscopic strain $\boldsymbol{E}$ under periodic boundary condition. Due to the local heterogeneous setting of the microstructure, the microscopic strain field strongly depends on the location of microscopic material points $\boldsymbol{x}$. Therefore, the local strain field $\boldsymbol{\varepsilon}(\boldsymbol{x})$ at each point can be decomposed into a spatially average strain $\boldsymbol{E}$ which would act in a completely homogeneous microstructure and a fluctuation stain field $\boldsymbol{\varepsilon}^*(\boldsymbol{x})$ that accounts for the heterogeneities of the microstructure.

$$\boldsymbol{\varepsilon}(\boldsymbol{x}) = \boldsymbol{E} + \boldsymbol{\varepsilon}^*(\boldsymbol{x}) \tag{I .19}$$

where the average strain denotes $\boldsymbol{E} = \langle \boldsymbol{\varepsilon}(\boldsymbol{x}) \rangle$. The strain fluctuation field $\boldsymbol{\varepsilon}^*(\boldsymbol{x})$ is compatible with the fluctuating displacement field $u^*(\boldsymbol{x})$. According to the kinematical relations, it is taken the following form:

$$\boldsymbol{\varepsilon}(u^*(\boldsymbol{x})) = \frac{1}{2}(\nabla u^*(\boldsymbol{x}) + (\nabla u^*(\boldsymbol{x}))^T) \tag{I .20}$$

Thus, the displacement field at each material point $\boldsymbol{x}$ reads as follow:

$$u(\boldsymbol{x}) = \boldsymbol{E} \cdot \boldsymbol{x} + u^*(\boldsymbol{x}) \tag{I .21}$$

Due to the fact that the $u^*(\boldsymbol{x})$ and $\boldsymbol{\varepsilon}(u^*(\boldsymbol{x}))$ are periodic, which implies that their averages over the total volume vanish:

$$\begin{aligned} \langle u^*(\boldsymbol{x}) \rangle &= \frac{1}{\Omega} \int_{\Omega} u^*(\boldsymbol{x}) dV = 0 \\ \langle \varepsilon^*(\boldsymbol{x}) \rangle &= \frac{1}{\Omega} \int_{\Omega} \varepsilon^*(\boldsymbol{x}) dV = 0 \end{aligned} \tag{I .22}$$

In fact, the solution of this local problem is governed by the equilibrium equations, local constitutive relations and boundary condition. So the following the local boundary

© 2018 Tous droits réservés. lilliad.univ-lille.fr

Thèse de Yajun Cao, Université de Lille, 2018

value problem is summarized:

$$\begin{cases} \boldsymbol{\sigma}(\boldsymbol{x}) = \dfrac{\partial \omega}{\partial \boldsymbol{\varepsilon}}(\boldsymbol{x}) \qquad \forall \boldsymbol{x} \in \Omega \\ div\boldsymbol{\sigma}(\boldsymbol{x}) = 0 \qquad \forall \boldsymbol{x} \in \Omega, \quad u^*\#, \quad \boldsymbol{\sigma} \cdot n - \# \\ \boldsymbol{\varepsilon}(\boldsymbol{x}) = \frac{1}{2}(\nabla \boldsymbol{u}^*(\boldsymbol{x}) + \nabla^T \boldsymbol{u}^*(\boldsymbol{x})) + \boldsymbol{E} \qquad \forall \boldsymbol{x} \in \Omega \end{cases} \tag{I .23}$$

In this relations, the symbol $\#$ denotes the periodic condition while $-\#$ the anti-periodic one.

3.1.2 Lippmann-Schwinger Equation

Before solving the heterogeneous problem previous mentioned , let us consider a auxiliary problem that a reference homogeneous linear elastic medium with stiffness $\mathbb{C}_0$ subjected to a polarization field $\boldsymbol{\tau}(\boldsymbol{x})$. The local stress field can read as follows:

$$\boldsymbol{\sigma}(\boldsymbol{x}) = \mathbb{C}_0 : \boldsymbol{\varepsilon}^*(\boldsymbol{x}) + \boldsymbol{\tau}(\boldsymbol{x}) \tag{I .24}$$

Meanwhile, the equilibrium equation and kinematical relations also should be satisfied, so we have:

$$div(\mathbb{C}_0 : \nabla u^*(\boldsymbol{x})) + div(\boldsymbol{\tau}(\boldsymbol{x})) = 0 \tag{I .25}$$

In this relation, the divergence of $\boldsymbol{\tau}$ can be considered as a body force acting in the whole microstructure. Hence, we can reduce the problem to find the fluctuation field in an equilibrated homogeneous medium with constant stiffness $\mathbb{C}_0$ subjected to its body force $div(\boldsymbol{\tau}(\boldsymbol{x}))$. An alternative method by making use of the relevant Green's function of the problem can refer to the solution of (I .25) by solving the following equation:

$$\boldsymbol{\varepsilon}^*(\boldsymbol{x}) = -\int_{\Omega} \Gamma^0(\boldsymbol{x}, \boldsymbol{y}) \tau(\boldsymbol{y}) d\boldsymbol{y} \tag{I .26}$$

where the last term of (I .26) is defined as the convolution on the Green's function Γ^0 and the porarization field $\boldsymbol{\tau}$:

$$\boldsymbol{\Gamma}^0 * \boldsymbol{\tau} = \int_{\Omega} \Gamma^0(\boldsymbol{x}, \boldsymbol{y}) \tau(\boldsymbol{y}) d\boldsymbol{y} \tag{I .27}$$

So the problem can be simply reformulated as:

$$\boldsymbol{\varepsilon}^*(\boldsymbol{x}) = -\boldsymbol{\Gamma}^0 * \boldsymbol{\tau} \tag{I .28}$$

which is known as the Lippmann-Schwinger equation. It is convenient to solve this by transforming (I .28) into Fourier space based on using the convolution theorem with:

$$\hat{\varepsilon}^*(\boldsymbol{\xi}) = -\hat{\boldsymbol{\Gamma}}(\boldsymbol{\xi})^0 : \hat{\boldsymbol{\tau}}(\boldsymbol{\xi}) \quad \xi \neq 0; \quad \hat{\varepsilon}(\boldsymbol{0}) = \boldsymbol{0} \tag{I .29}$$

© 2018 Tous droits réservés. lilliad.univ-lille.fr

where $\boldsymbol{\xi}$ is the coordinates in Fourier space. Similarly, the local problem also can be transformed into Fourier space, which can read as:

$$\begin{cases} \hat{\boldsymbol{\sigma}}_{\boldsymbol{ij}}(\boldsymbol{\xi}) = i\mathbb{C}^0_{ijkl}\xi_h\hat{u}^*_k(\boldsymbol{\xi}) + \hat{\boldsymbol{\tau}}_{\boldsymbol{ij}}(\boldsymbol{\xi}) \\ i\hat{\boldsymbol{\sigma}}_{\boldsymbol{ij}}(\boldsymbol{\xi})\xi_j = 0 \\ \hat{\boldsymbol{\varepsilon}}_{\boldsymbol{jk}} = \frac{i}{2}(\xi_j\hat{u}^*_k(\boldsymbol{\xi}) + \xi_k\hat{u}^*_j(\boldsymbol{\xi})) \end{cases} \tag{I .30}$$

where $i = \sqrt{-1}$. Combining the first two equation in (I .30), so we have:

$$i\hat{\sigma}_{ij}(\boldsymbol{\xi})\xi_j = -K^0_{ik}(\boldsymbol{\xi})\hat{u}^*_k + i\hat{\tau}_{ij}\xi_j = 0 \tag{I .31}$$

where $K^0_{ik}(\boldsymbol{\xi}) = \mathbb{C}^0_{ijkh}\xi_h\xi_j$, then one can get that:

$$K^0_{ik}(\boldsymbol{\xi})\hat{u}^*_k = i\hat{\tau}_{ij}\xi_j \tag{I .32}$$

We defined $N^0(\boldsymbol{\xi})$ as the inverse of $K^0(\boldsymbol{\xi})$, Hence, $\hat{u}^*_k$ can be expressed as:

$$\hat{u}^*_k = iK^{0-1}_{ki}(\boldsymbol{\xi})\hat{\tau}_{ij}\xi_j = iN^0_{ki}(\boldsymbol{\xi})\hat{\tau}_{ij}\xi_j \tag{I .33}$$

Substitute (I .33) into last equation in (I .30), one can get

$$\hat{\varepsilon}(\boldsymbol{\xi}) = -\frac{1}{4}(N^0_{hi}(\boldsymbol{\xi})\xi_j\xi_k + N^0_{ki}(\boldsymbol{\xi})\xi_j\xi_k + N^0_{hj}(\boldsymbol{\xi})\xi_i\xi_k + N^0_{kj}(\boldsymbol{\xi})\xi_i\xi_h)\hat{\tau}_{ij} \tag{I .34}$$

If the reference medium is isotropic with the Lame coefficients λ^0 and μ^0. The stiffness tensor $\mathbb{C}^0$ can be taken the following form:

$$\mathbb{C}^0_{ijkh} = \lambda^0\delta_{ij}\delta_{kh} + \mu^0(\delta_{ik}\delta_{jh} + \delta_{ih}\delta_{jk}) \tag{I .35}$$

Combing with the formulations (I .29), (I .34) and (I .35). We can get the explicit expression of Γ^0 in Fourier space as the following form:

$$\hat{\Gamma}_{khij}(\boldsymbol{\xi}) = \frac{1}{4\mu^0|\boldsymbol{\xi}|^2}(\delta_{ki}\xi_h\xi_j + \delta_{hi}\xi_k\xi_j + \delta_{kj}\xi_h\xi_i + \delta_{hj}\xi_k\xi_i) - \frac{\lambda^0 + \mu^0}{\mu^0(\lambda^0 + 2\mu^0)}\frac{\xi_i\xi_j\xi_k\xi_h}{|\boldsymbol{\xi}|^4}. \tag{I .36}$$

According to previous analysis, the local problem considered in Section 3.1.1 can be reduced to the homogenous reference material with elastic stiffness $\mathbb{C}_0$ subjected to a average macroscopic strain $\boldsymbol{E}$ and a polarization stress $\boldsymbol{\tau}(\boldsymbol{x})$. For elastic problem, the local stress is expressed as:

$$\begin{aligned} \boldsymbol{\sigma}(\boldsymbol{x}) &= \mathbb{C}(\boldsymbol{x}) : \boldsymbol{\varepsilon}(\boldsymbol{x}) \\ &= \mathbb{C}_0 : \boldsymbol{\varepsilon}^*(\boldsymbol{x}) + \boldsymbol{\tau}(\boldsymbol{x}) \end{aligned} \tag{I .37}$$

© 2018 Tous droits réservés.

Thèse de Yajun Cao, Université de Lille, 2018

where $\boldsymbol{\tau}(\boldsymbol{x}) = \mathbb{C}_0 : \boldsymbol{E} + \boldsymbol{\delta C} : \boldsymbol{\varepsilon}(\boldsymbol{x})$, $\boldsymbol{\delta C} = (\mathbb{C}(\boldsymbol{x}) - \mathbb{C}_0)$. Following the solution of previous auxiliary problem, we can get that:

$$\begin{aligned} \boldsymbol{\varepsilon}^*(\boldsymbol{x}) &= -\boldsymbol{\Gamma}^0 * \boldsymbol{\tau} \\ &= -\boldsymbol{\Gamma}^0 * (\boldsymbol{\delta C} : \varepsilon) - \boldsymbol{\Gamma}^0 * (\mathbb{C}_0 : \boldsymbol{E}) \\ &= -\boldsymbol{\Gamma}^0 * (\boldsymbol{\delta C} : \varepsilon) = \boldsymbol{\varepsilon}(\boldsymbol{x}) - \boldsymbol{E} \end{aligned} \tag{I .38}$$

Then in Fourier space, it is given as:

$$\boldsymbol{\varepsilon}(\boldsymbol{x}) = -\boldsymbol{\Gamma}^0(\boldsymbol{\xi}) : \boldsymbol{\tau}(\boldsymbol{\xi}) \quad \boldsymbol{\xi} \neq 0; \;\; \hat{\varepsilon}(\mathbf{0}) = \boldsymbol{E} \tag{I .39}$$

3.1.3 Unit cell Discretization and Fast Fourier Transformation

Now we are proceeding to state the discrete Fourier transform(DFT) techanique. The definition of discrete Fourier transform(DFT) is quite similar with the basic Fourier transform. The sequence of N complex numbers x_0, x_1, ..., x_{N-1} is transformed into another sequence of N complex numbers according to the DFT formula:

$$X_\xi = \sum_{n=0}^{N-1} x_n \cdot e^{-i\xi n/N} \tag{I .40}$$

where the N-point inverse DFT(IDFT) is defined as follows:

$$x_n = \frac{1}{N} \sum_{n=0}^{N-1} X_\xi \cdot e^{i\xi n/N} \tag{I .41}$$

For three dimensional problems in this work, the DFT formula in three dimensional problem is given by:

$$X_{\xi_i\xi_j\xi_k} = \sum_{k=0}^{N_x-1} \sum_{l=0}^{N_y-1} \sum_{m=0}^{N_z-1} x_{klm} \cdot e^{-i\xi_i k/N_x} e^{-i\xi_j l/N_y} e^{-i\xi_k m/N_z} \tag{I .42}$$

$$x_{klm} = \frac{1}{N_x N_y N_z} \sum_{k=0}^{N_x-1} \sum_{l=0}^{N_y-1} \sum_{m=0}^{N_z-1} X_{\xi_i\xi_j\xi_k} \cdot e^{i\xi_i k/N_x} e^{i\xi_j l/N_y} e^{i\xi_k m/N_z} \tag{I .43}$$

The Fast Fourier Transform technique will be employed here to compute the DFT and produces exactly the same result as implementing the DFT definition directly. A FFT rapidly computes such transformations by factorizing the DFT matrix into a product of sparse (mostly zero) factors. As a result, it manages to reduce the complexity of computing the DFT from $O(n^2)$, which arises if one simply applies the definition of DFT, to $O(n \log n)$, where n is the data size. By using this technique, the resolution of the numerical homogenization problem requires to discretize the unit cell into a regular grid

© 2018 Tous droits réservés. lilliad.univ-lille.fr

Thèse de Yajun Cao, Université de Lille, 2018

composed of $N_1 \times N_2 \times N_3$ voxels in three dimensions. The coordinates of voxels in the real space are denoted by $\boldsymbol{x}_p(i_1, i_2, i_3)$ which are linked to the coordinates in the Fourier space, $\boldsymbol{\xi_p}(i_1, i_2, i_3)$. The number of points in each direction depends on the choice of resolution. In a three dimensional case, the coordinates of voxel are given by:

$$\boldsymbol{x}_p(i_1, i_2, i_3) = i_k \cdot \frac{T_k}{N_k}, i_k = 0, 1, \ldots, N_{k-1}, \quad k = 1, 2, 3 \tag{I .44}$$

The corresponding frequencies in Fourier space are:

$$\boldsymbol{\xi}_p(i_1, i_2, i_3) = (i_k - \frac{N_k - 1}{2})\frac{1}{T_k}, i_k = 0, 1, \ldots, N_{k-1}, \quad k = 1, 2, 3 \tag{I .45}$$

when N_k is even, and when N_k is odd:

$$\boldsymbol{\xi}_p(i_1, i_2, i_3) = (i_k - \frac{N_k}{2} + 1)\frac{1}{T_k}, i_k = 0, 1, \ldots, N_{k-1}, \quad k = 1, 2, 3 \tag{I .46}$$

3.1.4 Numerical algorithm

To compute the local and overall responses of heterogenous materials with complex microstructure, Moulinec and Suquet [Moulinec and Suquet, 1994, Moulinec and Suquet, 1998] proposed a basic iterate algorithm. This method afterwards extended by various accelerated algorithms to overcome its low convergence rate ([Eyre and Milton, 1999, Michel et al., 2001, Monchiet and Bonnet, 2012, Brisard and Dormieux, 2010, Zeman et al., 2010, Moulinec and Silva, 2014]. The mathematical analysis of such schemes was summarized by [Moulinec and Silva, 2014] and a unified scheme was developed as

© 2018 Tous droits réservés. lilliad.univ-lille.fr

Thèse de Yajun Cao, Université de Lille, 2018

following:

$$
\begin{aligned}
&\textit{Iterate } i+1 \quad \textit{The previous } \varepsilon^i(\boldsymbol{x}) \textit{ and } \sigma^i(\boldsymbol{x}),\ \boldsymbol{E} \textit{ are known}\\
&\qquad 1)\ \boldsymbol{s}_a^i(\boldsymbol{x}) = \boldsymbol{\sigma}^i(\boldsymbol{x}) + (1-\beta)\mathbb{C}^0 : (\boldsymbol{\varepsilon}^i(\boldsymbol{x}))\\
&\qquad\quad \boldsymbol{s}_b^i(\boldsymbol{x}) = \alpha\boldsymbol{\sigma}^i(\boldsymbol{x}) - \beta\mathbb{C}^0 : (\boldsymbol{\varepsilon}^i(\boldsymbol{x}))\\
&\qquad 2)\ \hat{\boldsymbol{s}}_b^i(\boldsymbol{\xi}) = \mathcal{F}(\boldsymbol{s}_b^i(\boldsymbol{x}))\\
&\qquad 3)\ \hat{\boldsymbol{e}}_b^i(\boldsymbol{x}) = -\Gamma^0(\boldsymbol{\xi}) : \hat{\boldsymbol{s}}_b^i(\boldsymbol{\xi}) \quad \forall\boldsymbol{\xi} \neq 0,\ \hat{\varepsilon}_b^i(\mathbf{0}) = \beta\boldsymbol{E}\\
&\qquad 4)\ \boldsymbol{e}_b^i(\boldsymbol{x}) = \mathcal{F}(\varepsilon_b^i(\boldsymbol{\xi}))\\
&\qquad 5)\ \boldsymbol{e}^{i+1}(x) = (\boldsymbol{c}(\boldsymbol{x}) + \boldsymbol{c}^0)^{-1} : (\boldsymbol{s}_a^i(\boldsymbol{x}) + \boldsymbol{e}_b^i(\boldsymbol{x}))\\
&\qquad 6)\ \boldsymbol{\sigma}^{i+1}(\boldsymbol{x}) = \boldsymbol{c}(\boldsymbol{x}) : \boldsymbol{e}^{i+1}(x)\\
&\qquad 7)\ \textit{Convergence tests}:\\
&\qquad\quad \epsilon_{equilibrium} = \frac{\|div(\boldsymbol{\sigma}^{i+1})\|_2}{\|\boldsymbol{\sigma}^{i+1}\|} = \frac{\sqrt{\sum_{\boldsymbol{\xi}} |\boldsymbol{\xi}\cdot\hat{\boldsymbol{\sigma}}^{i+1}(\boldsymbol{\xi})|^2}}{\|\hat{\boldsymbol{\sigma}}^{i+1}(\mathbf{0})\|}\\
&\qquad\quad \epsilon_{load} = \frac{\|\langle \boldsymbol{e}^{i+1} - \boldsymbol{E}\rangle\|}{\|\boldsymbol{E}\|}\\
&\qquad\quad \epsilon_{compatibility} = \frac{max_{\boldsymbol{\xi}}(max_{j=1,\ldots,6}|\hat{c}_i(\boldsymbol{\xi})|)}{\sqrt{\sum_{\boldsymbol{\xi}} \hat{e}_{ij}(\boldsymbol{\xi}) : \hat{e}_{ij}^*(\boldsymbol{\xi})}}
\end{aligned}
\tag{I .47}
$$

In has been known that when $\alpha = \beta = 1$, the above algorithm is corresponding to the augmented Lagrangian scheme ([Michel et al., 2001]). For the case $\alpha = \beta = 2$, the above algorithm is corresponding to the iterative schemes proposed by [Eyre and Milton, 1999]. They are both the special cases of the method of [Monchiet and Bonnet, 2012]. Actually, the above united algorithm is suitable for linear case. For nonlinear case, it needs special analysis.

3.2 Comparison with the FEM solution

For the purpose of validation, the accuracy of the FFT-based method is verified by comparing with reference solutions obtained from finite element simulations. The basic scheme is adopted here for nonlinear case following the study of [Jiang and Shao, 2012]. A simplified porous medium is considered with a porosity $f = 10\%$: a cubic unit cell containing a centered spherical pore (Fig.I .4). These two methods adopt totally different strategies to discretize the structure. The FEM method meshes the structure with certain shape of elements (37040 hexagonal elements in Figure I .4-a). On the contrary, the FFT-based method discretizes the structure with regular voxels ($128 \times 128 \times 128$ voxels in Fig. I .4-b).

© 2018 Tous droits réservés. lilliad.univ-lille.fr

Thèse de Yajun Cao, Université de Lille, 2018

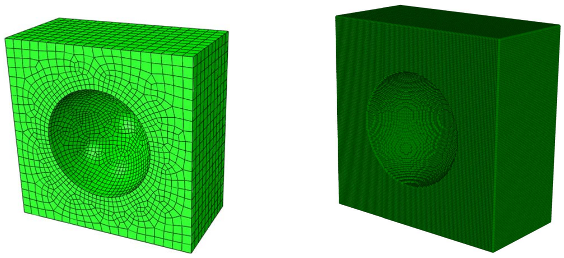

(a) (b)

Figure I .4: Microstructure with a centered spherical void: porosity $f = 10\%$. (a) FEM mesh with 37040 hexagonal elements; (b) FFT discritization with regular $128 \times 128 \times 128$ voxels.

The solid matrix in Fig. I .4(a) and Fig. I .4(b) is characterized by von Mises criterion with an isotropic plastic hardening:

$$F = \sigma_{eq} - (\sigma_0 + H\gamma^m) = 0 \tag{I .48}$$

where σ_{eq} indicates the equivalent stress and computed as $\sigma_{eq} = (\frac{3}{2}\boldsymbol{s} : \boldsymbol{s})^{1/2}$. $\boldsymbol{s}$ is the deviatoric part of the stress $\boldsymbol{\sigma}$. H and m are two plastic hardening parameters. The plastic variable γ is determined by an associated plastic flow rule:

$$\dot{\boldsymbol{\varepsilon}}^p = \dot{\lambda}\frac{\partial F}{\partial \boldsymbol{\sigma}} = \frac{3}{2}\dot{\gamma}\frac{\boldsymbol{s}}{\sigma_{eq}}, \qquad \dot{\gamma} = \dot{\lambda}. \tag{I .49}$$

Table I .1: Elastic and plastic parameters of the solid matrix

$E(GPa)$	ν	$\sigma_0(MPa)$	$H(MPa)$	m
10.0	0.25	45.0	150.0	0.5

The elastic and plastic parameters of the solid phase for the two methods are given in Table I .1. The unit cell is subjected to a uniaxial strain tension along its $3rd$ axis and the prescribed macroscopic strains are: $E_{33} > 0$, $E_{11} = E_{22} = E_{12} = E_{23} = E_{31} = 0$. In order to compare the accuracy and efficiency of these two methods, five different types of mesh for FEM method and five different sorts of resolution for FFT-based method are performed as shown in the Table I .2. All calculations were performed with parallelization of multiple processors on an x64-based Dell computer with 8 processors: Intel(R) Core(TM) i7-4790 CPU @3.6GHz.

© 2018 Tous droits réservés. lilliad.univ-lille.fr

Thèse de Yajun Cao, Université de Lille, 2018

Table I .2: Computational CPU time between FFT method and FE solution.

FFT					FEM				
Resolution(N)	**Points**	**CPU time(s)**	**σ^p (MPa)**	**Error(%)**	**Mesh**	**Nodes**	**CPU time(s)**	**σ^p (MPa)**	**Error(%)**
8	512	**388.2**	63.1	**1.54**	**1**	1920	**409.1**	71.1	**10.92**
16	4096	**1341.8**	64.3	**0.31**	**2**	17810	**8982.9**	67.3	**4.99**
32	32768	**13578.9**	63.3	**1.25**	**3**	40887	**50393.0**	65.5	**2.18**
64	262144	**25908.9**	63.7	**0.62**	**4**	215850	**454392.0**	64.5	**0.62**
128	2097152	**226831.0**	63.9	**0.31**	**5**	313324	**877980.0**	64.1	--

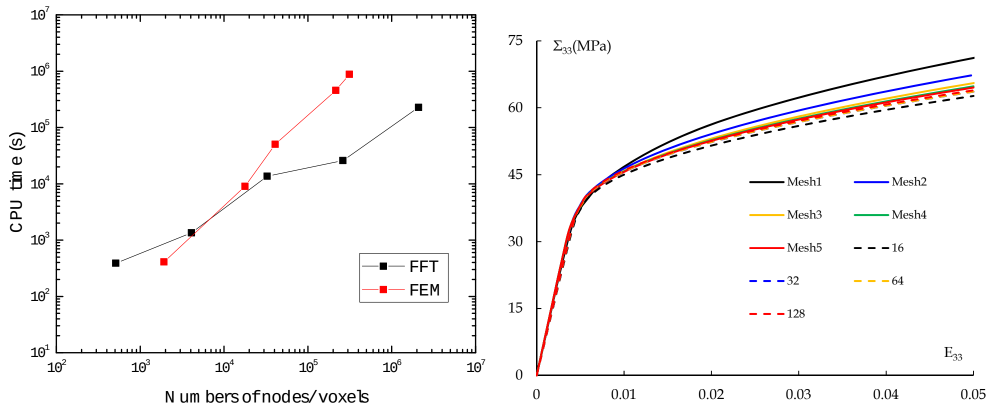

(a) CPU time consumption (b) stress-strain curves

Figure I .5: Comparison of CPU time and stress-strain curves between FFT method and FEM solution with the different mesh and resolution

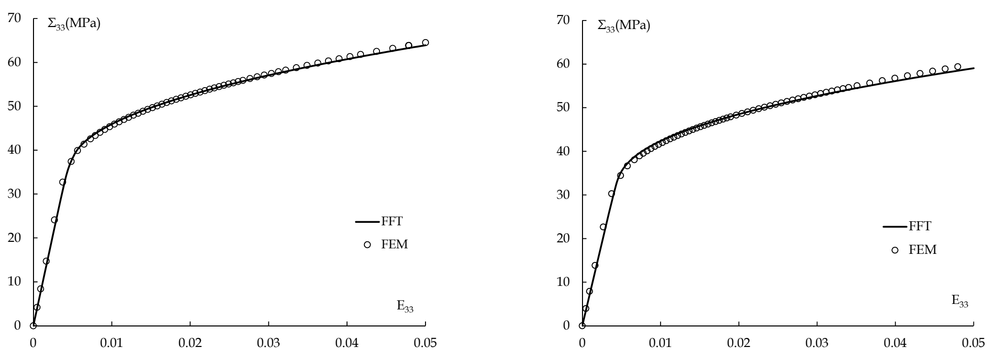

(a) f=10% (b) f=15%

Figure I .6: Comparison of stress-strain curves between FFT method and FEM solution with the most fine mesh and resolution.

© 2018 Tous droits réservés. lilliad.univ-lille.fr

Thèse de Yajun Cao, Université de Lille, 2018

For the matter of efficiency, the CPU time consumption for different meshes and resolutions are illustrated in Figure I .5(a). As expected for the both methods, the CPU time is increasing with the nodes and resolution. However, for a higher resolution and a large number of nodes, the FFT method exhibits a faster efficiency than the FEM method as presented in the Table I .2.

Meanwhile, it is also worth noting that the FFT method is able to provide a good accuracy with a relative low resolution, for example, with a resolution of $32 \times 32 \times 32$ voxels, which makes the FFT method more efficient since the accuracy of the FEM requires a much larger number of nodes. Therefore, it is obvious that the FFT method is more efficient than the finite element method.

To complete computational results, the same structure, a cubic unit cell with a centered spherical void, with a porosity $f = 15\%$ is also performed. As shown in Fig.I .6, the numerical results predicted by the two methods are in good agreement. Therefore, the FFT-based method will be adopted for the following studies in this work.

4 Conclusions

In this chapter, we have recalled a brief introduction of the classical elastic homogenization methods and the well known homogenized strength criteria for the heterogenous material with Von Mises and Drucker-Prager type matrix. The effective elastic properties and macroscopic plastic yield surfaces predicted by different methods are also presented. The closed-form solutions are mainly depended on the porosity or the inclusion volume fraction, while the detailed microstructure geometrical information couldn't be accurately considered. For this reason, the Fast Fourier transform method is introduced here, and its accuracy and efficiency have been validated by the Finite element method. Further, combing the analytical solution and the FFT-based method, a multi-scale homogenization procedure will be developed in the proceeding chapters to estimate the full-field mechanical properties of porous materials across multi-scale characters.

© 2018 Tous droits réservés. lilliad.univ-lille.fr

Thèse de Yajun Cao, Université de Lille, 2018

© 2018 Tous droits réservés. lilliad.univ-lille.fr

Chapter II

Influences of micro- and meso-pores on the effective properties of porous materials

Contents

© 2018 Tous droits réservés.

Thèse de Yajun Cao, Université de Lille, 2018

Summary

Many engineering materials contain families of pores at different scales. In this chapter, a numerical homogenization analysis method is developed to describe the effective elastic and plastic properties of a class of porous materials with two populations of pores at two separated scales. The solid phase at the micro-scale is described by the Drucker-Prager criterion. An analytical plastic criterion is used for the effective plastic criterion of the porous matrix with the micro-porosity. The influence of the meso-porosity, which is embedded in the homogenized porous matrix, is investigated by developing a numerical method based on the Fast Fourier Transform (FFT). With this two-step homogenization method in hand, a series of numerical assessments are performed. The relative roles of both families of pores on the macroscopic elastic properties and plastic yield stresses for a given total porosity are particularly investigated and compared with existing analytical solutions. Moreover, the proposed numerical method is applied to describe the local strain fields under various loading paths.

1 Introduction

Different types of porous materials with embedded voids at different scales, such as rocks, concrete materials, composites and polymers, are widely used in a range of engineering applications. Based on experimental investigations of characteristics of microstructure and local mechanisms, it is required to estimate effective mechanical properties of these materials by using different analytical and numerical homogenization methods. The estimation of effective properties are generally performed on a representative unit-cell of material microstructure. In the framework of analytical homogenization of porous materials, it is indispensable to mention the pioneer's work performed by [Gurson, 1977] who established an analytical strength criterion for porous materials with a von-Mises type solid matrix and one population of spherical voids by using a limit analysis technique. Starting from this, different kinds of nonlinear homogenization techniques have been developed for the determination of effective strength criteria of porous materials. For instance, effective strength criteria for porous materials with a Drucker-Prager type pressure sensitive solid matrix and one population of spherical voids have been established in [Guo et al., 2008] and [Maghous et al., 2009]. Similar studies for other types of solid matrix have also been conducted by [Pastor et al., 2013] and [Cazacu et al., 2014]. Different extensions of these criteria have been proposed in recent years mainly in order to consider void shape effects, plastic matrix anisotropy ([Gologanu et al., 1993]; [Gologanu et al., 1994]; [Monchiet et al.,

© 2018 Tous droits réservés. lilliad.univ-lille.fr

Thèse de Yajun Cao, Université de Lille, 2018

2006]; [Shen et al., 2015b]; [Shen et al., 2017a]). Some studies have focused on porous materials reinforced with rigid particles ([He et al., 2013]; [Shen and Shao, 2016a]).

On the other hand, pore distributions are generally complex in real materials and several families of pores can be found at different scales. To investigate the relative effects of each pore family and interactions between different families of pores, one considers here the case of porous materials with two families of pores at two different scales, for instance, the micro-porosity at the microscopic scale and the meso-porosity at the mesoscopic scale. By using two-step homogenization procedures, some previous studies have contributed to the establishment of analytical macroscopic strength criteria for this class of porous materials, for instance [Vincent et al., 2009a]; [Ortega and Ulm, 2013]; [Shen et al., 2014] and [Shen and Shao, 2016b].

However, in all analytical homogenization methods, strong assumptions are generally introduced on the description of microstructure in order to perform mathematical calculations. Some assumptions, especially on the size and shape of voids, may lead to a bad approximation of effective properties of real materials. Therefore, the validity of analytical models is usually questionable for materials with a complex microstructure. Moreover, interactions between voids and other heterogeneities, for example mineral inclusions, cannot be easily taken into account in analytical micro-mechanical models.

In order to represent real microstructure as closely as possible, different kinds of full-field simulations have been developed in recent years. Among them, a FFT-based numerical homogenization method has been proposed by [Moulinec and Suquet, 1994] for the estimation of effective mechanical properties of composite materials with a strong microstructure contrast. This method has been extended and applied to other engineering materials ([Moulinec and Suquet, 1998]; [Jiang and Shao, 2012]; [Lebensohn et al., 2012]; [Vincent et al., 2014b]; [Li et al., 2016]). The efficiency of the FFT based method has been demonstrated in various situations, for instance, elastic materials ([Gélébart and Mondon-Cancel, 2013]; [Kabel et al., 2014]), nonlinear plastic materials([Jiang and Shao, 2012]), viscoplastic materials ([Lebensohn et al., 2012]), Darcy's conduction problems ([Monchiet et al., 2009]) and cracking modeling ([Li et al., 2012]). A particular attention has been paid on the numerical convergence of this method for nonlinear problems ([Eyre and Milton, 1999]; [Michel et al., 2001];[Monchiet and Bonnet, 2012]; [Moulinec and Silva, 2014].

In this study, a FFT based multi-scale numerical model is proposed to describe the macroscopic mechanical behavior of a class of porous materials with two populations of pores at two different scales. One of the aims here is to explore the relative roles of two families of pores on the effective elastic properties and plastic yield stresses of porous ma-

© 2018 Tous droits réservés. lilliad.univ-lille.fr

Thèse de Yajun Cao, Université de Lille, 2018

terials. For this purpose, the results obtained with the proposed numerical model will be compared with those obtained in the previous studies by analytical homogenization techniques [Shen et al., 2014] and [Shen and Shao, 2016a]. As a complementary contribution to existing studies, we shall investigate in depth the effects of interactions between the two populations of pores on the elastic and plastic properties of materials. We extend this method to the material with compressible porous matrix, both local and overall responses of double porous materials under various loading paths will be studied .

The paper is organized as follows. The general framework of the two-step numerical homogenization model is first presented in Section 2. An analytical plastic model is used for the description of plastic criterion of porous matrix with micro-porosity and the FFT based numerical method is established for the estimation of macroscopic behavior of porous materials with meso-porosity. In section 3, a series of numerical assessments are performed and discussed to investigate effects of two proportions of pores on the effective elastic and plastic properties of double porous materials. In section 4, we extend this proposed method to the material with compressible porous matrix.

2 Homogenization model of double porous medium based on FFT method

In Fig.II .1, the selected representative element volume (REV) with two populations of pores at two separate scales is presented. For the sake of simplicity, it is assumed that both two families of pores are of spherical form. Let us denote Ω the total volume of the unit cell; ω_m the domain occupied by the solid phase at the microscopic scale; ω defines the volume of porous matrix at the mesoscopic scale. Then ω_1 and ω_2 are the volumes of small and large pores located at the microscopic and mesoscopic scales, respectively. With these notations, the porosity at the microscale f and that at the mesoscale ϕ as well as the total porosity Γ at the macroscopic scale can be given as:

$$f = \frac{\omega_1}{\omega_m + \omega_1} = \frac{\omega_1}{\omega}, \qquad \phi = \frac{\omega_2}{\Omega}, \qquad \Gamma = \frac{\omega_1 + \omega_2}{\Omega} = f(1-\phi) + \phi \tag{II .1}$$

A two-step homogenization procedure is here adopted for the upscaling from microscale to mesoscale and from mesoscale to macroscale. In the first homogenization step, the microscopic pores and the properties of the solid phase are taken into account. The effect of mesoscopic pore on the overall behavior is considered in the second homogenization step.

© 2018 Tous droits réservés. lilliad.univ-lille.fr

Thèse de Yajun Cao, Université de Lille, 2018

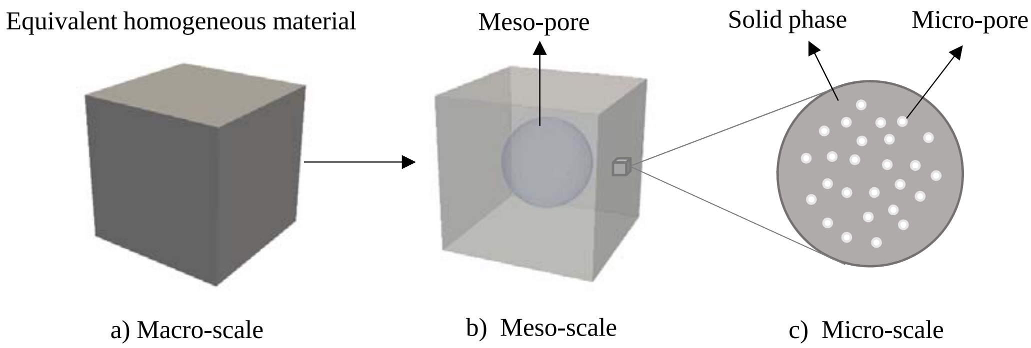

Figure II .1: The selected REV of double porous medium with three scales.

2.1 Effective behavior of porous matrix

The porous matrix is composed of a solid phase and spherical pores at the microscopic scale. Compared with metal materials, the pressure sensitivity and volumetric deformation are two crucial characteristics of rock-like materials. In order to consider these aspects, the solid phase is assumed to obey to a Drucker-Prager type plastic criterion:

$$\Phi(\boldsymbol{\sigma}) = \sigma_d + \alpha(\sigma_m - h) \leq 0 \qquad \text{(II .2)}$$

in which $\boldsymbol{\sigma}$ denotes the microscopic stress tensor. $\sigma_m = tr\boldsymbol{\sigma}/3$ is the mean stress. σ_d is defined as $\sigma_d = \sqrt{\boldsymbol{\sigma'} : \boldsymbol{\sigma'}}$, with $\boldsymbol{\sigma'}$ being the deviatoric stress tensor. The parameter α is the frictional coefficient and h the yield stress under hydrostatic tension of the solid phase.

For a porous material as illustrated in Figure II .1-c with a Drucker-Prager type solid matrix containing a spherical void, an analytical yield criterion has been derived using a modified secant method in [Maghous et al., 2009] :

$$F = \frac{1 + 2f/3}{\alpha^2}\tilde{\Sigma}_d^2 + (\frac{3f}{2\alpha^2} - 1)\tilde{\Sigma}_m^2 + 2(1-f)h\tilde{\Sigma}_m - (1-f)^2h^2 \leq 0 \qquad \text{(II .3)}$$

This criterion (II .3) explicitly depends on the porosity f at the microscopic scale and the pressure sensitivity parameter α of the solid phase. This criterion is selected here as the first homogenization step from micoscale to mesoscale to describe the effective plastic yield criterion of the porous matrix.

It is reminded that $\boldsymbol{\sigma}$ is the local stress in the solid phase (Figure II .1-c) at the microscopic scale. For the sake of clarity, $\tilde{\boldsymbol{\Sigma}}$ is introduced to denote the local stress in the porous matrix at the mesoscopic scale (Figure II .1-b). The macroscopic stress is denoted as $\boldsymbol{\Sigma}$ (Figure II .1-a). The total strain rate $\boldsymbol{D}$ of the porous matrix is further divided into an elastic part $\boldsymbol{D}^e$ and a plastic part $\boldsymbol{D}^p$. The effective stress-strain relations of the porous matrix can be expressed in the following incremental form:

$$\boldsymbol{D} = \boldsymbol{D^e} + \boldsymbol{D^p}, \quad \dot{\tilde{\boldsymbol{\Sigma}}} = \mathbb{C}_m : (\boldsymbol{D} - \boldsymbol{D^p}) \qquad \text{(II .4)}$$

© 2018 Tous droits réservés. lilliad.univ-lille.fr

where $\mathbb{C}_m$ is the effective elastic stiffness tensor of porous matrix. By assuming an isotropic material, $\mathbb{C}_m$ can be written as $\mathbb{C}_m = 3k_0^{hom}\mathbb{J} + 2\mu_0^{hom}\mathbb{K}$, where $J_{ijkl} = (\delta_{ij}\delta_{kl})/3$, $K_{ijkl} = I_{ijkl} - J_{ijkl}$ and $I_{ijkl} = (\delta_{ik}\delta_{jl} + \delta_{il}\delta_{jk})/2$ with δ_{ij} being the Kronecker's symbol. k_0^{hom} and μ_0^{hom} are respectively the effective bulk modulus and shear modulus of the porous matrix which are dependent on porosity and can be determined by using Mori-Tanaka scheme ([Mori and Tanaka, 1973]), corresponding to a Hashin-Shtrikman upper bound ([Hashin and Shtrikman, 1963, Weng, 1984]) :

$$k_0^{hom} = \frac{4(1-f)k_s\mu_s}{4\mu_s + 3fk_s}, \quad \mu_0^{hom} = \frac{(1-f)\mu_s}{1 + 6f\frac{k_s+2\mu_s}{9k_s+8\mu_s}} \tag{II .5}$$

in which k_s and μ_s are the bulk and shear modulus of the solid phase.

It is assumed that the porous matrix exhibits an elastic perfect-plastic behavior without plastic hardening. The plastic deformation of the porous matrix is further described by an associated plastic flow rule using the analytical yield function given in (II .3). As a consequence, the plastic strain rate of the porous matrix is given by:

$$\boldsymbol{D^p} = \dot{\lambda}\frac{\partial F}{\partial \tilde{\boldsymbol{\Sigma}}}(\tilde{\boldsymbol{\Sigma}}) \tag{II .6}$$

where $\dot{\lambda}$ is the plastic multiplier and it verifies the following loading-unloading condition:

$$\begin{cases} \dot{\lambda} = 0 \quad if \quad F < 0 \quad or \quad if \quad F = 0 \quad and \quad \dot{F} < 0 \\ \dot{\lambda} \geq 0 \quad if \quad F = 0 \quad and \quad \dot{F} = 0 \end{cases} \tag{II .7}$$

The plastic multiplier is determined from the consistency condition:

$$\dot{F}(\tilde{\boldsymbol{\Sigma}}) = \frac{\partial F(\tilde{\boldsymbol{\Sigma}})}{\partial \tilde{\boldsymbol{\Sigma}}} : \dot{\tilde{\boldsymbol{\Sigma}}} = 0 \tag{II .8}$$

Substituting (II .4) and (II .6) for (II .8), the plastic multiplier for the porous matrix is determined as follows:

$$\dot{\lambda} = \frac{\frac{\partial F}{\partial \tilde{\boldsymbol{\Sigma}}} : \mathbb{C}_m : \boldsymbol{D}}{\frac{\partial F}{\partial \tilde{\boldsymbol{\Sigma}}} : \mathbb{C}_m : \frac{\partial F}{\partial \tilde{\boldsymbol{\Sigma}}}} \tag{II .9}$$

The rate form of the effective constitutive relations of the porous matrix can also be written as follows:

$$\dot{\tilde{\boldsymbol{\Sigma}}} = \mathbb{C}_{meso}^{tan} : \boldsymbol{D} \tag{II .10}$$

Combining Equations (II .4), (II .6), (II .9) and (II .10), the effective tangent elastic-plastic stiffness operator $\mathbb{C}_{meso}^{tan}$ of the porous matrix at the mesoscopic scale is given by:

$$\mathbb{C}_{meso}^{tan} = \begin{cases} \mathbb{C}_m & (F \leq 0, \dot{F} < 0) \\ \mathbb{C}_m - \dfrac{\mathbb{C}_m : \frac{\partial F}{\partial \tilde{\boldsymbol{\Sigma}}} \otimes \frac{\partial F}{\partial \tilde{\boldsymbol{\Sigma}}} : \mathbb{C}_m}{H^G} & (F = 0, \dot{F} = 0) \end{cases} \tag{II .11}$$

© 2018 Tous droits réservés. lilliad.univ-lille.fr

Thèse de Yajun Cao, Université de Lille, 2018

with:

$$H^G = \frac{\partial F}{\partial \tilde{\boldsymbol{\Sigma}}} : \mathbb{C}_m : \frac{\partial F}{\partial \tilde{\boldsymbol{\Sigma}}} \tag{II .12}$$

2.2 Macroscopic mechanical behavior of double porous material

In the first homogenization step from microscale to mesoscale, the micro porosity f in the porous matrix has been considered in the analytical yield criterion (II .3). However, other microstructure information (pore shape, spatial distribution, etc.) have been ignored due to the small size of microscopic pores. In the second homogenization step, in order to well explicitly consider the interaction of microstructure between the matrix and meso-pore, we shall develop a numerical two-step homogenization method based on the discrete Fast Fourier Transform technique proposed by [Moulinec and Suquet, 1998, Moulinec and Suquet, 1994]. This method can avoid the difficulty of meshing for complex microstructure and of assembling the global stiffness matrix like in finite element method. The outline of the discrete FFT based numerical method have been summarized in Chapter I .

For the porous material containing a plastic porous matrix, the problem to be solved here is to determine the macroscopic stress corresponding to the prescribed macroscopic strain. This is done by making the volumetric average of the local stress field over the unit cell. Due to the plastic behavior of the porous material, a nonlinear homogenization problem should be solved. For this purpose, the total loading path is divided into a limit number of steps N. Considering now the loading step $n+1$, an incremental of macroscopic strain $\Delta \boldsymbol{E}^{n+1}$ is applied to the unit cell. We shall find the corresponding macroscopic stress increment $\Delta \boldsymbol{\Sigma}^{n+1}$. The local constitutive relations are then expressed in the following incremental form:

$$\Delta \boldsymbol{\sigma}(\boldsymbol{x}) = \mathbb{C}^{tan}_{meso}(\boldsymbol{x}) : \Delta \boldsymbol{\varepsilon}(\boldsymbol{x}) \tag{II .13}$$

The fourth order tensor $\mathbb{C}^{tan}_{meso}(\boldsymbol{x})$ denotes the tangent operator filed at the mesoscopic scale. Therefore, the local problem to be solved is formulated as follows:

$$\begin{cases} \Delta \boldsymbol{\sigma}(\boldsymbol{x}) = \mathbb{C}^{tan}_{meso}(\boldsymbol{x}) : \Delta \boldsymbol{\varepsilon}(\boldsymbol{x}) & \forall \boldsymbol{x} \in \Omega \\ div\boldsymbol{\sigma}(\boldsymbol{x}) = 0 \quad \forall \boldsymbol{x} \in \Omega, \quad u^* \#, \quad \boldsymbol{\sigma} \cdot n - \# \\ \boldsymbol{\varepsilon}(\boldsymbol{x}) = \frac{1}{2}(\nabla \boldsymbol{u}^*(\boldsymbol{x}) + \nabla^T \boldsymbol{u}^*(\boldsymbol{x})) + \boldsymbol{E} & \forall \boldsymbol{x} \in \Omega \end{cases} \tag{II .14}$$

In this relations, the symbol $\#$ denotes the periodic condition while $-\#$ the anti-periodic one. To solve this nonlinear problem, the local stress field can be rewritten as:

$$\begin{aligned} \boldsymbol{\sigma}(\boldsymbol{x}) &= \mathbb{C}^0 : \boldsymbol{\varepsilon}^*(\boldsymbol{x}) + \boldsymbol{\sigma}(\boldsymbol{x}) - \mathbb{C}^0 : (\boldsymbol{\varepsilon}(\boldsymbol{x}) - \boldsymbol{E}) \\ &= \mathbb{C}^0 : \boldsymbol{\varepsilon}^*(\boldsymbol{x}) + \boldsymbol{\tau}(\boldsymbol{x}) \end{aligned} \tag{II .15}$$

© 2018 Tous droits réservés. lilliad.univ-lille.fr

Thèse de Yajun Cao, Université de Lille, 2018

where $\boldsymbol{\tau}(\boldsymbol{x}) = \sigma(\boldsymbol{x}) - \mathbb{C}^0 : \boldsymbol{\varepsilon}(\boldsymbol{x}) + \mathbb{C}^0 : \boldsymbol{E}$

By using the solution of auxiliary problem mentioned in Chapter I , the solution of local strain field can be reduced to an iterative form in the Fourier space with:

$$\hat{\varepsilon}^{i+1}(\boldsymbol{\xi}) = \hat{\varepsilon}^{i}(\boldsymbol{\xi}) - \hat{\Gamma}^0(\boldsymbol{\xi}) : \hat{\boldsymbol{\sigma}}(\boldsymbol{\xi}) \qquad \forall \boldsymbol{\xi} \neq \boldsymbol{0}, \hat{\varepsilon}(\boldsymbol{0}) = \boldsymbol{E}. \tag{II .16}$$

The numerical algorithm is outlined as shown in Algorithm 1:

Algorithm 1: Two-step homogenization procedure

Input: $\boldsymbol{\varepsilon}(t_n, \boldsymbol{x}_p), \Delta \boldsymbol{E}(t_{n+1}), \Delta t_{n+1}$
Output: $\boldsymbol{E}(t_{n+1}), \boldsymbol{\Sigma}(t_{n+1})$
Initialization:$t_{n+1} = t_n + \Delta t_{n+1}$;
$\boldsymbol{E}(t_{n+1}) = \boldsymbol{E}(t_n) + \Delta \boldsymbol{E}(t_{n+1})$;
$\boldsymbol{\varepsilon}^0(t_{n+1}, \boldsymbol{x}_p) = \boldsymbol{\varepsilon}(t_n, \boldsymbol{x}_p) + \Delta \boldsymbol{E}(t_{n+1}) \qquad \forall \boldsymbol{x}_p \in \Omega$;
if $\boldsymbol{x}_p \in \omega$ **then**
  The first step homogenization: according to expression (II .3), (II .13) and using radial return algorithm to compute $\tilde{\boldsymbol{\Sigma}}^0(t_{n+1}, \boldsymbol{x}_{\boldsymbol{p}})$;
else
  $\tilde{\boldsymbol{\Sigma}}^0(t_{n+1}, \boldsymbol{x}_p) = 0$;
end
for $i = 0 : N_{iter}$ **do**
  The previous $\tilde{\boldsymbol{\Sigma}}(t_n)$ and $\boldsymbol{\varepsilon}(t_n)$ at each point $\boldsymbol{x}_{\boldsymbol{p}}$ are known ;
  $\hat{\boldsymbol{\Sigma}}^i(t_{n+1}, \boldsymbol{\xi}_p) = \mathcal{FFT}(\tilde{\boldsymbol{\Sigma}}^i(t_{n+1}, \boldsymbol{x}_{\boldsymbol{p}}))$;
  Convergence test $E_{error} = \frac{(\langle \| \boldsymbol{\xi} \cdot \hat{\boldsymbol{\sigma}}^i(\boldsymbol{\xi}) \|^2 \rangle)^{1/2}}{\| \hat{\boldsymbol{\sigma}}^i(\boldsymbol{0}) \|}$;
  if $\epsilon_{error} < 10^{-4}$ **then**
    Return;
  else
    $\hat{\varepsilon}^{i+1}(t_{n+1}, \boldsymbol{\xi}_p) = \hat{\varepsilon}^i(t_{n+1}, \boldsymbol{\xi}_p) - \hat{\Gamma}^0(\boldsymbol{\xi}_p) : \hat{\boldsymbol{\Sigma}}^i(t_{n+1}, \boldsymbol{\xi}_p) \qquad \forall \boldsymbol{\xi}_p \neq \boldsymbol{0}, \quad \hat{\varepsilon}^{i+1}(\boldsymbol{0}) = \boldsymbol{E}(t_{n+1})$;
    $\boldsymbol{\varepsilon}^{i+1}(t_{n+1}, \boldsymbol{x}_{\boldsymbol{p}}) = \mathcal{FFT}^{-1}(\hat{\varepsilon}^{i+1}(t_{n+1}, \boldsymbol{\xi}_p))$;
    if $\boldsymbol{x}_p \in \omega$ **then**
      The first step homogenization: according to expression (II .3), (II .13) and using radial return algorithm to compute $\tilde{\boldsymbol{\Sigma}}^{i+1}(t_{n+1}, \boldsymbol{x}_{\boldsymbol{p}})$;
    else
      $\tilde{\boldsymbol{\Sigma}}^{i+1}(t_{n+1}, \boldsymbol{x}_p) = 0$;
    end
    $i = i + 1$;
  end
end
Calculate the macroscopic stress $\boldsymbol{\Sigma}(t_{n+1}) = \frac{1}{|\Omega|} \int_\Omega \tilde{\boldsymbol{\Sigma}}(t_{n+1}, \boldsymbol{x}_{\boldsymbol{p}}) dV$

In this context, the elastic-plastic constitutive relations at each point $\boldsymbol{x}_{\boldsymbol{p}}$ of the porous matrix should be solved for a given loading history. In the present study, only the time-independent behavior is considered. Due to the nonlinear behavior of the porous matrix, the whole loading history is discretized into a finite number of increments. The current loading increment is represented by the time increment Δt during the interval $[t_n, t_{n+1}]$. Starting from the initial conditions, the field variables (ε_n, ε_n^p, $\Delta\varepsilon$) at each point $\boldsymbol{x}_p$ are

© 2018 Tous droits réservés. lilliad.univ-lille.fr

Thèse de Yajun Cao, Université de Lille, 2018

known at the loading step t_n. The unknown plastic strain and stress fields ε^p_{n+1} and σ_{n+1} at the loading step t_{n+1} should be determined with the help of an implicit standard return mapping iterate procedure. The symbol $\mathcal{FFT}$ and $\mathcal{FFT}^{-1}$ represent correspondingly the FFT and inverse FFT operators. It can be seen that an iterative algorithm is needed to find an appropriate non-uniform strain field and the corresponding stress field, verifying the local constitutive relations, equilibrium equations and boundary conditions on the unit cell. The choice of the reference stiffness tensor $\mathbb{C}^0$ can significantly affect the rate of convergence. In practice, according to [Moulinec and Suquet, 1998, Moulinec and Suquet, 1994], the best rate of convergence is provided with the following values of Lamé coefficients (λ^0 and μ^0) for the reference material:

$$\begin{aligned} \lambda^0 &= \frac{1}{2}(\inf_{\boldsymbol{x}\in V} \lambda(\boldsymbol{x}) + \sup_{\boldsymbol{x}\in V} \lambda(\boldsymbol{x})) \\ \mu^0 &= \frac{1}{2}(\inf_{\boldsymbol{x}\in V} \mu(\boldsymbol{x}) + \sup_{\boldsymbol{x}\in V} \mu(\boldsymbol{x})) \end{aligned} \tag{II .17}$$

2.3 Validation of the model by Finite element method

In order to verify the accuracy of FFT-based models in estimating effective behaviors of composite materials, the numerical results provided by finite element method (FEM) for some simple configurations of the unit cell are generally used as the reference solutions to compare with those given by the FFT-based models [Michel et al., 1999]. With this methodology, the accuracy of the FFT-based homogenization method has been verified and demonstrated in [Michel et al., 1999] for porous materials with one population of pores and in [Li et al., 2018] for composites with one family of inclusions. Following the same methodology, we shall here verify the accuracy of the FFT-based numerical model for porous materials with two populations of pores. For this propose, a series of simulations are performed by using both the FFT-based model and finite element method on the same unit cell and with the same periodic boundary conditions as indicated in (II .14).

For the sake of simplicity, both mesoscopic and microscopic pores are assumed spherical. The unit cell contains one centered pore at the mesoscopic scale. As shown in Fig.II .2, the unit cell is divided into $150 \times 150 \times 150$ voxels of identical size for the FFT-based calculations. For the FEM calculations, the mesh contains 11999 nodes and 7878 elements. The elastic and plastic parameters of the porous matrix are selected as $E_s = 5GPa, v_s = 0.15, \alpha = 0.2 \sim 0.3, h = 10MPa$.

© 2018 Tous droits réservés. lilliad.univ-lille.fr

Thèse de Yajun Cao, Université de Lille, 2018

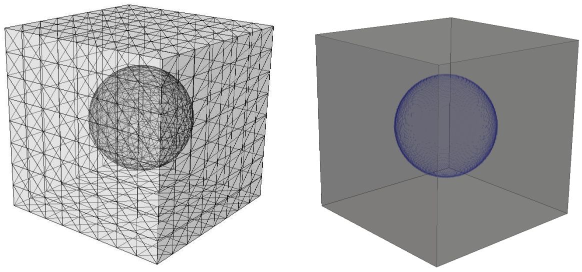

(a) FEM (b) FFT

Figure II .2: The representative unit cells with one centered meso-pore used by FEM and FFT method: $f/\phi = 0, \Gamma = 0.1$ (For FEM mesh: 11999 nodes and 7878 elements, and for FFT unit cell: $150 \times 150 \times 150$ voxels)

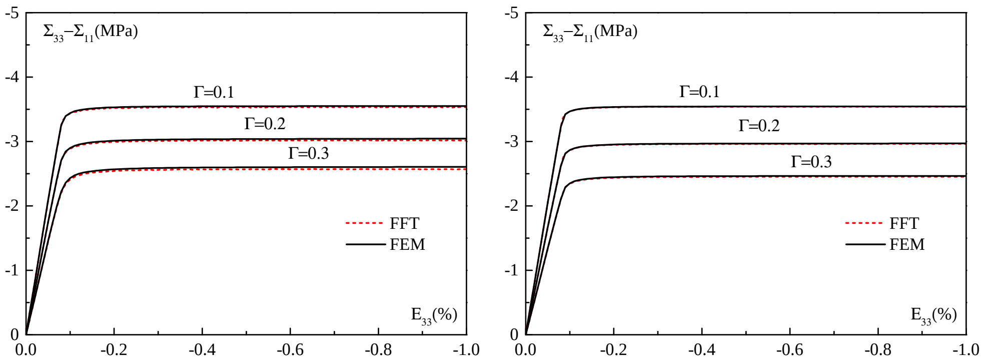

(a) (b)

Figure II .3: Comparison of overall stress-strain relations between FEM and FFT-based numerical method for unit cell under uniaxial compression test : (a) $f/\phi = 0$, $\alpha = 0.3$. (b) $f/\phi = 1$, $\alpha = 0.3$

The overall stress-strain responses of the unit cell with single porosity and double porosity under the uniaxial compression are compared between the two numerical methods and presented in Fig.II .3. There is a very good concordance of overall stress-strain curves at both the elastic and plastic stages. The macroscopic plastic yield stresses of the unit cell are also presented in Fig.II .4 and Fig.II .5 for different values of porosity ratio f/ϕ. It is found that the results given by the two methods are very close each to other. These results seem to confirm that the FFT-based numerical homogenization method is able to provide accurate estimations of macroscopic behaviors of porous materials with two populations of pores. For materials with complex distributions of pores, it is generally difficult to find suitable reference solutions so that the validation of FFT-based models is a delicate task.

© 2018 Tous droits réservés. lilliad.univ-lille.fr

Thèse de Yajun Cao, Université de Lille, 2018

Experimental validations should be also considered in future studies.

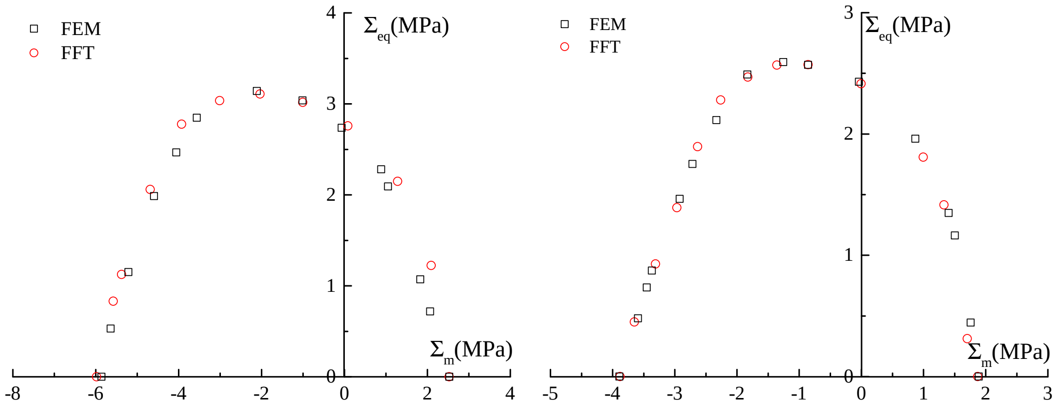

(a) (b)

Figure II .4: Comparison of yield surfaces between FEM and FFT-based numerical method for unit cell with single porosity ($f/\phi = 0$, $\alpha = 0.3$): (a) $\Gamma = 0.2$. (b) $\Gamma = 0.3$

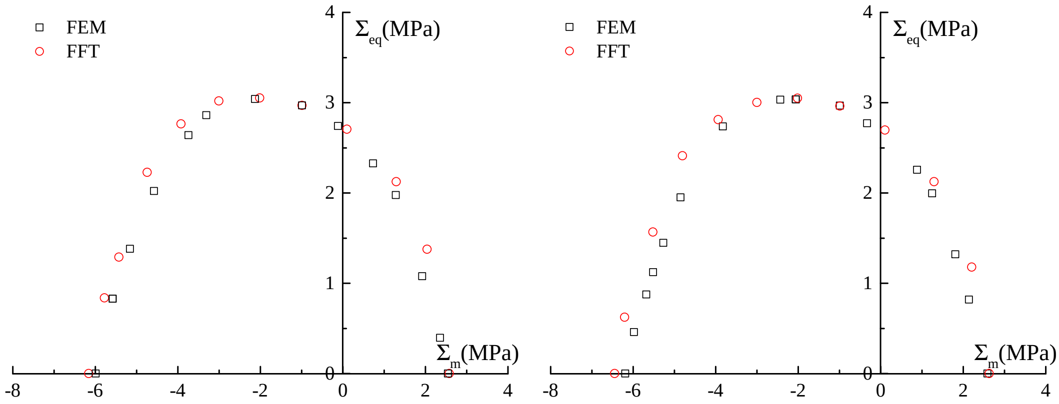

(a) (b)

Figure II .5: Comparison of yield surfaces between FEM and FFT-based numerical method for unit cell with double porosities ($\alpha = 0.3$, $\Gamma = 0.2$): (a) $f/\phi = 0.5$. (b) $f/\phi = 1$

3 Comparisons between FFT-based method and analytical models

In order to further assess the effective properties of double porous materials provided by FFT-based model, comparisons with results issued from existing analytical models are

© 2018 Tous droits réservés. lilliad.univ-lille.fr

Thèse de Yajun Cao, Université de Lille, 2018

here presented for some selected micro-structures. The elastic and plastic parameters used are the same as those used in Section 2.3. We shall especially investigate effects of the porosity ratio f/ϕ on effective elastic stiffness and plastic yield stress of a double porous material for a given total porosity Γ. Further, as the analytical models have been formulated for a constant value of porosity, in order to make meaningful comparisons between FFT-based results and analytical models, both the micro-porosity and meso-porosity are taken constant in all numerical calculations. More precisely, the evolution of the micro-porosity is neglected during plastic deformation of the porous matrix, namely $\dot{f} = 0$.

3.1 Case of elastic behavior

The effective elastic bulk modulus k_{hom} and shear modulus μ_{hom} are determined by a two-step homogenization procedure. The elastic properties of the porous matrix containing the microscopic pores are determined by using the Hashin-Shtrikman upper bound at the first step of homogenization. For the estimation of elastic properties of the porous material at the second step of homogenization with the mesoscopic pores, three different methods are used and compared, namely the Hashin-Shtrikman upper bound, the dilute scheme and the FFT-based numerical model. The solutions of two analytical homogenization methods are given in Appendix A. Further, as the analytical predictions of effective properties are based on the assumption of an isotropic distribution of pores, FFT-based numerical calculations are performed unit cells with randomly distributed spherical pores at the mesoscopic scale.

In Fig.II .6 to II .9, one can see the evolutions of the normalized modulus k_{hom}/k_s and μ_{hom}/μ_s with f/ϕ for four different values of total porosity. As a first remark, it is found that the results of three methods are significantly different for small values of f/ϕ, especially for the HS+dilute scheme. This is mainly due to the fact that in the dilute scheme, the effect of interaction between pores is neglected.

For the HS+HS upper bound method, the relative bulk modulus k_{hom}/k_s firstly decreases with the increase of f/ϕ and reaches a minimum value when f/ϕ is close to 1, and then it slowly increases. The predictions by the FFT-based model are well lower than the upper bounds.Starting a very low value, the HS+dilute scheme shows a continuous increase of k_{hom}/k_s and then approaches the two other methods when $f/\phi = 5$. The three different methods provide all an asymptotic value of k_{hom}/k_s when f/ϕ becomes higher enough, depending on the value of total porosity. The evolution of the effective shear modulus μ_{hom}/μ_s is qualitatively similar to that of the bulk modulus.

© 2018 Tous droits réservés. lilliad.univ-lille.fr

Thèse de Yajun Cao, Université de Lille, 2018

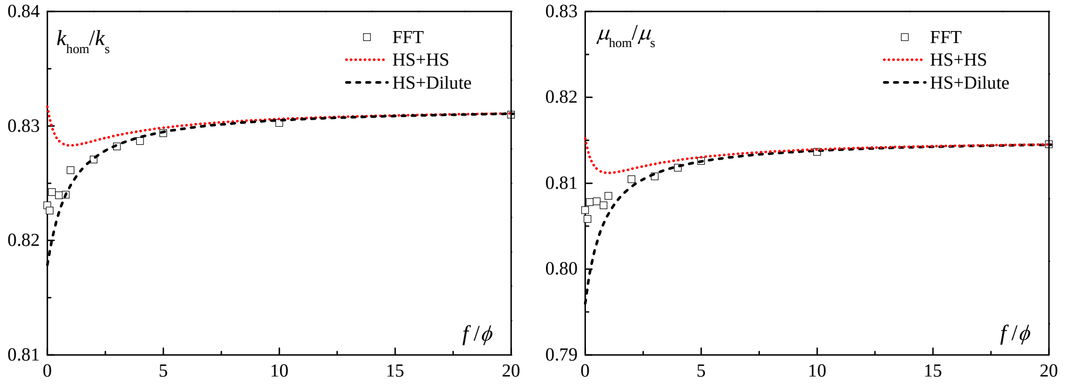

(a) (b)

Figure II .6: Evolutions of effective elastic moduli with f/ϕ for a total porosity $\Gamma = 0.1$ with three different two-step homogenization methods

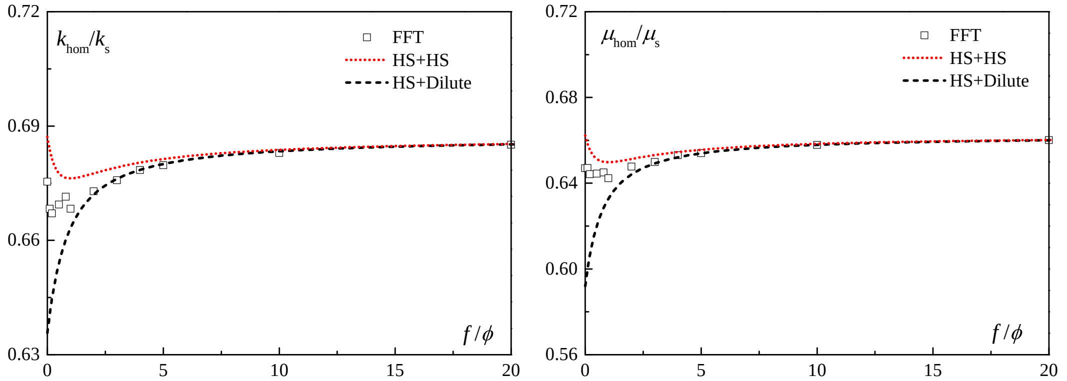

(a) (b)

Figure II .7: Evolutions of effective elastic moduli with f/ϕ for a total porosity $\Gamma = 0.2$ with three different two-step homogenization methods

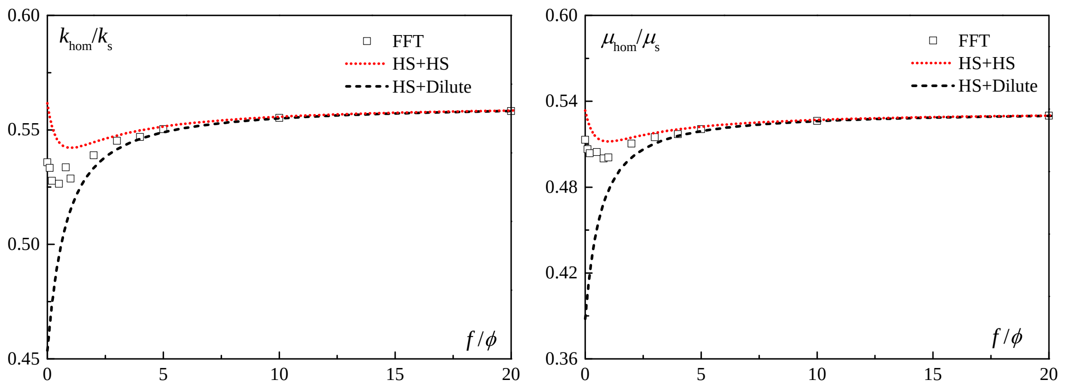

(a) (b)

Figure II .8: Evolutions of effective elastic moduli with f/ϕ for a total porosity $\Gamma = 0.3$ with three different two-step homogenization methods

© 2018 Tous droits réservés. lilliad.univ-lille.fr

Thèse de Yajun Cao, Université de Lille, 2018

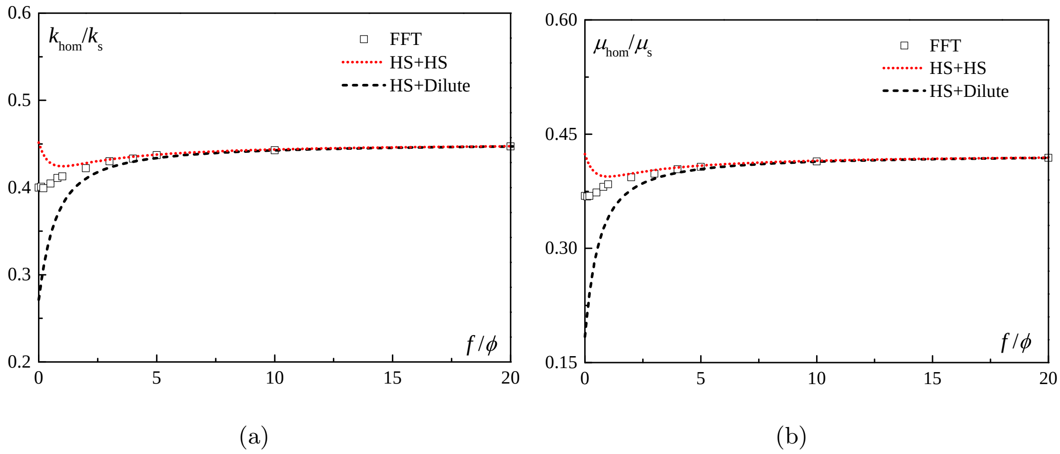

Figure II .9: Evolutions of effective elastic moduli with f/ϕ for a total porosity $\Gamma = 0.4$ with three different two-step homogenization methods

From these results, it is concluded that for the values of total porosity considered in our study, the results predicted by the three methods are nearly identical when the porosity ratio f/ϕ is greater than 5. In other cases, the results provided by the analytical models can be significantly different with those given by the FFT-based numerical model.

3.2 Case of plastic behavior

The macroscopic yield stress of porous materials with a Drucker-Prager solid matrix containing spherical pores has been previously investigated by different methods ([Guo et al., 2008]; [Maghous et al., 2009]; [Shen et al., 2017b]). Based on the study of [Maghous et al., 2009], [Shen et al., 2014] and [Shen and Shao, 2016a] have derived two different analytical macroscopic yield criteria respectively using a modified secant method and a kinematical limit analysis approach. The detailed formulations of two criteria are presented in Appendix B. The validity of these criteria has not so far been assessed with any numerical results issued from full-field simulations. This issue is discussed in the present paper.

3.2.1 Effects of distribution of meso-pores

As an advantage of the FFT-based numerical model in studying effects of spatial distribution of pore, the influence of pore distribution at the mesoscopic scale on the macroscopic plastic yield stress is first investigated. To this end, a series of calculations are performed respectively on the unit cell with randomly distributed pores (pore number

© 2018 Tous droits réservés. lilliad.univ-lille.fr

Thèse de Yajun Cao, Université de Lille, 2018

N=200) and the unit cell with one centered pore, for different values of porosity ratio but for the same given total porosity.

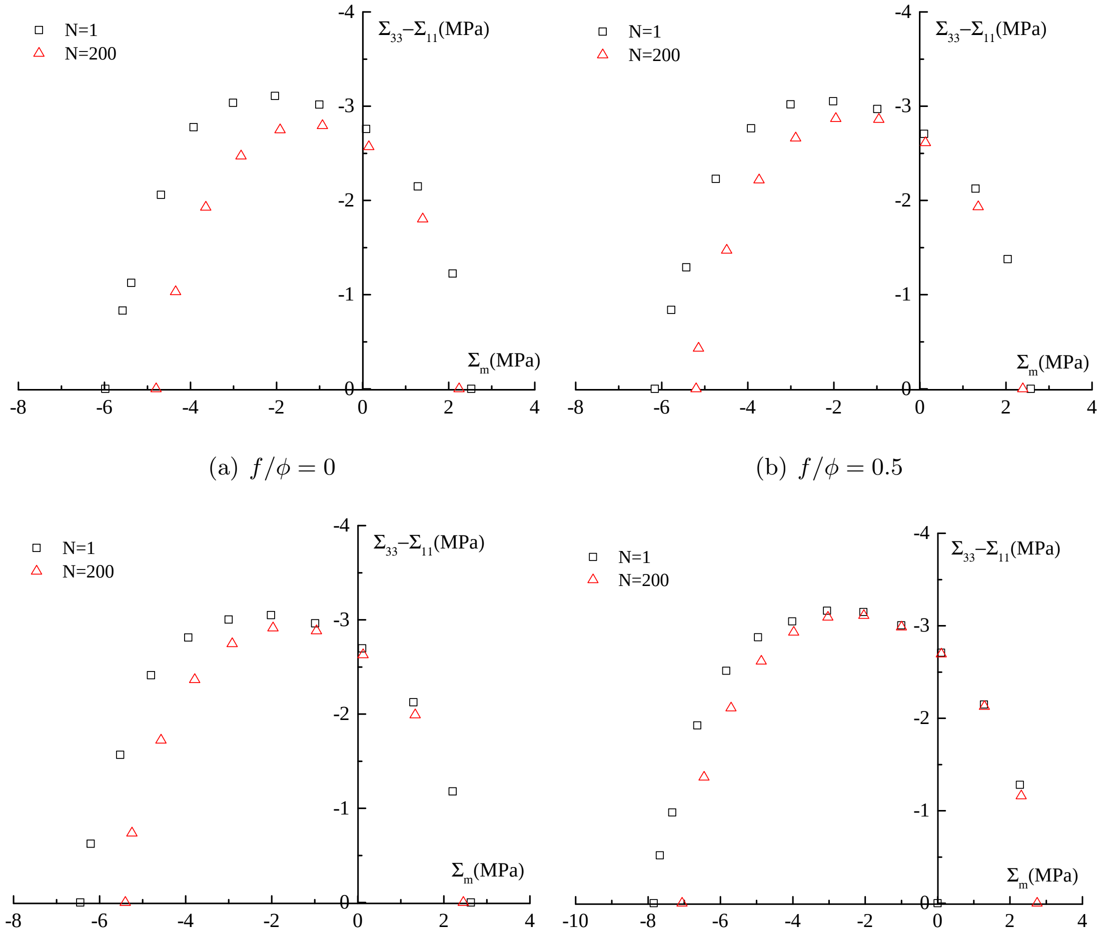

(a) $f/\phi = 0$ (b) $f/\phi = 0.5$

(c) $f/\phi = 1$ (d) $f/\phi = 5$

Figure II .10: Evolution of macroscopic yield surfaces with different f/ϕ predicted by unit cells with random distributed pores and one centered pore for $\alpha = 0.3$, $\Gamma = 0.2$

The obtained values of macroscopic yield stress of the unit cell are illustrated in Fig.II .10 for four values of f/ϕ. One can see some important differences between pore distributions in the unit cell, especially in the compression region. It is found that the yield stresses of the unit cell with a random distribution of pores are systematically lower than those of the unit cell with one single pore. However, the difference between two distributions becomes smaller when the porosity ratio f/ϕ is higher due to the fact that the meso-porosity becomes smaller. These results clearly show the effect of distribution of meso-pores on the macroscopic yield stress. However, the calculation time is much longer

© 2018 Tous droits réservés. lilliad.univ-lille.fr

for the random distribution than for the single pore. Further, the analytical criterion given in [Shen et al., 2014] has been formulated on the unit cell with one meso-pore. Therefore, in the subsequent sub-sections, we shall use the unit cell with a centered spherical meso-pore to perform sensitivity studies and comparisons with the analytical criteria.

3.2.2 Influences of the porosity ratio f/ϕ

The influences of the porosity ratio f/ϕ on the evolution of macroscopic yield stress are evaluated. According to plastic criterion given in [Shen and Shao, 2016a], for a given total porosity, the macroscopic yield surfaces are very close each to other for two reciprocal values of porosity ratio f/ϕ. For instance and as shown in Fig.II .11 (additional results can be found in II .27), the plastic yield surface for $f/\phi = 0.1$ almost coincides with that corresponding to $f/\phi = 10$.

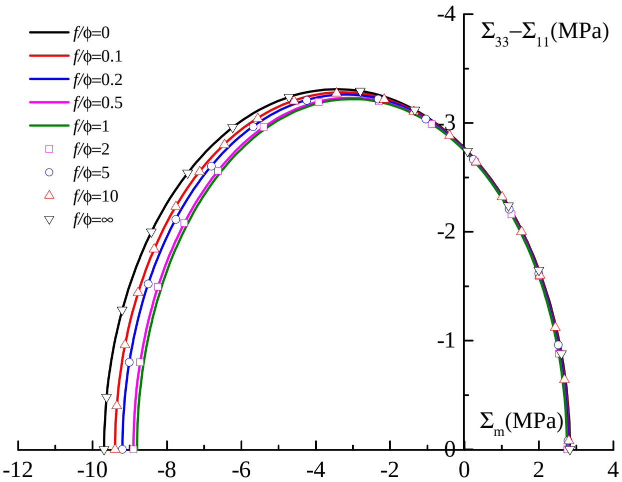

Figure II .11: Evolution of macroscopic yield surface with f/ϕ predicted by the criterion given in [Shen and Shao, 2016a] for $\alpha = 0.3$ and $\Gamma = 0.2$

This is due to the fact that the values of the term Θ appeared in Equation (II .33) are very close each to other but not strictly identical for two reciprocal values of porosity ratio f/ϕ. Some additional discussions on the evolution of Θ in (II .33) respectively as a function of f and ϕ are presented in Appendix B and shown in Fig.II .26. However, according the analytical criterion, the yield stresses under hydrostatic loading are rigorously identical each to other for two reciprocal values of porosity ratio f/ϕ. Moreover, the smallest yield surface is obtained for $f/\phi = 1$.

© 2018 Tous droits réservés.

Thèse de Yajun Cao, Université de Lille, 2018

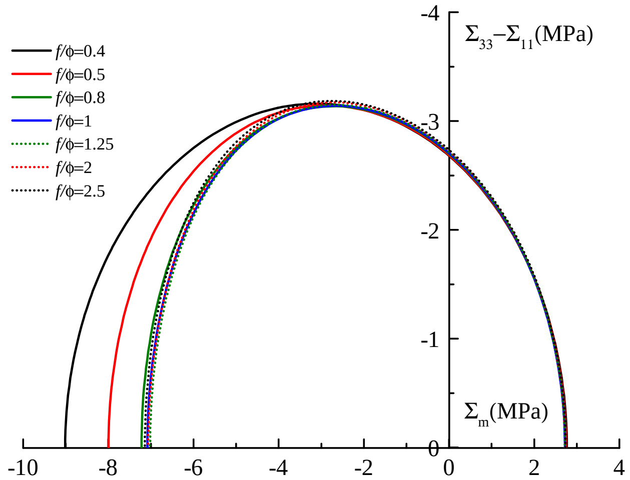

Figure II .12: Evolution of macroscopic yield surface with f/ϕ predicted by the criterion given in [Shen et al., 2014] for $\alpha = 0.3$ and $\Gamma = 0.2$

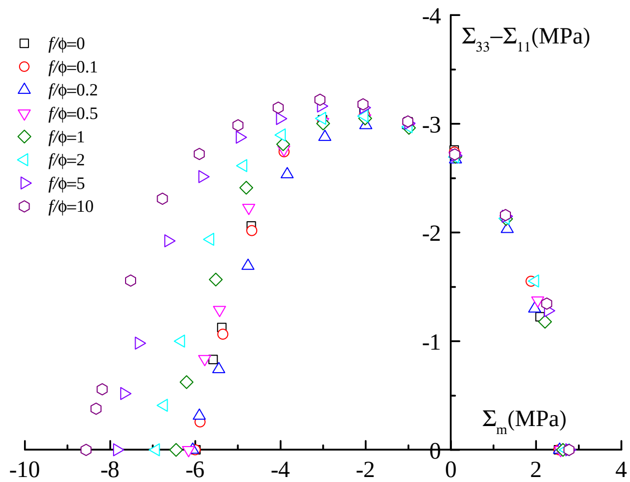

Figure II .13: Evolution of macroscopic yield surface with f/ϕ predicted by the FFT-based model for $\alpha = 0.3$ and $\Gamma = 0.2$

For the other analytical criterion given in [Shen et al., 2014] and for the FFT-based numerical model, the different roles of two populations of pores are taken into account, as shown in Fig.II .12 and Fig.II .13. For the FFT-based model, the yield surface monotonically increases with the increase of porosity ratio f/ϕ. The smallest surface is obtained for $f/\phi = 0$. This means that the macroscopic yield stress is more sensitive to the mesoscopic porosity than the microscopic one. The analytical criterion given in [Shen et al., 2014] provides a similar trend as and is less sensitive to the porosity ratio f/ϕ than the FFT-based model.

- *Special case of macroscopic hydrostatic strength*

© 2018 Tous droits réservés. lilliad.univ-lille.fr

The macroscopic yield stress under hydrostatic compression and tension is now investigated for the three homogenization methods. Different values of total porosity Γ and frictional coefficient α are considered.

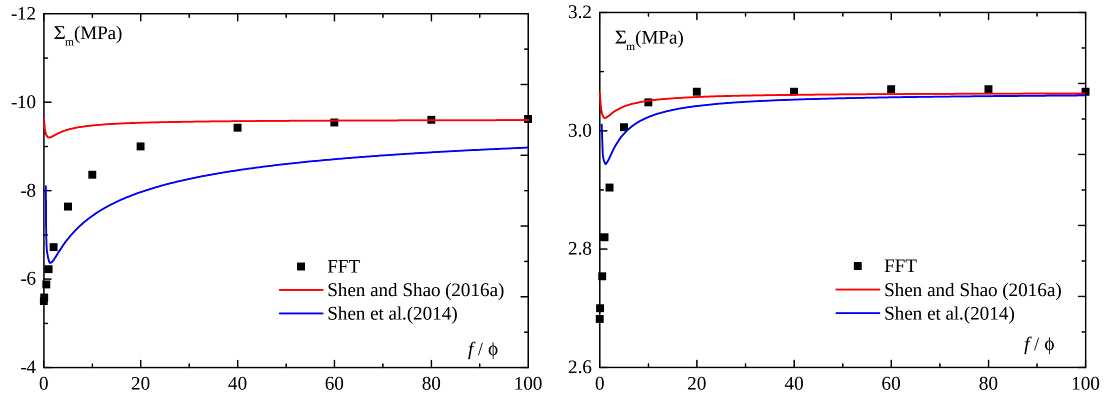

(a) (b)

Figure II .14: Evolution of yield stress in hydrostatic compression (a) and tension (b) for $\alpha = 0.2$ and $\Gamma = 0.1$

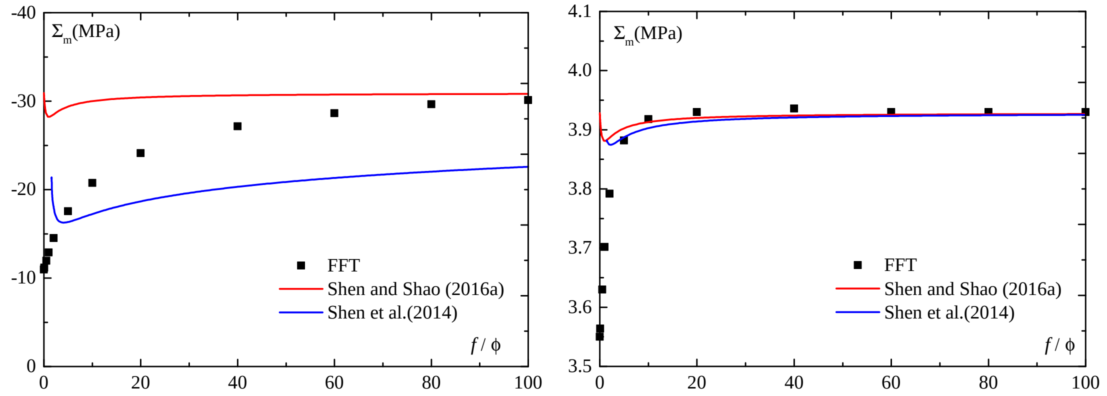

(a) (b)

Figure II .15: Evolution of yield stress in hydrostatic compression (a) and tension (b) for $\alpha = 0.3$ and $\Gamma = 0.1$

© 2018 Tous droits réservés. lilliad.univ-lille.fr

Thèse de Yajun Cao, Université de Lille, 2018

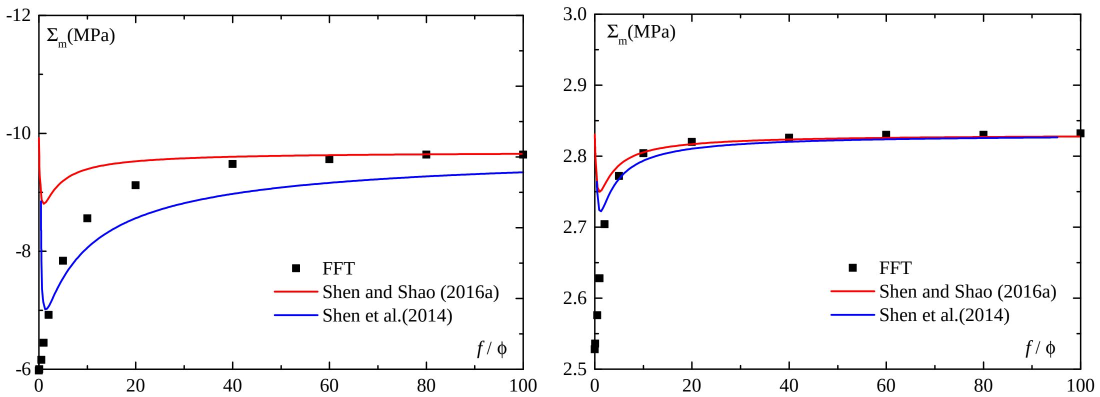

(a) (b)

Figure II .16: Evolution of yield stress in hydrostatic compression (a) and tension (b) for $\alpha = 0.3$ and $\Gamma = 0.2$

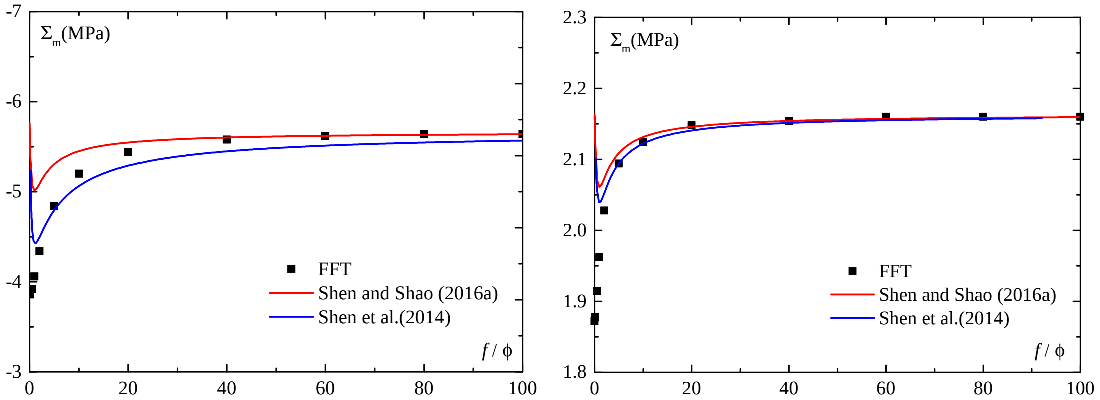

(a) (b)

Figure II .17: Evolution of yield stress in hydrostatic compression (a) and tension (b) for $\alpha = 0.3$ and $\Gamma = 0.3$

In Fig.II .14 to Fig.II .17, we present the variation of yield stress in hydrostatic compression and tension with the porosity ratio f/ϕ. It is found that the values predicted the two analytical criteria do not always coincide with the numerical results given by the FFT-based model method, especially in hydrostatic compression and for low values of f/ϕ. The differences between the analytical criteria and the FFT-based model are amplified by the increase of frictional coefficient α for a given total porosity Γ, but little sensitive to the total porosity increase when the frictional coefficient is constant.

In a general way, the criterion [Shen and Shao, 2016a] overestimates the yield stresses

© 2018 Tous droits réservés. lilliad.univ-lille.fr

Thèse de Yajun Cao, Université de Lille, 2018

when the porosity ration $f/\phi \leq 40$. After that, a good agreement is found between the analytical criterion and the FFT-based model. For the analytical criterion given in [Shen et al., 2014], the hydrostatic compression yield stress is overestimated for low values of f/ϕ but underestimated for high values of f/ϕ. A good agreement with the FFT-based model is observed only for the hydrostatic tension yield stress when the porosity ratio is higher than 40.

As shown in the previous section, it exists the critical porosity ratio corresponding to the smallest yield stress. The value of f/ϕ related to the smallest yield stress under hydrostatic compression is here discussed. According to the criterion [Shen and Shao, 2016a], the smallest yield stress is obtained for $f/\phi = 1$ whatever the stress path. However, for the criterion [Shen et al., 2014], the critical value of f/ϕ depends on the frictional coefficient α and total porosity Γ, as shown in Fig.II .18. For a given α, the value of f/ϕ to get the smallest yield stress decreases with the increasing total porosity. With a given value of total porosity, the critical value of f/ϕ increases with the increasing α. For the FFT-based numerical model, the smallest yield stress is obtained for $f/\phi = 0$, corresponding to vanishing of microscopic pores because interactions between pores are intensified at the mesoscopic scale.

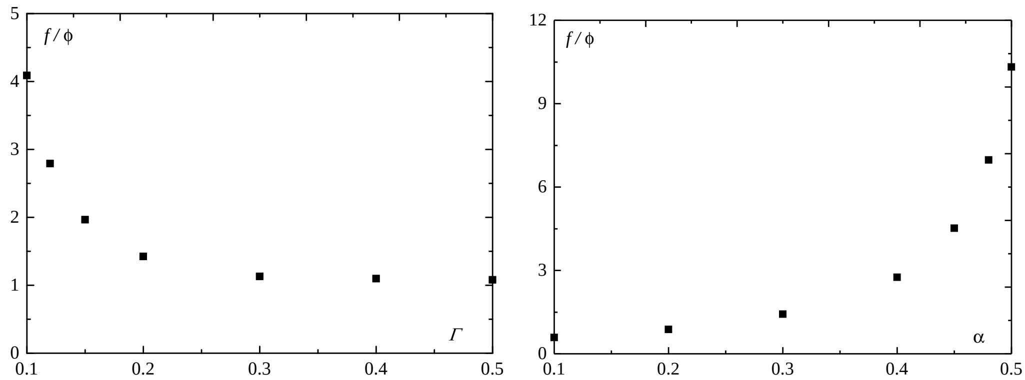

(a) $T = 0.$ (b) $\Gamma = 0.2$

Figure II .18: Evolution of critical value of f/ϕ corresponding to the smallest hydrostatic compression yield stress according to the criterion [Shen et al., 2014] as a function of total porosity Γ (a) and frictional coefficient α (b)

3.2.3 Comparisons with analytical macroscopic yield surfaces

The macroscopic yield stresses predicted respectively by the two analytical criteria and the FFT-based numerical model are presented in Fig.II .19 to II .22, for different values

© 2018 Tous droits réservés. lilliad.univ-lille.fr

of total porosity $\Gamma = 0.1$, the porosity ratio f/ϕ and the local friction coefficient α of the solid matrix.

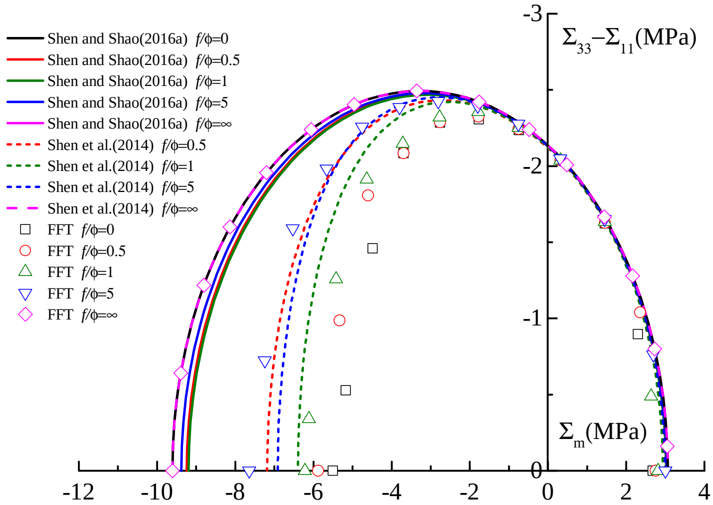

Figure II .19: Comparisons of macroscopic yield stresses between FFT-based numerical model and two analytical criteria for $\alpha = 0.2$, $\Gamma = 0.1$

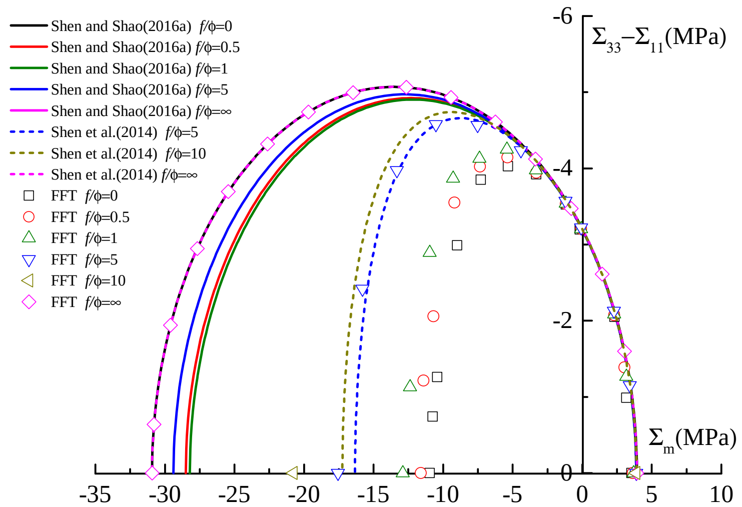

Figure II .20: Comparisons of macroscopic yield stresses between FFT-based numerical model and two analytical criteria for $\alpha = 0.3$, $\Gamma = 0.1$.

As a starting point, when the mesoscopic porosity vanished, $\phi = 0$ and $f/\phi = \infty$, the results provided by the three homogenization methods are identical because they are using the same yield criterion proposed by [Maghous et al., 2009] for the porous matrix at the microscopic scale. This also shows the accuracy of the numerical solutions given by the FFT-based model. In all other cases, significant differences of macroscopic yield stress are observed for the compressive mean stress region. The yield stresses in the tensile

© 2018 Tous droits réservés.

mean stress regime are however very similar between three methods. This is due to the fact that the internal friction in the Drucker-Prager solid matrix plays a more important role on the yield stress under a compressive mean stress than a tensile one. Furthermore, it is interesting to see that the results provided by the two analytical criteria are also significantly different each to other. The macroscopic yield stress is therefore sensitive to the assumptions used on the analytical homogenization schemes.

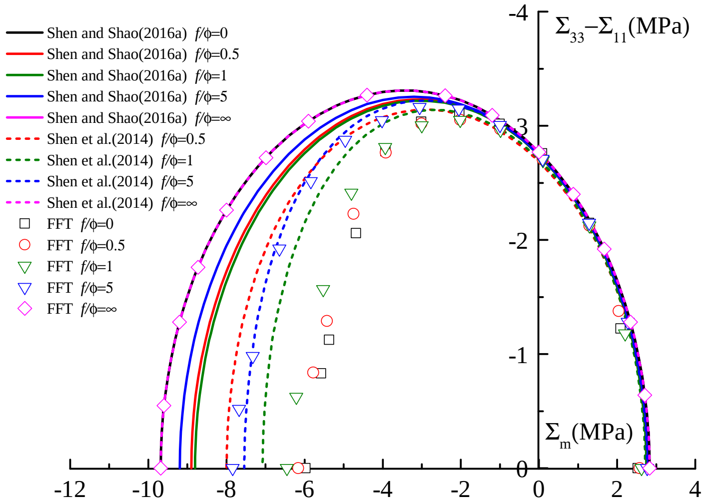

Figure II .21: Comparisons of macroscopic yield stresses between FFT-based numerical model and two analytical criteria for $\alpha = 0.3$, $\Gamma = 0.2$.

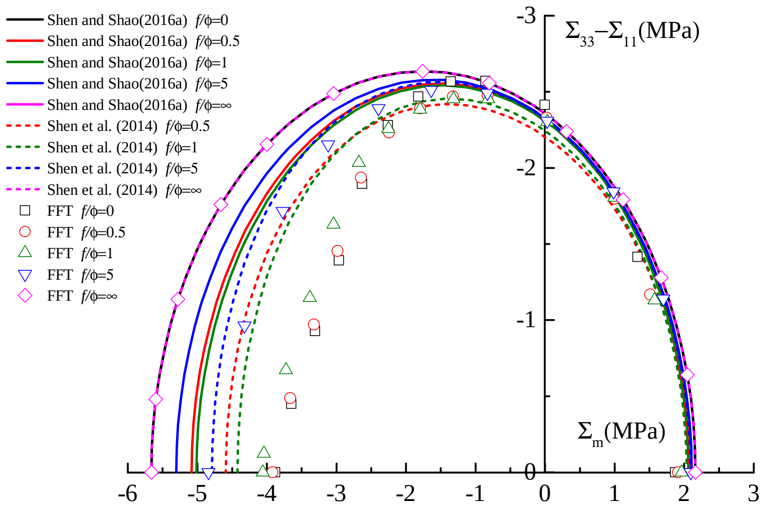

Figure II .22: Comparisons of macroscopic yield stresses between FFT-based numerical model and two analytical criteria for $\alpha = 0.3$, $\Gamma = 0.3$.

Let consider the particular case where the microscopic porosity vanishes, say $f = 0$ and $f/\phi = 0$, the results from the FFT-based method provide the smallest values of

© 2018 Tous droits réservés.

Thèse de Yajun Cao, Université de Lille, 2018

macroscopic yield stress. It is useful to note that in this case the results from the criterion [Shen and Shao, 2016a] are equivalent with those given by the FFT-based model for $f/\phi = \infty$. However, it is not possible to get the solution from the criterion [Shen et al., 2014] when $f = 0$ due to the mathematical singularity in the denominator of the criterion as shown in (II .32).

4 Local and overall responses with the evolution of micro-porosity

In the previous sections, in view of comparisons between analytical models and FFT-based numerical results, the micro-porosity of porous matrix is kept constant. In actual situations, due to plastic deformation, the micro-porosity evolves and its variation induces a plastic hardening or softening of the porous matrix.

In this section, we shall investigate local and overall responses of porous materials by considering the variation of micro-porosity. To this end, it is assumed that the pore volume change at the microscopic scale only depends on plastic pore compaction or dilation. The nucleation of new pores is not considered here. According to the first term of (II .1), one has:

$$\dot{f} = d(\frac{\omega_1}{\omega}) = \frac{d\omega_1}{\omega} - \frac{\omega_1}{\omega}\frac{d\omega}{\omega} = (1-f)(\frac{d\omega}{\omega} - \frac{d\omega_m}{\omega_m}) \tag{II .18}$$

in which $\frac{d\omega}{\omega}$ is the average mesoscopic volumetric strain rate ($tr\boldsymbol{D}^p$), and $\frac{d\omega_m}{\omega_m}$ denotes the volumetric strain rate ($tr\boldsymbol{d}$) of the solid phase. It is assumed that the solid phase is described by a Drucker-Prager type criterion and an associate plastic flow rule. Thus, the microscopic strain rate $\boldsymbol{d}$ can be calculated by:

$$\boldsymbol{d} = \dot{\Lambda}\frac{\partial \Phi}{\partial \boldsymbol{\sigma}}; \quad \boldsymbol{d}' = \dot{\Lambda}\frac{\boldsymbol{\sigma}'}{\sigma_d}; \quad d_m = \frac{1}{3}\dot{\Lambda}\alpha \tag{II .19}$$

where $\boldsymbol{d}'$ is the deviatoric strain rate tensor with $\boldsymbol{d} = \boldsymbol{d}' + d_m\boldsymbol{\delta}$. $\dot{\Lambda}$ is the plastic multiplier of the solid phase. The equivalent plastic strain rate $\dot{\epsilon^p}$ takes the following form:

$$\dot{\epsilon^p} = \sqrt{\boldsymbol{d}' : \boldsymbol{d}'} = \dot{\Lambda} \tag{II .20}$$

Owing to the energy-based equivalence condition introduced by [Gurson, 1977], it is possible to associate the average plastic strain rate of porous matrix with that of the solid phase ([Shen et al., 2012a]), that is:

$$\tilde{\boldsymbol{\Sigma}} : \boldsymbol{D}^p = \frac{1}{\omega}\int_{\omega_m} \boldsymbol{\sigma} : \boldsymbol{d} dV = \frac{1}{\omega}\int_{\omega_m} \dot{\epsilon^p}(\sigma_d + \alpha\sigma_m)dV = (1-f)\alpha h\dot{\epsilon^p} \tag{II .21}$$

© 2018 Tous droits réservés. lilliad.univ-lille.fr

Therefore $\dot{\epsilon^p}$ is obtained by:

$$\dot{\epsilon^p} = \frac{\tilde{\mathbf{\Sigma}} : \boldsymbol{D^p}}{(1-f)\alpha h} \tag{II .22}$$

With the relations (II .19) and (II .20) in hand, the plastic dilation rate is related to the equivalent plastic strain rate by $tr\boldsymbol{d}^p = \alpha\dot{\epsilon^p}$. The variation of porosity in (II .18) can be determined from the following kinematical compatibility condition:

$$\dot{f} = (1-f)(tr\boldsymbol{D^p} - \alpha\dot{\epsilon^p}) \tag{II .23}$$

Thus the plastic multiplier is given by:

$$\dot{\lambda} = \frac{\frac{\partial F}{\partial \tilde{\mathbf{\Sigma}}} : \mathbb{C}_m : \boldsymbol{D}}{\frac{\partial F}{\partial \tilde{\mathbf{\Sigma}}} : \mathbb{C}_m : \frac{\partial F}{\partial \tilde{\mathbf{\Sigma}}} - \frac{\partial F}{\partial f}(1-f)[\frac{\partial F}{\partial \tilde{\Sigma}_m} - \frac{\tilde{\mathbf{\Sigma}}:\frac{\partial F}{\partial \tilde{\mathbf{\Sigma}}}}{(1-f)h}]} \tag{II .24}$$

Finally, the effective tangent elastic-plastic stiffness operator $\mathbb{C}^{tan}_{meso}$ of the porous matrix at the mesoscopic scale takes the following form:

$$\mathbb{C}^{tan}_{meso} = \begin{cases} \mathbb{C}_m & (F \leq 0, \dot{F} < 0) \\ \mathbb{C}_m - \dfrac{\mathbb{C}_m : \frac{\partial F}{\partial \tilde{\mathbf{\Sigma}}} \otimes \frac{\partial F}{\partial \tilde{\mathbf{\Sigma}}} : \mathbb{C}_m}{H^G} & (F = 0, \dot{F} = 0) \end{cases} \tag{II .25}$$

with:

$$H^G = \frac{\partial F}{\partial \tilde{\mathbf{\Sigma}}} : \mathbb{C}_m : \frac{\partial F}{\partial \tilde{\mathbf{\Sigma}}} - \frac{\partial F}{\partial f}[\frac{\partial F}{\partial \tilde{\Sigma}_m}(1-f) - \frac{\tilde{\mathbf{\Sigma}} : \frac{\partial F}{\partial \tilde{\mathbf{\Sigma}}}}{h}] \tag{II .26}$$

With the previous relations in hand, it is possible to investigate macroscopic mechanical behaviors of porous materials with a compressible porous matrix, with the help of the FFT-based numerical homogenization model. As an advantage of this model, one can capture not only macroscopic mechanical responses but also local strain and stress fields. In order to illustrate this, the unit cell with one meso-pore is again considered here and it is subjected to the following two loading paths:

(1) $E = 2 \times 10^{-2}(e_1 \otimes e_1 - e_3 \otimes e_3)$

(2) $E = 2 \times 10^{-2}(e_1 \otimes e_1 - e_2 \otimes e_2 - e_3 \otimes e_3)$

In Fig.II .23, one shows the local strain field in the middle section of the unit-cell with four different values of f/ϕ under the loading path $E = 2 \times 10^{-2}(e_1 \otimes e_1 - e_3 \otimes e_3)$. Shear strain bands are observed at $\pm 45°$ with respect to e_1 or e_3 axis. With the decrease of f/ϕ or the increase of mesoporosity, the shear bands exhibit high strain gradients at the corners of the unit cell. The width of shear band increases with the decrease of mesoporosity. Some local strain concentration zones are found around the mesoscopic pore. In the second loading path with $E = 2 \times 10^{-2}(e_1 \otimes e_1 - e_2 \otimes e_2 - e_3 \otimes e_3)$, an additional compressive

© 2018 Tous droits réservés.

strain is applied along e_2 direction. The obtained local strain fields are shown in Fig.II .24. Again, strain concentration zones are found around the mesoscopic pore and amplified when the mesoporosity increases or when the ratio f/ϕ is smaller.

In Fig.II .25, one presents the macroscopic stress-strain curves for the two different loading paths. For the first loading path, the macroscopic response is not very sensitive to the porosity ratio f/ϕ. The peak stress Σ_{33} exhibits a small decrease when the increase of f/ϕ. However, in the second loading path, the macroscopic response is strongly influenced by the porosity ratio. The macroscopic stress Σ_{33} is significantly amplified by the increase of f/ϕ. This is the consequent of an important plastic hardening in the porous matrix due to the diminution of microscopic porosity.

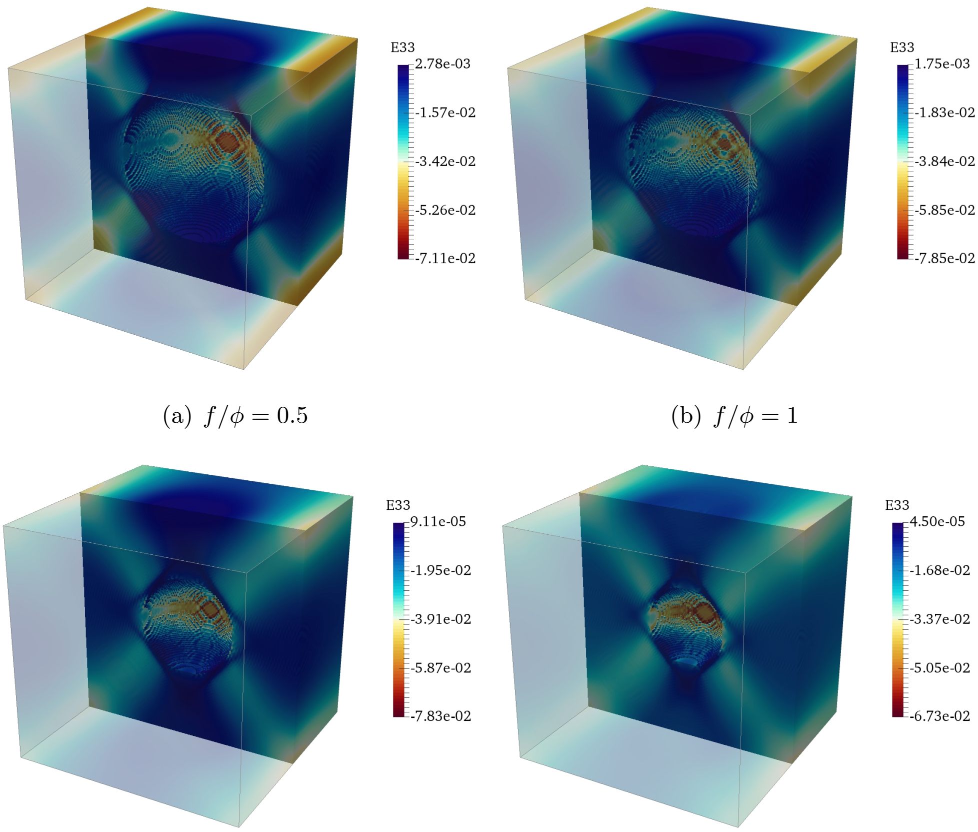

(a) $f/\phi = 0.5$

(b) $f/\phi = 1$

(c) $f/\phi = 5$

(d) $f/\phi = 10$

Figure II .23: Local strain distribution for different values of f/ϕ and with $\alpha = 0.3$, $\Gamma = 0.2$ in $E = 2 \times 10^{-2}(e_1 \otimes e_1 - e_3 \otimes e_3)$,

© 2018 Tous droits réservés.

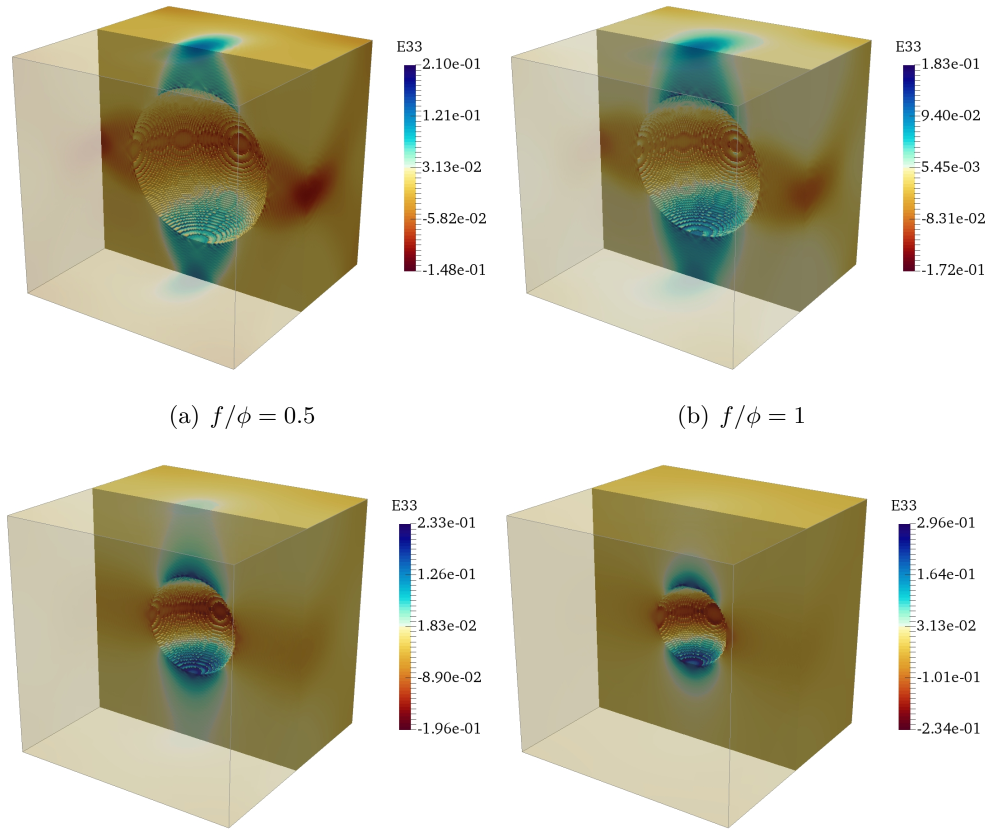

(a) $f/\phi = 0.5$ (b) $f/\phi = 1$

(c) $f/\phi = 5$ (d) $f/\phi = 10$

Figure II .24: Local strain distribution for different values of f/ϕ and with $\alpha = 0.3$, $\Gamma = 0.2$ in $E = 2 \times 10^{-2}(e_1 \otimes e_1 - e_2 \otimes e_2 - e_3 \otimes e_3)$

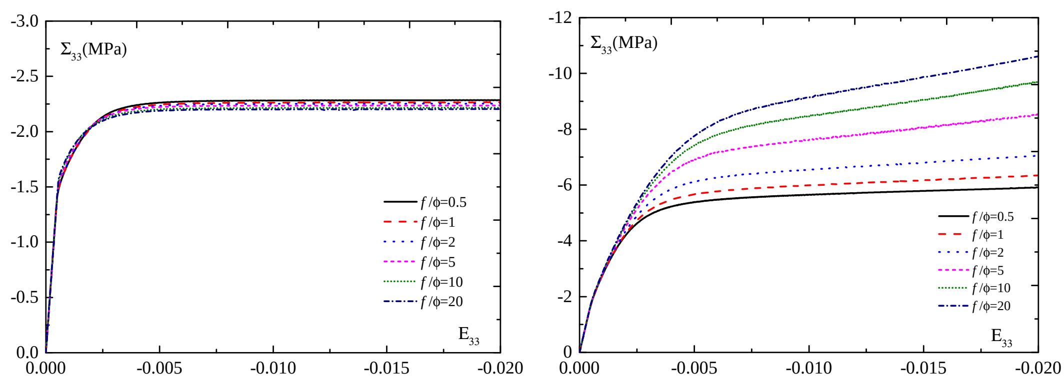

(a) $E = 2 \times 10^{-2}(e_1 \otimes e_1 - e_3 \otimes e_3)$ (b) $E = 2 \times 10^{-2}(e_1 \otimes e_1 - e_2 \otimes e_2 - e_3 \otimes e_3)$

Figure II .25: Macroscopic stress-strain curves in two different loading paths with $\alpha = 0.3$ and $\Gamma = 0.2$

© 2018 Tous droits réservés. lilliad.univ-lille.fr

Thèse de Yajun Cao, Université de Lille, 2018

5 Concluding remarks

In this paper, we have developed a FFT-based numerical model for the estimation of both elastic and plastic behaviours of a class of materials with two populations of pores at two different scales, and especially studied the effects of the ratio between two populations of pores f/ϕ on the macroscopic responses.

It is found that the effective elastic properties of double porous materials are significantly influenced by the porosity ratio and they are more sensitive to the meso-porosity than to the micro-porosity. The classical dilute homogenization scheme is not able to capture these effects. The double Hashin-Shtrikman upper bound model significantly differs from the FFT-based model for low values of porosity ratio f/ϕ (high values of meso-porosity) but the two models agree well for high values of porosity ratio f/ϕ (low values of meso-porosity).

The macroscopic yield stresses have also been studied for different values of the porosity ratio f/ϕ. Comparisons with two analytical criteria issued from two different homogenization techniques have been performed. Significant differences have been found between the two analytical criteria and the FFT-based numerical model. According to the numerical results obtained with the FFT-based full-field simulations, the macroscopic yield stresses are strongly influenced by the porosity ratio. For a given value of total porosity, the smallest yield stresses are obtained when the microscopic porosity vanishes. The mesoscopic porosity plays a more important role than the micro-porosity on the macroscopic yield stress. These effects of microstructure in terms of porosity ratio have not been correctly taken into account in the two analytical criteria.

Finally, for brittle rock-like materials, damage due to growth of micro-cracks is an essential inelastic process. In future studies, it will be interesting to consider the microcracking process of solid matrix by using a suitable damage model.

© 2018 Tous droits réservés. lilliad.univ-lille.fr

6 Appendix A: Analytical estimation of elastic properties

One considers an isotropic porous matrix with spherical pores at the microscopic scale. The bulk and shear moduli of the solid phase are denoted as k_s and μ_s and the microporosity as f. The effective bulk and shear moduli k_0^{hom} and μ_0^{hom} of the porous matrix at the mesoscopic scale are here calculated using the Hashin-Shtrikman upper bounds and one gets:

$$k_0^{hom} = \frac{4(1-f)k_s\mu_s}{4\mu_s + 3fk_s}, \mu_0^{hom} = \frac{(1-f)\mu_s}{1+6f\frac{k_s+2\mu_s}{9k_s+8\mu_s}} \tag{II .27}$$

In the second step of homogenization, the mesoscopic pores are taken into account and the mesoporosity is denoted as ϕ. The effective elastic properties of the double porous material are determined by using two different homogenization methods: the dilute scheme and the Hashin-Shtrikman upper bounds method. The macroscopic bulk and shear moduli k^{hom} and μ^{hom} of the double porous material are respectively given by the following relations:

$$k_{DI}^{hom} = k_0^{hom}(1-\phi\frac{3k_0^{hom}+4\mu_0^{hom}}{4\mu_0^{hom}}), \mu_{DI}^{hom} = \mu_0^{hom}(1-\phi\frac{5(3k_0^{hom}+4\mu_0^{hom})}{9k_0^{hom}+8\mu_0^{hom}}) \tag{II .28}$$

$$k_{HS}^{hom} = \frac{4(1-\phi)k_0^{hom}\mu_0^{hom}}{4\mu_0^{hom}+3\phi k_0^{hom}}, \mu_{HS}^{hom} = \frac{(1-\phi)\mu_0^{hom}}{1+6\phi\frac{k_0^{hom}+2\mu_0^{hom}}{9k_0^{hom}+8\mu_0^{hom}}} \tag{II .29}$$

7 Appendix B: Analytical yield criteria

The two analytical criteria have also been obtained from two-step homogenization methods. For the first step, the effective plastic criterion of the porous matrix is determined. In both analytical criteria, the criterion obtained by [Maghous et al., 2009] using a modified secant method has been adopted.

For the second step, two different techniques have been used for the determination of macroscopic yield criterion of the double porous material. For the criterion given in [Shen et al., 2014], the authors have used a kinematic limit analysis approach with an Eshelby-like trial velocity field. The obtained criterion is given by:

$$F = \beta\frac{\Sigma_{eq}^2}{\Sigma_0^2} + \frac{9\alpha}{2}(\frac{\Sigma_m - \frac{L}{9\alpha}(1-\phi)}{\Sigma_0})^2 + 2\phi\cosh(\sqrt{\frac{9}{4}\beta\frac{\Sigma_m^2}{\Sigma_0^2} + \frac{2\beta}{3\bar{\Gamma}(\phi)}\frac{\Sigma_{eq}^2}{\Sigma_0^2}}) - 1 - \phi^2 = 0 \tag{II .30}$$

where $\Sigma_{eq}^2 = \frac{3}{2}\mathbf{\Sigma'} : \mathbf{\Sigma'}$ with $\mathbf{\Sigma'}$ representing the deviatoric part of the macroscopic stress tensor $\mathbf{\Sigma}$. The coefficients β, α, L, Σ_0,σ_0 and $\bar{\Gamma}(\phi)$ are given by:

$$\beta = \frac{2}{3}\frac{1+2f/3}{\alpha^2}, \frac{9\alpha}{2} = \frac{3f}{2\alpha^2} - 1, L = -2(1-f)h \tag{II .31}$$

© 2018 Tous droits réservés.

Thèse de Yajun Cao, Université de Lille, 2018

$$\Sigma_0 = \sqrt{\sigma_0^2 + \frac{L^2}{18\alpha}}, \sigma_0 = (1-f) * h, \bar{\Gamma}(\phi) = 1 - 4\phi \frac{(1-\phi(2/3))^2}{1-\phi} \tag{II .32}$$

On the other hand, a modified secant method has been used to determine the macroscopic yield criterion given in [Shen and Shao, 2016a], which is expressed in the following form:

$$F = \Theta\Sigma_d^2 + \Upsilon\Sigma_m^2 + 2(1-f)h(1-\phi)\Sigma_m - (1-f)^2(1-\phi)^2h^2 = 0 \tag{II .33}$$

The coefficients Θ and Υ are calculated by:

$$\Theta = \frac{1+2f/3}{\alpha^2}(\frac{6\alpha^2 - 13f - 6}{4\alpha^2 - 12f - 9}\phi + 1), \Upsilon = \frac{3/2+f}{\alpha^2}\phi + \frac{3f}{2\alpha^2} - 1 \tag{II .34}$$

For a given couple of porosity Γ and f or Γ and ϕ, the corresponding meso-porosity ϕ or micro-porosity f can be obtained through relation (II .1). If the values of f/ϕ of two unit cells are reciprocal, it implies the values of micro-porosity and meso-porosity are inverse each to other. Thus we have:

$$\Theta_1 = \frac{1+2f/3}{\alpha^2}(\frac{6\alpha^2 - 13f - 6}{4\alpha^2 - 12f - 9}\phi + 1), \quad \Theta_2 = \frac{1+2\phi/3}{\alpha^2}(\frac{6\alpha^2 - 13\phi - 6}{4\alpha^2 - 12\phi - 9}f + 1) \tag{II .35}$$

The evolutions of Θ_1 and Θ_2 related to micro-porosity and meso-porosity of these two unit cells are presented in Fig.II .26. The corresponding macroscopic yield surfaces with several values of f/ϕ predicted by the criterion given in [Shen and Shao, 2016a] are shown in Fig.II .27. One can see that the difference of the value of Θ between the two configurations is very small so that the corresponding macroscopic yield surfaces are very close each to other. As an example, the macroscopic yield surfaces for $f/\phi = 0.5$ and $f/\phi = 2$ are shown in Fig.II .27.

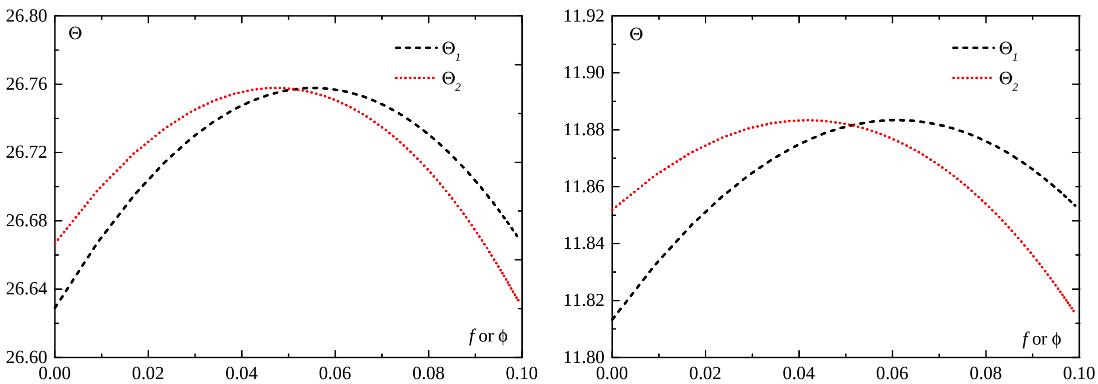

(a) $\alpha = 0.2$ (b) $\alpha = 0.3$

Figure II .26: Evolution of Θ with micro-porosity(f_1) and meso-porosity(ϕ_2) for a given total porosity: (a) $\alpha = 0.2$ and $\Gamma = 0.1$. (b) $\alpha = 0.3$ and $\Gamma = 0.1$

© 2018 Tous droits réservés. lilliad.univ-lille.fr

Thèse de Yajun Cao, Université de Lille, 2018

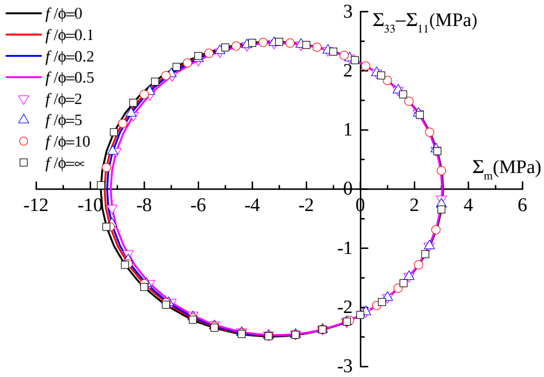

(a) $\alpha = 0.2$

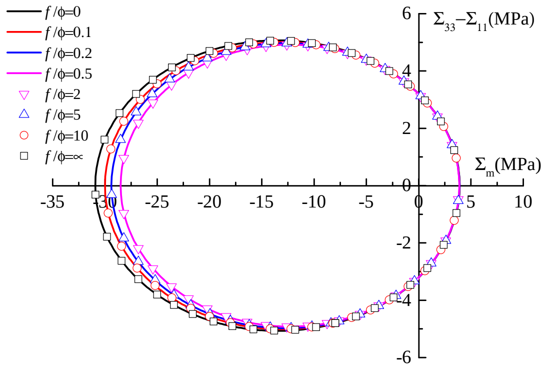

(b) $\alpha = 0.3$

Figure II .27: Evolution of macroscopic yield surfaces with different f/ϕ predicted by the criterion given in [Shen and Shao, 2016a] for $\Gamma = 0.1$

© 2018 Tous droits réservés. lilliad.univ-lille.fr

Chapter III

Effective behaviours of materials with meso-pores and meso-inclusions

Contents

© 2018 Tous droits réservés.

Thèse de Yajun Cao, Université de Lille, 2018

Summary

For most engineering materials, pores and mineral inclusions can be observed at same scale, for example, the rock, concrete and so on. Based on non-linear homogenization method, lots of macroscopic plastic yield criteria have been derived for porous materials taking into account the influences of porosity. Some works have been done for geomaterials, which consider simultaneously the effects of porosity and the volume fraction of inclusion with the assumption that the pores are embedded in the matrix and much smaller than inclusion. It still has difficulties to obtain a closed-form criterion to consider such kinds of composite as accuracy as possible. For this reason, the Fast Fourier Transform (FFT) based homogenization method has been employed to get a reference solution for this problem. In this case, a Drucker-Prager type matrix configured with both pore and inclusion at same scale is considered in this work. Due to the heterogeneity and anisotropy induced by the geometry of pore and inclusion, the macroscopic elastic and plastic behaviors with respect to inclusion and pore morphology characters are studied and compared in detail. The numerical results show that the evolution of macroscopic elastic behavior is sensitive to pore and inclusion geometry. However, the evolution of macroscopic yield stresses are mainly determined by the pore shape, distribution, aspect ratio, orientation as well as porosity, inclusion fraction. The inclusion shape and its orientation have no great effect on plastic yield stresses.

1 Introduction

Most composites such as rock, concrete and metal are well-known having a highly heterogeneous microstructure with a structure-sensitive characteristic, due to the presences of pores and various mineral inclusions. In the context of experimental mechanics, despite the macroscopic mechanical properties of this class materials can be measured, it still pose another challenge to derive its effective properties as accuracy as possible associated with well known physical microstructure though analytical expressions or numerical method. Starting with the Eshelby's inclusion problem, classical homogenization models are available for the elastic properties ([Mori and Tanaka, 1973,Hill, 1965b,Ponte Castañeda and Willis, 1995]). Based on these classical theories, the effective elastic properties of porous composite like geomaterial involved with multi-scale features have been investigated ([Miled et al., 2011,Giraud et al., 2012,Liang et al., 2017]) and enjoyed the significant success.

On the other hand, for plastic case, individual inhomogeneities like pores or inclusions in a given scale have attracted considerable attention in homogenization problem.

© 2018 Tous droits réservés. lilliad.univ-lille.fr

Thèse de Yajun Cao, Université de Lille, 2018

In the framework of limit-analysis approach, the determination of strength properties of porous materials are proposed by Gurson(1977) for porous materials with a von-Mises type solid matrix. Since then, various extensions have been made accounting for the void shape effects ([Gologanu et al., 1993, Gologanu et al., 1994, Monchiet et al., 2014]) and plastic anisotropy ([Benzerga and Besson, 2001, Monchiet et al., 2008, Keralavarma and Benzerga, 2010]). Pressure sensitive behavior was also taken into account by various nonlinear homogenization methods for one population of pores or inclusions ([Barthélémy and Dormieux, 2004, Guo et al., 2008, Maghous et al., 2009, Shen et al., 2017b]). Based on these existed models, approximate criteria involved in microstructural features like pores and inclusions arranged individually at two separated scales have also been developed by using a two-step homogenization producers ([Garajeu and Suquet, 1997, Vincent et al., 2009a, Vincent et al., 2014b, Shen et al., 2013, Shen et al., 2014]). Apart from the development of analytical solutions, considerable efforts have been made towards the assessment of previous criteria by using computational simulations like Finite Element Method ([Khdir et al., 2014, Julien et al., 2011, Vincent et al., 2009b]) and Fast Fourier Transform method ([Vincent et al., 2014a, Cao et al., 2018a, Cao et al., 2018b]). By means of these methods, numerical contributions for individual inhomogeneity considering pore or inclusion geometry such as distribution and shape have provided good basis for modeling their effective properties ([Bilger et al., 2005, Ghossein and Lévesque, 2012, Madou and Leblond, 2013, Drach et al., 2016, Bourih et al., 2018]). These simulations are try to estimate a link between the strength properties and microstructure.

Regarding the differences of macroscopic responses by comparisons between the computational results and closed-form solution, a brief descriptions of some known statistical microstructure features like porosity, inclusion fraction and shape are not enough to determine the effective properties as accuracy as possible. Although series of experimental results on porous material have provided a strong link between porosity and strength ([Al-Harthi et al., 1999, Chang et al., 2006, Lian et al., 2011, Heidari et al., 2014, Baud et al., 2014]), it is important to taken into account microscopic features for their roles on macroscopic behaviors. In addition, other concerns are mainly accounting for pore or inclusion at separated scale assuming one of their feature size is much smaller than another one ([Bernard et al., 2003, Shen et al., 2012a, Shen et al., 2013]). However, the interactions between pores and inclusions are neglected. To the author's knowledge, there is no available accurate model to capture the effective behavior for materials with both pores and inclusions arranged at same scale. Motivated by this, it is more appropriate to perform numerical simulations on microstructure for such materials, providing a reference

© 2018 Tous droits réservés. lilliad.univ-lille.fr

Thèse de Yajun Cao, Université de Lille, 2018

solution for future studies on its plastic criterion with suitable mathematical morphology formulation when specialize the details of a given microstructure. For this purpose, the FFT-based homogenization method is adopted here for all the simulations presented in this section. The goal of this study is to explore the macroscopic elastic and plastic properties for a periodic microstructure with both pore and inclusion at same scale.

The chapter is organized as follow: section 2 presents the studied materials and selected representative volume element. In section 3, a series of simulations are conducted by using the FFT-based homogenization method with different microstructures. The effect of inclusion and pore shape, distribution, aspect ratio and orientation on effective elastic and plastic yield stress are detailed investigated . In section 4, with the framework of this study, we shall estimate the macroscopic yield surface of porous Berea sandstone and compare with the experimental data.

2 Microstructure and mechanical behavior of studied material

Owing to a wide range of complementary imaging technique like scanning electron microscopy (SEM) in 2D or X-ray computed tomography (XCT) in 3D case for visualizing and quantifying the microstructure of rock-like materials, the distinctive mineral compositions and textural characteristics can be directly observed with both heterogeneity and anisotropy properties at a small scale ([Louis et al., 2007, Kelly et al., 2016, Ma et al., 2017, Saif et al., 2017b]), for instance, the shale rock ([Ougier-Simonin et al., 2016]), claystone ([Robinet, 2008]) and Berea sandstone ([Wong et al., 1997, Wong et al., 2001, Saxena and Mavko, 2016]) are composed of solid matrix and various mineral inclusions as well as pores, which are characterised as a multi-phase composite. There is an increasing awareness that the preferred microscopic geometries of mineral inclusions, pores (such as shape, orientation, size, distribution, etc.) and porosity are important contributors to elastic and plastic anisotropy for macroscopic mechanical responses.

In our study, in order to consider these factors, it is assumed that the pores and inclusions are approximately of spherical or spheroidal shape for the purpose of analytical studies, and both of them are periodic distributed at the same scale as presented in Fig.III .1-a. Based on these assumptions, a simplified representative volume element(RVE) with one centered pore and 1/8 inclusion in each corner is selected here as presented in Fig.III .1-b for the following simulations. Corresponding porosity and inclusion fraction respectively denote f and ρ in the whole study.

© 2018 Tous droits réservés. lilliad.univ-lille.fr

Thèse de Yajun Cao, Université de Lille, 2018

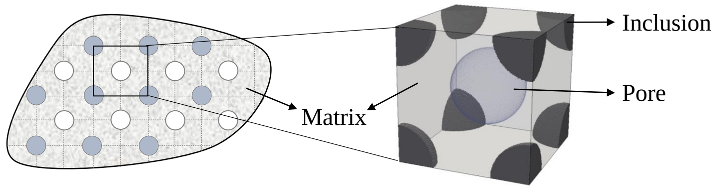

(a) 2D structure of studied materials (b) Selected 3D representative volume element

Figure III .1: The representative microstructure of unit cell with pores and inclusions embedded.

For pressure sensitive materials, the solid matrix of the material is assumed to obey a Drucker-Prager type criterion taken the following form:

$$\Phi(\boldsymbol{\sigma}) = \sigma_d + \alpha(\sigma_m - h) \leq 0 \tag{III .1}$$

in which $\boldsymbol{\sigma}$ denotes the microscopic stress tensor. $\sigma_m = tr\boldsymbol{\sigma}/3$ is the mean stress. σ_d is defined as $\sigma_d = \sqrt{\boldsymbol{\sigma'} : \boldsymbol{\sigma'}}$, with $\boldsymbol{\sigma'}$ being the deviatoric stress tensor. The parameter α is the frictional coefficient and h the yield stress under hydrostatic tension of the solid phase. The inclusion studied here is assumed to be elastic.

Due to the presences of inclusion and pore, the local stress and strain fields are not uniform. To minimize the size-effects of the unit cell for the determination of macroscopic properties, the periodic boundary condition is considered here. Therefore, the non-uniform strain field can be defined by a periodic fluctuation displacement field $\boldsymbol{u}^*(\boldsymbol{x})$ spliting into an average $\boldsymbol{E}$ and a fluctuation term $\boldsymbol{\varepsilon}(\boldsymbol{u}^*(\boldsymbol{x}))$. Thus the effective behaviors of the composite materials can be determined by solving the following local problem.

$$\begin{cases} \Delta\boldsymbol{\sigma}(\boldsymbol{x}) = \mathbb{C}^{tan}(\boldsymbol{x}) : \Delta\boldsymbol{\varepsilon}(\boldsymbol{x}) & \forall \boldsymbol{x} \in \Omega_s \\ \Delta\boldsymbol{\sigma}(\boldsymbol{x}) = \mathbb{C}(\boldsymbol{x}) : \Delta\boldsymbol{\varepsilon}(\boldsymbol{x}) & \forall \boldsymbol{x} \in \Omega_i \\ div\boldsymbol{\sigma}(\boldsymbol{x}) = 0 & \forall \boldsymbol{x} \in \Omega, u^*\#, \boldsymbol{\sigma} \cdot n - \# \\ \boldsymbol{\varepsilon}(\boldsymbol{x}) = \frac{1}{2}(\nabla \boldsymbol{u}^*(\boldsymbol{x}) + \nabla^T \boldsymbol{u}^*(\boldsymbol{x})) + \boldsymbol{E} & \forall \boldsymbol{x} \in \Omega \end{cases} \tag{III .2}$$

In this relations, the symbol # denotes the periodic condition while $-\#$ the anti-periodic one. Ω denotes the whole volume of the unit cell. Then Ω_s and Ω_i are the volumes of the solid matrix and inclusion, respectively. $\boldsymbol{\sigma}$, $\boldsymbol{\varepsilon}$, $\mathbb{C}$, denote the local stress, strain and stiffness tensor in Ω. $\mathbb{C}^{tan}$ is the effective tangent elastic-plastic stiffness operator which can be obtained by the incremental constitutive relation.

In the context of highly heterogeneous materials studied in this work, the following section will focus on both the effects and interactions of meso pore and inclusion on the effective behaviors which can be well considered by using FFT based method.

© 2018 Tous droits réservés. lilliad.univ-lille.fr

Thèse de Yajun Cao, Université de Lille, 2018

3 Overall elastic and plastic properties of the studied material

In order to present the heterogeneous and anisotropic properties induced by the microstructure, the morphology effects of the inclusion and pore are considered here based on the FFT homogenization method. The inclusion and pore shape, aspect ratio and orientation will be taken into account. For a better comparisons, two classes of unit cells with different arrangements are adopted here. The first class is the unit cell embedded with a centered spheroidal pore (oblate and prolate) and 1/8 spherical inclusion in each corner as shown in Fig.III .2(a) and Fig.III .2(b). Herein we define θ as the orientation angle between the major axis of the inclusion or pore and the loading direction. Then the second is the one configured with a centered spheroidal inclusion and 1/8 spherical pore in the corner as presented in Fig.III .2(c) and Fig.III .2(d). With a periodic boundary condition, its macroscopic properties is equivalent to the one which the pore and inclusion interchange their locations.

The studied unit cell is divided into 150 × 150 × 150 voxels of identical size for the FFT-based calculations. The elastic and plastic parameters of the solid matrix are selected as $E_s = 5GPa$, $v_s = 0.15$, $\alpha = 0.1 \sim 0.3$, $h = 10MPa$, and the elastic parameters of the inclusion are $E_i = 200GPa$, $v_i = 0.15$.

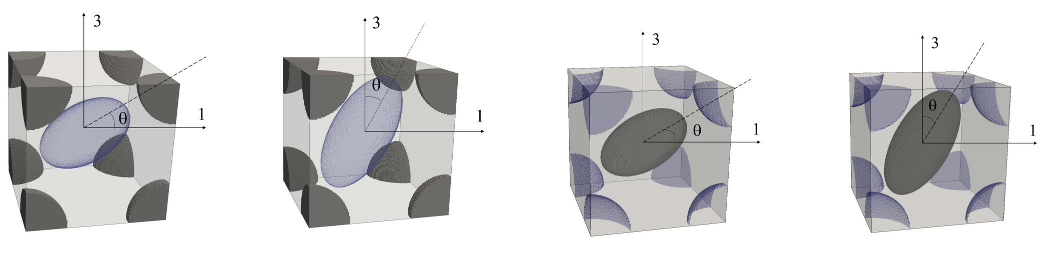

(a) oblate pore (b) prolate pore (c) oblate inclusion (d) prolate inclusion

Figure III .2: Studied unit cells with different pore and inclusion geometry

3.1 Estimation of macroscopic elastic modulus

To highlight the influences of pore shape and orientation on the macroscopic elastic modulus, we consider now the first class of unit cell with different pore orientations and aspect ratios as shown in Fig. III .2(a) and Fig. III .2(b). In this work, aspect ratio $a/c = 1.0 \sim 5.0$ for the oblate pore and $c/a = 1.0 \sim 2.25$ for the prolate one are selected with $f = 0.1$, $\rho = 0.1$(a and c respectively being the semi-major axis and semi-minor axis

© 2018 Tous droits réservés. lilliad.univ-lille.fr

Thèse de Yajun Cao, Université de Lille, 2018

of the spheroid).

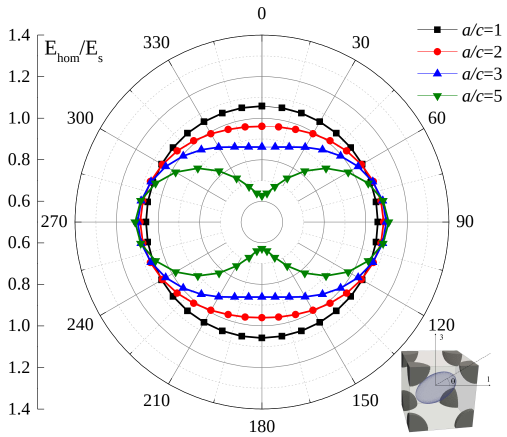

(a) oblate pore

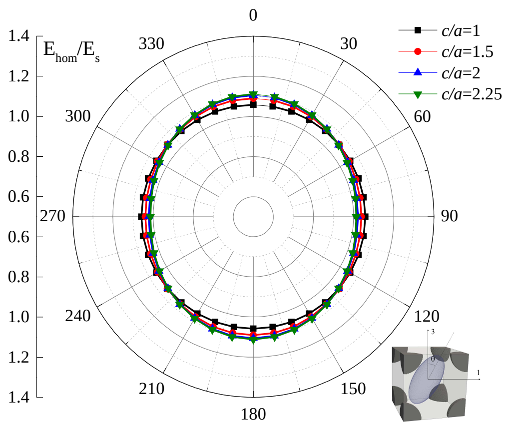

(b) prolate pore

Figure III .3: Evolution of effective normalized elastic modulus related to pore orientation: $f = 0.1$, $\rho = 0.1$

Unlike spherical pore (corresponding to $a/c = 1$) leading to an isotropic case, for spheroidal pore, Fig.III .3(a) and Fig.III .3(b) address that the pore shape provides significant differences of normalized elastic modulus (E_{hom}/E_s) for different pore orientations. The results indicate that the minimum elastic modulus always corresponds to the case of orientation angle $\theta = 0°$ for oblate pore, then gradually increased with the orientation from $\theta = 0°$ to $\theta = 90°$. While for prolate one, it exhibits an opposite trend. This confirms the anisotropy induced by the pore morphology. It should be noted that the value of E_{hom}/E_s reaches maximum when the orientation is parallel to the compression direction for both oblate and prolate pore. However, by comparing Fig.III .3(a) with Fig.III .3(b), it is clear

© 2018 Tous droits réservés. lilliad.univ-lille.fr

that the normalized elastic modulus of oblate pore is more sensitive to the orientations than the prolate one.

In addition, with these comparisons, the anisotropy is also more significant for both oblate and prolate pore with a large aspect ratio than the small one. However, the aspect ratio presents different influences on normalized effective modulus for different orientations. For example, when $\theta = 0°$, the value of E_{hom}/E_s becomes smaller with the increasing aspect ratio of oblate pore. But when $\theta = 90°$, E_{hom}/E_s is increased with the increasing aspect ratio. Therefore, it exists an orientation domain which the higher aspect ratio can decrease the effective elastic modulus. As an example, at the orientation domain $0° \sim 70°$ for oblate pore and $45° \sim 90°$ for prolate one, the normalized modulus becomes to be softer when having a higher aspect ratio.

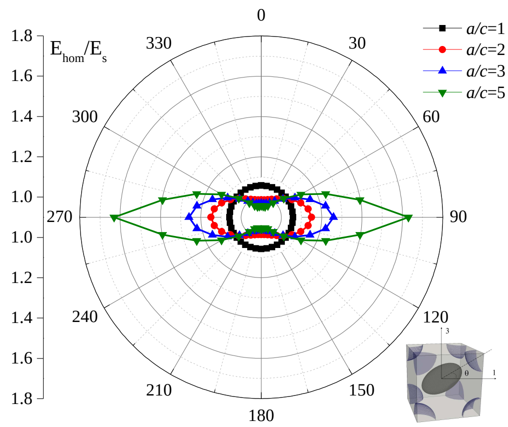

(a) oblate inclusion

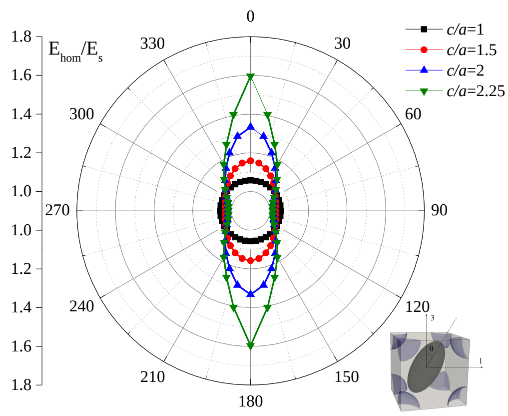

(b) prolate inclusion

Figure III .4: Evolution of effective normalized elastic modulus related to inclusion orientation: $f = 0.1$, $\rho = 0.1$

© 2018 Tous droits réservés. lilliad.univ-lille.fr

Thèse de Yajun Cao, Université de Lille, 2018

Fig.III .4 illustrates the effects of inclusion geometry with respect to inclusion orientations and aspect ratios. It is important to note that both the oblate and prolate inclusion orientation and aspect ratio are more sensitive to the variation of macroscopic elastic modulus than the pore. For instance, in the case of $a/c = 5$, the normalized elastic modulus is varied from 0.62 to 1.11 for oblate pore, while exhibits variations from 0.95 to 1.62 for oblate inclusion. At the orientation domain $45° \sim 90°$ for oblate pore and $0° \sim 45°$ for prolate one, the normalized modulus becomes to be softer when having a higher aspect ratio.

3.2 Determination of macroscopic plastic yield stress

Due to the fact that the absence of the macroscopic analytical criterion of the studies materials, we will focus on numerical simulations to derive a reference solution of the macroscopic plastic yield stress. To this end, the obtained yield stress is corresponding to a perfectly elastic-plastic case. For a better understanding of the studied material, the effect of inclusion and pore geometrical characters such as their shape, aspect ratio, orientations will be considered in detail. For the effect of random distributions, we will explain in Appendix A.

3.2.1 Effects of inclusion geometries

Influences of inclusion geometry on macroscopic plastic mechanical properties are now evaluated. To start, we will firstly explore the effect of inclusion volume fraction on the macroscopic yield stress for isotropic case. Here the microstructure presented in Fig.III .1 is considered. By using the FFT-based homogenization method, the computed macroscopic yield stresses are presented in Fig.III .5. With no doubt, it is significantly that the macroscopic yield stress can be enhanced at compressible stress state with a high inclusion fraction. However, the hydrostatic stress is not sensitive to the inclusion fraction as illustrated in the results when inclusion volume fraction varies from $\rho = 0$ to $\rho = 0.2$. The hydrostatic strengthes are almost the same with each other. This implies that the hydrostatic strengthes of the studied material can be approximated by the ones without spherical inclusion.

© 2018 Tous droits réservés. lilliad.univ-lille.fr

Thèse de Yajun Cao, Université de Lille, 2018

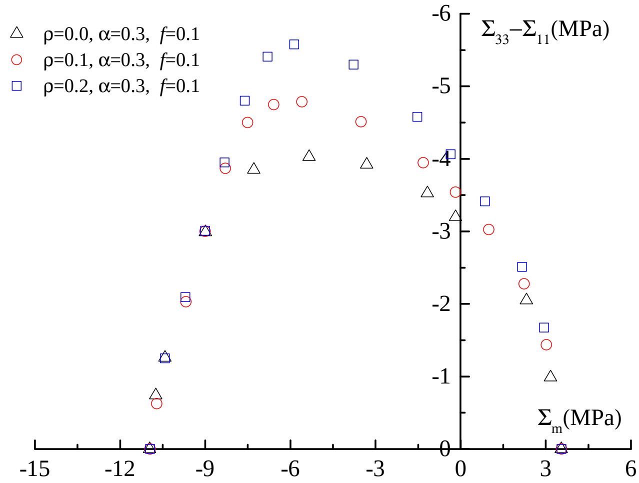

Figure III .5: Macroscopic yield stresses predicted by unit cells with one centered spherical inclusion for different inclusion fraction.

Then we are proceeding to focus on the case of spheroidal inclusion. For this purpose, the unit cells are selected corresponding to Fig.III .2(c) and Fig.III .2(d). Then a series of calculations were performed and compared. Fig.III .6 shows the macroscopic yield stress for different inclusion shape and aspect ratios . It is obviously that the evolutions of yield stresses are very closed between the unit cells with spherical and spheroidal inclusions.

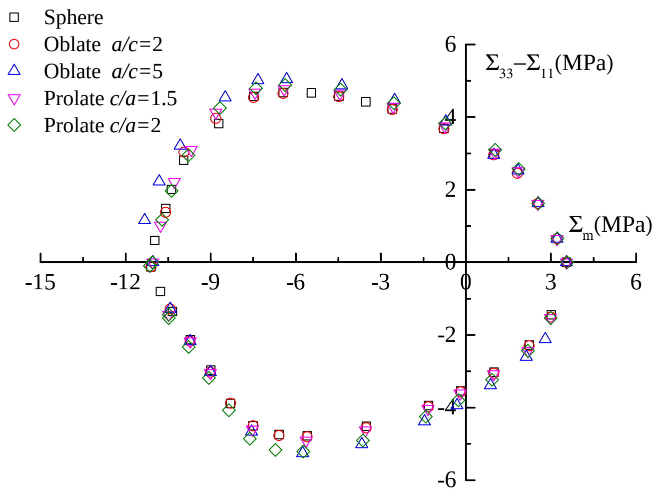

Figure III .6: Macroscopic yield stresses predicted by unit cells with one centered spheroidal inclusion for different aspect ratios with $\alpha = 0.3$, $f = 0.1$, $\rho = 0.1$.

© 2018 Tous droits réservés. lilliad.univ-lille.fr

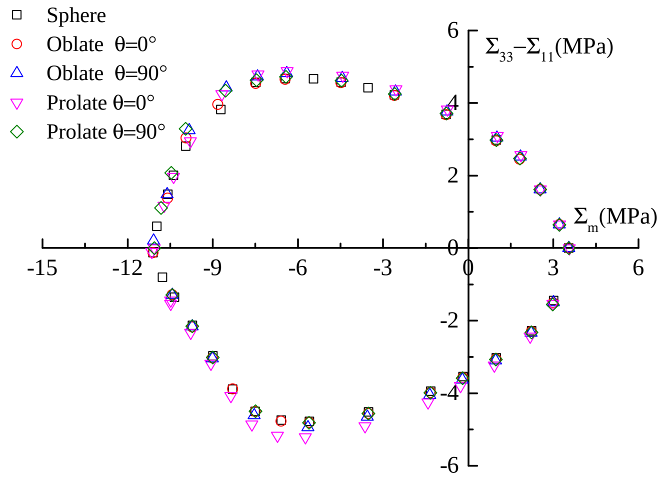

Figure III .7: Macroscopic yield stresses predicted by unit cells with one centered spheroidal inclusion for different orientation angles with $\alpha = 0.3$, $f = 0.1$, $\rho = 0.1$: $a/c = 2.0$ for oblate and $c/a = 2.0$ for prolate.

Then Fig.III .7 exhibits the effect of inclusion orientation, it is found that the discrepancies between them is not obvious. Despite the fact that the presences of this inhomogeneity associated with inclusion shapes and orientations can disturb an uniform strain field, the effect of stress fluctuation in the matrix caused by inclusion geometry are very small. This maybe due to the fact that the inclusion geometry has little influences on stress transferring to the matrix. Therefore, it no longer has significant influence on the macroscopic yield stress. As a consequence, the volume fraction is the main factor for inclusion which is sensitive to the macroscopic yield stresses except the case of hydrostatic stress state.

3.2.2 Influences of pore geometries

In this subsection, we are proceeding to consider the effect of pore shape, aspect ratio, orientation on the evolution of macroscopic yield stress. In contrast of inclusion that doesn't undergo stress-free, stress and strain in the pore are then zero leading to distinctly local stress concentration around the pore. Therefore, the effective mechanical properties induced by pore geometry should be different from the case of inclusion.

- unit cell with spherical pore

We first investigate the case of both spherical pore and inclusion embedded in the unit cell as show in Fig.III .1. Fig.III .8 gives a comparison of macroscopic yield stresses with different porosities. As well known, the porosity has a significant weaken effect on macroscopic yield stress. From the results, it is no surprised that the effective strength is decreased with an increasing porosity. We present it here for comparison of the anisotropic

© 2018 Tous droits réservés.

Thèse de Yajun Cao, Université de Lille, 2018

case in the following analysis.

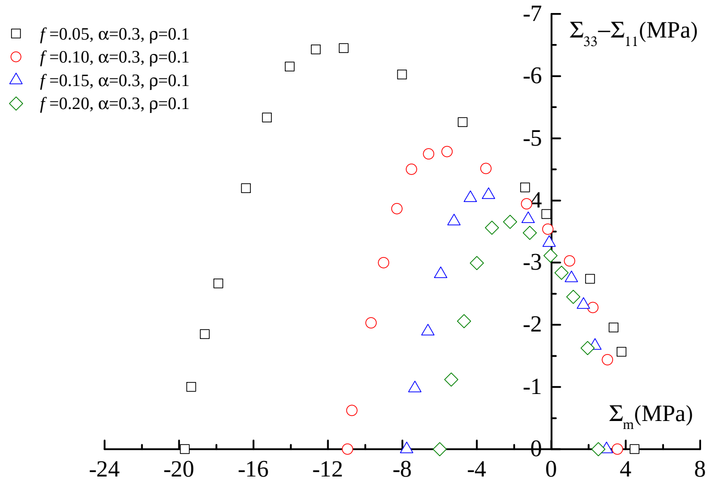

Figure III .8: Macroscopic yield stresses predicted with $\alpha = 0.3$, $f = 0.1$, $\rho = 0.1$.

- *unit cell with spheroidal pore*

To evaluate numerically the effect of spheroidal pore, the shape of pore is regarded as classical oblate or prolate, and the inclusion is assumed to be spherical. Corresponding studied unit cells are shown in Fig.III .2(a) and Fig.III .2(b). The pore morphology is mainly described by three factors: porosity, aspect ratio and orientation. These factors as well as inclusion fraction shall be considered for the determination of macroscopic yield stresses in this section.

In this context, a numbers of simulations are computed. Fig.III .9 displays the macroscopic yield stresses for oblate pore covering the effect of pore geometry. Fig.III .9(a) presents the evolution of yield stress with oblate aspect ratio $a/c = 2$ and orientation $\theta = 0°$ for different porosities. As expected, the evolution of the yield stresses are largely effected by the porosities like the case of spherical pore. In addition, the pore morphology with respect to aspect ratio is also an important factor. Motivated by this reason, the effective yield stresses of the unit cell with different pore aspect ratios are compared in Fig.III .9(b). According to this plot, the evolution of yield stresses is quite different with the increasing aspect ratio. The results well illustrate the anisotropic influence incorporating void shape effect comparing with the case of spherical pore($a/c = 1$). Particularly, significant reductions in hydrostatic strength coupled with an increase of pore aspect ratio. This significant shape effect is in contrast with the case of inclusion as previous presented. However, it is important to note that the higher aspect ratio does not always decrease the yield stress. For instance, as indicted in Fig.III .9(b), there exists a strength domain which is not sensitive to the pore aspect ratio. For the condition of high stress triaxialities, the

© 2018 Tous droits réservés. lilliad.univ-lille.fr

yield strength is decreased by the pore with a high aspect ratio.

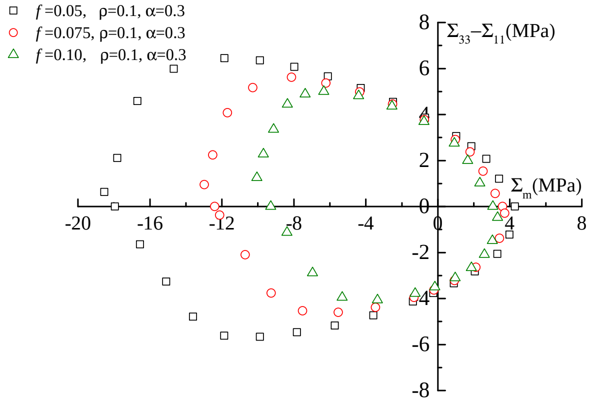

(a) Effect of porosity with $a/c = 2$, $\theta = 0°$

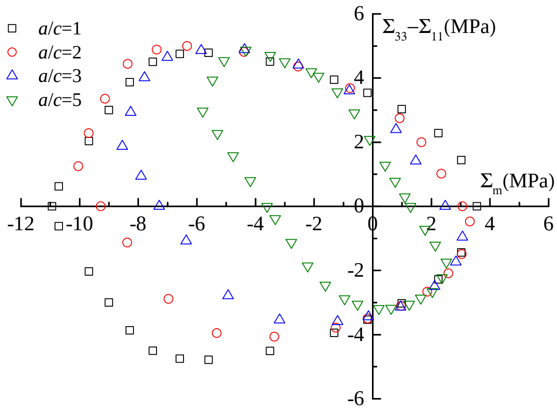

(b) Effect of aspect ratio with $f = 0.1$, $\theta = 0°$

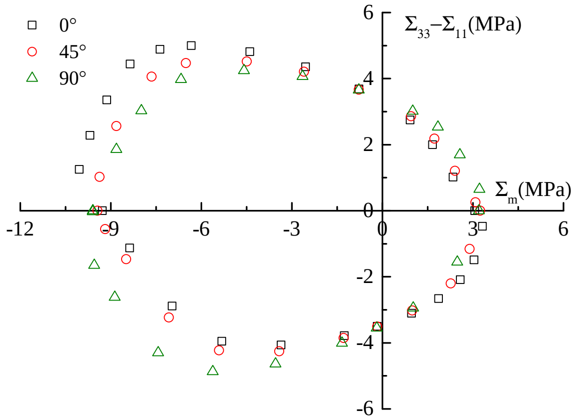

(c) Effect of pore orientation with $f = 0.1$, $a/c = 2$

Figure III .9: Evolution of macroscopic yield stresses predicted by unit cells with oblate pore for different porosities, aspect ratios and orientations with $\alpha = 0.3$, $\rho = 0.1$

© 2018 Tous droits réservés.

Thèse de Yajun Cao, Université de Lille, 2018

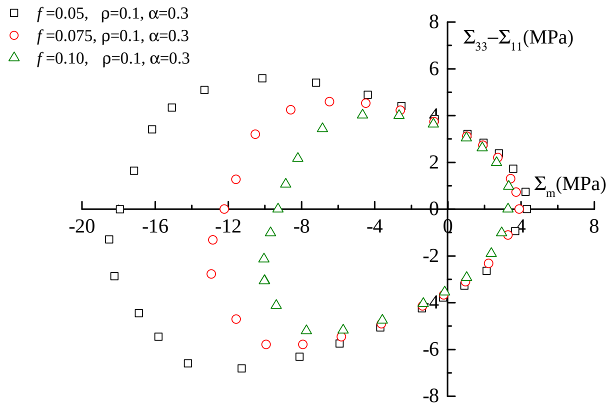

(a) Effect of porosity with $c/a = 2$, $\theta = 0°$

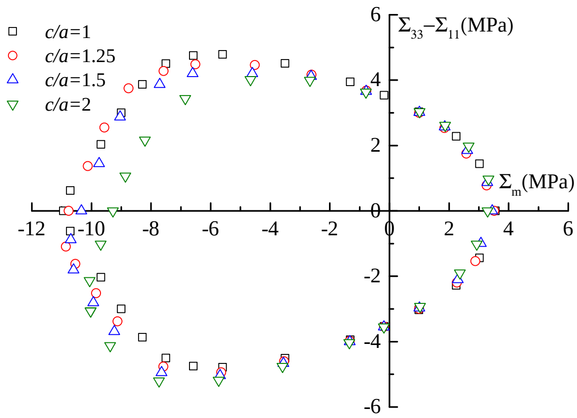

(b) Effect of aspect ratio with $f = 0.1$, $\theta = 0°$

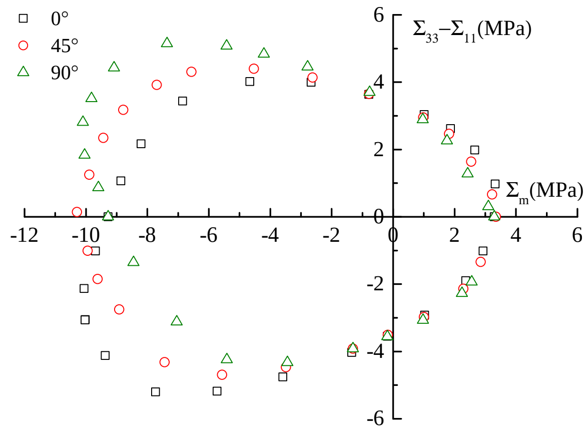

(c) Effect of pore orientation with $f = 0.1$,$c/a = 2$

Figure III .10: Evolution of macroscopic yield stresses predicted by unit cells with prolate pore for different porosities, aspect ratios and orientations with $\alpha = 0.3$, $\rho = 0.1$

© 2018 Tous droits réservés. lilliad.univ-lille.fr

Thèse de Yajun Cao, Université de Lille, 2018

As mentioned in previous studies, the pore orientations have significant influence on the elastic behavior, now we will address its further effect on plastic behavior. For this aim, three different orientations $\theta = 0°$, $45°$ and $90°$ are selected here to make comparisons. The evolutions of yield stress with respect to these orientations are presented in Fig.III .9(c), with porosity $f = 0.1$. As seen from the results, we notice that the evolution of plastic flow is strongly concerned with the pore orientations. It is observed that the shape orientation of the pore can result in changes in the size and shape of the yield surface. However, it should be remarked that the yield stress under hydrostatic loading case seems to be independent of the orientations for oblate pore.

Fig.III .10 illustrates the evolution of macroscopic yield stress induced by the prolate pore geometry. Similar to the oblate one, the determination of macroscopic yield stress also depends on the porosity, aspect ratio and orientation. But the shape and size of macroscopic surfaces are quite different compared with oblate one as displayed in Fig.III .10(a) and Fig.III .10(b). Moreover, the prolate orientations plays different roles on compression and tensile region, which implies the orientations have anisotropic hardening or softening effects at different stress state. However, this effect on the evolution of yield stresses for oblate and prolate pore is inverse. As mentioned previously, the yield stress is not sensitive to the the orientations of the oblate pore under the purely hydrostatic loading condition, while for prolate one, there is a significant hardening effect on the hydrostatic compressible loading when $\theta = 45°$ as shown in Fig.III .10(c). Specifically, it seems that there is a closed symmetry of the yield surfaces for $\theta = 0°$ and $\theta = 90°$ about the axes Σ_m from these plots. By comparison Fig.III .10(c) with Fig.III .9(c), the orientation effect is more sensitive to prolate pore than the oblate one. This trend also holds for the case of porosity $f = 0.05$ as presented in Appendix B. Therefore, it is important to note that the pore orientations also make a contribution to the anisotropic influence. This effect has never been reported and considered in an analytical solution.

Next we will examine the effect of inclusion fraction on the macroscopic yield stress. Fig.III .11 reflects the evolution of plastic surfaces predicted by unit cells with oblate and prolate pore. $\rho = 0$ is corresponding to the unit cell without inclusion. By comparison with the case of inclusion embedded, it is no doubt that the presence of inclusion can enhance the yield stress except the hydrostatic loading case. Combining the results from Fig.III .5, this suggests that the presence of inclusion does not influence the hydrostatic strength of the studied material with spherical or spheroidal pore. It is mainly dominated by the properties of matrix and pore geometries.

© 2018 Tous droits réservés. lilliad.univ-lille.fr

Thèse de Yajun Cao, Université de Lille, 2018

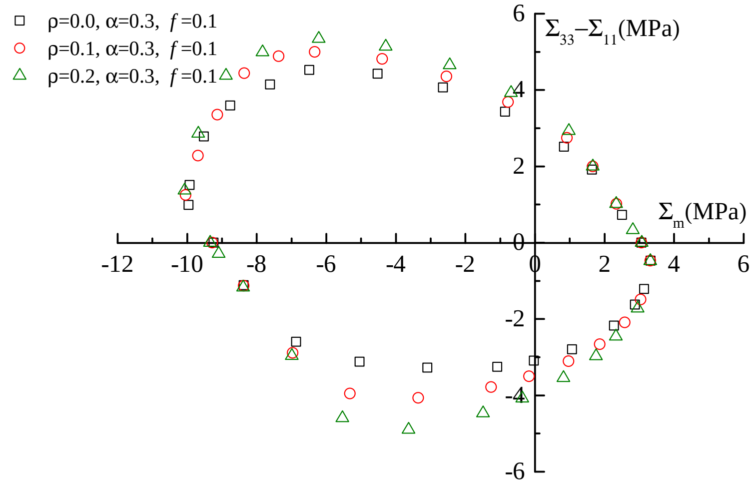

(a) oblate $a/c = 2$

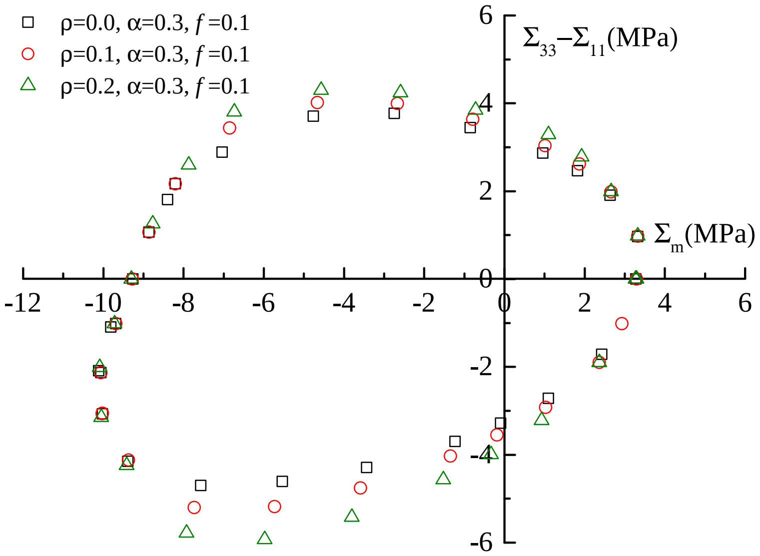

(b) prolate $c/a = 2$

Figure III .11: Evolution of macroscopic yield stresses predicted by unit cells with oblate and prolate pore for different ρ with $\alpha = 0.3,\ f = 0.1$

4 Estimations of yield stresses for porous Berea sandstone

In the previous section, we have estimated the yield stress for the macroscopic behaviour induced by the meso pore and inclusion geometry, it is confirmed that the exists of meso pores and inclusions have significant influences on the evolution of yield stress. In this section, this numerical model is also used to predict the macroscopic yield stress

© 2018 Tous droits réservés. lilliad.univ-lille.fr

Thèse de Yajun Cao, Université de Lille, 2018

of porous Berea sandstone. According to the SEM image analysis, the Berea sandstone is dominated by detrital grains such as quartz and feldspar ([Kareem et al., 2017], covering an average volume fraction of 0.64 which can be regarded as the matrix of Berea sandstone in our study, and with an average porosity of 0.21 as reported by [Wong et al., 1997, Wong et al., 2001]. Additional grains like carbonat are considered as hard inclusions. For simplicity, it is assumed that all the inclusions and pores are spherical and randomly distributed. With this information, a representative volume element is reconstructed as shown in Fig.III .12 for our study.

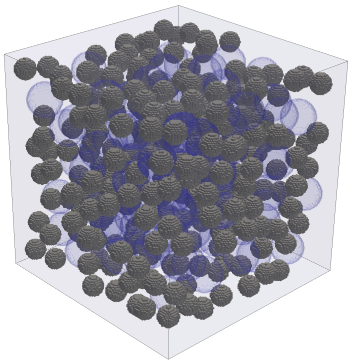

Figure III .12: The representative microstructure of Berea sandstone with porosity $f = 0.21$ and inclusion fraction $\rho = 0.15$.

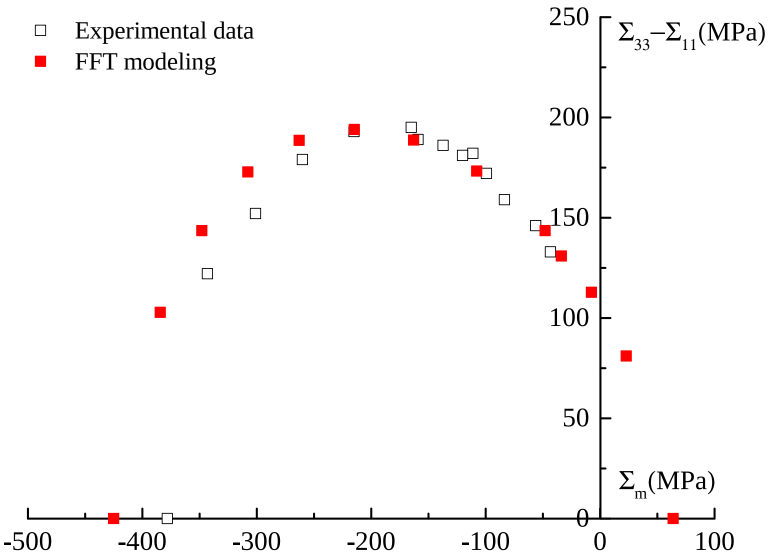

Figure III .13: Prediction of macroscopic yield stress by FFT-based method with $\alpha = 0.6$ and $H = 175MPa$ and compared with experimental data from [Baud et al., 2004].

For the aim of simulating the evolution macroscopic yield stress, the elastic parameters are adopted as same as previous studies, and plastic parameters are $\alpha = 0.6$ and

© 2018 Tous droits réservés. lilliad.univ-lille.fr

Thèse de Yajun Cao, Université de Lille, 2018

$h = 175MPa$. Fig.III .13 displays the prediction of marcroscopic yield stresses of Berea sandstone by means of FFT-based homogenization method. The shape of yield surface is of ellipse, this mainly due to the presence of pores. Moreover, it is also enhanced by reinforced inclusions. Experimental data documented from [Baud et al., 2004] is compared with the modeling results. From the comparison, one can see that the two results are in good agreement.

5 Concluding remarks

In this paper, the main objective of this study is to carry out a reference solutions for such a composite with both meso-pore and meso-inclusion configured at same scale. To perform its evolutions of macroscopic mechanical behavior, a series of simulations are computed by employing the FFT based homogenization method to consider the effect of inclusion and pore geometrical characters.

With a series of comparisons, both the pore and inclusion geometry is sensitive to the determination of macroscopic elastic behavior. Simulation results show that the anisotropy effect induced by pore and inclusion is obtained with respect to its aspect ratio and orientation, providing an increase or decrease effect on the effective elastic modulus. For plastic behaviors, the inclusion geometry does not have significant effect on macroscopic plastic yield stress except the inclusion fraction. However, this does not work for the case of pore. The corresponding results reveal that the pore shape, distribution, aspect ratios, orientations indeed have important effects and play different roles on plastic yield stress. In addition, we also use this framework to predict the macroscopic behavior of Berea sandstone, the modeling results are well closed with the experimental data. For future works, to characterize the effective behaviors of such kinds of composite as accuracy as possible by an analytical criterion, these factors should be taken into considerations.

© 2018 Tous droits réservés. lilliad.univ-lille.fr

Thèse de Yajun Cao, Université de Lille, 2018

6 Appendix A: Effect of randomly distributed pores and inclusions on the macroscopic yield stresses

- *unit cell with spherical pores and inclusions*

In order to consider the effect of randomly distributed pores and inclusions on macroscopic yield stress, we also carried out some comparisons on the unit cell configured with both randomly distributed pores and inclusions (pore number $N_1 = 50$, inclusion number $N_2 = 50$) and the one contained single pore and inclusion with previous mentioned arrangement. The sensitivities on macroscopic yield stress for different porosity f, inclusion fraction ρ, and frictional coefficient T are also taken into account as shown in Fig.III .14 to Fig.III .16. Several important differences for effective plastic behavior between these two distributions in the unit cell can be observed, especially in the compression region. As highlight from the plot, it is found that the yield stresses of the unit cell with a random distribution of pores and inclusions are systematically lower than those of the unit cell with one single pore and inclusion, leading to a weakening effect on the overall compressible plastic yield strength. However, the difference between two distributions becomes smaller with a higher porosity and lower frictional coefficient α according to the results presented in Fig.III .14 and Fig.III .15.

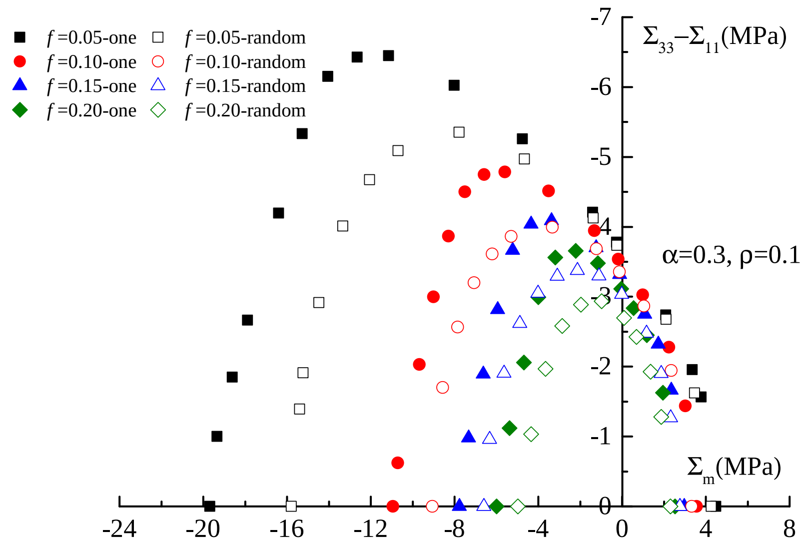

Figure III .14: Evolution of macroscopic yield stresses predicted by unit cells with two different distributions of pores and inclusions for different porosities.

© 2018 Tous droits réservés. lilliad.univ-lille.fr

Thèse de Yajun Cao, Université de Lille, 2018

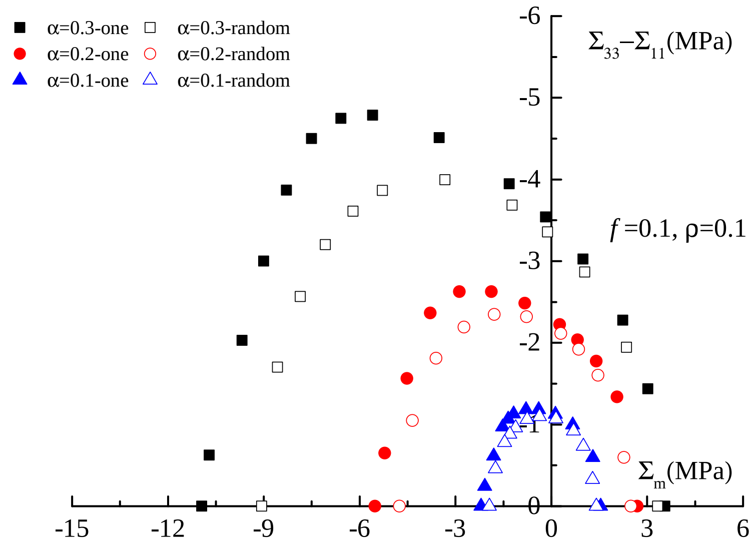

Figure III .15: Evolution of macroscopic yield stresses predicted by unit cells with two different distributions of pores and inclusions for different α.

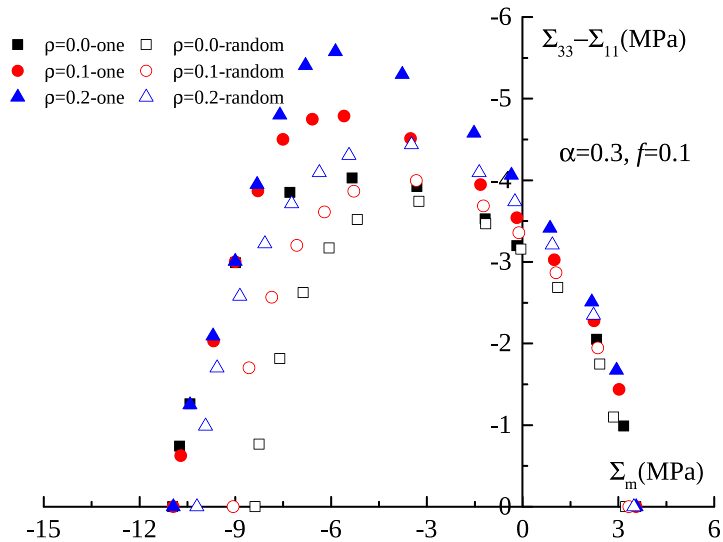

Figure III .16: Evolution of macroscopic yield stresses predicted by unit cells with two different distributions of pores and inclusions for different ρ.

Moreover, the random distribution plays more important role on macroscopic plastic yield stress, also resulting in apparent discrepancies at compression region. The hydrostatic compression strength is quite influenced by the inclusion fraction compared with the dilute distribution. This distinctly shows the effect of interactions between randomly distributed inclusions and pores.

- *unit cell with spheroidal pores and spherical inclusions*

© 2018 Tous droits réservés. lilliad.univ-lille.fr

For anisotropic case, we specially investigate the unit cells with both randomly distributed oblate or prolate pores, in which all the orientations of pores are chosen as 0°. To ignore the shape effect of inclusions, for simplicity, randomly distributed spherical inclusions are also embedded at the same scale.

Fig.III .17 and Fig.III .18 respectively display the comparisons of plastic yield stresses for unit cells contained spheroidal pores and spherical inclusions with different distributions. And the effect of aspect ratio is also considered. According to these results, it is clear that the shape dependence is also preserved for randomly distributions on plastic yield surface. Similar to the case of spherical pores, randomly distributions of spheroidal pores also have important influences on the plastic compressible region, providing a weaken effect on plastic yield than the unit cell with one single pore and inclusion configured. However, for tensile region, it exhibits no significant differences for these two distributions. Moreover, the influence of aspect ratio is more sensitive to oblate pore than prolate one at tension region.

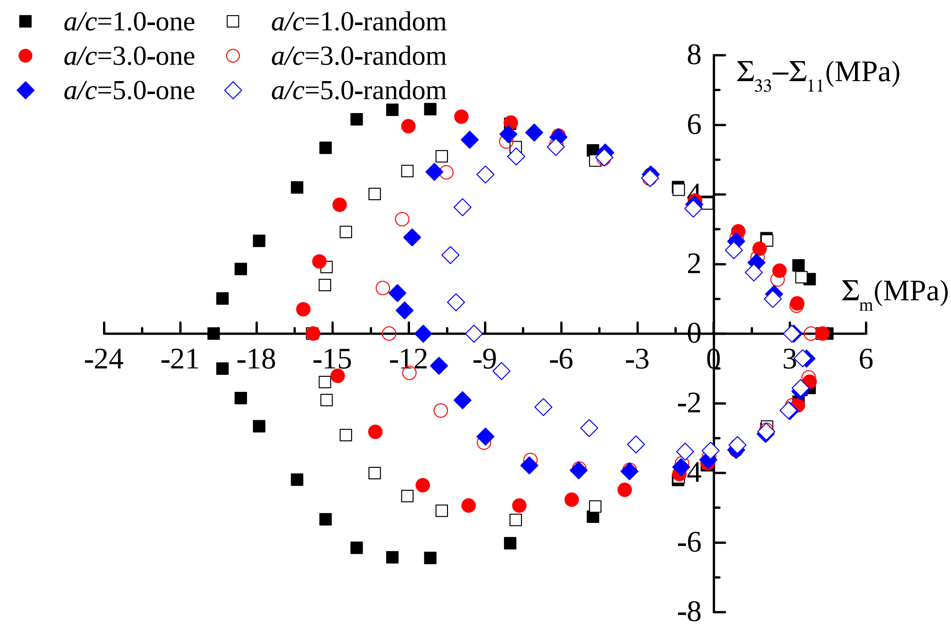

Figure III .17: Comparisons of macroscopic yield stresses predicted by unit cells with randomly distributed and regular arrangements for different aspect ratios of oblate pores with $\alpha = 0.3$, $f = 0.05$ and $\rho = 0.1$

© 2018 Tous droits réservés.

Thèse de Yajun Cao, Université de Lille, 2018

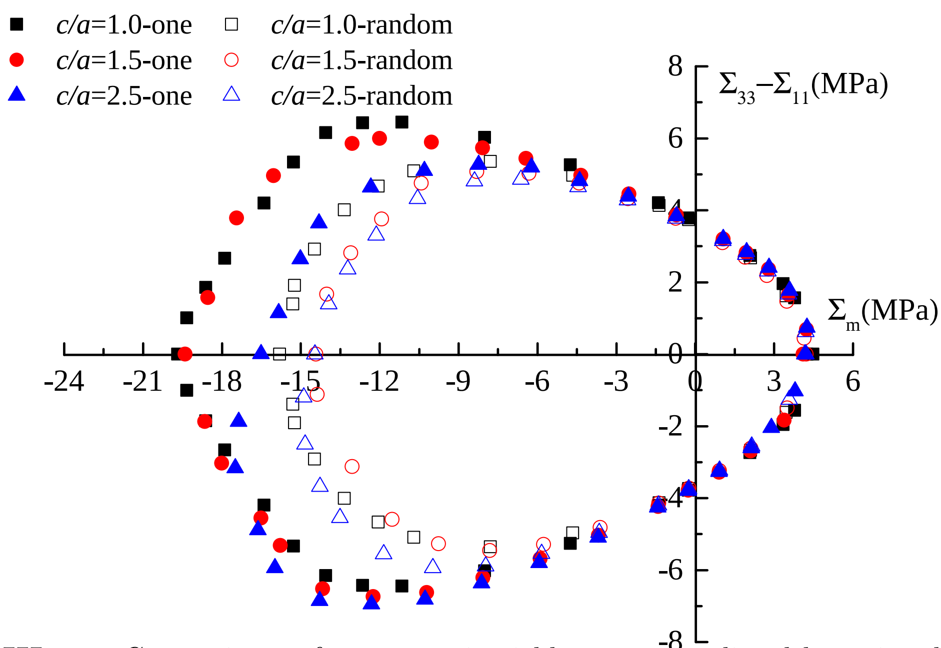

Figure III .18: Comparisons of macroscopic yield stresses predicted by unit cells with randomly distributed and regular arrangements for different aspect ratios of prolate pores with $\alpha = 0.3$, $f = 0.05$ and $\rho = 0.1$

© 2018 Tous droits réservés. lilliad.univ-lille.fr

Thèse de Yajun Cao, Université de Lille, 2018

7 Appendix B: Evolution of the macroscopic yield stresses for $f = 0.05$

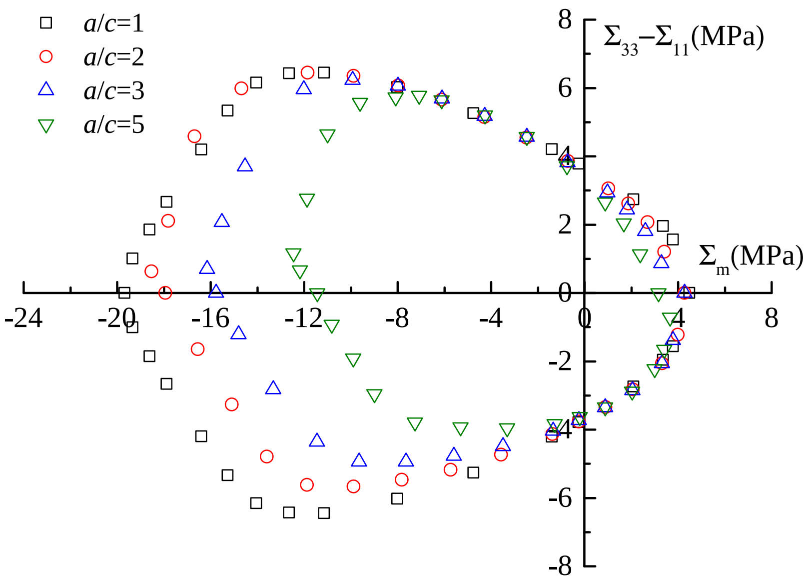

(a) $\theta = 0°$

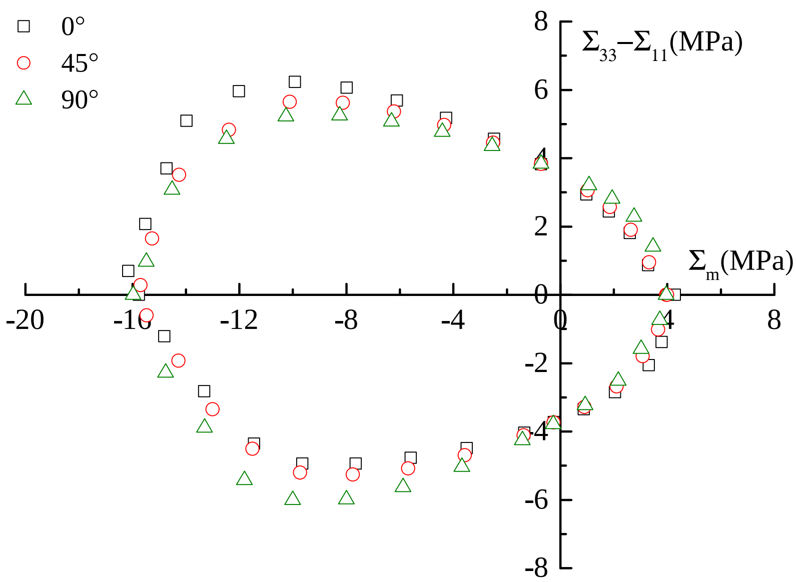

(b) $a/c = 3$

Figure III .19: Effect of aspect ratios and orientations of oblate pore on macroscopic yield stresses for $\alpha = 0.3$ and $\rho = 0.1$ with $f = 0.05$

© 2018 Tous droits réservés. lilliad.univ-lille.fr

Thèse de Yajun Cao, Université de Lille, 2018

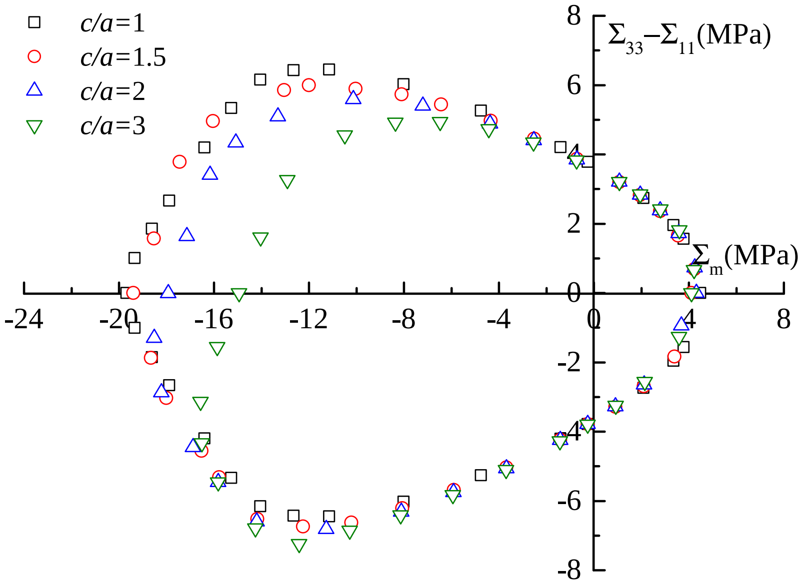

(a) $\theta = 0°$

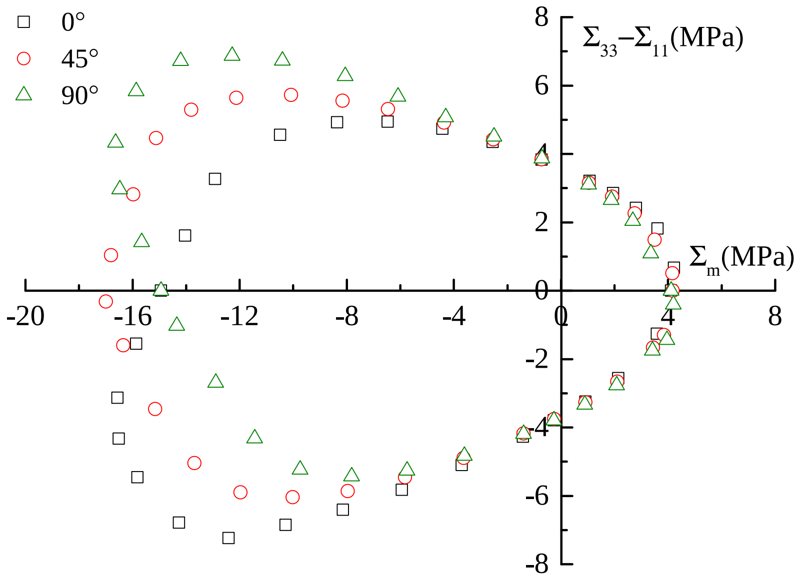

(b) $c/a = 3$

Figure III .20: Effect of aspect ratios and orientations of prolate pore on macroscopic yield stresses for $\alpha = 0.3$ and $\rho = 0.1$ with $f = 0.05$

© 2018 Tous droits réservés. lilliad.univ-lille.fr

Chapter IV

Effects of meso-inclusions and micro-pores on plastic and viscoplastic deformation of rock-like materials

Contents

© 2018 Tous droits réservés.

Thèse de Yajun Cao, Université de Lille, 2018

Summary

The aim of this chapter is to study effects of inclusion and pores on plastic and viscoplastic deformation of rock-like materials. We shall consider a class of clayey rocks with two separate scales of microstructure. At the mesoscopic scale, the material is constituted by a continuous matrix and embedded mineral inclusion. At the microscopic scale, the continuous matrix is a porous medium composed of a solid phase and spherical pores. Macroscopic deformation behavior of the material is determined by using a two-step homogenization procedure. At the mesoscopic scale, we shall investigate influences of inclusion stiffness, shape, orientation and volume fraction on plastic and viscoplastic deformation. A series of numerical simulations are performed and the obtained results show that the proposed numerical model is able to bring a finer description of complex microstructure effect than most analytical models. Finally, the efficacy of this numerical model is checked through comparisons between numerical results and experimental data in triaxial compression creep and relaxation tests on claystone.

1 Introduction

Pores and mineral inclusions are two main families of heterogeneities in rock-like materials. Macroscopic responses of those materials are generally affected not only by volume fractions but also shapes and spatial distributions of pores and inclusions induced un inhomogeneous deformation pattern. Classical phenomenological plastic and viscoplastic models are not able to explicitly take into account effects of such micro-structures accurately. Micro-mechanical models based on homogenization methods have been developed and significant progresses have been obtained during the last decades. Effective elastic properties have first been investigated and several homogenization schemes are now available and widely used in various materials, for instance the Dilute scheme, Mori Tanaka scheme ([Mori and Tanaka, 1973]), the self-consistent scheme ([Hill, 1965b]) and Ponte Castaneda and Willis scheme ([Ponte Castañeda and Willis, 1995]).

Nonlinear behaviors, for instance plastic deformation, have been investigated more recently. A series of homogenization techniques such as the incremental method ([Hill, 1965a]), the secant method ([Tandon and Weng, 1988]), the affine formulation ([Masson et al., 2000]) and the second-order estimates method([Ponte Castañeda, 2002]) have been proposed by one-step homogenization to estimate nonlinear behavior of a two-scale composite.

Based on these non-linear homogenization methods, some analytical or semi-analytical

© 2018 Tous droits réservés. lilliad.univ-lille.fr

Thèse de Yajun Cao, Université de Lille, 2018

macroscopic yield criteria have been proposed for porous materials containing rigid inclusions. For example, an effective criterion with inclusion effect has been established in [Garajeu and Suquet, 1997] with a Gurson-type porous matrix using a variational approach. An explicit expression of the macroscopic yield criterion has been formulated in [Shen et al., 2013] considering a porous matrix with a Drucker-Prager type solid phase. Considering perfect or imperfect interfaces between matrix and inclusions, an macroscopic strength criterion has been derived in [Bignonnet et al., 2015] with the help of the modified secant modulus method. Recently, a micro-mechanical model has been proposed [Bignonnet et al., 2016a] for cohesive granular materials with the evolution of porosity. The plastic compressibility of the matrix and pore shape effects have been studied in [Shen et al., 2017b]. Although the porosity and inclusion volume fraction can be taken into account, it is very difficult to evaluate the influences of inclusion or pore geometry on the macroscopic mechanical behaviors by those analytical models.

Modeling of time-dependent behaviors of heterogeneous materials is another challenge. Different approaches have also been proposed to determine effective behaviors of viscoplastic materials. For instance, an alternative method within the framework of Nonuniform Transformation Field Analysis was developed by the decomposition of local viscoplastic strain field within each phase into a set of plastic deformation modes ([Michel and Suquet, 2004, Roussette et al., 2009]). Other authors have presented a variational formulation for the homogenization of composites having viscoplastic constituents by considering the past history of deformation through internal variables ([Brassart et al., 2012]). In [Doghri et al., 2010], a general incrementally affine method for the mean-field homogenization of inclusion-reinforced elasto-viscoplastic composites has been developed. In all these methods, the presences of inclusions or pores are independently taken into account. Interactions between them in heterogenous materials still need further investigations.

In order to investigate effective behaviors of materials with complex micro-structures or high contrasts between constituent phases, full field numerical simulations provide an efficient way to have a deep understanding of micro-structure effects on macroscopic behaviors. Among various methods, Fast Fourier Transform (FFT) is one of the widely used techniques ([Moulinec and Suquet, 1994, Moulinec and Suquet, 1998]). Recently, the FFT based numerical method has been applied to describe the elasto-plastic behaviors of porous materials ([Vincent et al., 2014b, Bignonnet et al., 2016b, Li et al., 2018]) and inclusion-reinforced composites ([Idiart et al., 2006, Li et al., 2016]).

Rock-like materials are characterized by complex and multi-scale micro-structures. Pores and mineral inclusions are two main families of heterogeneities. Few studies are so

© 2018 Tous droits réservés. lilliad.univ-lille.fr

Thèse de Yajun Cao, Université de Lille, 2018

far available on studying visco-plastic deformation of rock-like materials by properly taking into account effects of micro-structure such as spatial distribution and geometrical shape of inclusion and pore. In the present paper, we shall propose a two-step homogenization method for modeling both plastic and viscoplastic strains of a class of rock-like materials containing pores and mineral inclusion at two different scales. The effect of pores is taken into account with an analytical homogenization method at the microscopic scale and the influence of inclusion by a FFT based numerical homogenization method. The results obtained from the proposed numerical model will be compared with those given by some analytical homogenized models with simple micro-structures. A sensitivity study will also be performed in terms of inclusion fraction, stiffness, shape and orientation . Finally, the proposed model will be verified by experimental data obtained from a typical claystone.

2 Basic description of microstructure for rock-like materials

We shall consider a class of rock-like materials with three separate scales. The macroscopic scale corresponds to the homogenized material whose mechanical properties should be determined. At the mesoscopic scale, the heterogeneous material is composed of periodically distributed representative unit cell. Each unit cell is composed by a homogenized matrix and embedded mineral inclusions of different volume fractions, stiffness, shapes and orientations. At the microscopic scale, the unit cell is a porous medium constituted by a continuous solid phase in which pores are embedded. The average pore size is much smaller than that of inclusion. In this study, the emphasis is put on the study of effects of inclusion and for the sake of simplicity, it is assumed that pores in the microscopic unit cell are spherical and randomly distributed. The selected three scales and unit cells are illustrated in Fig.IV .1.

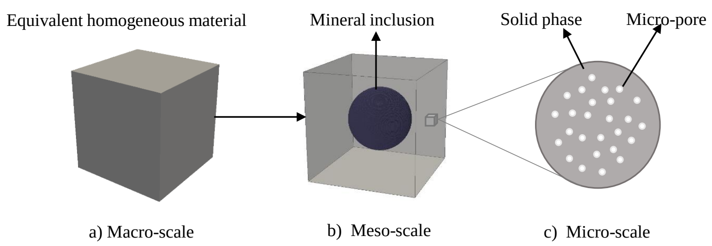

Figure IV .1: Illustration of selected scales and unit cells

Let us denote Ω the total volume of the unit cell at the macrocopic scale; ω_m the volume occupied by the solid phase at the microscopic scale; ω_1 and ω_2 the volumes of pores located at the microscopic scale and of inclusion embedded at the mesoscopic scale.

© 2018 Tous droits réservés. lilliad.univ-lille.fr

Thèse de Yajun Cao, Université de Lille, 2018

The local porosity f of the porous matrix, the volume fraction of inclusion ρ and the overall porosity Γ of the material can be given as:

$$f = \frac{\omega_1}{\omega_m + \omega_1}, \qquad \rho = \frac{\omega_2}{\Omega} = \frac{\omega_2}{\omega_m + \omega_1 + \omega_2}, \qquad \Gamma = \frac{\omega_1}{\Omega} = \frac{\omega_1}{\omega_m + \omega_1 + \omega_2} \tag{IV .1}$$

It is assumed that the mineral inclusion at the mesoscopic scale are characterized by an isotropic linear elastic behavior. However, the porous medium at the microscopic scale exhibits elastic, instantaneous plastic and time-dependent delayed plastic deformations. The solid phase is a pressure sensitive material verifying a Drucker-Prager type plastic criterion. While only spherical pores are considered at the microscopic scale, mineral inclusion at the mesoscopic scale can be of different volume fraction, stiffness, shape and orientation. We shall study effects of such geometrical factors on macroscopic properties of material. To solve this strongly non-linear multi-scale problem, a two-step homogenization procedure is here adopted. The effective properties of the porous matrix is first determined using an analytical method while those of heterogeneous rock by a FFT-based numerical method.

3 Effective mechanical behavior of the porous matrix

As mentioned above, the porous matrix is composed of a solid phase and spherical pores. The solid phase, for instance clay sheets, can exhibit both instantaneous and time-dependent plastic deformation. As a consequence, when subjected to prescribed stresses, the total strain rate (increment) of the porous matrix D_{ij} can be decomposed into an elastic part D^e_{ij} and a plastic part D^p_{ij}. The plastic strain is further decomposed in into an instantaneous plastic part D^{ip}_{ij} and a time-dependent visco-plastic part D^{vp}_{ij}:

$$D_{ij} = D^e_{ij} + D^{ip}_{ij} + D^{vp}_{ij} \tag{IV .2}$$

The effective stress-strain relations of the porous matrix can be expressed as:

$$\tilde{\boldsymbol{\Sigma}} = \tilde{\boldsymbol{C}}^{\boldsymbol{hom}} : (\boldsymbol{D} - \boldsymbol{D}^{\boldsymbol{ip}} - \boldsymbol{D}^{\boldsymbol{vp}}) \tag{IV .3}$$

$\tilde{\boldsymbol{\Sigma}}$ stands for the average stress tensor in the porous matrix. $\tilde{\boldsymbol{C}}^{\boldsymbol{hom}}$ is the effective elastic stiffness tensor of porous matrix. By assuming an isotropic material, $\tilde{\boldsymbol{C}}^{\boldsymbol{hom}}$ can be written as $\tilde{\boldsymbol{C}}^{\boldsymbol{hom}} = 3\tilde{k}_0^{hom}\boldsymbol{J} + 2\tilde{\mu}_0^{hom}\boldsymbol{K}$, where $J_{ijkl} = (\delta_{ij}\delta_{kl})/3$, $K_{ijkl} = I_{ijkl} - J_{ijkl}$ and $I_{ijkl} = (\delta_{ik}\delta_{jl} + \delta_{il}\delta_{jk})/2$ with δ_{ij} being the Kronecker's symbol. $\tilde{k}_0^{hom}$ and $\tilde{\mu}_0^{hom}$ are respectively the effective bulk modulus and shear modulus of the porous matrix which are dependent on porosity and can be determined by using Mori-Tanaka scheme([Mori and Tanaka, 1973]):

$$\tilde{k}_0^{hom} = \frac{4(1-f)k_s\mu_s}{4\mu_s + 3fk_s}, \tilde{\mu}_0^{hom} = \frac{(1-f)\mu_s}{1 + 6f\frac{k_s + 2\mu_s}{9k_s + 8\mu_s}} \tag{IV .4}$$

© 2018 Tous droits réservés. lilliad.univ-lille.fr

Thèse de Yajun Cao, Université de Lille, 2018

f denotes the porosity of the porous matrix, k_s and μ_s are the elastic moduli of the solid phase.

3.1 Instantaneous plastic behavior

The instantaneous plastic strain D_{ij}^{ip} of the porous matrix is determined form an analytical nonlinear homogenization method. For this purpose, the effective plastic yield function is first determined. It is known that the plastic behavior of most rock-like materials is sensitive to mean stress. Therefore, it is assumed that solid phase of porous material verifies a Drucker-Prager yield criterion which is written as follows:

$$\Phi^m(\boldsymbol{\sigma}) = \sigma_d + \alpha(\sigma_m - h) \leq 0 \qquad \text{(IV .5)}$$

$\boldsymbol{\sigma}$ denotes the local stress tensor. h and α respectively corresponds to the hydrostatic tensile strength and frictional coefficient of the solid phase. σ_m and σ_d are the local mean stress and generalized shear stress, respectively defined by $\sigma_m = tr\boldsymbol{\sigma}/3$ and $\sigma_d = \sqrt{\boldsymbol{\sigma}' : \boldsymbol{\sigma}'}$, with $\boldsymbol{\sigma}'$ being the local deviatoric stress tensor. According to the previous study by [Maghous et al., 2009], the effective plastic yield function of the porous matrix can be expressed in the following analytical form which is obtained by using a modified secant method:

$$F = \frac{1 + 2f/3}{\alpha^2}\tilde{\Sigma}_d^2 + (\frac{3f}{2\alpha^2} - 1)\tilde{\Sigma}_m^2 + 2(1-f)h\tilde{\Sigma}_m - (1-f)^2h^2 \leq 0 \qquad \text{(IV .6)}$$

$\tilde{\Sigma}_m$ and $\tilde{\Sigma}_d$ are respectively the average mean stress and generalized shear stress in the homogenized porous matrix, defined by $\tilde{\Sigma}_m = tr\tilde{\boldsymbol{\Sigma}}$ and $\tilde{\Sigma}_d = \sqrt{\tilde{\boldsymbol{\Sigma}}' : \tilde{\boldsymbol{\Sigma}}'}$, $\tilde{\boldsymbol{\Sigma}}'$ being the average deviatoric stress tensor of porous matrix. Unlike classical phenomenological plastic models, the plastic criterion issued from the nonlinear procedure (IV .6) explicitly takes into account the effect of porosity f at the microscopic scale.

According to [Barthélémy and Dormieux, 2003, Barthélémy and Dormieux, 2004] and [Maghous et al., 2009], for a porous medium with a Drucker-Prager type solid matrix, the same expression of macroscopic yield function (IV .6) can be obtained with either an associated or a non-associated plastic flow rule of the solid phase at the microscopic scale. A macroscopic plastic potential was also derived in [Maghous et al., 2009], which depends on the friction and dilatancy coefficients of the solid matrix. When these two local parameters at the microscopic scale are equal for the case of an associated flow rule, the macroscopic plastic flow rule of the porous medium is also associated in nature. In order to get a rigorous expression of the equivalent plastic deformation in the solid phase (IV .10) which will be used to calculate the evolution of porosity, the associated plastic

© 2018 Tous droits réservés. lilliad.univ-lille.fr

Thèse de Yajun Cao, Université de Lille, 2018

flow rule is here adopted for the solid phase. With this assumption, the normality rule can also be applied at the mesoscopic scale for the porous clay matrix. The corresponding plastic strain rate is given by:

$$\dot{\boldsymbol{D}}^{\boldsymbol{ip}} = \dot{\lambda_{ip}} \frac{\partial F}{\partial \tilde{\boldsymbol{\Sigma}}}(\tilde{\boldsymbol{\Sigma}}, f, \alpha) \tag{IV .7}$$

The plastic multiplier $\dot{\lambda_{ip}}$ verifies the following loading-unloading condition:

$$\begin{cases} \dot{\lambda_{ip}} = 0 \quad if \quad F < 0 \quad or \quad if \quad F = 0 \quad and \quad \dot{F} < 0 \\ \dot{\lambda_{ip}} \geq 0 \quad if \quad F = 0 \quad and \quad \dot{F} = 0 \end{cases} \tag{IV .8}$$

Following the energy-based argument introduced in [Gurson, 1977] and using the normality rule, the equivalent instantaneous plastic strain in the solid phase obeying a Drucker-Prager type criterion can be related to the average plastic strain tensor of the porous matrix ([Shen et al., 2012b, Shen et al., 2013]):

$$\dot{\epsilon^{ip}} = \frac{\tilde{\boldsymbol{\Sigma}} : \dot{\boldsymbol{D}}^{\boldsymbol{ip}}}{\alpha(1-f)h} \tag{IV .9}$$

Further, it is assumed that the frictional coefficient α of the solid phase evolves during the plastic deformation process. This evolution is described the following function of an equivalent total plastic strain ϵ^p in the solid phase:

$$\alpha = \alpha_m - (\alpha_m - \alpha_0) e^{b_1 \epsilon^p}, \epsilon^p = \epsilon^{ip} + \epsilon^{vp} \tag{IV .10}$$

The variation of porosity is related to both the macroscopic volumetric plastic strain and the plastic compressibility or dilation of the solid phase. According to previous studies ([Shen et al., 2012b, Shen and Shao, 2016a]), the porosity variation due to the instantaneous plastic deformation can be determined from the following kinematical compatibility condition:

$$\dot{f_{ip}} = (1-f)(tr\dot{\boldsymbol{D}}^{\boldsymbol{ip}} - \alpha \dot{\epsilon}^{ip}) \tag{IV .11}$$

According to (IV .7), (IV .9), (IV .11) and the consistency condition, one gets:

$$\dot{F}(\tilde{\boldsymbol{\Sigma}}, f, \alpha) = \frac{\partial F(\tilde{\boldsymbol{\Sigma}}, f, \alpha)}{\partial \tilde{\Sigma}} : \dot{\tilde{\Sigma}} + \frac{\partial F(\tilde{\Sigma}, f, \alpha)}{\partial f} \dot{f} + \frac{\partial F(\tilde{\Sigma}, f, \alpha)}{\partial \alpha} \dot{\alpha} = 0 \tag{IV .12}$$

And one can obtain the explicit expression of the plastic multiplier $\dot{\lambda_{ip}}$:

$$\dot{\lambda_{ip}} = \frac{\frac{\partial F}{\partial \tilde{\boldsymbol{\Sigma}}} : \boldsymbol{C} : (\dot{\boldsymbol{D}} - \dot{\boldsymbol{D}}^{\boldsymbol{vp}})}{\frac{\partial F}{\partial \tilde{\boldsymbol{\Sigma}}} : \boldsymbol{C} : \frac{\partial F}{\partial \tilde{\boldsymbol{\Sigma}}} - \frac{\partial F}{\partial f}(1-f)[\frac{\partial F}{\partial \tilde{\Sigma}_m} - \alpha \frac{\tilde{\boldsymbol{\Sigma}} : \frac{\partial F}{\partial \tilde{\boldsymbol{\Sigma}}}}{(1-f)h}] - \frac{\partial F}{\partial \alpha} \frac{\partial \alpha}{\partial \epsilon^p} \frac{\tilde{\boldsymbol{\Sigma}} : \frac{\partial F}{\partial \tilde{\boldsymbol{\Sigma}}}}{(1-f)h}} \tag{IV .13}$$

© 2018 Tous droits réservés. lilliad.univ-lille.fr

3.2 Time dependent behavior

In the present study, the viscoplastic deformation is seen as a time-dependent delayed plastic deformation. Therefore, a unified approach is proposed by [Zhou et al., 2008a] and [Farhat et al., 2017]. Two yield surfaces will be established to describe the instantaneous plastic deformation and the viscoplastic one, respectively. The evolution of viscoplastic deformation is delayed with respect to the instantaneous plastic one. Under a prescribed stress state, for instance in a creep test, the plastic yield surface is instantaneously reached while the viscoplastic loading surface evolves with time under constant stresses. With this idea in head, it is assumed that the effective yield function of the viscoplastic deformation can be obtained as a heuristic extension of the instantaneous plastic yield function with a delayed plastic hardening law. Therefore, the viscoplastic yield function is taken as the same form of the that given in (IV .6) but with a different plastic hardening law α_{vp}:

$$F_{vp} = \frac{1+2f/3}{\alpha_{vp}^2}\tilde{\Sigma}_d^2 + (\frac{3f}{2\alpha_{vp}^2} - 1)\tilde{\Sigma}_m^2 + 2(1-f)h\tilde{\Sigma}_m - (1-f)^2h^2 \geq 0 \tag{IV .14}$$

The delayed plastic hardening law $\alpha_{vp} \leq \alpha$ is introduced to control the evolution of viscoplastic loading surface and it is also a function of an equivalent viscoplastic strain in the solid phase:

$$\alpha_{vp} = \alpha_m - (\alpha_m - \alpha_0)e^{b_{vp}\epsilon^p}, \epsilon^p = \epsilon^{ip} + \epsilon^{vp} \tag{IV .15}$$

When the viscoplastic loading surface reaches the instantaneous plastic yield surface, the viscoplastic strain rate vanishes.

Inspired by the work of [Huang et al., 2014], the equivalent viscoplastic strain ϵ^{vp} of the solid phase can be obtained in a similar way to the evolution of $\boldsymbol{\epsilon^{ip}}$:

$$\dot{\epsilon}^{vp} = \frac{\tilde{\boldsymbol{\Sigma}} : \dot{\boldsymbol{D}}^{\boldsymbol{vp}}}{\alpha_{vp}(1-f)h} \tag{IV .16}$$

Similar to the case of instantaneous plastic deformation, the porosity evolution due to viscoplastic deformation is calculated by:

$$\dot{f}_{vp} = (1-f)(tr\dot{\boldsymbol{D}}^{\boldsymbol{vp}} - \alpha_{vp}\dot{\epsilon}^{vp}) \tag{IV .17}$$

The average viscoplastic strain rate of porous matrix is given by:

$$\dot{\boldsymbol{D}}^{\boldsymbol{vp}} = \dot{\lambda}_{vp}\frac{\partial F_{vp}}{\partial \tilde{\boldsymbol{\Sigma}}}(\tilde{\boldsymbol{\Sigma}}, f, \alpha_{vp}) \tag{IV .18}$$

The magnitude of viscoplastic strain is defined by the positive-valued multiplier $\dot{\lambda}_{vp}$. It depends on the distance between the current stress state and the viscoplastic loading surface. This distance is here interpreted by the positive value of loading function F_{vp}.

© 2018 Tous droits réservés.

Thèse de Yajun Cao, Université de Lille, 2018

Depending on the evolution of this function (decreasing, constant or decreasing), it is possible to produce three different viscoplastic flow regimes: primary creep, stationary creep and accelerated creep. In the present study, based on the overstress viscoplastic theory proposed by [Perzyna, 1963], the following power law is adopted to calculate the viscoplastic multiplier $\dot{\lambda}_{vp}$:

$$\dot{\lambda}_{vp} = \begin{cases} 0 & if \quad F_{vp} \leq 0 \\ \frac{1}{\eta}(\frac{F_{vp}}{h^2})^m & if \quad F_{vp} > 0 \end{cases} \tag{IV .19}$$

Algorithm 2: Compute the average stress of porous matrix $\tilde{\boldsymbol{\Sigma}}_{n+1}$

Input: $\boldsymbol{D}_n$,$\Delta\boldsymbol{D}_{n+1}$,$\boldsymbol{D}_n^{vp}$,$\boldsymbol{D}_n^{ip}$,$V_n$,$t_n$,$\Delta t_{n+1}$
Output: $\tilde{\boldsymbol{\Sigma}}_{n+1}$,$\boldsymbol{D}_{n+1}$,$\boldsymbol{D}_{n+1}^{ip}$,$\boldsymbol{D}_{n+1}^{vp}$,$V_{n+1}$
Initialization:$\boldsymbol{D}_{n+1} = \boldsymbol{D}_n + \Delta\boldsymbol{D}_{n+1}$,$t_{n+1} = t_n + \Delta t_{n+1}$;
$\tilde{\boldsymbol{\Sigma}}_{n+1}^{trial} = \tilde{C}^{hom} : (\boldsymbol{D}_{n+1} - \boldsymbol{D}_n^{ip} - \boldsymbol{D}_n^{vp})$;

```
if F_vp(Σ̃^trial_{n+1}, V_n) ≤ 0 then
    Σ̃_{n+1} = Σ̃^trial_{n+1};
    Δλ^ip_{n+1} = 0, Δλ^vp_{n+1} = 0;
else
    Calculate the viscoplastic multiplier Δλ^vp_{n+1};
    D^vp_{n+1} = D^vp_n + ΔD^vp_{n+1};
    Σ̃^trial_{n+1} = C̃^hom : (D_{n+1} − ΔD^vp_{n+1});
    if F(Σ̃^trial_{n+1}, V^i_n) ≤ 0 then
        Σ̃_{n+1} = Σ̃^trial_{n+1};
        Δλ^ip_{n+1} = 0, D^ip_{n+1} = 0;
    else
        for i = 1...m_iter do
            Calculate the plastic multiplier Δλ^{ip,i}_{n+1};
            D^{ip,i+1}_{n+1} = D^{ip,i}_{n+1} + Δλ^{ip,i}_{n+1} ∂Φ/∂Σ̃ (Σ̃, V^i_n);
            V^i_{n+1} = V_n + ΔV^i_{n+1};
            Σ̃^{i+1}_{n+1} = C : (D_{n+1} − D^vp_{n+1} − D^{ip,i+1}_{n+1});
            if F^{i+1}(Σ̃^{i+1}_{n+1}, V^i_{n+1}) ≤ 0 then
                Return;
            else
                i = i + 1;
            end
        end
    end
end
```

The parameters η and the power m are introduced to control the evolution rate of viscoplastic strain of the porous matrix. Let consider now a consider a time interval $[t_n, t_{n+1}]$ during the loading history. At the beginning of the interval t_n, the values of average strain D_n, average stress $\tilde{\boldsymbol{\Sigma}}_n$ as well as all interval variables are known. For a

© 2018 Tous droits réservés. lilliad.univ-lille.fr

Thèse de Yajun Cao, Université de Lille, 2018

prescribed average strain increment ΔD_n, the average stress at the end of interval $\tilde{\mathbf{\Sigma}}_{n+1}$ is given by the following stress-strain relations:

$$\tilde{\mathbf{\Sigma}}_{n+1} = \tilde{\mathbf{\Sigma}}_n + \tilde{\boldsymbol{C}}^{\boldsymbol{hom}} : (\boldsymbol{D}_{n+1} - \boldsymbol{D}_n - \Delta \boldsymbol{D}^{ip}_{n+1} - \Delta \boldsymbol{D}^{vp}_{n+1}) \tag{IV .20}$$

The flowchart of the calculation algorithm is given as presented in Algorithm 2.

4 Macroscopic mechanical properties of material

After the determination of effective mechanical properties of the porous matrix, it is now possible to investigate the macroscopic mechanical properties of material by considering effects of mineral inclusion. In the present study, we shall evaluate influences of inclusion shape, size and orientation. The task here is to solve a strong nonlinear homogenization problem. Unlike the first step of homogenization for the porous matrix, no analytical solution can be obtained in the present case. A suitable numerical homogenization method should be used. Based on previous studies [Moulinec and Suquet, 1994, Moulinec and Suquet, 1998], a FFT based method is here chosen. This method has been applied to rock-like materials in elastic and plastic cases ([Jiang et al., 2015, Li et al., 2018]). It is now extended to materials exhibiting both plastic and viscoplastic deformation.

By taking into account the time-dependent plastic deformation in the porous matrix, the nonlinear homogenization problem on the unit cell at the mesoscopic scale can be reformulated as follows. The local strain field inside the unit cell is defined by the periodic Lippmann-Schiwnger equations:

$$\boldsymbol{\varepsilon}(\boldsymbol{x}, \boldsymbol{t}) = E(t) - \mathbf{\Gamma}^0 * \boldsymbol{\tau}(\boldsymbol{x}, t) \tag{IV .21}$$

The convolution product is defined by:

$$\mathbf{\Gamma}^0 * \boldsymbol{\tau}(\boldsymbol{x}, t) = \int_\Omega \mathbf{\Gamma}^0(\boldsymbol{x} - \boldsymbol{y}) : \boldsymbol{\tau}(\boldsymbol{y}, t) d\boldsymbol{y} \tag{IV .22}$$

And the polarization stress $\boldsymbol{\tau}$ is expressed as: $\boldsymbol{\tau} = \tilde{\mathbf{\Sigma}}(\boldsymbol{\varepsilon}(\boldsymbol{x}, t)) - \mathbb{C}^0 : \boldsymbol{\varepsilon}(\boldsymbol{x}, t)$, with $\mathbb{C}^0$ being the reference stiffness tensor. The Green operator $\mathbf{\Gamma}^0$ in the Fourier space can be written as:

$$\hat{\Gamma}_{ijkl}(\boldsymbol{\xi}) = \frac{1}{4\mu^0 |\boldsymbol{\xi}|^2} (\delta_{ik}\xi_j\xi_l + \delta_{jk}\xi_i\xi_l + \delta_{il}\xi_j\xi_k + \delta_{jl}\xi_i\xi_k) - \frac{\lambda^0 + \mu^0}{\mu^0(\lambda^0 + 2\mu^0)} \frac{\xi_i\xi_j\xi_k\xi_l}{|\boldsymbol{\xi}|^4}. \tag{IV .23}$$

$\boldsymbol{\xi}$ denotes discrete frequencies in the Fourier space.λ^0 and μ^0 are the Lame coefficients related to the reference stiffness tensor.

© 2018 Tous droits réservés. lilliad.univ-lille.fr

Thèse de Yajun Cao, Université de Lille, 2018

Due to the nonlinear mechanical properties of the porous matrix, the homogenization problem on the unit cell is solved in an incremental way. Let consider a time interval and a constant rate of prescribed macroscopic strain, the macroscopic strain at the end of the interval is given by:

$$\boldsymbol{E}(t_{n+1}) = \boldsymbol{E}(t_n) + \dot{\boldsymbol{E}}(t_{n+1})\Delta t \qquad \text{(IV .24)}$$

The solution to be found here is to calculate the average macroscopic stress tensor $\boldsymbol{\Sigma}^{i+1}$ by considering the following elastic-plastic and viscoplastic stress-strain relations:

$$\tilde{\boldsymbol{\Sigma}}(t_{n+1},\boldsymbol{x}) = \boldsymbol{C}(\boldsymbol{x}) : (\boldsymbol{\varepsilon}(t_{n+1},\boldsymbol{x}) - \boldsymbol{\varepsilon}^{ip}(t_{n+1},\boldsymbol{x}) - \boldsymbol{\varepsilon}^{vp}(t_{n+1},\boldsymbol{x})) \qquad \text{(IV .25)}$$

In present study, the mineral inclusion is assumed as a linear elastic material. Only the porous matrix exhibits the plastic and viscoplastic deformation. The flowchart of the FFT based numerical homogenization procedure is summarized in Algorithm 2.

Algorithm 3: Discretized solution of the LS equations

Input: $\boldsymbol{\varepsilon}(t_n,\boldsymbol{x}_p), \Delta\boldsymbol{E}(t_{n+1}), \Delta t_{n+1}$
Output: $\boldsymbol{E}(t_{n+1}), \boldsymbol{\Sigma}(t_{n+1})$
Initialization:$t_{n+1} = t_n + \Delta t_{n+1}$;
$\boldsymbol{E}(t_{n+1}) = \boldsymbol{E}(t_n) + \Delta\boldsymbol{E}(t_{n+1})$;
$\boldsymbol{\varepsilon}^0(t_{n+1},\boldsymbol{x}_p) = \boldsymbol{\varepsilon}(t_n,\boldsymbol{x}_p) + \Delta\boldsymbol{E}(t_{n+1}) \qquad \forall\boldsymbol{x}_p \in \Omega$;
if $\boldsymbol{x}_p \in (\omega_m + \omega_1)$ **then**
  Call Algorithm 2 to compute $\tilde{\boldsymbol{\Sigma}}^0(t_{n+1},\boldsymbol{x_p})$;
else
  $\tilde{\boldsymbol{\Sigma}}^0(t_{n+1},\boldsymbol{x}_p) = \boldsymbol{C}(t_{n+1},\boldsymbol{x}_p) : \boldsymbol{\varepsilon}^0(t_{n+1},\boldsymbol{x}_p)$;
end
for $i = 0 : N_{iter}$ **do**
  The previous $\tilde{\boldsymbol{\Sigma}}(t_n)$ and $\boldsymbol{\varepsilon}(t_n)$ at each point $\boldsymbol{x_p}$ are known ;
  $\hat{\boldsymbol{\Sigma}}^i(t_{n+1},\boldsymbol{\xi}_p) = \mathcal{FFT}(\tilde{\boldsymbol{\Sigma}}^i(t_{n+1},\boldsymbol{x_p}))$;
  Convergence test;
  $E_{error} = \frac{(\langle\|\boldsymbol{\xi}\cdot\hat{\boldsymbol{\sigma}}^i(\boldsymbol{\xi})\|^2\rangle)^{1/2}}{\|\hat{\boldsymbol{\sigma}}^i(\boldsymbol{0})\|}$;
  if $E_{error} < 10^{-4}$ **then**
    Return;
  else
    $\hat{\varepsilon}^{i+1}(t_{n+1},\boldsymbol{\xi}_p) = \hat{\varepsilon}^i(t_{n+1},\boldsymbol{\xi}_p) - \hat{\Gamma}^0(\boldsymbol{\xi}_p) : \hat{\boldsymbol{\Sigma}}^i(t_{n+1},\boldsymbol{\xi}_p) \qquad \forall\boldsymbol{\xi}_p \neq \boldsymbol{0}, \quad \hat{\varepsilon}^{i+1}(\boldsymbol{0}) = \boldsymbol{E}(t_{n+1})$;
    $\boldsymbol{\varepsilon}^{i+1}(t_{n+1},\boldsymbol{x_p}) = \mathcal{FFT}^{-1}(\hat{\varepsilon}^{i+1}(t_{n+1},\boldsymbol{\xi}_p))$;
    if $\boldsymbol{x}_p \in (\omega_m + \omega_1)$ **then**
      Call Algorithm 2 to compute $\tilde{\boldsymbol{\Sigma}}^{i+1}(t_{n+1},\boldsymbol{x_p})$;
    else
      $\tilde{\boldsymbol{\Sigma}}^{i+1}(t_{n+1},\boldsymbol{x}_p) = \boldsymbol{C}(t_{n+1},\boldsymbol{x}_p) : \boldsymbol{\varepsilon}^{i+1}(t_{n+1},\boldsymbol{x}_p)$;
    end
    $i = i + 1$;
  end
end
Calculate the macroscopic stress $\boldsymbol{\Sigma}^{i+1} = \frac{1}{|\Omega|}\int_\Omega \tilde{\boldsymbol{\Sigma}}(t_{n+1},\boldsymbol{x_p})d\Omega$

© 2018 Tous droits réservés. lilliad.univ-lille.fr

Thèse de Yajun Cao, Université de Lille, 2018

5 Full-field modeling and comparisons

A series of numerical simulations are presented in this section by considering different cases about inclusion stiffness,shape,orientation and volume fraction. For this purpose, the elastic properties of the solid phase of porous matrix are chosen as $E_s = 5.027GPa, \nu_s = 0.33$ and the reference values for the inclusion as $E_i = 20E_s, \nu_i = 0.33$. Also the reference values of inclusion volume fraction and of porosity in the porous matrix are respectively $\rho = 0.1$ and $f = 0.1$. The spatial resolution for all calculations is fixed to $128 \times 128 \times 128$. In order to reduce the influence of the spatial discretization, and to better illustrate the effects of inclusion volume fraction, stiffness, shape and orientation on macroscopic responses, the REV with one single inclusion centered in the periodic unit cell is adopted here for the simulations of sensitive studies. The study of microstructure effects on the effective plastic yield stress is presented in appendix A, with different spatial distributions of inclusions (cubic array of inclusions and random distributed inclusions).

5.1 Evaluation of macroscopic yield surface

The macroscopic plastic yield surface of homogenized material is first evaluated. To this end, a perfectly plastic behavior of assumed for the solid phase of porous matrix with the following friction coefficient $\alpha_m = \alpha_0 = 0.3$ and hydrostatic tensile strength $h = 10MPa$.

5.1.1 Effect of porosity and inclusion fraction

In Fig.IV .2, we show computed macroscopic yield stresses in the meridian stress plane for different values of porosity and inclusion fraction. It is clearly seen that the macroscopic yield stress is more sensitive to porosity than to inclusion fraction. For instance, the hydrostatic tensile and compression strengths are insensitive to the inclusion volume fraction (see Fig.IV .2(a)) while they are strongly dependent on the porosity (see Fig.IV .2(b)). Moreover, the hydrostatic compression strength is more sensitive to porosity than the tensile one. On the other hand, we have compared the FFT computed yield stress with the analytical solution obtained from a two-step homogenization method by [Shen et al., 2013] for heterogeneous rocks with the same porous matrix as that considered here and spherical inclusions. In such an analytical criterion, only the inclusion volumetric fraction can be taken into account. It is seen that for a low volume fraction of inclusion, for instance $\rho = 0.1$ and as shown in Fig.IV .2(b), the analytical yield surfaces are very close to the numerically computed yield stresses for different values of porosity. However,

© 2018 Tous droits réservés. lilliad.univ-lille.fr

Thèse de Yajun Cao, Université de Lille, 2018

when the volume fraction of inclusion is higher than 0.1, large differences are obtained, in particular for the shear stress under a high mean stress, as shown in Fig.IV .2(a). The numerically computed shear stress is higher than that predicted by the analytical criterion. This difference is mainly due to the interaction between the porous matrix and inclusion, which becomes important when the inclusion fraction is high. This interaction induces a macroscopic hardening effect which is correctly taken into account in the FFT-based numerical model but not by the analytical criterion.

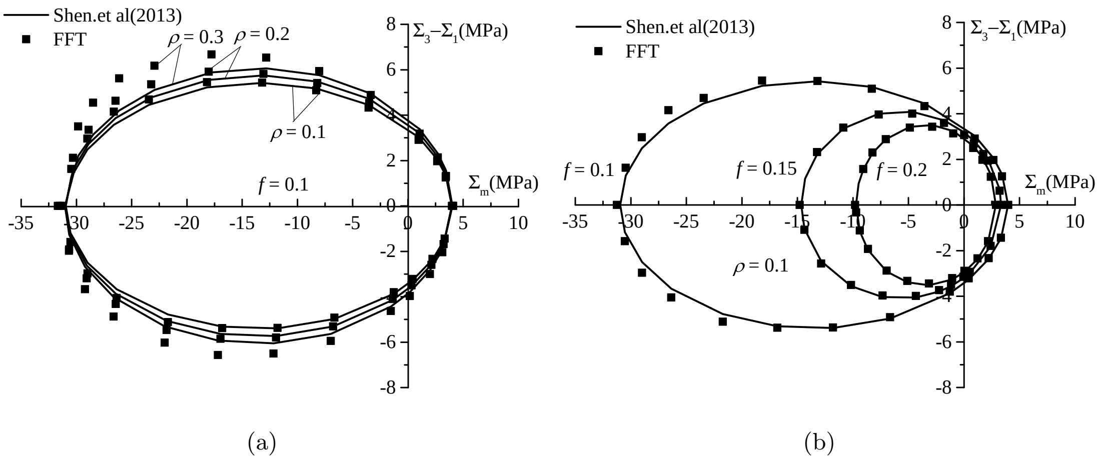

Figure IV .2: Numerically computed yield stresses and analytical yield surfaces:(a) for different values of inclusion volume fraction from 0.1 to 0.3 with $f = 0.1$;(b) for different values of porosity from 0.1 to 0.2 with $\rho = 0.1$

5.1.2 Effect of inclusion stiffness

The influence of inclusion elastic modulus on the macroscopic yield stress is here studied. For this purpose, an elastic soft inclusion with $E_i = 0.01E_s, v_i = v_s$ and the special case with $E_i = 0, v_i = 0$ corresponding to a void have been considered. In Fig.IV .3, the obtained macroscopic yield stresses are compared with those of the porous matrix alone (without inclusion) and of the reference case with hard inclusion. One can see that the yield stress of the material with two populations of pores, respectively at the microscopic scale (porous matrix) and the mesoscopic scale (inclusion with $E_i = 0, v_i = 0$) is much smaller that that of the porous matrix alone. This means that the mesoscopic porosity significantly affects the macroscopic yield stress. However, the difference of yield stress between the soft inclusion $E_i = 0.01E_s, v_i = v_s$ and the hard one $E_i = 20E_s, v_i = v_s$ is relatively small. As the plastic yielding occurs only in the porous matrix, the macroscopic yield stress is mainly related to the evolution of local stress field in the porous matrix.

© 2018 Tous droits réservés. lilliad.univ-lille.fr

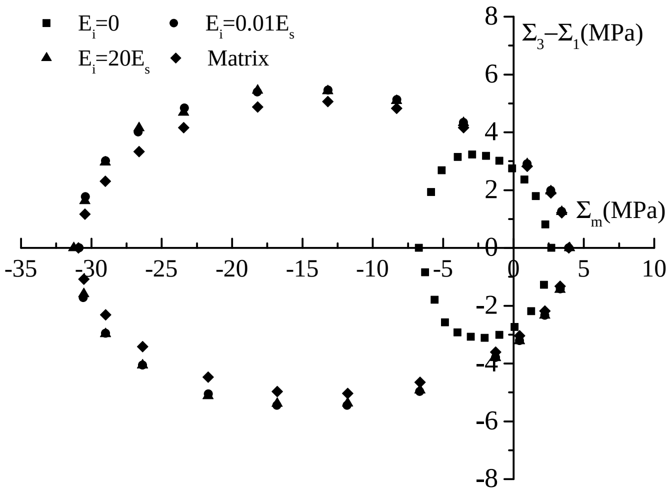

Figure IV .3: Computed yield stresses for different values of elastic modulus of inclusion with $f = 0.1, \rho = 0.1$

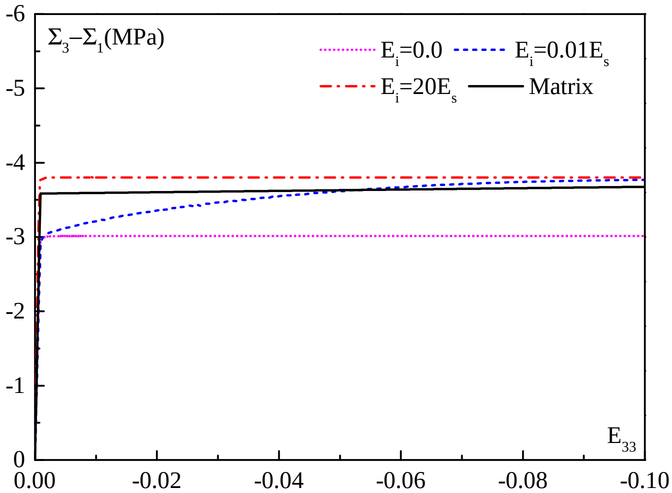

Figure IV .4: Computed macroscopic stress-strain responses for different values of inclusion stiffness with $f = 0.1$ and $\rho = 0.1$, and for the porous matrix alone

In Fig.IV .4, we show the macroscopic stress-strain curves in the uniaxial compression for the different cases studies. It is seen that the material with the soft inclusion $E_i = 0.01E_s$ exhibits a plastic hardening behavior due to the inclusion-matrix interaction. But when the macroscopic plastic yielding is reached at the asymptotic state, the macroscopic yield stress is very close to that obtained for the material with the hard inclusion $E_i = 20E_s$, exhibiting a nearly perfect plastic behavior. Therefore, the decrease of inclusion stiffness enhances the macroscopic plastic ductility of material but not significantly affects the macroscopic yield stress. However, when the inclusion are replaced by void, the macroscopic yield stress is largely reduced because the stress field in the porous matrix is

© 2018 Tous droits réservés.

Thèse de Yajun Cao, Université de Lille, 2018

strongly modified.

5.1.3 Effect of inclusion shape and orientation

To highlight the influence of inclusion shape and orientation, we consider now the unit cells containing a centered inclusion with the volume fraction of $\rho = 0.1$ and the porosity of $f = 0.1$. Both oblate and prolate inclusion with different aspect ratios, $a/c = 2.0 \sim 5.0$ for the oblate and $c/a = 1.25 \sim 2.0$ for the prolate (a and c respectively being the semi-major axis and semi-minor axis of the spheroid) are selected.

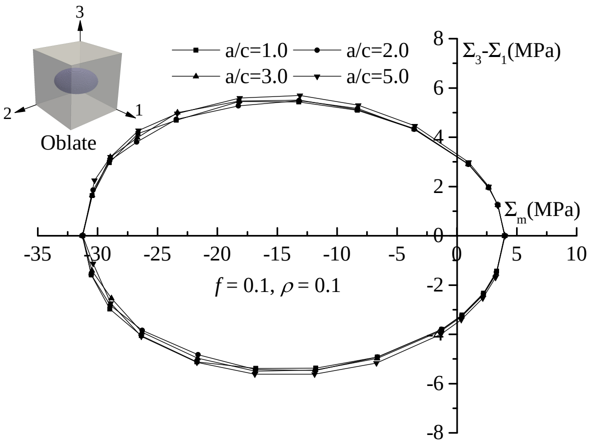

(a)

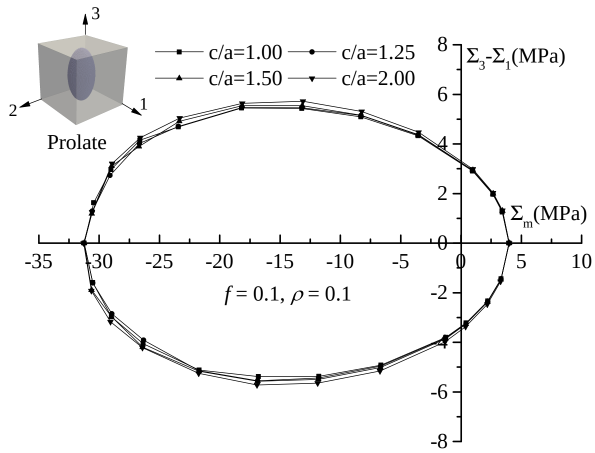

(b)

Figure IV .5: Computed macroscopic yield stress for spheroidal inclusions:(a) Effect of aspect ratio for oblate inclusion;(b) Effect of aspect ratio for prolate inclusion

The computed macroscopic yield stresses are compared with that for the spherical

© 2018 Tous droits réservés. lilliad.univ-lille.fr

Thèse de Yajun Cao, Université de Lille, 2018

inclusion $a/c = 1.0$ in Fig.IV .5. There is no significant difference between two kinds of inclusions on the macroscopic plastic surface. The local stress distributions under uniaxial compression loading are illustrated in Fig.IV .21. Even if the inclusion exhibits an elastic behavior and its elastic stiffness is much higher than that of the matrix which is described by an elastoplastic behavior, it is interesting to see that the stress concentration around the inclusion boundary is not very different between the different inclusion shapes. This result is different with that observed in the pore centered unit cell.

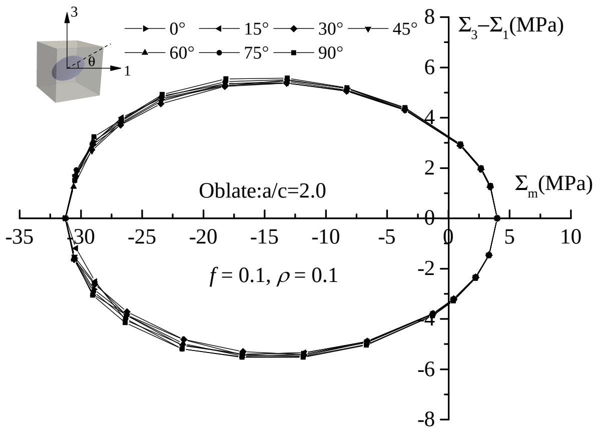

(a) Oblate

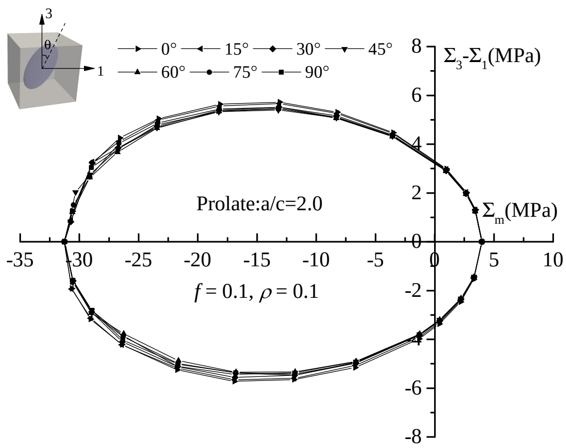

(b) Prolate

Figure IV .6: Effect of inclusion orientation on macroscopic yield stress

For both cases, the shear strength under compressive mean stress is slightly increased with the increasing aspect ratio, especially when the aspect ratio for the oblate inclusion is up to 5.0 or for the prolate reaches 2.0. The hydrostatic compression and tensile strengths are not influenced by the aspect ratio for both kinds of inclusions. These results confirm

© 2018 Tous droits réservés. lilliad.univ-lille.fr

Thèse de Yajun Cao, Université de Lille, 2018

that the macroscopic yield stress is essentially controlled by the yield strength of the porous matrix.

On the other hand, unlike spherical inclusion, for spheroidal inclusion, the macroscopic yield stress should also depend on the orientation of inclusion. For the simplicity, we consider here the unit cell with one centered oblate or prolate inclusion with different orientations. The inclusion orientation is defined by the angle between the major axis of the inclusion and the loading direction and seven different values $\theta = 0°, 15°, 30°, 45°, 60°, 75°, 90°$ are selected. The aspect ratio for is $a/c = 2.0$ for the oblate and $c/a = 2.0$ for the prolate. The computed macroscopic yield stresses are shown in Fig.IV .6(a) and Fig.IV .6(b). It can be seen that the inclusion orientation angle has a small effect on the macroscopic yield stress for both oblate and prolate inclusion. In Fig.IV .7, the evolutions of yield stress under uniaxial compression are presented for the oblate or prolate inclusion. The results confirm that the influence of inclusion orientation is not significant. Nevertheless, there is a small anisotropy of yield strength with the loading orientation. The maximum strength is obtained at $\theta = 0°$ for the prolate inclusion and at $\theta = 90°$ for the oblate one while the minimum strength is obtained for an orientation angle around $\theta = 45°$ for both inclusions.

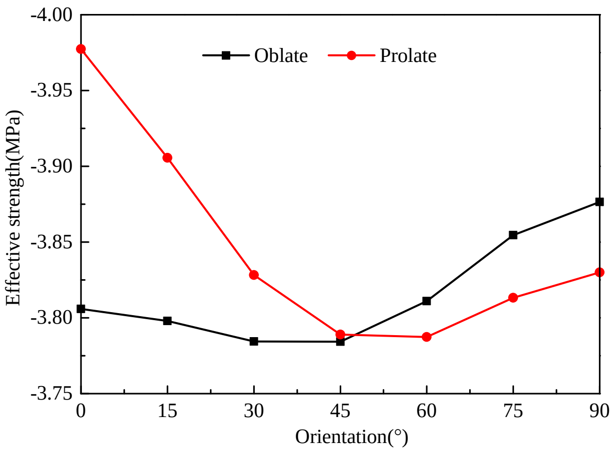

Figure IV .7: Evolution of macroscopic yield stress in uniaxial compression with inclusion orientation

5.2 Assessment of time-dependent deformation

Influences of microstructure on time-dependent deformation at the macroscopic scale are now evaluated. For this purpose, a series of calculations were performed to predict the evolution of axial strain during a uniaxial compression creep test under a constant axial stress of $\Sigma_{33} = -2MPa$. The following model's parameters were used in numerical

© 2018 Tous droits réservés. lilliad.univ-lille.fr

Thèse de Yajun Cao, Université de Lille, 2018

calculations: $\alpha_0 = 0.1, \alpha_m = 0.3, b_1 = 200, h = 10MPa, \eta = 2e10, m = 3, b_{vp} = 60$.

5.2.1 Effects of porosity and inclusion volume fraction

We shall here investigate effects of porosity and inclusion on both instantaneous plastic strains and creep strains using the proposed two-step homogenization method. For this purpose, we will compare numerical results obtained from the present FFT based numerical model and those given by an analytical micro-mechanical model presented in ([Shen et al., 2013,Farhat et al., 2017]). Using a modified secant method, [Shen et al., 2013] have determined a closed form of plastic criterion for rock-like materials composed of a porous matrix and mineral inclusions. As an analytical homogenization solution, spherical pores and inclusions were considered and randomly distributed in a matrix system. As a consequence, only the porosity and inclusion volume fraction are taken into account. Their shape and spatial distribution cannot be taken into account. Further, [Farhat et al., 2017] have studied time-dependent strains by using the homogenized plastic criterion as a viscoplastic loading function. In their study, the viscoplastic flow occurs in the homogenized composite at the macroscopic scale. In the present numerical model, the viscoplastic deformation is attributed to the porous clay matrix and provides a physical interpretation of macroscopic time dependent deformation because the mineral inclusion exhibits an linear elastic behavior.

In Fig.IV .8, we compare the axial strain versus axial stress in the uniaxial compression test between the FFT based numerical model and analytical model. In both models, the plastic criterion for the porous matrix is identical. Therefore, the results coincide for the two models for the case without inclusions $\rho = 0$, as shown in Fig. IV .8(a). With the increase of inclusion fraction, the differences between the two models become more and more large. It seems that the FFT based numerical model predicts a stronger sensitivity to inclusion volume fraction than the analytical one. In Fig. IV .8(b), the comparisons are presented for a given value of inclusion fraction $\rho = 0.1$ but for different values of porosity in the matrix. One can see that due to the different effects of inclusion predicted the two models, the results are different for the case without porosity $f = 0$. However, let look at the relative differences between the different values of porosity for each model. It seems that the relative differences are almost similar for the two models since both of the two models using the same matrix behavior.

© 2018 Tous droits réservés. lilliad.univ-lille.fr

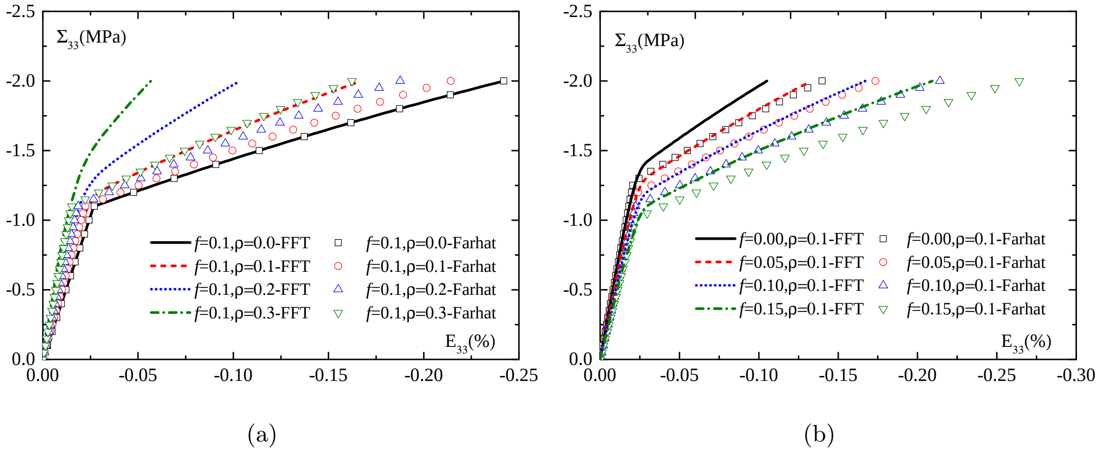

Figure IV .8: Axial strain versus axial stress in uniaxial compression test:(a) influence of volume fraction of inclusion from 0.0 to 0.3 with $f = 0.1$;(b) influence of porosity from 0.0 to 0.15 with $\rho = 0.1$

Therefore, the discrepancies between these two models result from the strong interactions between the inclusion and matrix. The FFT-based method well captures the local non-uniform stress distributions in the matrix. This is the main advantage of the full field numerical method compared with the analytical homogenization approach based on a mean stress field. So the analytical solution is inconsistent with the FFT-based homogenization method for predicting the plastic hardening behavior.

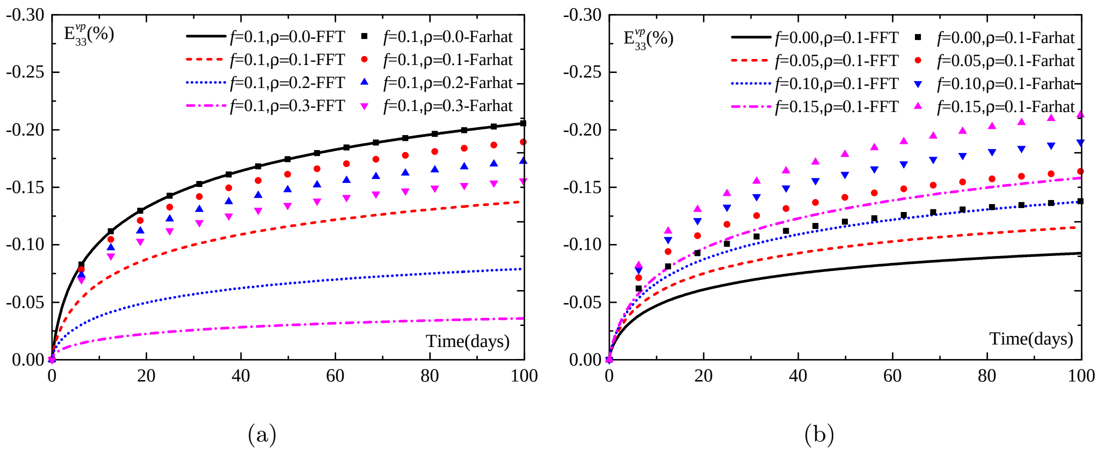

Figure IV .9: Evolutions with time of axial strain in a uniaxial compression creep test: (a) influence of volume fraction of inclusion from 0.0 to 0.3 with $f = 0.1$; (b) influence of porosity from 0.0 to 0.15 with $\rho = 0.1$

© 2018 Tous droits réservés.

In Fig.IV .9, we show the evolutions of axial strain with time for different values of porosity and inclusion volume fraction given by the two methods. One finds logically the same results for the specific case with $\rho = 0$, as shown in Fig.IV .9(a). However, similarly to the instantaneous plastic deformation, the FFT based numerical model depicts a stronger sensitivity of creep strain to the hard inclusion volume fraction. On the other hand, as illustrated in Fig.IV .9(b), the effect of porosity on the creep strain is not very different between the two models.

5.2.2 Effect of inclusion stiffness

In Fig.IV .10, the variations of axial strain with time are presented respectively for the porous matrix alone ($\rho = 0$), the materials with soft or hard inclusion and the material with voids at the mesoscopic scale. Compared with the porous matrix alone, the presence of hard inclusion reduces the evolution of creep deformation while the presence of soft inclusion may slightly enhance the creep deformation. The highest creep deformation is obtained for the material with mesoscopic void. It seems that the presence of even very soft inclusion can prevent the growth of creep deformation in the material.

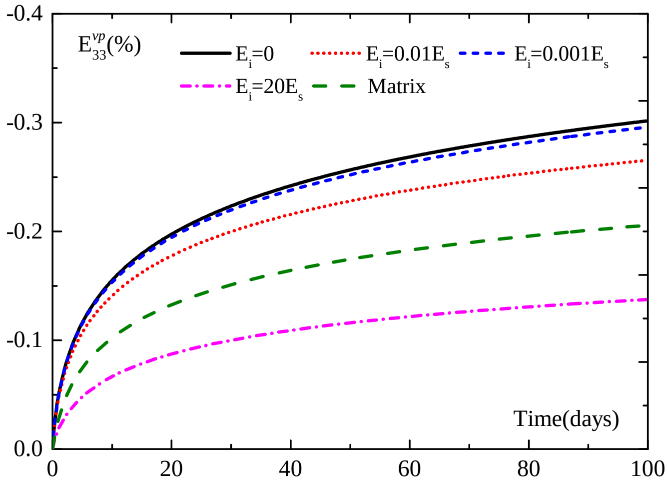

Figure IV .10: Influences of inclusion elastic modulus on macroscopic creep deformation ($f = 0.1, \rho = 0.1$)

5.2.3 Effect of inclusion shape

Computed creep strains for different values of aspect ratio for both oblate and prolate inclusions are presented in Fig.IV .11. Compared with the macroscopic yield stresses given in Fig.IV .5, the influence of inclusion shape on the creep deformation seems to be more important than the macroscopic yield stress. For both types of inclusion, the creep strain

© 2018 Tous droits réservés.

is smaller when the aspect ratio is higher. Further, the creep strain is more sensitive to aspect ratio for the prolate inclusion than for the oblate one.

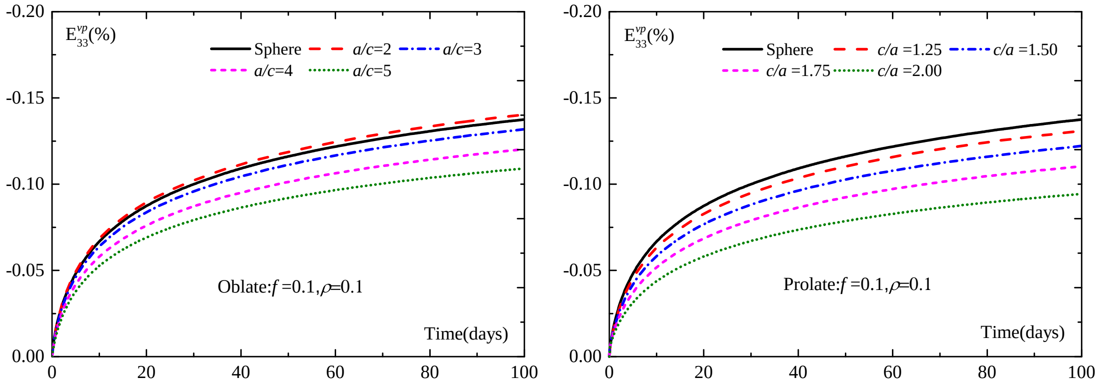

(a) (b)

Figure IV .11: Creep strains with time for different aspect ratios:(a) oblate inclusion; (b) prolate inclusion

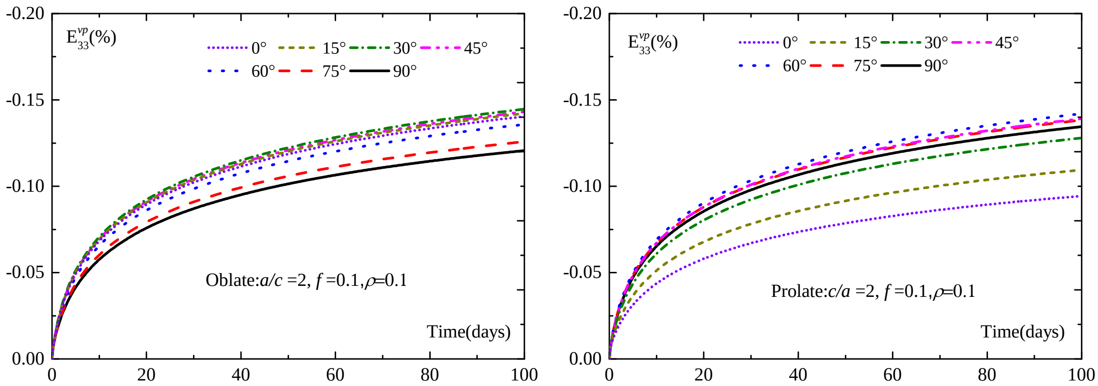

(a) Oblate inclusion $a/c = 2$ (b) Prolate inclusion $c/a = 2$

Figure IV .12: Creep strains with time for different inclusion orientations

5.2.4 Effect of inclusion orientation

The influence of inclusion orientation on creep deformation is finally assessed. The computed creep strains are presented in Fig.IV .12. One can see that the creep strain is dependent on the inclusion orientation. For instance, for the oblate inclusion as shown in Fig.IV .12(a), the maximum creep strain is obtained when the orientation angle is between 30° and 45°. For the prolate inclusion shown in Fig.IV .12(b), the maximum creep strain

© 2018 Tous droits réservés.

is obtained when the orientation angle is between 45° and 60°. This result is in agreement with the variation of macroscopic yield stress with inclusion orientation shown in Fig.IV .6. In order to have a deep insight, in Fig.IV .13 and Fig.IV .14, we show the local creep strain field E_{33}^{vp} in the porous matrix for three different orientation angles, respectively for the oblate and prolate inclusions. It is found that the local creep strain field is largely influenced by the inclusion orientation.

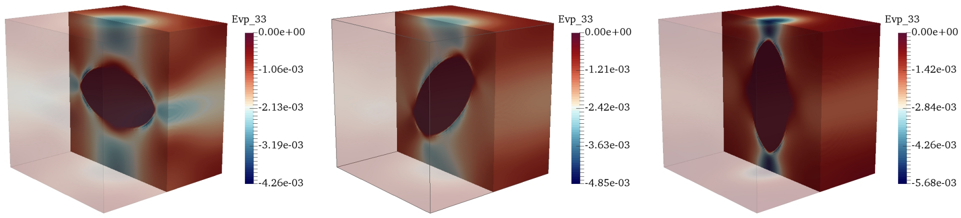

(a) $\theta = 0°$ (b) $\theta = 45°$ (c) $\theta = 90°$

Figure IV .13: Local creep strain field E_{33}^{vp} for the unit cell with oblate inclusion in three different orientations (aspect ratio: $a/c = 2$)

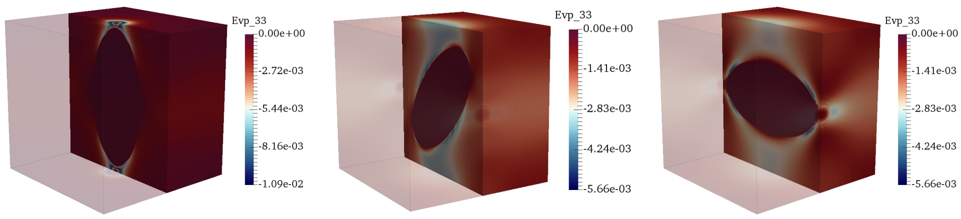

(a) $\theta = 0°$ (b) $\theta = 45°$ (c) $\theta = 90°$

Figure IV .14: Local creep strain field E_{33}^{vp} for the unit cell with prolate inclusion at three different orientations (aspect ratio: $c/a = 2$)

6 Application to claystone

The Callovo-Oxfordian claystone (COx) is investigated in France as a potential geological barrier for the underground disposal of nuclear waste. According to previous studies ([Robinet, 2008, Bornert et al., 2010]), the micro-structure of this material is complex and characterized by several scales. However, as a first approximation, it is reasonable to select two representative scales. At the mesoscopic scale (hundreds of micrometer), the claystone can be seen as a composite material containing a clay matrix in which quartz and calcite grains are embedded. The average mineralogical composition is 40% to 50% for the clay

© 2018 Tous droits réservés.

minerals, 20 to 27% for the quartz and 23 to 25% for the calcite. Some minor minerals are also found. For the studied claystone, at the microscopic scale (below micrometer), the clay matrix is an assemblage of clay particles with intra-particle voids. The majority of pores with an average size of 20nm is inside the clay matrix and the average porosity at the mesoscale is then typically $f = 30\%$. Therefore, with this two scales selected, the micro-structure of COx claystone can be reasonably represented by the unit cell with a total average volume fraction of mineral inclusions $\rho = 0.46$.

Some previous studies have been devoted to micro-mechanical modeling of the COx claystone. In [Guéry et al., 2008] and [Huang et al., 2014], micro-mechanical models have been proposed respectively using Hill's incremental method and incremental variational approach by neglecting porosity inside the clay matrix. In [Shen et al., 2013] and [Shen and Shao, 2016a], improved micro-mechanical models have been developed by taking into account one or two populations of pores. However, in all those analytical or semi-analytical models, it is not possible to evaluate influences of geometrical parameters and spatial distribution of inclusions. In the present study, the FFT based numerical homogenization method is applied to modeling mechanical response of the COx claystone. For this purpose, a random spatial distribution of mineral inclusions in the porous clay matrix is considered and shown in Fig.IV .15. The size of inclusions is also randomly generated in order to approximate the real distribution of quartz and calcite.

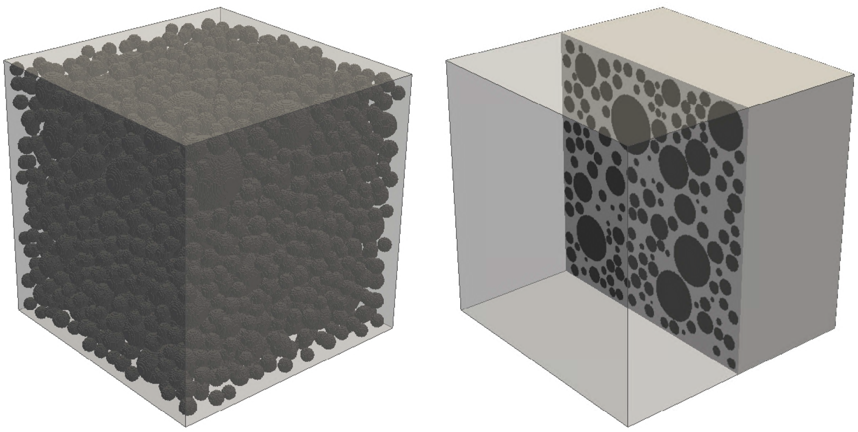

(a) (b)

Figure IV .15: Approximate microstructure of studied claystone:(a)Studied unit-cell with randomly distributed inclusions;(b)Half cross section view of the studied cell.

According to the studies reported in [Jiang and Shao, 2009] and [Shen et al., 2013] on

© 2018 Tous droits réservés. lilliad.univ-lille.fr

Thèse de Yajun Cao, Université de Lille, 2018

the same claystone, the grains of quartz and calcite have very similar elastic properties and can be treated as one equivalent family of inclusions. For instance,the corresponding elastic parameters of the equivalent inclusions are: $E_i = 98GPa$ and $v_i = 0.15$. The typical elastic values of the porous clay matrix have been investigated in [Guéry et al., 2008] and are typically: $E_0 = 3GPa$ and $v_0 = 0.3$. By using an iterative inverse procedure of the Mori-Tanaka homogenization scheme ([Mori and Tanaka, 1973]) and knowing the porosity f of the porous clay matrix, the elastic properties of the solid phase at the microscale are calculated: $E_s = 5.5GPa$ and $v_s = 0.34$. The plastic and viscoplastic parameters are identified by using a numerical optimal fitting method of the experimental data obtained from a triaxial creep test with a confining pressure of 2MPa and a differential stress of 17.45 MPa. However, once the parameters are identified from this particular test, they will be used in the simulations of all other tests with different loading paths and mineralogical compositions. The typical values of parameters obtained are given in Table IV .1.

Table IV .1: Typical values of parameters for COx claystone

Parameter	Clay matrix	Inclusion
Elastic parameters	$E_s = 5.5GPa$, $v_s = 0.34$	$E_i = 98GPa$, $v_i = 0.15$
Plastic parameters	$\alpha_0 = 0.05$, $\alpha_m = 0.38$, $b_1 = 100$ $h = 38MPa$	
Viscoplastic parameters	$\eta = 4.65e10$, $m = 1.3$, $b_{vp} = 22$	
Volume fraction	$f = 0.30$	$\rho = 0.46$

For instance, triaxial compression creep tests with a confining pressure of $2MPa$ and two different levels of differential stress are first studied. Comparisons between numerical results and experimental data are shown in Fig.IV .16 and Fig.IV .17. One can observe a good agreement. On the other hand, two relaxation tests are also investigated. In these tests, the samples are first subjected to a conventional triaxial compression loading until a selected value of differential stress. Then the axial strain is kept constant and the evolution of axial stress is measured. In Fig.IV .18 and Fig.IV .19, one can see that the numerical results well reproduce the experimental data for both tests under different loading conditions.

© 2018 Tous droits réservés. lilliad.univ-lille.fr

Thèse de Yajun Cao, Université de Lille, 2018

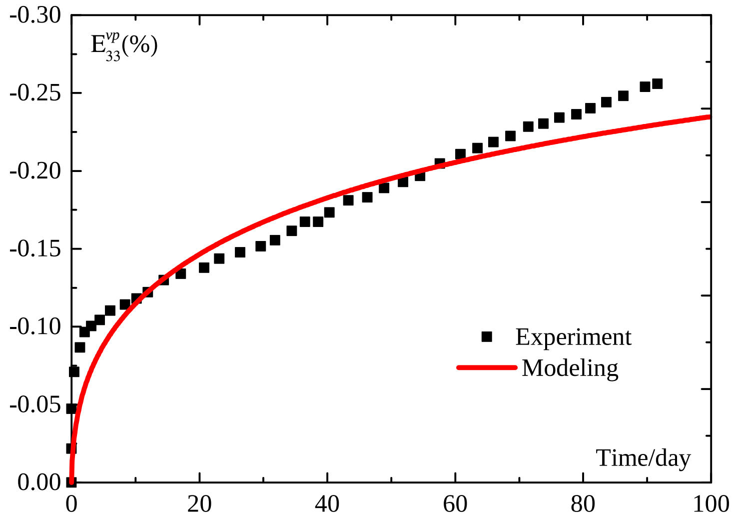

Figure IV .16: Evolution of axial strain with time in a triaxial creep test with a confining pressure of $2MPa$ and a differential stress of $11.5MPa$ on COx claystone (data from [Conil and Armand, 2015])

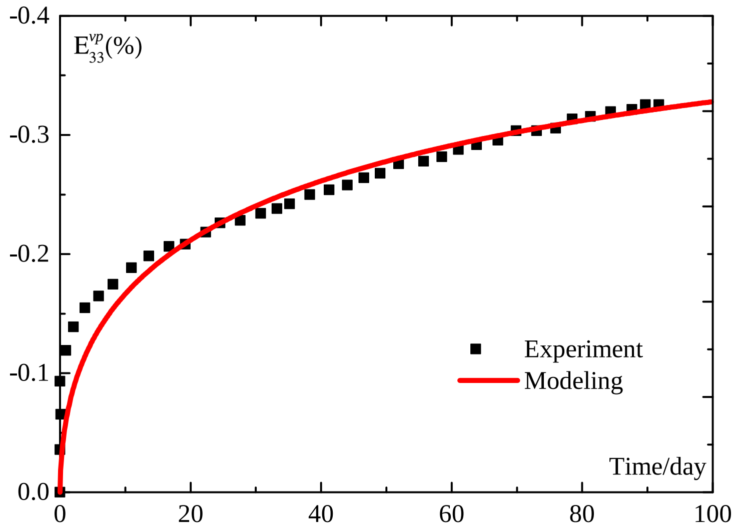

Figure IV .17: Evolution of axial strain with time in a triaxial creep test with a confining pressure of $2MPa$ and a differential stress of $17.45MPa$ on COx claystone (data from [Conil and Armand, 2015])

© 2018 Tous droits réservés. lilliad.univ-lille.fr

Thèse de Yajun Cao, Université de Lille, 2018

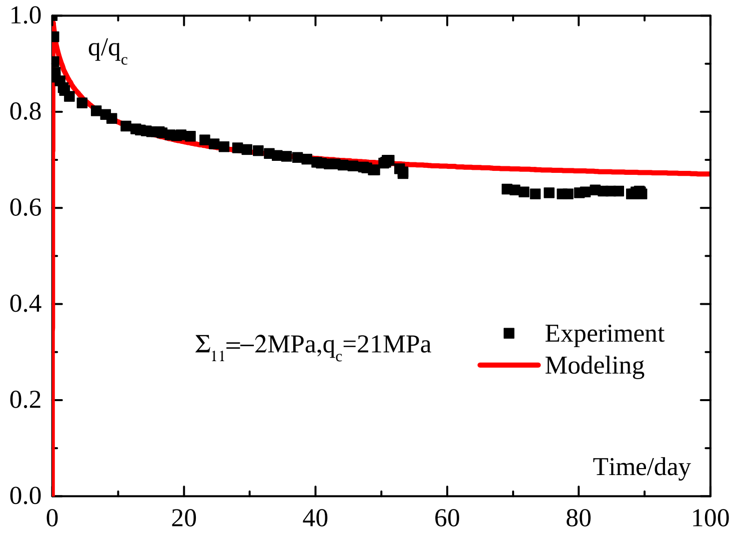

Figure IV .18: Evolution of axial stress with time in a triaxial relaxation test with a confining pressure of $2MPa$ and a differential stress of $21MPa$ on COx claystone (data from [Conil and Armand, 2015])

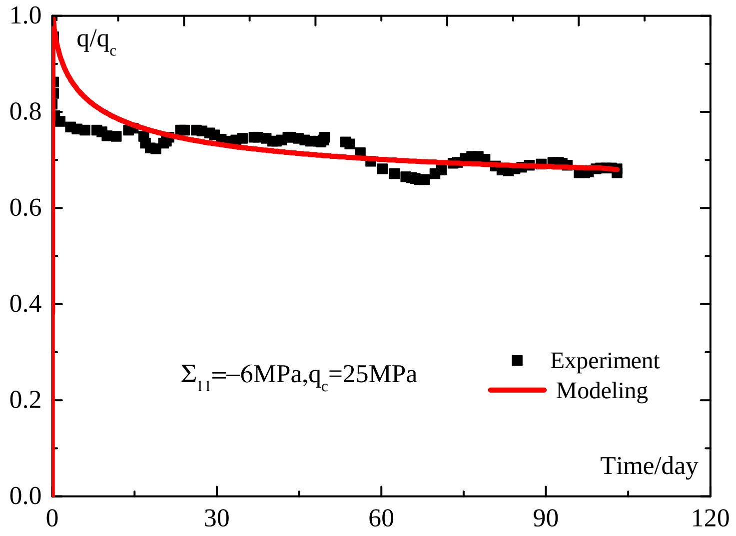

Figure IV .19: Evolution of axial stress with time in a triaxial relaxation test with a confining pressure of $6MPa$ and a differential stress of $25MPa$ on COx claystone (data from [Conil and Armand, 2015])

© 2018 Tous droits réservés. lilliad.univ-lille.fr

Thèse de Yajun Cao, Université de Lille, 2018

7 Concluding remarks

In this paper, we have investigated the influences of inclusion and pores on plastic and viscoplastic behaviors of rock-like materials using a two-scale homogenization method. The effective properties of the porous matrix at the microscopic scale is determined by an analytical homogenized solution, while the effects of inclusion at the mesoscopic scale are investigated with the help of a FFT based numerical homogenization method.

For the purpose of comparison, the macroscopic plastic yield condition has first been studied. The numerical yield stresses are compared with the yield surfaces predicted by an analytical homogenized criterion considering a single spherical inclusion embedded in the porous matrix. It is found that in general the macroscopic yield stress is more sensitive to porosity than inclusion content. The influences of inclusion shape, orientation and stiffness are relatively small on the macroscopic yield stress. However, they can have significant influences on the macroscopic plastic and viscoplastic strains. In particular, the numerical results obtained from the FFT based numerical model considering the plastic and viscoplastic flows in the porous matrix depict a stronger effect of hard inclusion than the analytical homogenized model considering the plastic and viscoplastic flows at the macroscopic scale and neglecting the shape and spatial distribution of inclusions.

The proposed model has also been applied to modeling the time-dependent behavior of COx claystone and was able to correctly reproduce time-dependent strains and stresses respectively in creep and relaxation tests.

© 2018 Tous droits réservés. lilliad.univ-lille.fr

Thèse de Yajun Cao, Université de Lille, 2018

8 Appendix A: Effect of microstructure with different inclusion distributions

In this section, the effects of microstructure with different inclusion distributions are studied, especially with a cubic array of inclusions and a random distribution of inclusions. In order to reduce the influence of the spatial discretization, the same inclusion number N and size are considered in two micro-structures ($N = 27$, $N = 125$, respectively). As illustrated in Fig.IV .20, one can find that no significant effects caused by the cubic array or random distribution of inclusions are observed from the results. In order to better illustrate the effects of inclusion volume fraction, stiffness, shape and orientation, the periodic unit cell with one centered single inclusion has been used for the simulations of sensitive studies.

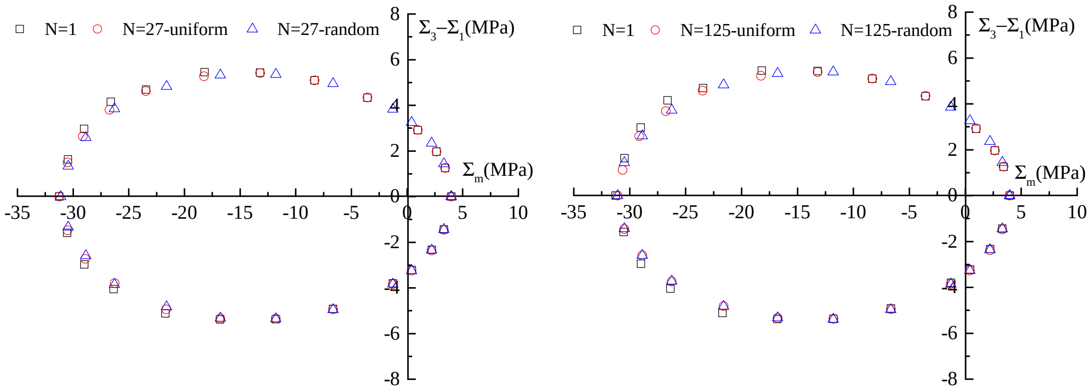

(a) $N = 27$ (b) $N = 125$

Figure IV .20: Comparisons of effective plastic surfaces between microstructure with random distributed and cubic array distributed inclusions vs one centered inclusion ($f = 0.1, \rho = 0.1$).

9 Appendix B: Local stress distribution under uniaxial compressive loading

With the help of the developed numerical method, the local stress distributions at 33-direction in the uniaxial compression test subjected a macroscopic strain $E_{33} = -0.01$ for micro-structures with different inclusion shapes are shown in Fig.IV .21. It is found that there is not a significant difference of stress concentration around the interfaces between the inclusion and matrix.

© 2018 Tous droits réservés. lilliad.univ-lille.fr

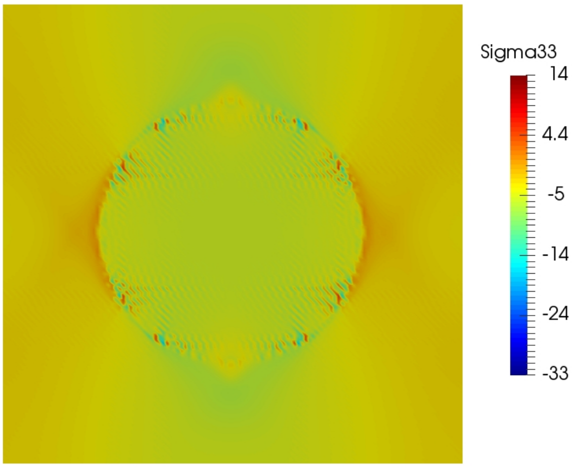

(a) Sphere $a/c = 1$

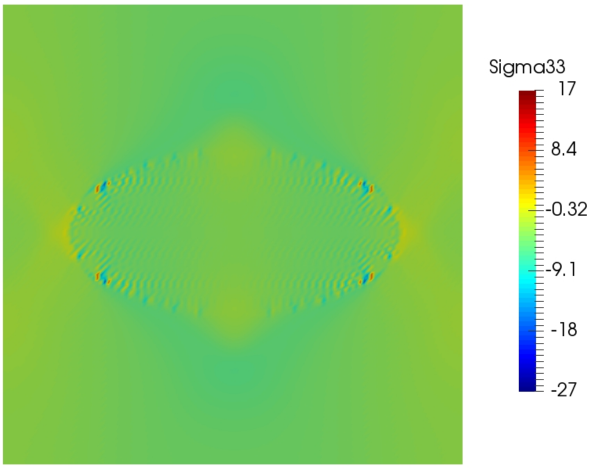

(b) Oblate $a/c = 2$

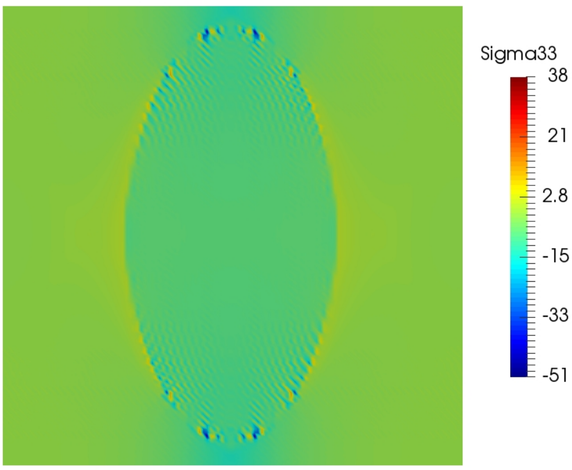

(c) Prolate $a/c = 1/2$

Figure IV .21: Comparisons of stress distribution for microstructure with different shape of inclusion under uniaxial compression test ($f = 0.1, \rho = 0.1$): oblate $a/c = 2$; prolate $c/a = 2$

© 2018 Tous droits réservés. lilliad.univ-lille.fr

Thèse de Yajun Cao, Université de Lille, 2018

© 2018 Tous droits réservés. lilliad.univ-lille.fr

Chapter V

A numerical damage model for geomaterials with pores and inclusions

Contents

© 2018 Tous droits réservés.

Thèse de Yajun Cao, Université de Lille, 2018

Summary

This chapter aiming at establishing an elastoplastic damage model to determine the macroscopic mechanical behavior for the geomaterials containing complex multi-scale features. To this end, inspired by the work of [Maghous et al., 2009] and [Shen and Shao, 2016a], a general strength criterion considering the elliptic form porous matrix and randomly distributed rigid inclusions is obtained by using a three step homogenization procedure. Typically, macroscopic mechanical behaviors observed in geomaterial always include strain softening. For this reason, it is assumed that the rock failure is a time-dependent progressive damage process, we introduce a rate-dependent damage model to describe the degradation effect on the elastic and plastic behavior. Then, by means of a new explicit integration algorithm for the damage solver, we successfully apply this damage constitutive relation on the claystone with two population of pores and rigid inclusions embedded at separated scales. Meanwhile, the developed model also provides a well extension on Vaca Muerta shale rock to account for the effect of two population of inclusions configured in a porous matrix. The comparisons between the simulation modeling and experimental data for these two applications are in good agreement. The results show that the validity of the proposed model which can take the effect of both the mineralogical compositions and porosity as well as the damage properties into account on the macroscopic behavior for porous geomaterials with multi-scale characters.

1 Introduction

Geomaterials have significant multi-scale characters. By using X-ray micro-tomography technique, the microstructural heterogeneity can be quantified at different length scales though characterizing its mineral compositions, pore structure characters, geometry and connectivity. For example, the Callovo-Oxfordian argillite is selected as the host formation for installation of a underground radioactive waste disposal facility in France, its mineralogy is mainly composed of clay minerals (mainly illite and interstratified illite/smectite), carbonates, and tectosilicates ([Robinet et al., 2012]). The pore structure is mainly observed in clay matrix having heterogeneous and complex pore spaces with sizes ranging $1nm$ to $100\mu m$ over multi-scales ([Robinet, 2008, Cariou et al., 2013]). Even though the detailed characters can be captured by combined X-ray technique and bulk chemical analysis procedure on COx samples, it still exists challenges to understand the roles of these heterogeneities across several length scales playing on macroscopic behavior.

It has long been recognized that the macroscopic mechanical behaviors of geomate-

© 2018 Tous droits réservés. lilliad.univ-lille.fr

Thèse de Yajun Cao, Université de Lille, 2018

rials is closely interlinked with its mineralogical compositions as well as pore characters beacause they might undergo different deformation processes. Experimental studies have revealed a correlation of several mineralogical and textural characteristics such as quartz content and porosity with the physical and mechanical properties of rocks ([Tu u grul and Zarif, 1999, Tandon and Gupta, 2013, Baud et al., 2014, Heidari et al., 2014, Ündül, 2016]). The inter relationships among mineral constituents, various textural parameters and unconfined compressive strength are preliminary established by simple regression analyses. On the other hand, in the framework of micromechanics, a plenty of research works have been focused on analytical strength homogenization theories of materials involving three-scale microstructure for double porous materials and porous materials contained rigid inclusions using a two-step homogenization procedure ([Garajeu and Suquet, 1997, Vincent et al., 2009a, Vincent et al., 2014b, Shen et al., 2013, Shen et al., 2014]). Thus, the effective plastic flow is mainly determined by the porosity and inclusion volume fraction. As an alternative way to consider the down-scale geometrical characters of inclusions and pores, combining closed-form solutions at the microscopic scale (eg. [Gurson, 1977, Maghous et al., 2009]) and computational homogenization methods at the mesoscopic scale such as the Finite Element Method ([Khdir et al., 2014, Julien et al., 2011, Vincent et al., 2009b]) and Fast Fourier Transform homogenization ([Moulinec and Suquet, 1994, Vincent et al., 2014a, Cao et al., 2018a, Cao et al., 2018b]), also provides well estimations for macroscopic mechanical properties to account for the interactions between different compositional configurations and geometrical features. Further, [Shen and Shao, 2016a] developed an incremental micro-macro model for porous geomaterials with double porosity and inclusion. This semi-analytical method still requires to adopt an isotropization technique for tangent operator of the matrix.

At the current state-of-the-art, multi-scale homogenization models on strength theories and computational techniques have been successfully applied to predict the macroscopic yield stress of materials having complex microstructure. However, it still needs to deal with the behaviors exhibiting the degradation of materials and its damage failure. Generally, the damage always incorporate with macroscopic phenomenological plastic model ([Shao et al., 2003, Shao et al., 2006, Salari et al., 2004, Zhou et al., 2008b, Parisio and Laloui, 2017, Huang et al., 2018]), in which the whole mechanical behavior is derived from thermodynamic potentials. The damage evolution is generally associated with the accumulation of irreversible plastic strains. In recent years, micromechanical approaches have attracted strong attentions on relating the macroscopic behaviors of the material to its microstructure characteristics like unilateral effects due to cracks' closure, damage-friction

© 2018 Tous droits réservés. lilliad.univ-lille.fr

Thèse de Yajun Cao, Université de Lille, 2018

coupling, induced anisotropy of microcracks and fluid filled crack ([Zhu et al., 2009, Xie et al., 2012, Qi et al., 2016, Zhu et al., 2016, Zhu and Shao, 2017]). In this framework, the failure of geomaterials is driven by the cracks-related dissipation mechanisms, owing to two dissipative processes: damage by cracking and inelastic deformation due to frictional sliding.

In the present study, we are aiming to develop a general criterion to account for the geomaterials contained pores and rigid inclusions across four length scales. More specially, the solid matrix is considered as cohesive-frictional material represented by a Drucker-Prager type strength criterion. Inspired by the work of [Maghous et al., 2009] and [Shen and Shao, 2016a], a three-step homogenization procedure is employed by using the modified secant method to homogenize the highly heterogenous materials. Due to the fact that the macroscopic inelastic deformation is mainly induced by the solid matrix, and the inclusions just behavior elastic. Therefore, in order to capture the failure behavior of geomaterials, a time-dependent damage behavior is introduced here to associate with the elastic and plastic properties of solid matrix. Finally, a multi-scale damage model is developed here and applied to simulate the macroscopic mechanical behaviors of typical claystone and shales with different microstructure.

2 Microstructure with multiscale characters

For the highly heterogenous geomaterials, pores and mineral inclusions might be respectively distributed at multi-scales with different length scales. In this study, the material contained four-scale characters is considered here. As a typical multiscale material like claystone, it is characterized as a porous matrix-inclusion system. Within the clay matrix, the pore network is composed of inter-particle and intra-particle pores with diameters ranging between 1 nm and a few hundreds of nanometers ([Robinet et al., 2012, Shen and Shao, 2016a]). Following a multi-scale thought, a representative volume element(RVE) is chosen here as illustrated in Fig.V .1 to be statistically representative of this class of medium. For the sake of simplicity, it is assumed that all the families of inclusions and pores at different scales are of spherical form. Let us denote ω the total volume of the studied unit cell composed of porous matrix and inclusions with the volume of ω_m and ω_i; ω_s denotes the domain occupied by the solid phase in porous matrix; ω_1 and ω_2 are the volumes of small and large pores located at the particles and porous matrix, respectively. With these notations, the volume fraction of inclusions ρ, the porosity f at the particle, the one ϕ at the porous matrix and the total porosity Γ at the macroscopic scale can be

© 2018 Tous droits réservés. lilliad.univ-lille.fr

Thèse de Yajun Cao, Université de Lille, 2018

given as:

$$\rho = \frac{\omega_i}{\omega}, \quad f = \frac{\omega_1}{\omega_s + \omega_1}, \quad \phi = \frac{\omega_2}{\omega_m} = \frac{\omega_2}{\omega_s + \omega_1 + \omega_2}$$
$$\Gamma = \frac{\omega_1 + \omega_2}{\omega} = [f(1-\phi) + \phi](1-\rho) \tag{V .1}$$

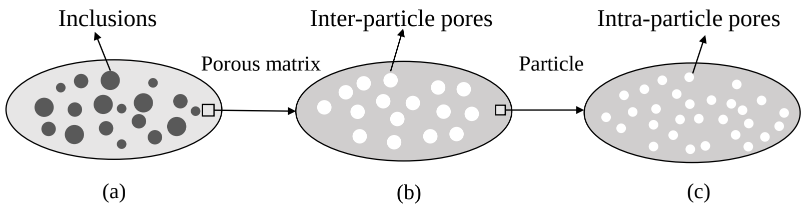

Figure V .1: Representative volume element of studied rock-like materials

3 Micro-macro constitutive formulation

3.1 Macroscopic criterion

As mentioned above, the porous matrix is composed of a solid phase and spherical pores at two different scales. Compared with metal materials, the pressure sensitivity and volumetric deformation are two crucial characteristics of rock-like materials. In order to consider these aspects, the solid phase is assumed to obey to a Drucker-Prager type plastic criterion:

$$F^s = \tilde{\sigma}_d + \alpha(\tilde{\sigma}_m - h) \leq 0 \tag{V .2}$$

in which $\tilde{\boldsymbol{\sigma}}$ denotes the stress tensor of the solid phase. $\tilde{\sigma}_m = tr\tilde{\boldsymbol{\sigma}}/3$ is the mean stress. $\tilde{\sigma}_d$ is the equivalent stress defined as $\tilde{\sigma}_d = \sqrt{\tilde{\boldsymbol{\sigma}}' : \tilde{\boldsymbol{\sigma}}'}$, with $\tilde{\boldsymbol{\sigma}}'$ being the deviatoric stress tensor. The parameter α is the frictional coefficient and h the yield stress under hydrostatic tension of the solid phase.

As illustrated in Figure V .1, the porous matrix is divided into two scales with different sizes of pores. With a Drucker-Prager type solid matrix containing spherical voids, an analytical yield criterion has been derived by using a modified secant method in [Maghous et al., 2009] :

$$F^p = \frac{1 + 2f/3}{\alpha^2}\tilde{\tilde{\sigma}}_d^2 + (\frac{3f}{2\alpha^2} - 1)\tilde{\tilde{\sigma}}_m^2 + 2(1-f)h\tilde{\tilde{\sigma}}_m - (1-f)^2h^2 \leq 0 \tag{V .3}$$

Where $\tilde{\tilde{\sigma}}_d$ and $\tilde{\tilde{\sigma}}_m$ correspond to the equivalent stress and mean stress of particles. This criterion (V .3) explicitly depends on the porosity f and the pressure sensitivity parameter α of the solid phase. Moreover, inspired by the work of [Maghous et al., 2009], [Shen and

© 2018 Tous droits réservés. lilliad.univ-lille.fr

Thèse de Yajun Cao, Université de Lille, 2018

Shao, 2016a] proposed a close-form plastic yield criterion for the porous matrix with double porosities by using a two-step nonlinear homogenization procedure. The obtained criterion is described in an elliptic form which will be useful here to formulate by a general expression reading:

$$F^{mp} = A\sigma_d^2 + B\sigma_m^2 + C\sigma_m - D \leq 0 \tag{V .4}$$

with following parameters:

$$\begin{aligned} &A = \frac{1+2f/3}{\alpha^2}(\frac{6\alpha^2-13f-6}{4\alpha^2-12f-9}\phi+1), \quad B = \frac{3/2+f}{\alpha^2}\phi + \frac{3f}{2\alpha^2} - 1 \\ &C = 2(1-f)(1-\phi)h, \quad D = (1-\phi)^2(1-f)^2h^2 \end{aligned} \tag{V .5}$$

As done in the study of [Shen and Shao, 2016a], the criterion (V .4) will be directly used here to take in account the plastic behavior of porous matrix with double porosities for the first two homogenization procedures. We now then aim at deriving a close-form criterion to consider the effects of inclusions for the third step homogenization. It is convenient to recall the modified secant method following an associated flow rule to determine the local plastic strain rate of porous matrix by the relation $\boldsymbol{d} = \dot{\lambda}\frac{\partial F^{mp}}{\partial \boldsymbol{\sigma}}$. So the strain rate of the porous matrix is governed by:

$$\boldsymbol{d} = \frac{1}{A}\frac{d_d}{2\sigma_d}(2A\boldsymbol{\sigma}' + \frac{2B\sigma_m}{3}\mathbf{1} + \frac{C}{3}\mathbf{1}) \tag{V .6}$$

$$d_m = \frac{1}{A}\frac{d_d}{2\sigma_d}[\frac{2\sigma_m}{3}B + \frac{C}{3}] \tag{V .7}$$

According to (V .4),(V .6) and (V .7), one has:

$$\frac{d_d}{\sigma_d} = \sqrt{\frac{A^2d_v^2 + ABd_d^2}{BD + \frac{C^2}{4}}} \tag{V .8}$$

in which $d_d = \sqrt{\boldsymbol{d}' : \boldsymbol{d}'}$ and $\boldsymbol{d}' = \boldsymbol{d} - d_m\mathbf{1}$. Hence the support function defined as $\pi_{mp} = \boldsymbol{\sigma} : \boldsymbol{d}$ can be written in the following form:

$$\pi_{mp} = -\frac{C}{2B}d_v + \sqrt{\frac{4BD + C^2}{4AB}}\sqrt{\frac{A}{B}d_v^2 + d_d^2} \tag{V .9}$$

where $d_v = tr\boldsymbol{d}$ is the volumetric deformation in the porous matrix.

The determination of the local stress-strain relationship of porous matrix achieved by the support function π_{mp} can be put in following form with:

$$\boldsymbol{\sigma} = \frac{\partial \pi_{mp}}{\partial \boldsymbol{d}} = 2\mu^{mp}\boldsymbol{d}' + k^{mp}d_v\mathbf{1} + \sigma^p\mathbf{1} \tag{V .10}$$

© 2018 Tous droits réservés. lilliad.univ-lille.fr

Thèse de Yajun Cao, Université de Lille, 2018

with following secant bulk and shear moduli and isotropic pretress:

$$k^{mp} = \frac{A}{B}\frac{N}{M}, \quad 2\mu^{mp} = \frac{N}{M}, \quad \sigma^p = -\frac{C}{2B}$$
$$M = \sqrt{\frac{A}{B}d_v^2 + d_d^2}, \quad N = \sqrt{\frac{4BD + C^2}{4AB}} \tag{V .11}$$

The secant moduli in (V .11) are non-uniform which is related to the non-uniform local strain rate $\boldsymbol{d}$ of the porous matrix. As done in [Maghous et al., 2009], the average of $\boldsymbol{d}$ over the porous matrix is appropriate as the effective stain rate $\boldsymbol{d}_{eff}$ to consider the effect of loading history on the nonlinear plastic properties which can be taken in the following form:

$$d_v^{eff} = \sqrt{\langle d_v^2 \rangle_{\omega_m}}, \quad d_d^{eff} = \sqrt{\langle d_d^2 \rangle_{\omega_m}} \tag{V .12}$$

Therefore, the approximated stress-stain relation can be expressed as:

$$\boldsymbol{\sigma} = \mathbb{C}^{mp}(d_v^{eff}, d_d^{eff}) : \boldsymbol{d} + \sigma_{eq}^p \mathbf{1}; \quad \mathbb{C}^{mp}(d_v^{eff}, d_d^{eff}) = 3k_{eq}^{mp}\mathbb{J} + 2\mu_{eq}^{mp}\mathbb{K}; \quad \sigma_{eq}^p = \sigma^p \tag{V .13}$$

Owing to the assumption of rigid inclusions, the macroscopic prestress simply reads $\Sigma^p = \sigma_{eq}^p$, considering the effective thermodynamic potential of the composite with the form of:

$$W = \frac{1}{2}\boldsymbol{D} : \mathbb{C}^{hom} : \boldsymbol{D} + \Sigma^p tr\boldsymbol{D} \tag{V .14}$$

the corresponding state equations can be deduced as:

$$\Sigma_m = k^{hom}(\boldsymbol{D}_v + \Sigma^p); \quad \Sigma_d = 2\mu^{hom} D_d \tag{V .15}$$

Following the study of [Barthélémy and Dormieux, 2004], the macroscopic free energy in the r.v.e. is associated with the effective strain rate of porous matrix, which is given by:

$$\frac{1}{2}(1-\rho){d_v^{eff}}^2 = \frac{1}{2}\frac{\partial k^{hom}}{\partial k_{eq}^{mp}} D_v^2 + \frac{\partial \mu^{hom}}{\partial k_{eq}^{mp}} D_d^2$$
$$\frac{1}{2}(1-\rho){d_d^{eff}}^2 = \frac{1}{2}\frac{\partial k^{hom}}{\partial \mu_{eq}^{mp}} D_v^2 + \frac{\partial k^{hom}}{\partial \mu_{eq}^{mp}} D_d^2 \tag{V .16}$$

To consider the interaction of randomly rigid inclusions, the Mori-Tanaka method is adopted here to describe the effective elastic moduli which reads:

$$k^{hom} = \frac{3k_{eq}^{mp} + 4\rho\mu_{eq}^{mp}}{3(1-\rho)}$$
$$\mu^{hom} = \mu_{eq}^{mp}\frac{k_{eq}^{mp}(6+9\rho) + \mu_{eq}^{mp}(12+8\rho)}{6(1-\rho)(k_{eq}^{mp} + 2\mu_{eq}^{mp})} \tag{V .17}$$

© 2018 Tous droits réservés. lilliad.univ-lille.fr

Combing (V .11),(V .15),(V .16) and (V .17), the generalise approximate macroscopic criterion of the composite constituted of porous matrix and rigid matrix can take the following form:

$$\frac{A+\frac{2B\rho}{3}}{1+\frac{3\rho}{2}-\frac{5\rho}{6(\frac{A}{B}+1)}}\Sigma_d^2+B\Sigma_m^2+C\Sigma_m-(D+\frac{4BD+C^2}{6A}\rho)=0 \tag{V .18}$$

3.2 Evolution of double porosities

In experimental rock deformation, the pore space undergoes significant inelastic compaction or dilatant while the rock strain hardens or softens. For instance, porosity reduction has been observed on porous rock for hydrostatic experiments ([Baud et al., 2006,Baud et al., 2009]). This phenomenon is often arised from the interplay of a diversity of micromechanical processes related to the evolution of microstructure. Actually it is responsible for the macroscopic mechanical responses. In this section, we shall consider the variation of inter-porosity and intra-porosity. To this end, it is assumed that the pore volume change only depends on plastic pore compaction or dilation. The nucleation of new pores is not considered here. According to the first term of (V .1), one has:

$$\dot{f}=d(\frac{\omega_1}{\omega_s+\omega_1})=(1-f)(\frac{d\omega_s+d\omega_1}{\omega_s+\omega_1}-\frac{d\omega_s}{\omega_s}) \tag{V .19}$$

$$\dot{\phi}=d(\frac{\omega_2}{\omega_s+\omega_1+\omega_2})=(1-\phi)(\frac{d\omega_m}{\omega_m}-\frac{d\omega_s+d\omega_1}{\omega_s+\omega_1}) \tag{V .20}$$

in which $\frac{d\omega_s}{\omega_s}$ and $\frac{d\omega_s+d\omega_1}{\omega_s+\omega_1}$ correspond to the average volumetric strain rate of solid phase ($\tilde{d}_v$) and porous particle ($\tilde{\tilde{d}}_v$), respectively. Then $\frac{d\omega_m}{\omega_m}$ denotes the volumetric strain rate of the double porous matrix (d_v). It is assumed that the solid phase is described by a Drucker-Prager type criterion and an associate plastic flow rule. Thus, the microscopic strain rate $\boldsymbol{d}$ can be calculated by:

$$\boldsymbol{d}=\dot{\Lambda}\frac{\partial\Phi}{\partial\boldsymbol{\sigma}};\quad \boldsymbol{d}'=\dot{\Lambda}\frac{\boldsymbol{\sigma}'}{\sigma_d};\quad d_m=\frac{1}{3}\dot{\Lambda}T \tag{V .21}$$

where $\boldsymbol{d}'$ is the deviatoric strain rate tensor with $\boldsymbol{d}=\boldsymbol{d}'+d_m\boldsymbol{\delta}$. $\dot{\Lambda}$ is the plastic multiplier of the solid phase. The equivalent plastic strain rate $\dot{\epsilon^p}$ takes the following form:

$$\dot{\epsilon^p}=\sqrt{\boldsymbol{d}':\boldsymbol{d}'}=\dot{\Lambda} \tag{V .22}$$

Owing to the energy-based equivalence condition introduced by [Gurson, 1977], it is possible to associate the macroscopic plastic strain rate with that of the solid phase ([Shen et al., 2012a]), that is:

$$\boldsymbol{\Sigma}:\boldsymbol{D}^p=\frac{1}{\omega}\int_{\omega_s}\tilde{\boldsymbol{\sigma}}:\tilde{\boldsymbol{d}}dV=\frac{1}{\omega}\int_{\omega_s}\dot{\epsilon^p}(\tilde{\sigma}_d+\alpha\tilde{\sigma}_m)dV=(1-\rho)(1-\phi)(1-f)\alpha h\dot{\epsilon^p} \tag{V .23}$$

© 2018 Tous droits réservés. lilliad.univ-lille.fr

Thèse de Yajun Cao, Université de Lille, 2018

Therefore $\dot{\epsilon^p}$ is obtained by:

$$\dot{\epsilon^p} = \frac{\boldsymbol{\Sigma} : \boldsymbol{D^p}}{(1-\rho)(1-\phi)(1-f)\alpha h} \tag{V .24}$$

On the other hand, for the porous matrix, similarly has:

$$\boldsymbol{\Sigma} : \boldsymbol{D}^p = \frac{1}{\omega}\int_{\omega_s+\omega_1} \tilde{\tilde{\boldsymbol{\sigma}}} : \tilde{\tilde{\boldsymbol{d}}} dV = \frac{1}{\omega}\int_{\omega_s+\omega_1} \frac{\alpha^2}{1+\frac{2}{3}f}\frac{\tilde{\tilde{d}}_d}{2\tilde{\tilde{\sigma}}_d}[(1-f)^2h^2 - 2(1-f)h\tilde{\tilde{\sigma}}_m]dV \tag{V .25}$$

One can obtain:

$$\frac{\tilde{\tilde{d}}_d}{\tilde{\tilde{\sigma}}_d} = \frac{(1+\frac{2f}{3})}{\alpha^2}\frac{2\boldsymbol{\Sigma} : \boldsymbol{D}^p}{(1-\rho)(1-\phi)[(1-f)^2h^2 - 2(1-f)h\tilde{\tilde{\sigma}}_m]} \tag{V .26}$$

$$\tilde{\tilde{d}}_v = \frac{(\frac{3f}{2\alpha^2}-1)\frac{2\Sigma_m}{(1-\rho)(1-\phi)} + 2(1-f)h}{(1-f)^2h^2 - 2(1-f)h\frac{\Sigma_m}{(1-\rho)(1-\phi)}}\frac{\boldsymbol{\Sigma} : \boldsymbol{D}^p}{(1-\rho)(1-\phi)} \tag{V .27}$$

With the relations (V .21) and (V .22) in hand, the plastic dilation rate is related to the equivalent plastic strain rate by $\tilde{d}_v = \alpha\dot{\epsilon^p}$. The variation of porosity in (V .19) can be determined from the following kinematical compatibility condition:

$$\dot{f} = (1-f)(\tilde{\tilde{d}}_v - \alpha\dot{\epsilon^p}) \tag{V .28}$$

$$\dot{\phi} = (1-\phi)(\frac{tr\boldsymbol{D^p}}{1-\rho} - \tilde{\tilde{d}}_v) \tag{V .29}$$

3.3 Evolution of damage

Inspired by the work of [Shao et al., 2003] and [Pietruszczak et al., 2004], the evolution of microstructure is also a time dependent progressive damage process, which can be quantified by a damage variable ζ associated with microstructure equilibrium state for a prescribed loading history. As a consequence of microcracking, dislocation and so on during the whole deformation process, it requires that when the $t \to \infty$, the microstructure evolution reaches to a self-equilibrated state with $\zeta = \bar{\zeta}$, which $\bar{\zeta}$ devotes to a stationary state corresponding to the microstructure equilibrium. Thus the description of damage evolution can be expressed in a rate-dependent form with:

$$\dot{\zeta} = \gamma(\bar{\zeta} - \zeta) \tag{V .30}$$

where γ is a material constant that control the rate of damage evolution. Then $\bar{\zeta} \in [0,1]$, $\zeta \in [0,\bar{\zeta}]$. Combining the Laplace transforms and convolution theorem, then taking $\zeta(0) = 0$, thus the function ζ can be formulated as:

© 2018 Tous droits réservés. lilliad.univ-lille.fr

Thèse de Yajun Cao, Université de Lille, 2018

$$\zeta(t) = \int_0^t \gamma\bar{\zeta}(\tau)e^{-\gamma(t-\tau)}d\tau \tag{V .31}$$

To solve the time-dependent variable ζ, [Zhao et al., 2016] has obtained a fast explicit integral algorithm by using the rectangular integration rule. In this study, we will use a trapezoid rule to get a new accurate estimate. The detailed derivation of integration solver is presented in Appendix A. For a time increment Δt_{n+1}, the variable ζ at t_{n+1} step is taken in the following form:

$$\zeta_{n+1} = \frac{\gamma}{2}\bar{\zeta}_{n+1}\Delta t_{n+1} + (\zeta_n + \frac{\gamma}{2}\bar{\zeta}_n\Delta t_{n+1})e^{-\gamma\Delta t_{n+1}} \tag{V .32}$$

In the present study, the parameter $\bar{\zeta}$ for stationary state of microstructure evolution is given as:

$$\bar{\zeta} = \frac{\bar{\alpha}}{\alpha_m} \tag{V .33}$$

in which the frictional coefficient $\bar{T}$ is defined as a plastic hardening function related to the equivalent plastic strain with the following form:

$$\bar{\alpha} = \alpha_m - (\alpha_m - \alpha_0)e^{-b\epsilon^p} \tag{V .34}$$

In this relation, the parameters α_0 and α_m respectively represent the initial threshold and asymptotic value of the frictional coefficients. Then the parameter b controls the evolution rate of plastic harden.

In this study, the rigid inclusions behaves elastic deformation. Therefore, it is assumed that the damage behavior is mainly characterized on solid matrix by two main components, namely the degradations on elastic stiffness and plastic yield. For this reason, the damage bulk and shear moduli of solid phase are given by:

$$k_d = (1-\beta\zeta)k^s, \quad \mu_d = (1-\beta\zeta)\mu^s \tag{V .35}$$

where β is a model parameter. On the other hand, the effect of damage on the plastic yield is assumed mainly though the degradation of frictional coefficient, with the following form:

$$\alpha = (1-\beta\zeta)\bar{\alpha} \tag{V .36}$$

3.4 Plastic damage constitutive relation

With above relations in hand, the incremental constitutive equation can be expressed as:

$$\dot{\boldsymbol{\Sigma}} = \mathbb{C}_d^{hom} : (\boldsymbol{D} - \boldsymbol{D}^p) - \dot{\mathbb{C}}_d^{hom} : (\tilde{\boldsymbol{D}} - \tilde{\boldsymbol{D}}^p) \tag{V .37}$$

© 2018 Tous droits réservés. lilliad.univ-lille.fr

where the tensor $\tilde{\boldsymbol{D}}$ is total strain tensor, then it is decomposed into an elasic part $\tilde{\boldsymbol{D}}^e$ and plastic part $\tilde{\boldsymbol{D}}^p$. $\mathbb{C}_d^{hom}$ and $\dot{\mathbb{C}}_d^{hom}$ respectively define as the damage homogenized elastic stiffness and its derivative with respect to ζ. For an associated flow, the plastic strain rate is given by:

$$\boldsymbol{D}^p = \dot{\lambda}\frac{\partial F}{\partial \boldsymbol{\Sigma}} \tag{V .38}$$

The plastic multiplier $\dot{\lambda}$ is determined by the consistency condition:

$$\boldsymbol{F} = \frac{\partial F}{\partial \boldsymbol{\Sigma}} : \dot{\boldsymbol{\Sigma}} + \frac{\partial F}{\partial f}\dot{f} + \frac{\partial F}{\partial \phi}\dot{\phi} + \frac{\partial F}{\partial \alpha}(\frac{\partial \alpha}{\partial \dot{\epsilon}^p} : \dot{\epsilon}^p + \frac{\partial \alpha}{\partial \zeta}\dot{\zeta}) \tag{V .39}$$

Substituting Eq.(V .24), (V .27), (V .28), (V .29), (V .37) and (V .38) into Eq.(V .40), one obtains:

$$\dot{\lambda} = \frac{\frac{\partial F}{\partial \boldsymbol{\Sigma}} : \mathbb{C}_d^{hom} : \boldsymbol{D} - \frac{\partial F}{\partial \boldsymbol{\Sigma}} : \dot{\mathbb{C}}_d^{hom} : \tilde{D}^e + \frac{\partial F}{\partial \alpha}\frac{\partial \alpha}{\partial \zeta}\dot{\zeta}}{\frac{\partial F}{\partial \boldsymbol{\Sigma}} : \mathbb{C}^{hom} : \frac{\partial F}{\partial \boldsymbol{\Sigma}} - \frac{\partial F}{\partial f}(1-f)[\tilde{\tilde{d}}_f - \alpha\tilde{\tilde{d}}_p] - \frac{\partial F}{\partial \phi}(1-\phi)(\frac{\frac{\partial F}{\partial \Sigma_m}}{1-\rho} - \tilde{\tilde{d}}_f) - \frac{\partial F}{\partial \alpha}\frac{\partial \alpha}{\partial \epsilon^p}\tilde{\tilde{d}}_p} \tag{V .40}$$

with

$$\tilde{\tilde{d}}_f = \frac{(\frac{3f}{2\alpha^2} - 1)\frac{2\Sigma_m}{(1-\rho)(1-\phi)} + 2(1-f)h}{(1-f)^2h^2 - 2(1-f)h\frac{\Sigma_m}{(1-\rho)(1-\phi)}}\frac{\boldsymbol{\Sigma} : \frac{\partial F}{\partial \boldsymbol{\Sigma}}}{(1-\rho)(1-\phi)} \tag{V .41}$$

$$\tilde{\tilde{d}}_p = \frac{\boldsymbol{\Sigma} : \frac{\partial F}{\partial \boldsymbol{\Sigma}}}{(1-\rho)(1-\phi)(1-f)\alpha h} \tag{V .42}$$

With this relations, then the proposed micro-macro damage constitutive model can be implemented in a standard finite element code.

4 Experimental verification: application to COx argillite

In order to verify the proposed damage model for describing the macroscopic behavior of geomaterials affected by the pores and inclusions. The typical porous Callovo-Oxfordian claystone (COx) is considered here, which has been investigated as a potential host rock for a radioactive waste repository on both experimental investigations and constitutive modeling ([Guéry et al., 2008,Bornert et al., 2010,Huang et al., 2014,Zhang et al., 2014,Liu et al., 2015,Shen and Shao, 2016a,Armand et al., 2017,Cao et al., 2018a]). By using the synchrotron X-ray microtomography, Callovo-Oxfordian sediments comprise a dominant clay fraction of 40 to 50%, 20 to 27% of quartz and 23 to 25% of calcite grains([Robinet, 2008]), with a total average porosity of 11.04-13.84%. Recent advancements in microscopy and sample preparation have enabled observations and accurate quantification of pores down to the nanometer size range, the spatial distribution of porosity in claystone are mainly observed within their clay matrix with characteristic sizes ranging between $1nm$ to

© 2018 Tous droits réservés.

Thèse de Yajun Cao, Université de Lille, 2018

$100\mu m$ across different scales. However, the mineralogical compositions can significantly vary with the depth. The influence of mineralogical variations and porosity on mechanical behaviour is clearly observed in the results of laboratory tests performed on samples ([Hu et al., 2014, Armand et al., 2017, Liu et al., 2018]). In the present study, the studied claystones have an average total porosity of 25% with two population of pores, having a proportion of 95% inter-particle pores and 5% intra-particle pores configured in porous clay matrix ([Shen and Shao, 2016a]).

For the sake of simplicity, the grains of quartz and calcite are replaced by a single equivalent inclusion phase by using the linear homogenization scheme ([Mori and Tanaka, 1973]). The effective elastic properties of the equivalent inclusion phase are taken as the average values of the ones of quartz and calcite grains according to the study of [Shen et al., 2013]. This leads to $E_{ei} = 98GPa$ and $E_{ei} = 0.15$. In this section, we will use the previous proposed damage model to consider the influences of double porosities and inclusions on macroscopic behavior of claystone. The predictions will be compared with the experimental data from [Shen and Shao, 2016a]. Typical elastic and platic values of the parameters adopted in this study are presented in Table V .1 for the studied claystone.

Table V .1: Typical values of parameters for the model

Parameter	Clay matrix	Inclusion
Elastic parameters	$E_s = 5.027GPa$, $v_s = 0.33$	$E_i = 98GPa$, $v_i = 0.15$
Plastic parameters	$\alpha_0 = 0.0001$, $\alpha_m = 0.9$, $b_1 = 140$, $h = 20MPa$	
Damage parameters	$\beta = 0.34$, $\gamma = 1 \times 10^{-4}$	
Porosity	$f_1 = 1.6\%$, $\phi = 23.75\%$	

Previous study performed by [Shen and Shao, 2016a] has been proposed a micro-macro model combining Hill's incremental method and analytical model to estimate the macroscopic behavior of claystone. By means of this method, the harden behavior of porous material can be well predicted. However, for most rock-like materials, significant soften behaviors induced by damage are often observed. Fig.V .2-Fig.V .7 present the comparisons between modeling results predicted by the proposed model and experimental data for compression test with different inclusion fractions. Different confining pressure are also considered here ($\sigma_{33} = 0, 5, 10MPa$). For the instantaneous compression test, here the simulated loading strain rate is set as $2 \times 10^{-6} s^{-1}$. It is obviously that there is a good agreement for both axial and lateral strain. Moreover, the proposed behavior can

© 2018 Tous droits réservés. lilliad.univ-lille.fr

Thèse de Yajun Cao, Université de Lille, 2018

predict the soften behavior of claystone.

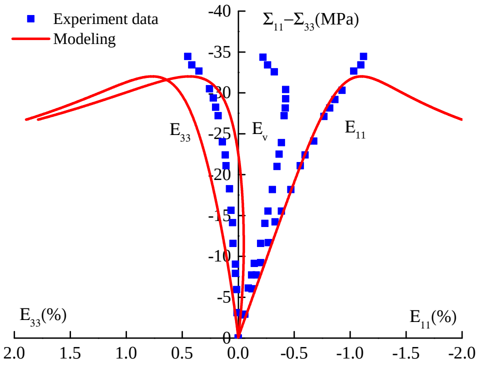

Figure V .2: Comparison between the experimental data and modeling results: $f = 1.6\%$, $\phi = 23.75\%$, $\rho = 49\%$, uniaxial compression test

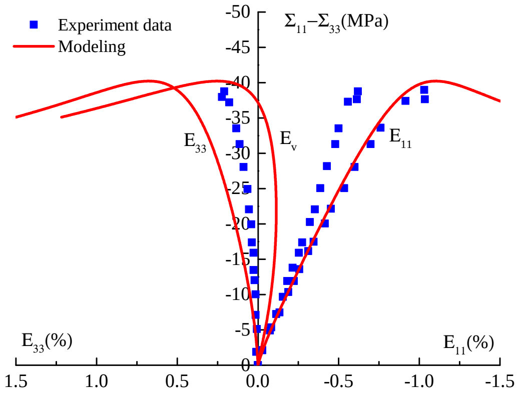

Figure V .3: Comparison between the experimental data and modeling results: $f = 1.6\%$, $\phi = 23.75\%$, $\rho = 51\%$, triaxial compression test with $\sigma_{33} = 5MPa$

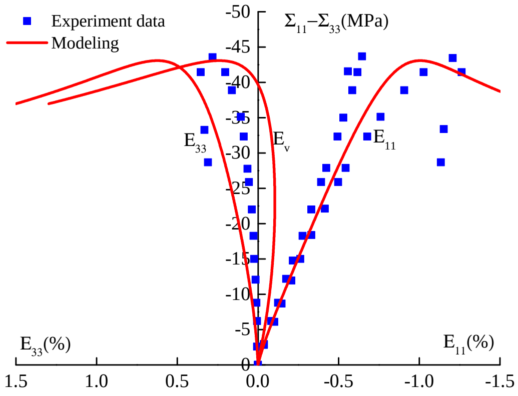

Figure V .4: Comparison between the experimental data and modeling results: $f = 1.6\%$, $\phi = 23.75\%$, $\rho = 56\%$, triaxial compression test with $\sigma_{33} = 5MPa$

© 2018 Tous droits réservés. lilliad.univ-lille.fr

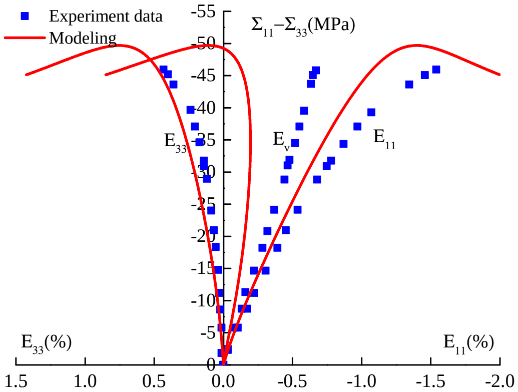

Figure V .5: Comparison between the experimental data and modeling results: $f = 1.6\%$, $\phi = 23.75\%$, $\rho = 45\%$, triaxial compression test with $\sigma_{33} = 10MPa$

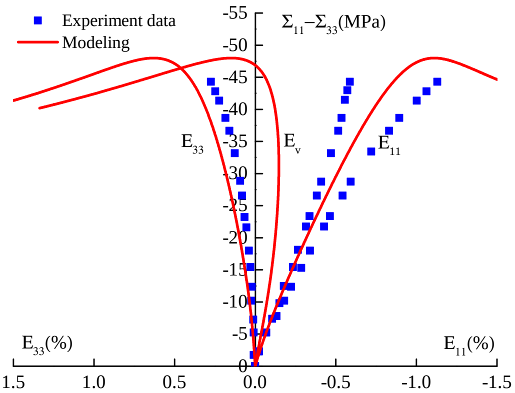

Figure V .6: Comparison between the experimental data and modeling results: $f = 1.6\%$, $\phi = 23.75\%$, $\rho = 53\%$, triaxial compression test with $\sigma_{33} = 10MPa$

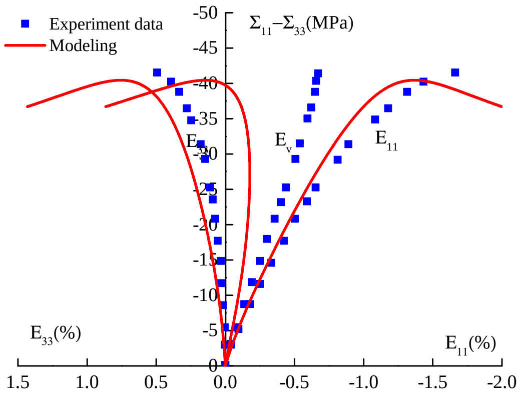

Figure V .7: Comparison between the experimental data and modeling results: $f = 1.6\%$, $\phi = 23.75\%$, $\rho = 60\%$, triaxial compression test with $\sigma_{33} = 10MPa$

© 2018 Tous droits réservés.

Thèse de Yajun Cao, Université de Lille, 2018

5 Extension to apply on Vaca Muerta shale rock

The shale rock is well known as an organic rich fine-grained sedimentary rock. It has been demonstrated both the compositional heterogeneity of the minerals and complex pore microstructure are characterized over many length scales ([Saif et al., 2017b]). Observations in 2-D and 3-D and across nm-μm-mm length scale reveals that its matrix consists of various minerals, including clays, carbonates, feldspars, quartz, and pyrite, exhibiting diameters from a few hundred micrometers to one or two millimeters ([Monfared and Ulm, 2016]) and dominated by the nanopores ([Ma et al., 2017, Saif et al., 2017b]). The investigated shale samples from Vaca Muerta Formation also show a general heterogeneous rock structure like previous mentioned microstructure features. To investigate its macroscopic mechanical behavior, a typical representative elementary volume (REV) is selected as shown in Fig.V .8.

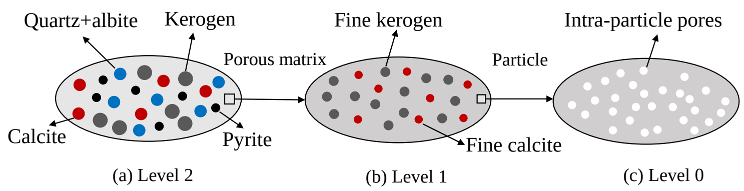

Figure V .8: Representative volume element of studied shale

In this context, level 0 is considered to be a nanoporous clay matrix. Level 1 is characterized as a inclusion-matrix system with fine mineral grains like fine kerogen (f_5) and calcite (f_6) . Level 2 is occupied by complex mineral inclusion assemblages contained calcite (f_1) , quartz/albite (f_2) , pyrite (f_3) and kerogen grains (f_4). The symbols previously presented in the brackets are corresponding to its volume fraction at the given scale. The main elastic properties of these mineral inclusions have been listed in Table V .2. Assuming that the mineral inclusions are all of spherical and to be self-consistently distributed. This implies that these inclusion assemblages at each scale can be considered as a class of equivalent inclusions. As a consequence of the self-consistent homogenization method ([Hill, 1965b]), the elastic properties of equivalent inclusion can be obtained. And the volume fractions of equivalent inclusions (ϕ and ρ) are respectively corresponding to the sum of the contained inclusions fractions at level 1 and level 2.

© 2018 Tous droits réservés. lilliad.univ-lille.fr

Table V .2: Typical values of parameters for the model

Mineral	Elastic modulus(GPa)	Poisson
Quartz/albite	95.5	0.155
Pyrite	311	0.15
Kerogen	2	0.25
Calcite	95	0.27
Clay	5	0.27

To investigate its macroscopic plastic behavior, we will make full use of the study of [Shen et al., 2013]. An approximate closed-form criterion considering the Maguhous([Maghous et al., 2009]) type porous matrix reinforced by rigid inclusions is introduced here, which also takes the general elliptic form of Eq.(V .4) with the following parameters:

$$\begin{aligned} A &= \frac{\frac{1+2f/3}{\alpha^2} + \frac{2}{3}\phi(\frac{3f}{2\alpha^2} - 1)}{\frac{6\alpha^2-13f-6}{4\alpha^2-12f-9}\phi + 1}, \quad B = \frac{3f}{2\alpha^2} - 1 \\ C &= 2(1-f)h, \quad D = \frac{3+2f+3f\phi}{3+2f}(1-f)^2h^2 \end{aligned} \tag{V .43}$$

where ϕ denotes the volume fraction of inclusions at the second scale. With these parameters, substitute Eq.(V .43) into Eq.(V .18), one can get a new criterion to consider the effect rigid inclusions arranged at two separated scales with porous matrix. Similarly to the previous study, the evolution of inclusion fraction is also neglected. Then evolution of porosity is given by:

$$\dot{f} = (1-f)(\frac{tr\boldsymbol{D^p}}{(1-\rho)(1-\phi)} - \alpha\dot{\epsilon^p}) \tag{V .44}$$

Incorporating the damage model mentioned in Section 3.3, we can extend the proposed model to account for the macroscopic behavior of geomaterials with two populations of inclusions embedded in porous matrix. To valide its application on Vaca Muerta shale rock, we also conducted a series of numerical modeling for triaxial compression test with different compositions and compared with the experimental data. The simulated loading strain rate is selected as $10^{-6}s^{-1}$. The following parameters of clay matrix are adopted in this study :

© 2018 Tous droits réservés.

Thèse de Yajun Cao, Université de Lille, 2018

Table V .3: Typical values of parameters for the model

Parameter	Clay matrix
Elastic parameters	$E_s = 5.0GPa$, $v_s = 0.27$
Plastic parameters	$\alpha_0 = 0.0001$, $\alpha_m = 0.75$, $b_1 = 600$, $h = 68MPa$
Damage parameters	$\beta = 0.4$, $\gamma = 6 \times 10^{-4}$

Fig.V .9 $\sim$ V .11 present the comparison results between simulated modeling and experimental data for different mineral compositions. One can see that a good agreement is found between them. The proposed damage model can well consider the main effect of two populations of inclusions with porous matrix on the macroscopic mechanical behaviors, as well as the failure of the rock induced by the damage behavior.

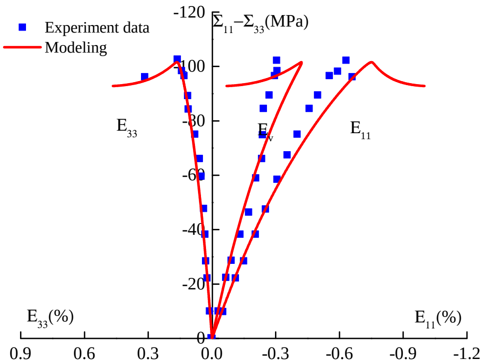

Figure V .9: Comparison between the experimental data and modeling result: $f_1 = 40\%$, $f_2 = 30\%$, $f_4 = 25.7\%$, $f_6 = 5\%$, $f = 5\%$, triaxial compression test with $\sigma_{33} = 2MPa$

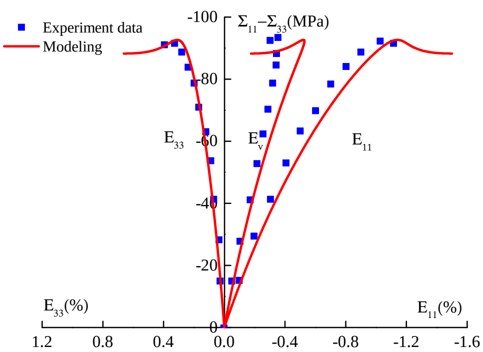

Figure V .10: Comparison between the experimental data and modeling result: $f_1 = 42.3\%$, $f_2 = 21.5\%$, $f_3 = 1.73\%$, $f_5 = 23\%$, $f = 9.4\%$, triaxial compression test with $\sigma_{33} = 10MPa$

© 2018 Tous droits réservés. lilliad.univ-lille.fr

Thèse de Yajun Cao, Université de Lille, 2018

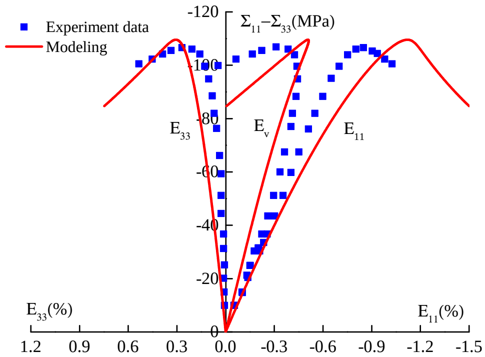

Figure V .11: Comparison between the experimental data and modeling result: $f_1 = 24.15\%$, $f_2 = 17.3\%$, $f_4 = 26.4\%$, $f_6 = 25\%$, $f = 8\%$, triaxial compression test with $\sigma_{33} = 10MPa$

6 Concluding remarks

In this work, a general strength criterion accounting for the elliptic form porous matrix and randomly distributed rigid inclusions is established by using the modified scant method inspired by the work of [Maghous et al., 2009] and [Shen and Shao, 2016a]. Based on this criterion, we incorporate a time-dependent damage model to account for the soften behavior induced by the degradation of elastic and plastic properties. Meanwhile, we employed a new explicit integration algorithm for the damage solver based on the trapezoid rule approximation, a good consistence is obtained by compared with existed algorithm. Finally, the developed plastic damage model are successfully applied and extended on modeling the COx argillite claystone and Vaca Muerta shale rock. The comparison results between the modeling and experimental data have validated the effectiveness of the proposed model which can well predict the macroscopic deformation and failure induced by the damage for porous geomaterials with complex mineral compositions embedded at multi-scales.

© 2018 Tous droits réservés. lilliad.univ-lille.fr

Thèse de Yajun Cao, Université de Lille, 2018

7 Appendix A: Integration algorithm of equation (V .31)

For the integration in time domain $[0, t]$ of Eq. (V .31), the total time t can be discretized into several subintervals $[t_n, t_{n+1}]$. Here the time increment is defined as $\Delta t_{n+1} = t_{n+1} - t_n$. Thus for the interval $[0, t_n]$, we can reformulate it with:

$$\zeta(t_n)e^{\gamma t_n} = \int_0^{t_n} \gamma\bar{\zeta}(\tau)e^{\gamma\tau}d\tau \tag{V .45}$$

Following Eq.(V .45), the integration for subintervals $[t_n, t_{n+1}]$ can read:

$$\int_{t_n}^{t_{n+1}} \gamma\bar{\zeta}(\tau)e^{\gamma\tau}d\tau = \int_0^{t_{n+1}} \gamma\bar{\zeta}(\tau)e^{\gamma\tau}d\tau - \int_0^{t_n} \gamma\bar{\zeta}(\tau)e^{\gamma\tau}d\tau = \zeta_{n+1}e^{\gamma t_{n+1}} - \zeta_n e^{\gamma t_n} \tag{V .46}$$

where the subscript n denotes the corresponding value at time t_n. To determine the integration of the left hand-side of Eq.(V .46), several approximate methods can be used here. Based on the trapezoid rule, one has

$$\int_{t_n}^{t_{n+1}} \gamma\bar{\zeta}(\tau)e^{\gamma\tau}d\tau \approx \gamma\frac{\bar{\zeta}_n e^{\gamma t_n} + \bar{\zeta}_{n+1}e^{\gamma t_{n+1}}}{2}\Delta t_{n+1} \tag{V .47}$$

Hence, according to Eq.(V .46) and (V .47), it follows that:

$$\zeta_{n+1} = \frac{\gamma}{2}\bar{\zeta}_{n+1}\Delta t_{n+1} + (\zeta_n + \frac{\gamma}{2}\bar{\zeta}_n\Delta t_{n+1})e^{-\gamma\Delta t_{n+1}} \tag{V .48}$$

Again, for rectangular integration rule, the integration of the left hand-side of E-q.(V .46) also approximately reads,

$$\int_{t_n}^{t_{n+1}} \gamma\bar{\zeta}(\tau)e^{\gamma\tau}d\tau \approx \gamma\bar{\zeta}_n e^{\gamma t_n}\Delta t_{n+1} \approx \gamma\bar{\zeta}_{n+1}e^{\gamma(t_n+\Delta t_{n+1})}\Delta t_{n+1} \tag{V .49}$$

Above, the last two approximations in Eq.(V .49) are corresponding to the well-known left Riemann rule and right Riemann rule. Therefore, another explicit algorithm solver is alternately taken the form of:

$$\zeta_{n+1} \approx \zeta_n e^{-\gamma\Delta t_{n+1}} + \gamma\bar{\zeta}_n e^{-\gamma\Delta t_n}\Delta t_{n+1} \approx \zeta_n e^{-\gamma\Delta t_{n+1}} + \gamma\bar{\zeta}_{n+1}\Delta t_{n+1} \tag{V .50}$$

By comparison with these three explicit integration forms, the trapezoidal rule is viewed as the result obtained by averaging the left Riemann and right Riemann sums, which is different from the explicit formulation obtained by [Zhao et al., 2016]. But it is important to note that the error for rectangular integration rule is higher than the trapezoid rule ([Anderson, 2004]). For all the methods, the approximation is more accurate as the time increment Δt_{n+1} becomes smaller. As a example, we conducted a series of simulations by using different algorithms mentioned above for four different loading strain

© 2018 Tous droits réservés. lilliad.univ-lille.fr

Thèse de Yajun Cao, Université de Lille, 2018

rates. The results are presented in Fig.V .12 ∼ V .15. From the stress-strain relations, one can see that the stress-strain curves for all the methods are consistent with each other when the loading strain rate is higher than $2\times10^{-7}s^{-1}$. For a lower loading strain rate, the left Riemann rule and right Riemann rule have a bad estimate. In this study, Eq.(V .48) will be adopted here for the simulations.

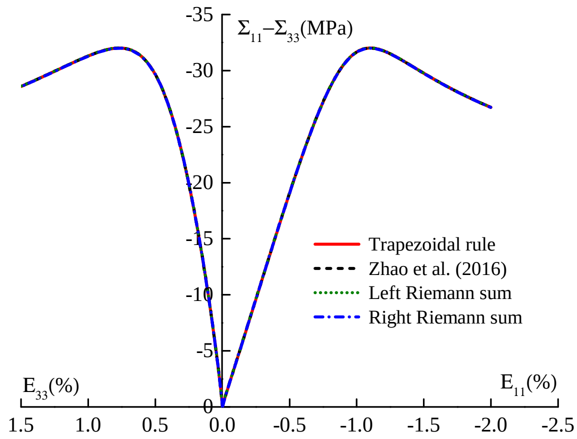

Figure V .12: Simulated results of stress-strain relation for different damage solver with: $f = 1.6\%$, $\phi = 23.75\%$, $\rho = 49\%$, uniaxial compression test with loading strain rate of $2 \times 10^{-6}s^{-1}$.

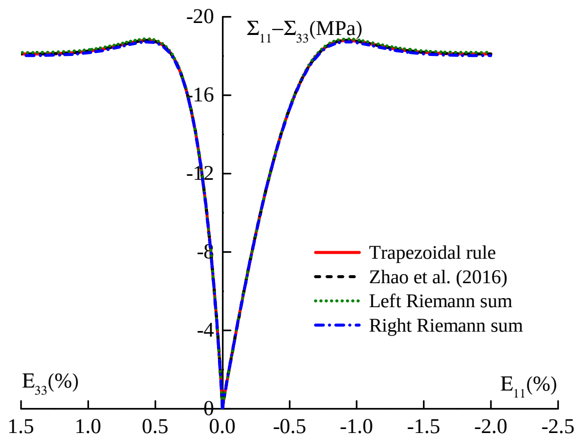

Figure V .13: Simulated results of stress-strain relation for different damage solver with: $f = 1.6\%$, $\phi = 23.75\%$, $\rho = 49\%$, uniaxial compression test with loading strain rate of $2 \times 10^{-7}s^{-1}$.

© 2018 Tous droits réservés. lilliad.univ-lille.fr

Thèse de Yajun Cao, Université de Lille, 2018

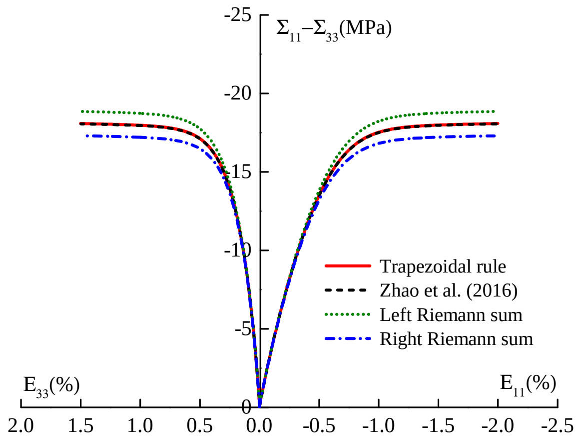

Figure V .14: Simulated results of stress-strain relation for different damage solver with: $f = 1.6\%$, $\phi = 23.75\%$, $\rho = 49\%$, uniaxial compression test with loading strain rate of $2 \times 10^{-8} s^{-1}$.

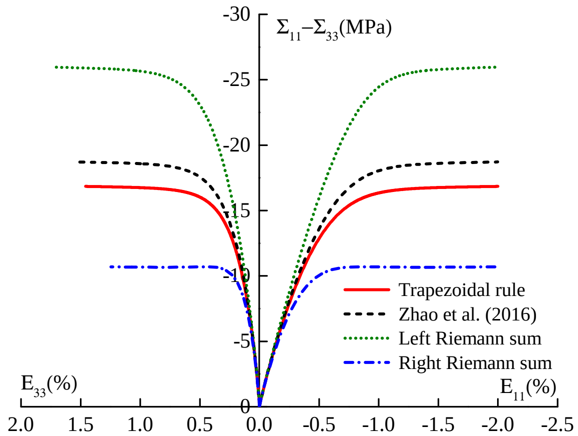

Figure V .15: Simulated results of stress-strain relation for different damage solver with: $f = 1.6\%$, $\phi = 23.75\%$, $\rho = 49\%$, uniaxial compression test with loading strain rate of $2 \times 10^{-9} s^{-1}$

© 2018 Tous droits réservés.

lilliad.univ-lille.fr

Thèse de Yajun Cao, Université de Lille, 2018

© 2018 Tous droits réservés. lilliad.univ-lille.fr

Chapter VI

Conclusions and perspectives

This thesis aims to explore the effective properties of porous materials involved with pores and inclusions problem with physical geometrical features across multiple scales. To this end, a multi-step homogenization numerical model has been developed for rock-like porous materials combining with the FFT-based method and analytical theories. The proposed homogenization model is able to account for the effect of geometrical features of pores and inclusions to estimate the main mechanical behaviours such as interaction between pores and inclusions, induced anisotropy, elastoplastic, damage, time-dependent effects. By means of the proposed method, the effective mechanical behaviors of four REV with different microstructure features have been specially studied in this work. The main results can be concluded as following:

For the class of porous materials with two populations of pores under consideration, it is found that both the effective elastic and plastic properties of double porous materials are significantly influenced by the porosity ratio and they are more sensitive to the meso-porosity than to the micro-porosity. The classical dilute homogenization scheme for the prediction of elastic modulus is not able to capture these effects. The double Hashin-Shtrikman upper bound model significantly differs from the FFT-based model for low values of porosity ratio f/ϕ (high values of meso-porosity) but the two models agree well for high values of porosity ratio f/ϕ (low values of meso-porosity). For the plastic case, by comparisons with two closed-form criteria, significant differences have been found between the two criteria and the FFT-based numerical model. According to the numerical results obtained with the FFT-based full-field simulations, the macroscopic yield stresses are strongly influenced by the porosity ratio especially at compression region. For a given value of total porosity, similar to the elastic case, the mesoscopic porosity plays a more

© 2018 Tous droits réservés.

Thèse de Yajun Cao, Université de Lille, 2018

important role than the micro-porosity on the macroscopic yield stress. However, these effects of microstructure in terms of porosity ratio have not been correctly taken into account in the two analytical criteria.

For the reason of lacking closed form criterion for the microstructure with both meso inclusions and pores embedded at same scale. The effective elastic properties of such kinds of materials are estimated using FFT-based method. With a series of simulations and comparisons, it is found that both the pore and inclusion geometry are sensitive to the determination of macroscopic elastic behavior. Simulation results show that the anisotropy effect induced by pore and inclusion is obtained with respect to its aspect ratio and orientation, providing an increase or decrease effect on the effective elastic modulus. For plastic behaviors, the inclusion geometry does not have significant effect on computing plastic yield stress except its volume fraction. However, this does not work for the case of pore. The corresponding results reveal that the pore shape, distribution, aspect ratios, orientations indeed have important effect and play different roles on plastic yield stress. For future works, to characterize the effective behaviors of such kinds of composite as accuracy as possible by an analytical criterion, these factors should be taken into considerations.

In order to consider a class of rock-like materials containing pores and mineral inclusion at two different scales, we established an unified model to account for the effect of pores and inclusions on the plastic and viscoplastic behavior. The numerical yield stresses are compared with the ones predicted by an analytical homogenized criterion considering a single spherical inclusion embedded in the porous matrix. It is found that in general the macroscopic yield stress is more sensitive to porosity than inclusion content. The influences of inclusion shape, orientation and stiffness are relatively small on the macroscopic yield stress. However, they can have significant influences on the macroscopic plastic and viscoplastic strains. In particular, the numerical results obtained from the FFT based numerical model considering the plastic and viscoplastic flows in the porous matrix depict a stronger effect of hard inclusion than the analytical homogenized model considering the plastic and viscoplastic flows at the macroscopic scale and neglecting the shape and spatial distribution of inclusions.

Finally, for the purpose of obtaining a closed-form of analytical criterion considering the pores and inclusions configured at multiscales, a general strength criterion is established though three-step homogenization procdure by using the modified scant method inspired by the work of [Maghous et al., 2009] and [Shen and Shao, 2016a]. Based on this criterion, we incorporate a time-dependent damage model to account for the soften behavior induced by the degradation of elastic and plastic properties of solid matrix.

© 2018 Tous droits réservés. lilliad.univ-lille.fr

Meanwhile, we employed a new explicit integration algorithm for the damage solver based on the trapezoid rule approximation, a good consistence is obtained by compared with existed algorithm. Finally, the developed plastic damage model are successfully applied and extended on modeling the COx argillite claystone and Vaca Muerta shale rock. The comparison results between the modeling and experimental data have validated the effectiveness of the proposed model which can well predict the macroscopic deformation and failure induced by the damage for porous geomaterials with complex mineral compositions embedded at multi-scales.

Many extensions can be considered in future works, we would like to extend the FFT-based method to consider the crack propagation and coalescence, hydromechanical coupling effect of porous materials combining a phase-field method. Then an closed-form strength criterion is still needed to account for the effects of meso pores and inclusions, especially to incorporate the induced anisotropy by the pore geometrical information.

© 2018 Tous droits réservés.

lilliad.univ-lille.fr

Thèse de Yajun Cao, Université de Lille, 2018

© 2018 Tous droits réservés. lilliad.univ-lille.fr

Bibliography

[Al-Harthi et al., 1999] Al-Harthi, A., Al-Amri, R., and Shehata, W. (1999). The porosity and engineering properties of vesicular basalt in saudi arabia. *Engineering Geology*, 54(3-4):313–320.

[Anderson, 2004] Anderson, D. (2004). Student solutions manual for stewart's single variable calculus (early transcendentals), brooks/cole (1999). Technical report, ISBN 0-534-36301-6.

[Armand et al., 2017] Armand, G., Conil, N., Talandier, J., and Seyedi, D. M. (2017). Fundamental aspects of the hydromechanical behaviour of callovo-oxfordian claystone: from experimental studies to model calibration and validation. *Computers and Geotechnics*, 85:277–286.

[Barthélémy and Dormieux, 2003] Barthélémy, J.-F. and Dormieux, L. (2003). Détermination du critère de rupture macroscopique d'un milieu poreux par homogénéisation non linéaire. *Comptes Rendus Mécanique*, 331(4):271–276.

[Barthélémy and Dormieux, 2004] Barthélémy, J.-F. and Dormieux, L. (2004). A micromechanical approach to the strength criterion of drucker-prager materials reinforced by rigid inclusions. *International Journal for Numerical and Analytical Methods in Geomechanics*, 28(7-8):565–582.

[Baud et al., 2004] Baud, P., Klein, E., and Wong, T.-f. (2004). Compaction localization in porous sandstones: spatial evolution of damage and acoustic emission activity. *Journal of Structural Geology*, 26(4):603–624.

[Baud et al., 2006] Baud, P., Vajdova, V., and Wong, T.-f. (2006). Shear-enhanced compaction and strain localization: Inelastic deformation and constitutive modeling of four porous sandstones. *Journal of Geophysical Research: Solid Earth*, 111(B12).

[Baud et al., 2009] Baud, P., Vinciguerra, S., David, C., Cavallo, A., Walker, E., and Reuschlé, T. (2009). Compaction and failure in high porosity carbonates: Mechanical data and microstructural observations. In *Rock Physics and Natural Hazards*, pages 869–898. Springer.

© 2018 Tous droits réservés.

Thèse de Yajun Cao, Université de Lille, 2018

[Baud et al., 2014] Baud, P., Wong, T.-f., and Zhu, W. (2014). Effects of porosity and crack density on the compressive strength of rocks. *International Journal of Rock Mechanics and Mining Sciences*, 67:202–211.

[Benzerga and Besson, 2001] Benzerga, A. A. and Besson, J. (2001). Plastic potentials for anisotropic porous solids. *European Journal of Mechanics-A/Solids*, 20(3):397–434.

[Bernard et al., 2003] Bernard, O., Ulm, F.-J., and Lemarchand, E. (2003). A multiscale micromechanics-hydration model for the early-age elastic properties of cement-based materials. *Cement and Concrete Research*, 33(9):1293–1309.

[Bignonnet et al., 2016a] Bignonnet, F., Dormieux, L., and Kondo, D. (2016a). A micromechanical model for the plasticity of porous granular media and link with the cam clay model. *International Journal of Plasticity*, 79:259–274.

[Bignonnet et al., 2015] Bignonnet, F., Dormieux, L., and Lemarchand, E. (2015). Strength of a matrix with elliptic criterion reinforced by rigid inclusions with imperfect interfaces. *European Journal of Mechanics-A/Solids*, 52:95–106.

[Bignonnet et al., 2016b] Bignonnet, F., Hassen, G., and Dormieux, L. (2016b). Fourier-based strength homogenization of porous media. *Computational Mechanics*, 58(5):833–859.

[Bilger et al., 2005] Bilger, N., Auslender, F., Bornert, M., Michel, J.-C., Moulinec, H., Suquet, P., and Zaoui, A. (2005). Effect of a nonuniform distribution of voids on the plastic response of voided materials: a computational and statistical analysis. *International Journal of Solids and Structures*, 42(2):517–538.

[Bornert et al., 2010] Bornert, M., Vales, F., Gharbi, H., and Nguyen Minh, D. (2010). Multiscale full-field strain measurements for micromechanical investigations of the hydromechanical behaviour of clayey rocks. *Strain*, 46(1):33–46.

[Bourih et al., 2018] Bourih, A., Kaddouri, W., Kanit, T., Madani, S., and Imad, A. (2018). Effective yield surface of porous media with random overlapping identical spherical voids. *Journal of Materials Research and Technology*, 7(2):103–117.

[Brassart et al., 2012] Brassart, L., Stainier, L., Doghri, I., and Delannay, L. (2012). Homogenization of elasto-(visco) plastic composites based on an incremental variational principle. *International Journal of Plasticity*, 36:86–112.

© 2018 Tous droits réservés. lilliad.univ-lille.fr

Thèse de Yajun Cao, Université de Lille, 2018

[Brisard and Dormieux, 2010] Brisard, S. and Dormieux, L. (2010). Fft-based methods for the mechanics of composites: A general variational framework. *Computational Materials Science*, 49(3):663–671.

[Cao et al., 2018a] Cao, Y., Shen, W., Burlion, N., and Shao, J. (2018a). Effects of inclusions and pores on plastic and viscoplastic deformation of rock-like materials. *International Journal of Plasticity*, 108:107 – 124.

[Cao et al., 2018b] Cao, Y., Shen, W., Shao, J., and Burlion, N. (2018b). Influences of micro-pores and meso-pores on elastic and plastic properties of porous materials. *European Journal of Mechanics - A/Solids*, 72:407 – 423.

[Cariou et al., 2013] Cariou, S., Dormieux, L., and Skoczylas, F. (2013). An original constitutive law for callovo-oxfordian argillite, a two-scale double-porosity material. *Applied Clay Science*, 80:18–30.

[Castañeda, 1991] Castañeda, P. (1991). The effective mechanical properties of nonlinear isotropic composites. *Journal of the Mechanics and Physics of Solids*, 39(1):45–71.

[Castaneda, 1992] Castaneda, P. P. (1992). New variational principles in plasticity and their application to composite materials. *Journal of the Mechanics and Physics of Solids*, 40(8):1757–1788.

[Cazacu et al., 2014] Cazacu, O., Revil-Baudard, B., Chandola, N., and Kondo, D. (2014). New analytical criterion for porous solids with tresca matrix under axisymmetric loadings. *International Journal of Solids and Structures*, 51(3):861–874.

[Chang et al., 2006] Chang, C., Zoback, M. D., and Khaksar, A. (2006). Empirical relations between rock strength and physical properties in sedimentary rocks. *Journal of Petroleum Science and Engineering*, 51(3-4):223–237.

[Cheng et al., 2014] Cheng, L., de Saxce, G., and Kondo, D. (2014). A stress-based variational model for ductile porous materials. *International Journal of Plasticity*, 55:133–151.

[Conil and Armand, 2015] Conil, N. and Armand, G. (2015). Essais complémentaires sur le comportement différé des argilittes du callovo-oxfordian. *Rapport GL Géomécanique*, (D.RP.AMFS.14.0015).

© 2018 Tous droits réservés. lilliad.univ-lille.fr

Thèse de Yajun Cao, Université de Lille, 2018

[Doghri et al., 2010] Doghri, I., Adam, L., and Bilger, N. (2010). Mean-field homogenization of elasto-viscoplastic composites based on a general incrementally affine linearization method. *International Journal of Plasticity*, 26(2):219–238.

[Drach et al., 2016] Drach, B., Tsukrov, I., and Trofimov, A. (2016). Comparison of full field and single pore approaches to homogenization of linearly elastic materials with pores of regular and irregular shapes. *International Journal of Solids and Structures*, 96:48–63.

[Eshelby, 1957] Eshelby, J. D. (1957). The determination of the elastic field of an ellipsoidal inclusion, and related problems. In *Proceedings of the Royal Society of London A: Mathematical, Physical and Engineering Sciences*, volume 241, pages 376–396. The Royal Society.

[Eyre and Milton, 1999] Eyre, D. and Milton, G. W. (1999). A fast numerical scheme for computing the response of composites using grid refinement. *The European Physical Journal Applied Physics*, 6(1):41–47.

[Farhat et al., 2017] Farhat, F., Shen, W., and Shao, J.-F. (2017). A micro-mechanics based viscoplastic model for clayey rocks. *Computers and Geotechnics*, 89:92–102.

[Garajeu and Suquet, 1997] Garajeu, M. and Suquet, P. (1997). Effective properties of porous ideally plastic or viscoplastic materials containing rigid particles. *Journal of the Mechanics and Physics of Solids*, 45(6):873 – 902.

[Gélébart and Mondon-Cancel, 2013] Gélébart, L. and Mondon-Cancel, R. (2013). Non-linear extension of fft-based methods accelerated by conjugate gradients to evaluate the mechanical behavior of composite materials. *Computational Materials Science*, 77:430–439.

[Ghossein and Lévesque, 2012] Ghossein, E. and Lévesque, M. (2012). A fully automated numerical tool for a comprehensive validation of homogenization models and its application to spherical particles reinforced composites. *International Journal of Solids and Structures*, 49(11-12):1387–1398.

[Giraud et al., 2012] Giraud, A., Nguyen, N., and Grgic, D. (2012). Effective poroelastic coefficients of isotropic oolitic rocks with micro and meso porosities. *International Journal of Engineering Science*, 58:57–77.

© 2018 Tous droits réservés. lilliad.univ-lille.fr

Thèse de Yajun Cao, Université de Lille, 2018

[Gologanu et al., 1993] Gologanu, M., Leblond, J.-B., and Devaux, J. (1993). Approximate models for ductile metals containing non-spherical voids–case of axisymmetric prolate ellipsoidal cavities. *Journal of the Mechanics and Physics of Solids*, 41(11):1723–1754.

[Gologanu et al., 1994] Gologanu, M., Leblond, J.-B., and Devaux, J. (1994). Approximate models for ductile metals containing nonspherical voids–case of axisymmetric oblate ellipsoidal cavities. *Journal of Engineering Materials and Technology*, 116(3):290–297.

[Gologanu et al., 1997] Gologanu, M., Leblond, J.-B., Perrin, G., and Devaux, J. (1997). Recent extensions of gurson's model for porous ductile metals. In *Continuum micromechanics*, pages 61–130. Springer.

[Guéry et al., 2008] Guéry, A. A.-C., Cormery, F., Shao, J.-F., and Kondo, D. (2008). A micromechanical model of elastoplastic and damage behavior of a cohesive geomaterial. *International Journal of Solids and structures*, 45(5):1406–1429.

[Guo et al., 2008] Guo, T., Faleskog, J., and Shih, C. (2008). Continuum modeling of a porous solid with pressure-sensitive dilatant matrix. *Journal of the Mechanics and Physics of Solids*, 56(6):2188–2212.

[Gurson, 1977] Gurson, A. L. (1977). Continuum theory of ductile rupture by void nucleation and growth: Part i–yield criteria and flow rules for porous ductile media. *Journal of engineering materials and technology*, 99(1):2–15.

[Hashin and Shtrikman, 1962] Hashin, Z. and Shtrikman, S. (1962). A variational approach to the theory of the elastic behaviour of polycrystals. *Journal of the Mechanics and Physics of Solids*, 10(4):343–352.

[Hashin and Shtrikman, 1963] Hashin, Z. and Shtrikman, S. (1963). A variational approach to the theory of the elastic behaviour of multiphase materials. *Journal of the Mechanics and Physics of Solids*, 11(2):127–140.

[He et al., 2013] He, Z., Dormieux, L., and Kondo, D. (2013). Strength properties of a drucker–prager porous medium reinforced by rigid particles. *International Journal of Plasticity*, 51:218–240.

[Heidari et al., 2014] Heidari, M., Khanlari, G., Torabi-Kaveh, M., Kargarian, S., and Saneie, S. (2014). Effect of porosity on rock brittleness. *Rock mechanics and rock engineering*, 47(2):785–790.

© 2018 Tous droits réservés. lilliad.univ-lille.fr

Thèse de Yajun Cao, Université de Lille, 2018

[Hill, 1952] Hill, R. (1952). The elastic behaviour of a crystalline aggregate. *Proceedings of the Physical Society. Section A*, 65(5):349.

[Hill, 1965a] Hill, R. (1965a). Continuum micro-mechanics of elastoplastic polycrystals. *Journal of the Mechanics and Physics of Solids*, 13(2):89–101.

[Hill, 1965b] Hill, R. (1965b). A self-consistent mechanics of composite materials. *Journal of the Mechanics and Physics of Solids*, 13(4):213–222.

[Hu et al., 2014] Hu, D., Zhang, F., Shao, J.-F., and Gatmiri, B. (2014). Influences of mineralogy and water content on the mechanical properties of argillite. *Rock mechanics and rock engineering*, 47(1):157–166.

[Hu and Weng, 2000] Hu, G. and Weng, G. (2000). Some reflections on the mori-tanaka and ponte castaneda-willis methods with randomly oriented ellipsoidal inclusions. *Acta Mechanica*, 140(1-2):31–40.

[Huang et al., 2018] Huang, J., Zhao, M., Du, X., Dai, F., Ma, C., and Liu, J. (2018). An elasto-plastic damage model for rocks based on a new nonlinear strength criterion. *Rock Mechanics and Rock Engineering*, 51(5):1413–1429.

[Huang et al., 2014] Huang, Y., Shen, W., Shao, J.-F., Guéry, A. A.-C., and Jia, Y. (2014). Multi-scale modeling of time-dependent behavior of claystones with a viscoplastic compressible porous matrix. *Mechanics of Materials*, 79:25–34.

[Idiart et al., 2006] Idiart, M., Moulinec, H., Ponte Castañeda, P., and Suquet, P. (2006). Macroscopic behavior and field fluctuations in viscoplastic composites: second-order estimates versus full-field simulations. *Journal of the Mechanics and Physics of Solids*, 54(5):1029–1063.

[Jiang and Shao, 2009] Jiang, T. and Shao, J.-F. (2009). On the incremental approach for nonlinear homogenization of composite and influence of isotropization. *Computational Materials Science*, 46(2):447–451.

[Jiang and Shao, 2012] Jiang, T. and Shao, J.-F. (2012). Micromechanical analysis of the nonlinear behavior of porous geomaterials based on the fast fourier transform. *Computers and Geotechnics*, 46:69–74.

[Jiang et al., 2015] Jiang, T., Xu, W., and Shao, J. (2015). Multiscale study of the nonlinear behavior of heterogeneous clayey rocks based on the fft method. *Rock Mechanics and Rock Engineering*, 48(2):417–426.

© 2018 Tous droits réservés. lilliad.univ-lille.fr

Thèse de Yajun Cao, Université de Lille, 2018

[Julien et al., 2011] Julien, J., G u ar u ajeu, M., and Michel, J.-C. (2011). A semi-analytical model for the behavior of saturated viscoplastic materials containing two populations of voids of different sizes. *International Journal of Solids and Structures*, 48(10):1485–1498.

[Kabel et al., 2014] Kabel, M., Böhlke, T., and Schneider, M. (2014). Efficient fixed point and newton–krylov solvers for fft-based homogenization of elasticity at large deformations. *Computational Mechanics*, 54(6):1497–1514.

[Kareem et al., 2017] Kareem, R., Cubillas, P., Gluyas, J., Bowen, L., Hillier, S., and Greenwell, H. C. (2017). Multi-technique approach to the petrophysical characterization of berea sandstone core plugs (cleveland quarries, usa). *Journal of Petroleum Science and Engineering*, 149:436–455.

[Kelly et al., 2016] Kelly, S., El-Sobky, H., Torres-Verdín, C., and Balhoff, M. T. (2016). Assessing the utility of fib-sem images for shale digital rock physics. *Advances in water resources*, 95:302–316.

[Keralavarma and Benzerga, 2010] Keralavarma, S. and Benzerga, A. (2010). A constitutive model for plastically anisotropic solids with non-spherical voids. *Journal of the Mechanics and Physics of Solids*, 58(6):874–901.

[Khdir et al., 2014] Khdir, Y.-K., Kanit, T., Zaïri, F., and Naït-Abdelaziz, M. (2014). Computational homogenization of plastic porous media with two populations of voids. *Materials Science and Engineering: A*, 597:324–330.

[Klinkenberg et al., 2009] Klinkenberg, M., Kaufhold, S., Dohrmann, R., and Siegesmund, S. (2009). Influence of carbonate microfabrics on the failure strength of claystones. *Engineering Geology*, 107(1-2):42–54.

[Lebensohn et al., 2012] Lebensohn, R. A., Kanjarla, A. K., and Eisenlohr, P. (2012). An elasto-viscoplastic formulation based on fast fourier transforms for the prediction of micromechanical fields in polycrystalline materials. *International Journal of Plasticity*, 32:59–69.

[Li et al., 2012] Li, J., Tian, X.-X., and Abdelmoula, R. (2012). A damage model for crack prediction in brittle and quasi-brittle materials solved by the fft method. *International journal of fracture*, 173(2):135–146.

© 2018 Tous droits réservés. lilliad.univ-lille.fr

Thèse de Yajun Cao, Université de Lille, 2018

[Li et al., 2018] Li, M., Cao, Y., Shen, W., and Shao, J. (2018). A damage model of mechanical behavior of porous materials: Application to sandstone. *International Journal of Damage Mechanics*, 27(9):1325–1351.

[Li et al., 2016] Li, M. Y., Shen, W. Q., and Shao, J. F. (2016). A numerical study of effective mechanical behaviors of rock like materials based on fast fourier transform. *Mechanics of Materials*, 92:275–288.

[Lian et al., 2011] Lian, C., Zhuge, Y., and Beecham, S. (2011). The relationship between porosity and strength for porous concrete. *Construction and Building Materials*, 25(11):4294–4298.

[Liang et al., 2017] Liang, S., Wei, Y., and Wu, Z. (2017). Multiscale modeling elastic properties of cement-based materials considering imperfect interface effect. *Construction and Building Materials*, 154:567–579.

[Liu et al., 2018] Liu, Z., Shao, J., Xie, S., Conil, N., and Zha, W. (2018). Effects of relative humidity and mineral compositions on creep deformation and failure of a claystone under compression. *International Journal of Rock Mechanics and Mining Sciences*, 103:68–76.

[Liu et al., 2015] Liu, Z., Xie, S., Shao, J.-F., and Conil, N. (2015). Effects of deviatoric stress and structural anisotropy on compressive creep behavior of a clayey rock. *Applied Clay Science*, 114:491–496.

[Louis et al., 2007] Louis, L., Baud, P., and Wong, T.-F. (2007). Characterization of pore-space heterogeneity in sandstone by x-ray computed tomography. *Geological Society, London, Special Publications*, 284(1):127–146.

[Ma et al., 2017] Ma, L., Taylor, K. G., Dowey, P. J., Courtois, L., Gholinia, A., and Lee, P. D. (2017). Multi-scale 3d characterisation of porosity and organic matter in shales with variable toc content and thermal maturity: Examples from the lublin and baltic basins, poland and lithuania. *International Journal of Coal Geology*, 180:100–112.

[Madou and Leblond, 2013] Madou, K. and Leblond, J.-B. (2013). Numerical studies of porous ductile materials containing arbitrary ellipsoidal voids–i: Yield surfaces of representative cells. *European Journal of Mechanics-A/Solids*, 42:480–489.

[Maghous et al., 2009] Maghous, S., Dormieux, L., and Barthélémy, J. (2009). Micromechanical approach to the strength properties of frictional geomaterials. *European Journal of Mechanics-A/Solids*, 28(1):179–188.

© 2018 Tous droits réservés. lilliad.univ-lille.fr

Thèse de Yajun Cao, Université de Lille, 2018

[Masson et al., 2000] Masson, R., Bornert, M., Suquet, P., and Zaoui, A. (2000). An affine formulation for the prediction of the effective properties of nonlinear composites and polycrystals. *Journal of the Mechanics and Physics of Solids*, 48(6):1203–1227.

[Matouš et al., 2017] Matouš, K., Geers, M. G., Kouznetsova, V. G., and Gillman, A. (2017). A review of predictive nonlinear theories for multiscale modeling of heterogeneous materials. *Journal of Computational Physics*, 330:192–220.

[Menaceur et al., 2015] Menaceur, H., Delage, P., Tang, A.-M., and Conil, N. (2015). The thermo-mechanical behaviour of the callovo-oxfordian claystone. *International Journal of Rock Mechanics and Mining Sciences*, 78:290–303.

[Michel et al., 2001] Michel, J., Moulinec, H., and Suquet, P. (2001). A computational scheme for linear and non-linear composites with arbitrary phase contrast. *International Journal for Numerical Methods in Engineering*, 52(1-2):139–160.

[Michel and Suquet, 1992] Michel, J. and Suquet, P. (1992). The constitutive law of nonlinear viscous and porous materials. *Journal of the Mechanics and Physics of Solids*, 40(4):783–812.

[Michel et al., 1999] Michel, J.-C., Moulinec, H., and Suquet, P. (1999). Effective properties of composite materials with periodic microstructure: a computational approach. *Computer methods in applied mechanics and engineering*, 172(1-4):109–143.

[Michel and Suquet, 2004] Michel, J.-C. and Suquet, P. (2004). Computational analysis of nonlinear composite structures using the nonuniform transformation field analysis. *Computer methods in applied mechanics and engineering*, 193(48):5477–5502.

[Miled et al., 2011] Miled, K., Sab, K., and Le Roy, R. (2011). Effective elastic properties of porous materials: Homogenization schemes vs experimental data. *Mechanics Research Communications*, 38(2):131–135.

[Monchiet and Bonnet, 2012] Monchiet, V. and Bonnet, G. (2012). A polarization-based fft iterative scheme for computing the effective properties of elastic composites with arbitrary contrast. *International Journal for Numerical Methods in Engineering*, 89(11):1419–1436.

[Monchiet et al., 2009] Monchiet, V., Bonnet, G., and Lauriat, G. (2009). A fft-based method to compute the permeability induced by a stokes slip flow through a porous medium. *Comptes Rendus Mécanique*, 337(4):192–197.

© 2018 Tous droits réservés. lilliad.univ-lille.fr

Thèse de Yajun Cao, Université de Lille, 2018

[Monchiet et al., 2008] Monchiet, V., Cazacu, O., Charkaluk, E., and Kondo, D. (2008). Macroscopic yield criteria for plastic anisotropic materials containing spheroidal voids. *International Journal of Plasticity*, 24(7):1158–1189.

[Monchiet et al., 2007] Monchiet, V., Charkaluk, E., and Kondo, D. (2007). An improvement of gurson-type models of porous materials by using eshelby-like trial velocity fields. *Comptes Rendus Mécanique*, 335(1):32–41.

[Monchiet et al., 2011] Monchiet, V., Charkaluk, E., and Kondo, D. (2011). A micromechanics-based modification of the gurson criterion by using eshelby-like velocity fields. *European Journal of Mechanics-A/Solids*, 30(6):940–949.

[Monchiet et al., 2014] Monchiet, V., Charkaluk, E., and Kondo, D. (2014). Macroscopic yield criteria for ductile materials containing spheroidal voids: an eshelby-like velocity fields approach. *Mechanics of Materials*, 72:1–18.

[Monchiet et al., 2006] Monchiet, V., Gruescu, C., Charkaluk, E., and Kondo, D. (2006). Approximate yield criteria for anisotropic metals with prolate or oblate voids. *Comptes Rendus Mecanique*, 334(7):431–439.

[Monfared and Ulm, 2016] Monfared, S. and Ulm, F.-J. (2016). A molecular informed poroelastic model for organic-rich, naturally occurring porous geocomposites. *Journal of the Mechanics and Physics of Solids*, 88:186–203.

[Mori and Tanaka, 1973] Mori, T. and Tanaka, K. (1973). Average stress in matrix and average elastic energy of materials with misfitting inclusions. *Acta metallurgica*, 21(5):571–574.

[Moulinec and Silva, 2014] Moulinec, H. and Silva, F. (2014). Comparison of three accelerated fft-based schemes for computing the mechanical response of composite materials. *International Journal for Numerical Methods in Engineering*, 97(13):960–985.

[Moulinec and Suquet, 1994] Moulinec, H. and Suquet, P. (1994). A fast numerical method for computing the linear and nonlinear mechanical properties of composites. *Comptes rendus de l'Académie des sciences. Série II, Mécanique, physique, chimie, astronomie*, 318(11):1417–1423.

[Moulinec and Suquet, 1998] Moulinec, H. and Suquet, P. (1998). A numerical method for computing the overall response of nonlinear composites with complex microstructure. *Computer methods in applied mechanics and engineering*, 157(1):69–94.

© 2018 Tous droits réservés. lilliad.univ-lille.fr

Thèse de Yajun Cao, Université de Lille, 2018

[Ortega et al., 2011] Ortega, J. A., Gathier, B., and Ulm, F.-J. (2011). Homogenization of cohesive-frictional strength properties of porous composites: Linear comparison composite approach. *Journal of Nanomechanics and Micromechanics*, 1(1):11–23.

[Ortega and Ulm, 2013] Ortega, J. A. and Ulm, F.-J. (2013). Strength homogenization of double-porosity cohesive-frictional solids. *Journal of Applied Mechanics*, 80(2):020902.

[Ougier-Simonin et al., 2016] Ougier-Simonin, A., Renard, F., Boehm, C., and Vidal-Gilbert, S. (2016). Microfracturing and microporosity in shales. *Earth-Science Reviews*, 162:198–226.

[Özdemir et al., 2008] Özdemir, I., Brekelmans, W., and Geers, M. G. (2008). Fe2 computational homogenization for the thermo-mechanical analysis of heterogeneous solids. *Computer Methods in Applied Mechanics and Engineering*, 198(3-4):602–613.

[Parisio and Laloui, 2017] Parisio, F. and Laloui, L. (2017). Plastic-damage modeling of saturated quasi-brittle shales. *International Journal of Rock Mechanics and Mining Sciences*, 93:295–306.

[Pastor et al., 2013] Pastor, F., Kondo, D., and Pastor, J. (2013). Limit analysis and computational modeling of the hollow sphere model with a mises–schleicher matrix. *International Journal of Engineering Science*, 66:60–73.

[Pastor et al., 2010] Pastor, J., Thoré, P., and Pastor, F. (2010). Limit analysis and numerical modeling of spherically porous solids with coulomb and drucker–prager matrices. *Journal of computational and applied mathematics*, 234(7):2162–2174.

[Perzyna, 1963] Perzyna, P. (1963). The constitutive equations for rate sensitive plastic materials. *Quarterly of applied mathematics*, 20(4):321–332.

[Pietruszczak et al., 2004] Pietruszczak, S., Lydzba, D., and Shao, J.-F. (2004). Description of creep in inherently anisotropic frictional materials. *Journal of Engineering Mechanics*, 130(6):681–690.

[Ponte Castañeda, 2002] Ponte Castañeda, P. (2002). Second-order homogenization estimates for nonlinear composites incorporating field fluctuations: I-theory. *Journal of the Mechanics and Physics of Solids*, 50(4):737–757.

[Ponte Castañeda and Willis, 1995] Ponte Castañeda, P. and Willis, J. R. (1995). The effect of spatial distribution on the effective behavior of composite materials and cracked media. *Journal of the Mechanics and Physics of Solids*, 43(12):1919–1951.

© 2018 Tous droits réservés. lilliad.univ-lille.fr

Thèse de Yajun Cao, Université de Lille, 2018

[Qi et al., 2016] Qi, M., Shao, J., Giraud, A., Zhu, Q., and Colliat, J. (2016). Damage and plastic friction in initially anisotropic quasi brittle materials. *International Journal of Plasticity*, 82:260–282.

[Reuss, 1929] Reuss, A. (1929). Berechnung der fließgrenze von mischkristallen auf grund der plastizitätsbedingung für einkristalle. *ZAMM-Journal of Applied Mathematics and Mechanics/Zeitschrift für Angewandte Mathematik und Mechanik*, 9(1):49–58.

[Robinet, 2008] Robinet, J.-C. (2008). *Minéralogie, porosité et diffusion des solutés dans l'argilite du Callovo-Oxfordien de Bure (Meuse, Haute-Marne, France) de l'échelle centimétrique à micrométrique.* PhD thesis, Université de Poitiers. UFR des sciences fondamentales et appliquées.

[Robinet et al., 2012] Robinet, J.-C., Sardini, P., Coelho, D., Parneix, J.-C., Prêt, D., Sammartino, S., Boller, E., and Altmann, S. (2012). Effects of mineral distribution at mesoscopic scale on solute diffusion in a clay-rich rock: Example of the callovo-oxfordian mudstone (bure, france). *Water Resources Research*, 48(5).

[Roussette et al., 2009] Roussette, S., Michel, J.-C., and Suquet, P. (2009). Nonuniform transformation field analysis of elastic–viscoplastic composites. *Composites Science and Technology*, 69(1):22–27.

[Saif et al., 2017a] Saif, T., Lin, Q., Bijeljic, B., and Blunt, M. J. (2017a). Microstructural imaging and characterization of oil shale before and after pyrolysis. *Fuel*, 197:562–574.

[Saif et al., 2017b] Saif, T., Lin, Q., Butcher, A. R., Bijeljic, B., and Blunt, M. J. (2017b). Multi-scale multi-dimensional microstructure imaging of oil shale pyrolysis using x-ray micro-tomography, automated ultra-high resolution sem, maps mineralogy and fib-sem. *Applied energy*, 202:628–647.

[Salari et al., 2004] Salari, M., Saeb, S., Willam, K., Patchet, S., and Carrasco, R. (2004). A coupled elastoplastic damage model for geomaterials. *Computer methods in applied mechanics and engineering*, 193(27-29):2625–2643.

[Saxena and Mavko, 2016] Saxena, N. and Mavko, G. (2016). Estimating elastic moduli of rocks from thin sections: digital rock study of 3d properties from 2d images. *Computers & Geosciences*, 88:9–21.

[Shao et al., 2006] Shao, J.-F., Jia, Y., Kondo, D., and Chiarelli, A.-S. (2006). A coupled elastoplastic damage model for semi-brittle materials and extension to unsaturated conditions. *Mechanics of materials*, 38(3):218–232.

© 2018 Tous droits réservés.

lilliad.univ-lille.fr

Thèse de Yajun Cao, Université de Lille, 2018

[Shao et al., 2003] Shao, J.-F., Zhu, Q.-Z., and Su, K. (2003). Modeling of creep in rock materials in terms of material degradation. *Computers and Geotechnics*, 30(7):549–555.

[Shen et al., 2014] Shen, W., He, Z., Dormieux, L., and Kondo, D. (2014). Effective strength of saturated double porous media with a drucker–prager solid phase. *International Journal for Numerical and Analytical Methods in Geomechanics*, 38(3):281–296.

[Shen et al., 2011] Shen, W., Lin, J., Zhu, Q.-Z., Monchiet, V., and Kondo, D. (2011). Macroscopic yield criterion for ductile materials containing randomly oriented spheroidal cavities. *International Journal of Damage Mechanics*, 20(8):1198–1216.

[Shen and Shao, 2016a] Shen, W. and Shao, J. (2016a). An incremental micro-macro model for porous geomaterials with double porosity and inclusion. *International Journal of Plasticity*, 83:37–54.

[Shen et al., 2017a] Shen, W., Shao, J.-F., and Kondo, D. (2017a). Macroscopic criteria for green type porous materials with spheroidal voids: application to double porous materials. *International Journal for Numerical and Analytical Methods in Geomechanics*, 41(13):1453–1473.

[Shen et al., 2012a] Shen, W., Shao, J.-F., Kondo, D., and Gatmiri, B. (2012a). A micro–macro model for clayey rocks with a plastic compressible porous matrix. *International journal of plasticity*, 36:64–85.

[Shen et al., 2017b] Shen, W., Zhang, J., Shao, J., and Kondo, D. (2017b). Approximate macroscopic yield criteria for drucker-prager type solids with spheroidal voids. *International Journal of Plasticity*, 99:221–247.

[Shen et al., 2013] Shen, W. Q., Kondo, D., Dormieux, L., and Shao, J. (2013). A closed-form three scale model for ductile rocks with a plastically compressible porous matrix. *Mechanics of Materials*, 59:73–86.

[Shen et al., 2015a] Shen, W. Q., Oueslati, A., and De Saxce, G. (2015a). Macroscopic criterion for ductile porous materials based on a statically admissible microscopic stress field. *International Journal of Plasticity*, 70:60–76.

[Shen and Shao, 2016b] Shen, W. Q. and Shao, J. F. (2016b). An elastic-plastic model for porous rocks with two populations of voids. *Computers and Geotechnics*, 76:194–200.

© 2018 Tous droits réservés. lilliad.univ-lille.fr

Thèse de Yajun Cao, Université de Lille, 2018

[Shen et al., 2015b] Shen, W. Q., Shao, J. F., Kondo, D., and De Saxcé, G. (2015b). A new macroscopic criterion of porous materials with a mises-schleicher compressible matrix. *European Journal of Mechanics-A/Solids*, 49:531–538.

[Shen et al., 2012b] Shen, W. Q., Shao, J. F., Kondo, D., and Gatmiri, B. (2012b). A micro-macro model for clayey rocks with a plastic compressible porous matrix. *International Journal of Plasticity*, 36:64–85.

[Talbot and Willis, 1985] Talbot, D. and Willis, J. (1985). Variational principles for inhomogeneous non-linear media. *IMA Journal of Applied Mathematics*, 35(1):39–54.

[Tandon and Weng, 1988] Tandon, G. and Weng, G. (1988). A theory of particle-reinforced plasticity. *Journal of Applied Mechanics*, 55(1):126–135.

[Tandon and Gupta, 2013] Tandon, R. S. and Gupta, V. (2013). The control of mineral constituents and textural characteristics on the petrophysical & mechanical (pm) properties of different rocks of the himalaya. *Engineering Geology*, 153:125–143.

[Tu u grul and Zarif, 1999] Tu u grul, A. and Zarif, I. (1999). Correlation of mineralogical and textural characteristics with engineering properties of selected granitic rocks from turkey. *Engineering Geology*, 51(4):303–317.

[Tvergaard, 1981] Tvergaard, V. (1981). Influence of voids on shear band instabilities under plane strain conditions. *International Journal of fracture*, 17(4):389–407.

[Tvergaard and Needleman, 1984] Tvergaard, V. and Needleman, A. (1984). Analysis of the cup-cone fracture in a round tensile bar. *Acta metallurgica*, 32(1):157–169.

[Uchic et al., 2006] Uchic, M. D., Groeber, M. A., Dimiduk, D. M., and Simmons, J. (2006). 3d microstructural characterization of nickel superalloys via serial-sectioning using a dual beam fib-sem. *Scripta Materialia*, 55(1):23–28.

[Ündül, 2016] Ündül, Ö. (2016). Assessment of mineralogical and petrographic factors affecting petro-physical properties, strength and cracking processes of volcanic rocks. *Engineering Geology*, 210:10–22.

[Vincent et al., 2009a] Vincent, P.-G., Monerie, Y., and Suquet, P. (2009a). Porous materials with two populations of voids under internal pressure: I. instantaneous constitutive relations. *International Journal of Solids and Structures*, 46(3):480–506.

© 2018 Tous droits réservés. lilliad.univ-lille.fr

Thèse de Yajun Cao, Université de Lille, 2018

[Vincent et al., 2009b] Vincent, P.-G., Monerie, Y., and Suquet, P. (2009b). Porous materials with two populations of voids under internal pressure: Ii. growth and coalescence of voids. *International Journal of Solids and Structures*, 46(3):507 – 526.

[Vincent et al., 2014a] Vincent, P.-G., Suquet, P., Monerie, Y., and Herv?Moulinec (2014a). Effective flow surface of porous materials with two populations of voids under internal pressure: Ii. full-field simulations. *International Journal of Plasticity*, 56:74 – 98.

[Vincent et al., 2014b] Vincent, P.-G., Suquet, P., Monerie, Y., and Moulinec, H. (2014b). Effective flow surface of porous materials with two populations of voids under internal pressure: Ii. full-field simulations. *International Journal of Plasticity*, 56:74–98.

[Voigt, 1889] Voigt, W. (1889). Ueber die beziehung zwischen den beiden elasticitätsconstanten isotroper körper. *Annalen der physik*, 274(12):573–587.

[Weng, 1984] Weng, G. (1984). Some elastic properties of reinforced solids, with special reference to isotropic ones containing spherical inclusions. *International Journal of Engineering Science*, 22(7):845–856.

[Willis, 1977] Willis, J. (1977). Bounds and self-consistent estimates for the overall properties of anisotropic composites. *Journal of the Mechanics and Physics of Solids*, 25(3):185–202.

[Willis, 1983] Willis, J. R. (1983). The overall elastic response of composite materials. *Journal of applied mechanics*, 50(4b):1202–1209.

[Wong et al., 2001] Wong, T.-f., Baud, P., and Klein, E. (2001). Localized failure modes in a compactant porous rock. *Geophysical Research Letters*, 28(13):2521–2524.

[Wong et al., 1997] Wong, T.-f., David, C., and Zhu, W. (1997). The transition from brittle faulting to cataclastic flow in porous sandstones: Mechanical deformation. *Journal of Geophysical Research: Solid Earth*, 102(B2):3009–3025.

[Xie et al., 2012] Xie, N., Zhu, Q.-Z., Shao, J.-F., and Xu, L.-H. (2012). Micromechanical analysis of damage in saturated quasi brittle materials. *International Journal of Solids and Structures*, 49(6):919–928.

[Zeman et al., 2010] Zeman, J., Vondr̲ejc, J., Novák, J., and Marek, I. (2010). Accelerating a fft-based solver for numerical homogenization of periodic media by conjugate gradients. *Journal of Computational Physics*, 229(21):8065–8071.

© 2018 Tous droits réservés. lilliad.univ-lille.fr

Thèse de Yajun Cao, Université de Lille, 2018

[Zhang et al., 2014] Zhang, F., Shao, J. F., et al. (2014). Experimental study of poromechanical behavior of saturated claystone under triaxial compression. *Acta Geotechnica*, 9(2):207–214.

[Zhang et al., 2012] Zhang, F., Xie, S., Hu, D., Shao, J.-F., and Gatmiri, B. (2012). Effect of water content and structural anisotropy on mechanical property of claystone. *Applied Clay Science*, 69:79–86.

[Zhao et al., 2016] Zhao, L., Zhu, Q., Xu, W., Dai, F., and Shao, J.-F. (2016). A unified micromechanics-based damage model for instantaneous and time-dependent behaviors of brittle rocks. *International Journal of Rock Mechanics and Mining Sciences*, 84:187–196.

[Zheng and Du, 2001] Zheng, Q.-S. and Du, D.-X. (2001). An explicit and universally applicable estimate for the effective properties of multiphase composites which accounts for inclusion distribution. *Journal of the Mechanics and Physics of Solids*, 49(11):2765–2788.

[Zhou et al., 2008a] Zhou, H., Jia, Y., and Shao, J. (2008a). A unified elastic-plastic and viscoplastic damage model for quasi-brittle rocks. *International Journal of Rock Mechanics and Mining Sciences*, 45:1237–1251.

[Zhou et al., 2008b] Zhou, H., Jia, Y., and Shao, J.-F. (2008b). A unified elastic–plastic and viscoplastic damage model for quasi-brittle rocks. *International Journal of Rock Mechanics and Mining Sciences*, 45(8):1237–1251.

[Zhu and Shao, 2017] Zhu, Q. and Shao, J. (2017). Micromechanics of rock damage: Advances in the quasi-brittle field. *Journal of Rock Mechanics and Geotechnical Engineering*, 9(1):29–40.

[Zhu et al., 2016] Zhu, Q., Zhao, L., and Shao, J. (2016). Analytical and numerical analysis of frictional damage in quasi brittle materials. *Journal of the Mechanics and Physics of Solids*, 92:137–163.

[Zhu et al., 2009] Zhu, Q.-Z., Kondo, D., and Shao, J.-F. (2009). Homogenization-based analysis of anisotropic damage in brittle materials with unilateral effect and interactions between microcracks. *International Journal for Numerical and Analytical Methods in Geomechanics*, 33(6):749–772.

[Zohdi and Wriggers, 2008] Zohdi, T. I. and Wriggers, P. (2008). *An introduction to computational micromechanics*. Springer Science & Business Media.

© 2018 Tous droits réservés.

lilliad.univ-lille.fr

Thèse de Yajun Cao, Université de Lille, 2018

© 2018 Tous droits réservés. lilliad.univ-lille.fr